Title

Quantum-Field Effects in Ultrafast Nonlinear X-Ray and Optical Spectroscopy of Molecules

Author

Bennett, Kochise

Publication Date

2017

UNIVERSITY OF CALIFORNIA,
IRVINE

Quantum-Field Effects in Ultrafast Nonlinear X-Ray and Optical Spectroscopy of Molecules

DISSERTATION

submitted in partial satisfaction of the requirements
for the degree of

DOCTOR OF PHILOSOPHY

in Physics

by

Kochise Bennett

Dissertation Committee:
Professor Shaul Mukamel, Chair
Professor Craig Martens
Professor Eric Potma

2017

TABLE OF CONTENTS

Page

LIST OF FIGURES **iv**

ACKNOWLEDGMENTS **viii**

CURRICULUM VITAE **x**

ABSTRACT OF THE DISSERTATION **xi**

1 Introduction **1**
- 1.1 Background 2
  - 1.1.1 Outline 8

2 Light Scattering and Spontaneous Emission **11**
  - 2.0.2 Change in Photon Number 12
  - 2.0.3 Electric Field Intensity 16
- 2.1 Pump-Probe X-Ray Diffraction 29
  - 2.1.1 Ordered *vs.* Disordered Samples 31
- 2.2 Frequency-Resolved Diffraction of a Single Cysteine Molecule 33
- 2.3 Time-Resolved Diffraction of Nonadiabatic Molecular Dynamics 41
  - 2.3.1 Application to the Nonadiabatic Avoided-Crossing Dynamics in NaF 46
- 2.4 Discussion 49

3 Many-Body Effects; Cascading **55**
- 3.1 Direct *vs.* Cascading Signals 59
  - 3.1.1 Microscopic Derivation of Cascading Signals 64
  - 3.1.2 Alternative Derivation of the Macroscopic Homogeneous Limit 71
  - 3.1.3 Field Vacuum Expectation Value 73
- 3.2 Sample Geometry Determines the Phase of the Cascading Signal 75
  - 3.2.1 A Simplified Treatment for a Scalar Field 76
  - 3.2.2 The Vector Guage Field 80
- 3.3 Conclusions 82

4 Molecules in Optical Cavities **86**
- 4.1 Molecule-Cavity Coupling in the Rotating Wave Approximation 90
  - 4.1.1 Photochemistry in the Strong-Coupling Regime 95

4.2 Molecule-Cavity Coupling Beyond the Rotating Wave Approximation 101
  4.2.1 Application to Avoided Crossing in Sodium Iodide 104
  4.2.2 Wavepacket Simulations and the Field Quadrature 108
4.3 Discussion 114

5 Conclusion **118**

Bibliography **122**

A Definitions and Useful Formulas **138**
A.1 The Electronic Charge Density Operator 139
  A.1.1 The One-Electron Charge Density Operator of a Many-Electron System 140
A.2 Frequency-Dispersed Photon Number Change 141

B Simulation Methods **145**
B.1 X-Ray Scattering and Raman Excitation of Cysteine 145
B.2 Electronic Structure Calculations and Nonadiabatic Wavepacket Dynamics of NaF 146
B.3 Model Parameters for Cavity-Modified Photochemistry 151

C Geometric Derivations for Cascading **153**
C.1 Cylindrical Geometry 153
C.2 Integration Measure for Inhomogeneous Coordinates 156
  C.2.1 Polar Coordinates 156
  C.2.2 Spherical Coordinates 158
  C.2.3 Estimates for the Boundary Contributions Using the Saddle-Point Approximation 158

D Cavity-Molecule Coupling Beyond the Rotating Wave Approximation **160**
D.1 Working Formulas for the Tunable-Coherent-State Basis 160
D.2 Derivation of the Non-BOA Couplings 163
D.3 Normalization 167
D.4 Summary of Formulas 169

LIST OF FIGURES

Page

2.1 (i) Loop diagram representing light scattering and spontaneous emission as obtained from the photon-number-change approach. In the minimal coupling, this corresponds to Eq. (2.12) and the material operator that accompany the interaction arrows is the current $\hat{\mathbf{J}}$. If the field-matter interaction is dipolar, the same diagram pertains but with the material operator associated with interaction arrows then being the transition dipole operator. The shaded area represents an unspecified process that prepares the system in an arbitrary state. We denote the signal modes s, s'. (ii) Loop diagram representing bare spectrogram for light scattering and spontaneous emission calculated as the gated field intensity at a detector. Photon emission at the material sample is shown with blue arrows while photon absorption at the detector is shown with red arrows. For example, Eq. (2.33) is represented by this diagram when the field-matter interaction is treated in the minimal coupling and only the off-resonant scattering is considered. In this case, the material operator associated with the interaction arrows would be the charge density operator. 17

2.2 Loop diagrams for single- (i) and two-molecule (ii) x-ray scattering processes. The shaded area represents an unspecified process that prepares the system in an arbitrary state ($|g\rangle$ is the electronic ground state) and T is the pump-probe delay time. The amplitude-squared form of the two-molecule contribution is explicitly indicated. We denote modes of the pump with p and p' whereas s, s' represent relevant scattering modes ($\mathbf{k}_{p(')}$ has frequency $\omega_{p(')}$ and $\mathbf{k}_{s(')}$ has frequency $\omega_{s(')}$). Elastic scattering corresponds to $\omega_{ki} = \omega_{kj} = 0$ for the single-molecule and $\omega_{ij} = \omega_{kl} = 0$ for the two-molecule contributions. Elastic scattering therefore originates from scattering off populations. For diagram rules, see [64, 88] 32

2.3 Off-resonant scattering of a Gaussian x-ray pulse from cysteine for different detection frequencies. On the right we show the pulse power spectrum in blue, with the detection frequency marked as a red line. The pulse propagation vector is shown as a red arrow, pointing at the molecule aligned in the lab frame, with the scattering pattern shown in the background. **a**: The detection frequency ω_s is set equal to the pulse center frequency Ω_p, and the scattering signal is dominated by the elastic term. **b**: The detection frequency is set to $\Omega_p - 9\,\text{eV}$, and the inelastic terms are dominant. **c**: Chemical structure (left) and lab-frame orientation (right) of the cysteine molecule (O is red, S is green, N is blue, C is grey, H is white. 36

2.4 Background: time-dependent x-ray scattering (with $\omega_s = \Omega_p$) following x-ray Raman scattering (equation (2.77)) for various interpulse delay times. Foreground: real-space transition charge densities for the Raman wavepacket (equation (2.78)). Refer to Fig. 2.3c for the positions lab-frame orientation. . 39

2.5 Time-dependence of the off-resonant x-ray scattering plot (with $\omega_s = \Omega_p$). Left: The scattering signal for $T = 5\,\text{fs}$, with six different features labeled. Right: The evolution of these different features with increasing interpulse delay. 40

2.6 Variation of the six features in the $T = 0\,\text{fs}$ scattering signal in Fig. (5) with detection frequency ω_s and delay time T. 40

2.7 Ground state contributions to the gas phase diffraction signal of NaF ($S_1(q,T)$) : (a) $\rho_{gg}\langle\chi_g(t)|\hat{\sigma}^\dagger_{gg}\hat{\sigma}_{gg}|\chi_g(t)\rangle$, (b) $\rho_{gg}\langle\chi_g(t)|\hat{\sigma}^\dagger_{eg}\hat{\sigma}_{ge}|\chi_g(t)\rangle$. Probe pulse length 2.5 fs (FWHM). 47

2.8 Contributions to the real space signal $S_1(q_z,T)$ (Fourier transform of $S_1(q_z,T)$) of the electronic ground state: The various panels are in the same order as in Fig. 2.10: (a) Contribution from $\hat{\sigma}^2_{gg}$, (b) $\hat{\sigma}^\dagger_{gg}\hat{\sigma}_{eg}$ and $\hat{\sigma}^\dagger_{gg}\hat{\sigma}_{eg}$. Signal intensities are relative to Fig. 2.10(a). 48

2.9 Relevant adiabatic potential energy surfaces of NaF (ionic $X^1\Sigma$ black, covalent $A^1\Sigma$, blue, $^1\Pi$, red). 49

2.10 Excited state contributions to the gas-phase diffraction signal of NaF ($S_1(q,T)$) : (a) $\rho_{ee}\langle\chi_e(t)|\hat{\sigma}^\dagger_{ee}\hat{\sigma}_{ee}|\chi_e(t)\rangle$, (b) $2\Re\big[\rho_{eg}(t)\langle\chi_e(t)|\hat{\sigma}^\dagger_{ee}\hat{\sigma}_{eg} + \hat{\sigma}^\dagger_{eg}\hat{\sigma}_{gg}|\chi_g(t)\rangle\big]$, (c) $\rho_{ee}\langle\chi_e(t)|\hat{\sigma}^\dagger_{eg}\hat{\sigma}_{ge}|\chi_e(t)\rangle$. Signal intensities are relative to (a). Probe pulse length 2.5 fs (FWHM). 50

2.11 Contributions to the real space signal $S_1(q_z,T)$ (Fourier transform of $S_1(z,T)$). The various panels are in the same order as in Fig. 2.10: (a) Contribution from $\hat{\sigma}^2_{ee}$, (b) $\hat{\sigma}^\dagger_{ee}\hat{\sigma}_{eg}$ and $\hat{\sigma}^\dagger_{gg}\hat{\sigma}_{eg}$, (c) $\hat{\sigma}^2_{ge}$. Signal intensities are relative to (a). . . . 51

3.1 This diagram depicts the material quantities relevant for an arbitrary cascading (or, more generally, 2nd-order vacuum-mediated interaction) contribution. The vertical lines represent the density matrices of molecule a or b and associated propagators. We use doubled lines to clarify that the propagation is with respect to the full Hamiltonian, including interactions with externally applied fields, and not simply the free material propagation. The straight intersecting the density matrices of molecule a represents the heterodyne signal field while the wavy lines represent interactions with vacuum modes. In contrast to the more familiar double-sided Feynman diagrams, we make no distinction between action on the ket or bra. This is permissible since we work in Liouville space and convenient since it permits us to work in the $+/-$ representation in which the Liouvillian H_- is more compactly written. This therefore greatly reduces the number of diagrams. Since we work in the $+/-$ representation and without the rotating wave approximation, dressing the interactions with arrows (to indicate positive or negative Fourier components) is unneccesary. This diagram corresponds to the quantities relevant for equation (3.13). . . . 65

4.1 (Upper) Schematic depiction of the Hamiltonian. Under the RWA, $\hat{H}$ has a block-diagonal structure. Each block with nonzero total excitation number is 2-by-2 and composed, in this basis, of $|e, n_c\rangle, |g, n_c + 1\rangle$. Adding back in the counter-rotating terms couples states that differ by 2 in total excitation number $\hat{N}$. (Lower) The simultaneous eigenstates of parity and excitation number. States with even (odd) excitation number have even (odd) parity. . 88
4.2 (a) Bare state PESs used for the photonic catalyst model as well as the photonic bound state model. The minimum of the S_2 state is displaced by 0.3 Å with respect to the ground state. (b) Transition dipole curve used in the different models. The parameters for the model are given in Appendix B.3. . 95
4.3 (a) Dressed state PESs for the photonic-catalyst model. The S_2 state is now coupled to the dissociative state. (b) Non-adiabatic coupling matrix element for the polariton states. Dominated by the gradient difference term of Eq. 4.15. Parameters: $g = 54\,\mathrm{meV}$ 96
4.4 Transition dipole moments in the dressed state basis for the photonic-catalyst model: μ_{g+} (red), μ_{g-} (blue),μ_{-+} (black). 97
4.5 (a) Populations of the dressed states $|+\rangle$ (red) and $|-\rangle$ (blue) in the photonic catalyst model *vs.* time. The decay of the $|+\rangle$ state can be fitted to a bi-exponential model yielding the time constants 228 fs and 42 ps. (b) Transient absorption signal in depenence of the probe delay T and. The laser is set to be resonant between S_1 and the $|\pm\rangle$ state (1.5 eV) and has a pulse length of 10 fs (FWHM). The dashed line is the signal for a wave packet in the S_2 bare state potential. 98
4.6 (a) Dressed state PESs for the photonic-bound-state model. (b) Non-adiabatic coupling matrix element causing transition between the dressed states. . . . 98
4.7 Tranistion dipole moments for the photonic-bound-state model in the dressed state basis: μ_{g+} (red), μ_{g-} (blue), μ_{-+} (black). 99

4.8 (a) Population of the dressed states $|+\rangle$ (red) and $|-\rangle$ (blue) in the photonic-bound-state model *vs.* time. The decay of the $|+\rangle$ state can be fitted to a bi-exponential model yielding the time constants 234 fs and 5.2 ps. (b) Transient absorption signal. Laser is set to be resonant between S_1 and the $|\pm\rangle$ state (1.5 eV) and has a pulse length of 10 fs (FWHM). The dashed line is the signal for a wave packet in the S_1 bare state potential 100
4.9 (a) Bare ground (^{1}X) and excited (^{1}A) electronic potential energy surfaces of NaI. Dissociation on the ^{1}X potential leads to the neutral reaction products. (b) Transition dipole moment μ_{eg} (blue) and the derivative coupling matrix element f_{eg} (red). 105
4.10 Potential curve crossings for two different cavity detunings: ground state potential wave function shifted by the cavity frequency ($V_g + \omega_c$), for $\omega_c =$ 815 meV (blue, dashed) and $\omega_c = 52.6$ meV (red, dashed). 106
4.11 Positive (red solid) and negative (black solid) parity electronic potential energy surfaces of NaI dressed with a $\omega_c = 815$ meV cavity mode obtained from Eq. (4.31) and the first five solutions to Eq. (4.33) with $\pi_l = +1$ and $\pi_l = -1$ respectively. Vertical gray lines indicate points where the bare states are resonant with integer multiples of the cavity frequency ($\omega_0 = n\omega_c$ for n an integer, $n = 1$ for the rightmost line and counts up going to the left). (a) Peak coupling of 200 meV. (b) Peak coupling of 300 meV. (c) Peak coupling of 600 meV. (d) Peak coupling of 1240 meV. 107
4.12 (a): Potential curves for the lowest energy positive-parity eigenstate (black) and the 4 lowest energy negative-parity eigenstates (upper) and their corresponding NACs (all couplings are betwen the "black" state and one of the others and therefore labeled by the color of the latter state). (b): Potential curves for the second-lowest positive-parity state (black) and the 4 lowest energy negative-parity eigenstates (upper) and their corresponding NACs. . . 109
4.13 (a): Potential curves (upper) and corresponding NACs (lower) for 3 different pairs of opposite-parity eigenstates. (b): Potential curves for 3 different pairs of same-parity eigenstates. Corresponding NACs are sharply peaked at the avoided crossings near the gray line and are otherwise negligible. 110
4.14 Cavity coupling with $\omega_c = 815$ meV. (a) Population of the covalent states after 480 fs for a cavity with initially zero photons (black) and one photons (blue) *vs.* the coupling strength. (b) Average photon number 480 fs. 113
4.15 Selected time traces of the ^{1}X state population ($\omega_c = 815$ meV). No cavity (black line), $g = (0.0502, 0.1256, 0.1884, 0.2512, 0.3793)$ red, blue, black, green, magenta respectively. 114

ACKNOWLEDGMENTS

I would foremost like to thank my adviser, Professor Shaul Mukamel, for all that he has done for me. There is an exciting dynamism about working in this research group and Professor Mukamel's passion and unflagging dedication to science are infectious; one cannot help but be inspired. So thank you Professor, for all that you have taught me; I will never forget the once-in-a-lifetime privilege it has been to learn under your guidance.

I would also like to thank my committee members, Professors Craig Martens and Eric Potma, for their generous contribution of time and effort as well as for our many enjoyable and enlightening discussions. I would like to thank all those incredible scientists and friends with whom I have worked in the Mukamel group over the years. They are too many to name in totality but doctors Konstantin Dorfman and Markus Kowalewski deserve some special mention. Both have been long-term mentors of mine from whom I have learned a great deal and to whom I owe much of my success. I would also like to thank my co-authors on the articles that formed this thesis: Dr. Yu Zhang, Dr. Konstantin Dorfman, Dr. Jason Biggs, Dr. Markus Kowalewski, Dr. Jeremy Rouxel, and Professor Vladimir Chernyak. This manuscript has only been possible because of their contributions.

I would also like to thank all the friends, far too numerous to list, who have been a valuable source of companionship and support both during my time at UC-Irvine and in years past. I would also like to sincerely thank my parents for all they have done for me and contributed to my education; my mother for personally seeing to my early years of education, my father for working tirelessly to support me through college, and to both for their unending love and support. Finally, I would like to thank my wife May, who has been by my side throughout my graduate studies. She is the best friend I've ever had and has brought a happiness to my life I never thought possible. Thank you my love, for celebrating my successes, supporting me through the hard times, and sharing life with me. You are an inspiration and a pillar of strength without which I would not be where I am.

The support of the Chemical Sciences, Geosciences, and Biosciences Division, Office of Basic Energy Sciences, Office of Science, U.S. Department of Energy through award #DE-FG02-04ER15571 is gratefully acknowledged as well as the support of the National Science Foundation (grant CHE-1361516).

Chapter 2, section 2.2 and associated portions of appendix adapted with permission from *J. Chem. Phys.* **140**, 204311. Copyright (2014) American Institute of Physics

Chapter 2, section 2.3 and associated portions of appendix adapted with permission from an article recently submitted to *Phys. Rev.*

Chapter 3, and associated portions of appendix adapted with permission from an article recently accepted by *Phys. Rev. A* (preprint arXiv:1702.00756)

Chapter 4, section 4.1 and associated portions of appendix adapted with permission from *J. Chem. Phys.* **144**, 054309. Copyright (2016) American Institute of Physics.

Chapter 4, section 4.2 and associated portions of appendix adapted with permission from *Faraday Discuss.* **144**, 054309. Copyright (2016) American Institute of Physics.

The co-authors listed in the above publications were instrumental in conducting the research on which this thesis reports.

CURRICULUM VITAE

Kochise Bennett

EDUCATION

Doctor of Philosophy in Physics **2017**
University of California-Irvine *Irvine, CA*

Master of Science in Physics **2016**
University of California-Irvine *Irvine, CA*

Bachelor of Science in Physics **2009**
University of California-Los Angeles *Los Angeles, CA*

RESEARCH EXPERIENCE

Graduate Research Assistant-Shaul Mukamel Group **2011–2017**
University of California, Irvine *Irvine, California*

TEACHING EXPERIENCE

Teaching Assistant-Introductory Graduate Laboratory Skills **Summer 2014–2016**
University of California, Irvine *Irvine, California*

Teaching Assistant-Graduate Molecular Spectroscopy **Spring 2012, 2013**
University of California, Irvine *Irvine, California*

Teaching Assistant **2010–2011**
University of California, Irvine *Irvine, California*

ABSTRACT OF THE DISSERTATION

Quantum-Field Effects in Ultrafast Nonlinear X-Ray and Optical Spectroscopy of Molecules

By

Kochise Bennett

Doctor of Philosophy in Physics

University of California, Irvine, 2017

Professor Shaul Mukamel, Chair

Spectroscopy, the study of matter via its interactions with light, is a vast subject that includes many of humanity's principle means of probing the fundamental structure of matter. Though usually understood from the perspective of classical light, important effects arise due to the quantum nature of the electromagnetic field. Additionally, the quantum vacuum can serve as an effective couple between molecules in the system, generating many-body interactions and cooperative processes in the material. While many techniques are well-described classically, quantum-field corrections can dominate the desired signals in certain cases, such as cascading in higher-order n-wave mixing signals, and are key for experimental interpretation. Even spontaneous emission and light scattering are best understood from the perspective of quantum fields. In this thesis, we utilize a systematic procedure, based on the density matrix in Liouville space, to give a rigorous description of elementary quantum-field effects in nonlinear spectroscopy, with specific examples made to ultrafast x-ray and optical techniques.

Chapter 1

Introduction

> "Light brings us the news of the Universe."
>
> *Sir William Bragg*
>
> The Universe of Light (1933)

We know the world through light. Spectroscopy, the study of light-matter interactions, encompasses a vast array of experimental techniques and forms the foundation for our understanding of much of the universe, from the makeup of stars to the structure and dynamics of atoms and molecules. Indeed, humanity's knowledge of the properties of light and of matter are historically concomitant and symbiotic. Accounting for spectral observables, such as blackbody radiation and atomic emission and absorption spectra, famously motivated early developments in quantum theory. The development of the laser opened up new possibilities to produce coherent light with a narrow spectral range, which allows the probing of molecules using precise frequencies, as well as short pulses of light that allow the temporal tracking of material quantities. Today, a variety of spectroscopic techniques are routinely employed to reveal the energy levels, dipolar couplings, and other quantities that reflect the structure and conformation of molecules and determine their dynamics.

Spectroscopic signals are commonly simulated by treating the material quantum mechanically but the electric field classically. This is known as the semiclassical approximation and is sufficient for understanding most techniques. However, many signals and effects are due to the quantum nature of light. Even the common phenomenon of spontaneous emission is best understood as the creation of a photon in a vacuum mode of the electromagnetic field, i.e., with a quantum description of the radiation field. Scattering processes, such as x-ray diffraction, are also best understood in these terms since the light-matter interaction generates photons in modes of the electromagnetic field that were unoccupied prior to the scattering event. The goal of this thesis is to provide an introduction to quantum-field effects in molecular spectroscopy and the formalism needed to calculate them. We begin with light scattering and spontaneous emission (Chapter 2). We specialize to the simple and illustrative example of x-ray scattering and mention some important recent results relevent for the ultrafast x-ray diffraction experiments. We then show that there is a deep connection between quantum-field and many-body effects and discuss one such many-body effect that has played a vexing role in the history of hyper-Raman experiments: cascading (Chapter 3). Finally, we discuss the possibility of actively utilizing coupling to quantum-field modes of an optical cavity to maniuplate chemical reactions (Chapter 4).

1.1 Background

Light-matter interactions at the molecular scale are conveniently described using atomic units, in which $e = m_e = \hbar = k_e = 1$ and we employ this system throughout the manuscript. We will not consider dissipative effects and all time evolutions will therefore be unitary. Nonetheless, derivations will generally be done in Liouville-space, where the system is described by a vectorized version of the density matrix $\rho = |\psi\rangle\langle\psi| \to |\rho\rangle\rangle$ (we consider only pure states since the evolution is unitary and we use a "double-ket" to indicate a Liouville-space vector). This allows convenient expression of the time propagator in terms of Liouville-space superoperators $\hat{O}_{L/R}$ and $\hat{O}_\pm$ defined by their equivalent action in Hilbert space:

$$\hat{O}_L|\rho\rangle\rangle \leftrightarrow \hat{O}\rho, \qquad \hat{O}_R|\rho\rangle\rangle \leftrightarrow \rho\hat{O} \tag{1.1}$$

$$\hat{O}_- = \hat{O}_L - \hat{O}_R, \qquad \hat{O}_+ = \frac{1}{2}\left(\hat{O}_L + \hat{O}_R\right) \tag{1.2}$$

where, in the first two relations, the left-hand-sides are in Liouville space and the right-hand-sides are written in Hilbert space. The assymetry in the definitions of $\hat{O}_\pm$ is so that a $-$ subscript exactly represents the commutator but we also have $\langle\hat{O}_L\rangle = \langle\hat{O}_R\rangle = \langle\hat{O}_+\rangle$ and, for any two commuting operators $\hat{A}, \hat{B}$, we have $(\hat{A}\hat{B})_- = \hat{A}_-\hat{B}_+ + \hat{A}_+\hat{B}_-$, which would otherwise carry factors of two. This identity is useful because the field-matter interaction Hamiltonian is a product of field and matter opertors and it will make an appearance in chapter 3. The time-dependent density matrix can then be compactly written as

$$|\rho(t)\rangle\rangle = \mathcal{T}e^{-i\int_{-\infty}^{t} dt'\hat{H}_-(t')}|\rho(-\infty)\rangle\rangle \tag{1.3}$$

where $\hat{H}$ is the Hamiltonian, $|\rho(-\infty)\rangle\rangle$ is the equilibrium density matrix, and $\mathcal{T}$ is the time-ordering operator, which re-arranges the order of operator products so that earlier times are to the right of later times [1]. Expectation values of operators are then evaluated *via* a trace

$$\langle\langle\mathbb{1}|\hat{O}_L|\rho\rangle\rangle \leftrightarrow \mathrm{Tr}\big[\hat{O}\rho\big] \tag{1.4}$$

Besides permitting compact representation of the various terms that arise in the perturbative evaluation of expectation values, performing derivations from the Liouville-space perspective allows one to more easily go back and generalize if environmental coupling is relevant. The total system Hamiltonian is the sum of material, field, and interaction components

$$\hat{H} = \hat{H}_0 + \hat{H}_\mathrm{F} + \hat{H}_\mathrm{int} \tag{1.5}$$

where $\hat{H}_0$ is the field-free material Hamiltonian and

$$\hat{H}_{\mathrm{F}} = \sum_{\mathbf{k},\lambda} \omega_{\mathbf{k}} \left(\hat{a}^{\dagger}_{\mathbf{k}_s\lambda} \hat{a}_{\mathbf{k}_s\lambda} + \frac{1}{2} \right) \tag{1.6}$$

is the Hamiltonian for the quantum electromagnetic field written as a mode sum with $\hat{a}^{(\dagger)}_{\mathbf{k}}$ the annihilation (creation) operators for photons in mode $\mathbf{k}$. Time evolution will be carried out in the interaction picture with respect to the non-interacting system $\hat{H}_0 + \hat{H}_{\mathrm{F}}$ [1].

The material hamiltonian $\hat{H}_0$ is the sum of the nuclear kinetic energy operator $\hat{T}$ and the electronic Hamiltonian $\hat{H}_{\mathrm{el}}(\mathbf{q})$, the latter of which is a function of the nuclear coordinates $\mathbf{q}$. When the nuclear kinetic energy is small compared to the electronic energy scales, we may employ the Born-Oppenheimer approximation, whereby the nuclear wavepacket evolves separately on the various potential energy surfaces determined by the $\mathbf{q}$-dependent eigenvalues of $\hat{H}_{\mathrm{el}}(\mathbf{q})$. Corrections to this picture arise when the electronic energy levels become nearby or cross each other [2, 3]. In these situations, nuclear wavepackets on nearby surfaces become coupled and so-called non-adiabatic transitions can occur between electronic states. Such non-adiabatic dynamics is extremely common and determine the outcomes and rates of a broad variety of photochemical and photophysical reactions [4, 5, 6, 7, 8]. Crossings in the potential surfaces, known as conical intersections, open up fast, non-radiative relaxation pathways by which the molecule is funneled back to the ground state, possibly avoiding a more violent fate such as dissosciation (as in the case of the photo-damage protection mechanism exhibited in the DNA bases [9, 10, 11]). Several of the signals we discuss will focus on detecting the passage of nuclear wavepackets through conical intersections. Such signals offer a probe of the ultrafast nonadiabatic dynamics and reveal information about the region of the conical intersection.

We will compute signals under one of two assumptions. If the spectroscopic experiment is temporally shorter than the reaction time of the nuclei, they may be taken as frozen and we may thus concern ourselves only with the electrons. Electronic energies and couplings are then the object of study in such circumstances. We term these signals "static" because, the electronic properties do not vary in time, though these signals still show time-dependence due to the evolution of nonstationary electronic states. These signals will ultimately be written in a sum-over-states fashion assuming we have diagonalized the electronic Hamiltonian. Frequently, the object of spectroscopic study is a chemical reaction or other molecular dynamics that involves nuclear motion. Complete diagonalization of the Hamiltonian is then impractical for all but the smallest molecules and signals are calculated by real-time propagation. Expansion in adiabatic electronic eigenstates is still useful for making analogy to static signals and pursuing quasi-static approximations [12]. In both cases, we will find it convenient to introduce the pump-probe conceptual framework, whereby we take as given an initial state that is the result of an arbitrary, unspecified pumping process that has completely terminated. We can then evolve the system freely for some variable time delay before analysis with a probe, which may consist of one or more pulses. As long as the pumping and probing processes are temporally well-separated, this dissection is unambiguous. This separation might be seen as artificial, any technique can just be described as a complex probe of the ground state, but it is useful to analyze what information about a given initial state may be obtained by a particular probing process. The arbitrary pumping process described here is depicted by a shaded gray rectange inside the loop diagrams that represent terms of the perturbative expansion of expectation values (see for example Figs. 2.1 and 2.2)

The light-matter interaction Hamiltonian is written according to the minimal coupling prescription $\hat{\mathbf{p}} \to \hat{\mathbf{p}} - \hat{\mathbf{A}}$ where $\hat{\mathbf{p}}$ is the momentum operator of the fermionic field and $\hat{\mathbf{A}}$ is the magnetic vector potential (see appendix A). This yields the interaction Hamiltonian

$$\hat{H}_{\text{int}}(t) = -\int d\mathbf{r} \left(\hat{\mathbf{j}}(\mathbf{r}, t) - \frac{1}{2}\hat{\sigma}(\mathbf{r}, t)\hat{\mathbf{A}}(\mathbf{r}, t) \right) \cdot \hat{\mathbf{A}}(\mathbf{r}, t) \tag{1.7}$$

where $\hat{\mathbf{j}}$ and $\hat{\sigma}$ are the elementary field-free current operator and the charge density operator respectively, defined also in appendix A. The first ($\hat{\mathbf{j}} \cdot \hat{\mathbf{A}}$) term in Eq. (1.7) is dominant when the externally applied fields are (near) resonant with material transitions while the second ($\hat{\sigma}\hat{\mathbf{A}}^2$) term dominates the response to off-resonant fields. This will be discussed in more detail in Chapter 2, where Eq. (1.7) will be used to obtain expressions for x-ray scattering.

The minimal coupling Hamiltonian is entirely general but requires undwieldy real-space integrations. It is well-known that a simpler form for the interaction can be obtained by making a canonical transformation to the so-called multipolar interaction Hamiltonian. This consists of an infinite series of interaction terms, the lowest order of which is the electric dipole interaction

$$\hat{H}_{\text{int}}(t) = -\int d\mathbf{r}\hat{\mathbf{E}}(\mathbf{r},t) \cdot \hat{\boldsymbol{\mathcal{V}}}(\mathbf{r},t) \tag{1.8}$$

where $\hat{\mathbf{E}}(t)$ is the electric field operator (defined in Appendix A) and $\hat{\boldsymbol{\mathcal{V}}}(\mathbf{r}) = \sum_\alpha \hat{\mathbf{V}}\delta(\mathbf{r}-\mathbf{r}_\alpha)$ is the total system dipole operator written as a sum over molecular dipoles. In this manuscript, we will take the sample to consist of identical molecules with non-overlapping charge distributions so that each molecule may be considered to have its own electron field (the generalization to non-idential molecules is not difficult but clutters the presentation). Intermolecular interactions will not be considered except as mediated through the electromagnetic field. The electric dipole approximation is appropriate for resonant or near-resonant interactions for which the spatial extent of the electronic states involved in the interaction is small compared to the wavelength of the impinging light [1, 13]. The light-matter interaction Hamiltonian given in Eq. (1.8) will be used to model pump-matter interaction throughout and will be used exclusively in Chapters 3-4

There are several levels of theory at which spectroscopic signals can be developed. One option is the so-called matter perspective, in which the change in energy of the material system due to interaction with the electromagnetic fields is calculated. In this thesis, we instead take the field perspective. This allows us to directly calculate the electromagnetic field quantity that is the actual observable in a spectroscopic experiment. Such an approach is obviously essential for signals dominated by elastic contributions such as x-ray diffraction.

From the field perspective, the simplest definition of the signal is then the time-integrated rate of change of photon number in some specified signal mode

$$S(\mathbf{k}_s, \Lambda) = \int dt \langle \frac{d}{dt} \hat{N}_s \rangle = -i \int dt \langle [\hat{N}_s, \hat{H}_{\text{int}}] \rangle. \tag{1.9}$$

Here, $\hat{N}_s = \hat{a}_s^\dagger \hat{a}_s$ is the photon number operator for the signal mode s, $\mathbf{k}_s$ is the associated wavevector, and we have used the fact that $[\hat{N}_s, \hat{H}_0 + \hat{H}_{\text{F}}] = 0$, i.e., the non-interacting Hamiltonian conserves the photon number. Generalizing to account for polarization-sensitive detection is not difficult but we retain this simpler version for clarity and ease of presentation. The signal is a function of the set of parameters Λ that define the extenally applied electromagnetic fields. Equation (1.9) is just the total change in photon number dispersed in frequency and wavevector. It thus assumes ideal spectrographic resolution. One can introduce a finite spectral resolution after the fact by convoluting with a detector sensitivity function. A more rigorous approach is to incorporate a description of the detection process and define the signal as the gated electric field at the detector overlap of Wigner spectrograms describing the detector gating

$$S(\bar{\Lambda}) = \int d\mathbf{r} \int dt \langle \hat{\mathbf{E}}_R^{(-)}(\mathbf{r}, t, \bar{\Lambda}) \hat{\mathbf{E}}_L^{(+)}(\mathbf{r}, t, \bar{\Lambda}) \rangle \tag{1.10}$$

where $\bar{\Lambda}$ stands for the parameters defining the gating functions. When the detector is pointlike, this will consist primarily of the central frequencies and times of the detection windows and the position of the detector [14]. This allows a consistent treatment of temporal, spectral, spatial, and directional resolution in spontaneous signals. In fact, we will reserve Eq. (1.10) for spontaneous signals and utilize only the simpler Eq. (1.9) for stimulated signals since the temporal field envelope suffices to set the time-resolution in the latter case. Additionally, there are certain techniques for which the signal emitted at the source is not identical to the observed signal (what is emitted is not the same as what is detected). In these cases, post-emission effects must be taken into account and this is best handled from the field-perspective. Although this type of situation is more common for electronic spectroscopies (in which electrons rather than photons are detected, e.g., streaking [15]), accounting for the propagation between sample and detector, as well as detector gating functions, requires such a treatment. This treatment is relevant in photon coincidence counting experiments as well [14].

1.1.1 Outline

Chapter 2 discusses light scattering and x-ray diffraction in particular. Free-electron laser hard x-ray light sources can provide high fluence, ultrashort pulses down to the femtosecond scale [16, 17, 18, 19, 20, 21]. This allows structural dynamics and elementary relaxation processes in molecules to be probed in time. X-ray scattering from crystals is elastic and consists of sharp Bragg diffraction peaks that arise from the interference between light coming from different molecules. This has been used to reveal snapshots of the evolving charge density [22, 23, 24, 25, 26, 27, 28, 29, 30, 31, 32]. Scattering of ultrashort x-ray pulses from gases, liquids, and even single molecules is more complex and involves both single- and two-molecule contributions, diffuse (non-Bragg) features, elastic and inelastic components, and contributions of electronic coherences in nonstationary states [33, 34].

In chapter 2, we derive expressions for the x-ray scattering signal using both Eqs. (1.9) and (1.10) to make clear the difference between the two approaches. We will also discuss how the time-resolved x-ray diffraction differs from the square of the time-dependent momentum space charge density, an issue that is known from the literature but has created some confusion recently [33, 35, 36, ?]. Finally, we present some calculations for the time-resolved diffraction from NaF, an interesting case study in which coherences generated near an avoided crossing can be detected in the diffraction signal. These corrections are about 2-3 orders of magnitude weaker than the diffraction from electronic populations but could in principle be detected. For reasons we will discuss in chapter 2, these coherence contributions are generally weaker for molecules with heavier atoms and are frequently negligible. Nonetheless, they constitute an object of interest in their own right and can reveal spatial information on the electronic states involved in the coherence.

In chapter 3, we shift the discussion to heterodyne detected (stimulated) signals. In this case, the signal mode is macroscopically occupied by a laser rather than initially unoccupied and populated by the field-matter interaction. As before, the laser field is approximated classically. We will show that this treatment immediately leads to a signal that scales linearly in the molecule number N. We show that accounting for the infinitely-many vacuum modes of the electromagnetic field in addition to the laser fields results in additional, many-body contributions to the signal that scale as N^2. These "cascading" terms carry the same phase-matching and scaling in the laser fields as the direct, single-molecule signals. The direct signals were historically obscured by the cascading signals in multidimensional Raman experiments, an issue that took several years to fully resolve [37, 38, 39, 40, 41, 42, 43, 44, 45, 46].

Chapter 3 presents a derivation of cascading as a lowest-order correction due to photon exchange and demonstrates how, in macroscopic samples, a phase shift of $\pi/2$ arises relative to the direct signal. This has been used to filter out the unwanted cascading signal [44, 43, 47, 48]. We discuss this phase in the case of arbitrary geometry and show how it will look in the case of a few-molecule sample. Finally, we discuss possible avenues of cascade suppression or manipulation when the usual $\pi/2$ phase-selection is inadequate.

Chapter 4 discusses molecules coupled to modes of an optical cavity. In the previous chapters, the only quantum fields considered were the bare vacuum modes and their interactions with the matter were treated perturbatively. The development of high-finesse optical cavities capable of achieving the ultrastrong coupling regime calls for a non-perturbative approach. Strong coupling can be achieved in nano cavities [49], nano plasmon antennas [50], and nano guides [51]. The underlying theoretical framework is well studied in theory and experiment with atoms [52, 53, 54, 55] and has been demonstrated more recently for molecules [56, 57], the dynamics being described using joint photon-matter states called polaritons [58]. The inclusion of internal nuclear degerees of freedom complicates matters, leading to nonadiabatic dynamics [59] (this effect is seen also in strong laser fields but utilizing cavities avoids certain damage problems associated with (multi-photon) absorption [60, 61, 62, 63]).

In chapter 4, we present a multi-pronged strategy to simulate spectroscopic signals of molecules strongly coupled to modes of an optical cavity. If the rotating wave approximation is valid, a conserved excitation number operator exists and the problem is not too difficult (section 4.1). If the rotating wave approximation breaks down, more elaborate tools (section 4.2) are required to obtain the new potential energy surfaces. Unfortunately, these tools are difficult to apply to obtain non-adiabatic couplings, making the simulation of non-Born-Oppenheimer dynamics and associated signals difficult. Section 4.2 also presents a solution that allows direct time-propagation of the system, allowing simulation of signals without ever calculating the Born-Oppenheimer surfaces or their non-adiabatic couplings.

Chapter 2

Light Scattering and Spontaneous Emission

In this chapter, we discuss scattering and spontaneous emission processes as photon creation in vacuum modes of the electromagnetic field. As discussed in section 1.1, these signals can be calculated in two different ways. To illustrate in detail the differences that arise in these two approaches, we first calculate the total photon number change in the signal mode (section 2.0.2) and then the gated electric field at the detector (section 2.0.3), using the minimal coupling Hamiltonian in both cases, and focusing on the off-resonant, $\hat{\sigma}\hat{\mathbf{A}}^2$ scattering that is relevant for diffraction. We then discuss time-resolved x-ray diffraction experiments and examine a separation of the signal into single- and two-molecule contributions (section 2.1). In the context of x-ray diffraction, the two-molecule contributions provide the intermolecular structure while the single-molecule contributions provide information only on the single-molecule charge density. We discuss the differences between these two contributions and how they are calculated, which recently lead to a confusion in gas-phase pump-probe diffraction [36, **?**] and present some simulations for ultrafast diffraction in NaF.

2.0.2 Change in Photon Number

At the core of our approach is a separation of the electromagnetic field modes into two disjoint sets: field modes which are initially in the vacuum state and form the set of possible signal modes, and field modes corresponding to an external light pulse. We then have

$$\hat{\mathbf{A}}(\mathbf{r}) = \hat{\mathbf{A}}^{(\mathrm{v})}(\mathbf{r}) + \hat{\mathbf{A}}^{(\mathrm{p})}(\mathbf{r}) \tag{2.1}$$

where the "v" superscript indicates the vacuum modes and the "p" indicates modes externally populated by an incoming pulse. Later, we will make a semiclassical approximation and replace $\hat{\mathbf{A}}^{(\mathrm{p})}(\mathbf{r})$ by its expectation value. For now, our treatment will remain general and the pulse modes will be kept quantum-mechanical. We start with the Heisenberg equation of motion for the photon number operator $\hat{N}_s = a^\dagger a$

$$\begin{aligned} \frac{\mathrm{d}\hat{N}_s}{\mathrm{d}t} &= -i[\hat{N}_s, \hat{H}_{\mathrm{int}}] \qquad (2.2) \\ = i\int \mathrm{d}\mathbf{r}\Big(\hat{\mathbf{j}}(\mathbf{r})\cdot[\hat{N}_s, \hat{\mathbf{A}}^{(\mathrm{v})}(\mathbf{r})] &- \frac{1}{2}\hat{\sigma}(\mathbf{r})\{[\hat{N}_s, \hat{\mathbf{A}}^{(\mathrm{v})2}(\mathbf{r})] + 2\hat{\mathbf{A}}^{(\mathrm{p})}(\mathbf{r})\cdot[\hat{N}_s, \hat{\mathbf{A}}^{(\mathrm{v})}(\mathbf{r})]\}\Big) \end{aligned}$$

where we have used the relations $[\hat{N}_s, \hat{\mathbf{A}}^{(\mathrm{p})}(\mathbf{r})] = 0 = [\hat{\mathbf{A}}^{(\mathrm{v})}(\mathbf{r}), \hat{\mathbf{A}}^{(\mathrm{p})}(\mathbf{r})]$. It is straightforward to calculate the commutators

$$[\hat{N}_s, \hat{\mathbf{A}}^{(\mathrm{v})}(\mathbf{r})] = \mathbf{A}_s^*(\mathbf{r})\hat{a}_s^\dagger - \mathrm{c.c.} \tag{2.3}$$

$$[\hat{N}_s, \hat{\mathbf{A}}^{(\mathrm{v})2}(\mathbf{r})] = 2(\hat{a}_s^\dagger \mathbf{A}_s^* \cdot \hat{\mathbf{A}}^{(\mathrm{v})}(\mathbf{r}) - \mathrm{c.c.}). \tag{2.4}$$

Here, $\mathbf{A}_s(\mathbf{r}) = \sqrt{\frac{2\pi}{\Omega\omega_s}}\epsilon^{(\lambda_s)}(\mathbf{k}_s)e^{i\mathbf{k}_s\cdot\mathbf{r}}$ (and complex conjugate). Inserting these commutators into Eq. (2.2) then gives

$$\dot{\hat{N}}_s = 2\Im\Big[\int \mathrm{d}\mathbf{r}\Big(\hat{\mathbf{j}}(\mathbf{r})\cdot\mathbf{A}_s(\mathbf{r})\hat{a}_s - \hat{\sigma}(\mathbf{r})\{\hat{\mathbf{A}}^{(\mathrm{v})}(\mathbf{r})\cdot\mathbf{A}_s(\mathbf{r})\hat{a}_s + \hat{\mathbf{A}}^{(\mathrm{p})}(\mathbf{r})\cdot\mathbf{A}_s(\mathbf{r})\hat{a}_s\}\Big)\Big] \tag{2.5}$$

Defining the total electromagnetic current in the presence of the vector potential

$$\hat{\mathbf{J}}(\mathbf{r}) = -\frac{1}{2}\left[\hat{\psi}^\dagger(\mathbf{r})\mathbf{v}\hat{\psi}(\mathbf{r}) + (\mathbf{v}\hat{\psi}(\mathbf{r}))^\dagger\hat{\psi}(\mathbf{r})\right] = \hat{\mathbf{j}}(\mathbf{r}) - \hat{\sigma}(\mathbf{r})\hat{\mathbf{A}}(\mathbf{r}), \tag{2.6}$$

where the $\mathbf{v} = (-i\nabla + \hat{\mathbf{A}})$ is the velocity operator, we then have for the signal

$$S(\mathbf{k}_s) = -2\Im\left[\int \mathrm{d}t\mathrm{d}\mathbf{r}\langle \hat{a}_s^\dagger \mathbf{A}_s^*(\mathbf{r}) \cdot \mathbf{J}(\mathbf{r})\rangle\right] \tag{2.7}$$

where we have used $\Im[z] = -\Im[z^\dagger]$ to bring the expression to the conventional form in which the last interaction may be interpreted as an emission from the ket. Equation (2.7) is exact as we have made no approximations thus far. The time-dependence in this equation comes through the expectation value, which we evaluate in the interaction picture with respect to $\hat{H}_{\text{int}}$

$$\langle \hat{a}_s^\dagger \mathbf{A}_s^*(\mathbf{r}) \cdot \mathbf{J}(\mathbf{r})\rangle = \mathrm{Tr}\left[\hat{a}_s^\dagger \mathbf{A}_s^*(\mathbf{r}) \cdot \mathbf{J}(\mathbf{r})\mathcal{T}\ e^{-i\int_{-\infty}^{t} d\tau \hat{H}_{\text{int}-}(\tau)}\right] \tag{2.8}$$

Thus far, we have instead worked in the Heisenberg picture for compactness. The difference will be to add an explicit time-dependence to all material operators and doesn't alter the commutation relations since the pictures differ by a canonical transformation. The free-evolution time-dependence for the fields will be absorbed into their coefficients $\mathbf{A}_j(\mathbf{r}) \mapsto \mathbf{A}_j(\mathbf{r}, t) = \mathbf{A}_j(\mathbf{r})e^{-i\omega_j t}$. We note that a zeroth-order expansion of the expectation value in (2.7) would vanish due to the $\langle 0_s|\hat{a}_s^\dagger$ factor. We thus require an additional order in $\hat{H}_{\text{int}}$ which must act on the bra, to yield

$$S(\mathbf{k}_s) = 2\Re\left[\int \mathrm{d}t\mathrm{d}\mathbf{r}\mathrm{d}\mathbf{r}' \int_{-\infty}^{t} \langle \hat{\mathbf{J}}_{\text{int}}(\mathbf{r}', t') \cdot \hat{\mathbf{A}}(\mathbf{r}', t')\hat{a}_s^\dagger \mathbf{A}_s^*(\mathbf{r}, t) \cdot \mathbf{J}(\mathbf{r}, t)\rangle\right]. \tag{2.9}$$

This expression does not vanish even without further expansion of the propagator in Eq. (2.7). We may thus obtain the lowest-order contribution to the photon scattering into mode

s by tracing over that mode at this point. Using the commutators

$$[\hat{a}_s^\dagger, \hat{\mathbf{A}}(\mathbf{r})] = -\mathbf{A}_s(\mathbf{r}) \tag{2.10}$$

$$[\hat{a}_s^\dagger, \hat{\mathbf{J}}_{\text{int}}(\mathbf{r})] = \frac{1}{2}\hat{\sigma}(\mathbf{r})\mathbf{A}_s(\mathbf{r}), \tag{2.11}$$

and taking the trace over mode s (using the fact that $\hat{a}_s|0\rangle_s = 0$), we obtain

$$S(\mathbf{k}_s) = 2\Re\left[\int \mathrm{d}t\mathrm{d}\mathbf{r}\mathrm{d}\mathbf{r}' \int_{-\infty}^{t} \mathrm{d}t' \langle \mathbf{A}_s(\mathbf{r}', t') \cdot \hat{\mathbf{J}}(\mathbf{r}', t')\hat{\mathbf{J}}(\mathbf{r}, t) \cdot \mathbf{A}_s^*(\mathbf{r}, t)\rangle\right]. \tag{2.12}$$

The expectation value in the above expression excludes mode s (since it was already traced over) and it is not technically the same as those in previous expressions, we keep the notation $\langle \dots \rangle$ rather than making the difference explicit. The dot products in Eq. (2.12) serve merely to pick out the projection of the current $\mathbf{J}$ along the vector potential $\mathbf{A}_s$. This signal is represented diagramatically in Fig. 2.1(i). Equation (2.12) can also be recast in the symmetric form

$$S(\mathbf{k}_s) = \int \mathrm{d}t\mathrm{d}t'\mathrm{d}\mathbf{r}\mathrm{d}\mathbf{r}' \langle \mathbf{A}_s(\mathbf{r}', t') \cdot \hat{\mathbf{J}}(\mathbf{r}', t')\hat{\mathbf{J}}(\mathbf{r}, t) \cdot \mathbf{A}_s^*(\mathbf{r}, t)\rangle \tag{2.13}$$

which further simplifies to

$$S(\mathbf{k}_s) = \frac{2\pi}{\Omega\omega_s} \int \mathrm{d}t\mathrm{d}t'\mathrm{d}\mathbf{r}\mathrm{d}\mathbf{r}' e^{-i\mathbf{k}_s\cdot(\mathbf{r}-\mathbf{r}')+i\omega_s(t-t')} \left[\epsilon^{(\lambda_s)}(\hat{\mathbf{k}}_s) \cdot \langle \hat{\mathbf{J}}(\mathbf{r}', t')\hat{\mathbf{J}}(\mathbf{r}, t)\rangle \cdot \epsilon^{(\lambda_s)*}(\hat{\mathbf{k}}_s)\right]. \tag{2.14}$$

Multiplying by the density $\Omega/(2\pi)^3$ of states in $\mathbf{k}_s$ space and by the volume element of $\mathbf{k}_s$ space per solid angle per unit frequency

$$\frac{\mathrm{d}\mathbf{k}_s}{\mathrm{d}\Omega_s\mathrm{d}\omega_s} = \frac{\omega_s^2}{c^3} \tag{2.15}$$

we obtain

$$S(\mathbf{k}_s) = \frac{\alpha^3\omega_s}{4\pi^2}\left[\epsilon^{(\lambda_s)}(\hat{\mathbf{k}}_s)\cdot\langle\hat{\mathbf{J}}(-\mathbf{k}_s,-\omega_s)\hat{\mathbf{J}}(\mathbf{k}_s,\omega_s)\rangle\cdot\epsilon^{(\lambda_s)*}(\hat{\mathbf{k}}_s)\right]. \tag{2.16}$$

where we have employed the Fourier transform for compactness. Turning our attention to the off-resonant regime, we substitute the definition of $\hat{\mathbf{J}}$ into Eq. (2.14) and retain only the $\hat{\sigma}$ terms yielding

$$S(\mathbf{q}) = \frac{\alpha^3\omega_s}{4\pi^2}|\epsilon^{(\lambda_s)}(\hat{\mathbf{k}}_s)\cdot\epsilon^{(\lambda_p)*}(\hat{\mathbf{k}}_p)|^2\int \mathrm{d}t|A_p(t)|^2\langle\hat{\sigma}(-\mathbf{q},t)\hat{\sigma}(\mathbf{q},t)\rangle \tag{2.17}$$

where $A_p(t)$ is the temporal envelope of the vector potential of the incoming x-ray pulse, we have defined the momentum transfer $\mathbf{q} = \mathbf{k}_s - \mathbf{k}_p$, and assumed an ultrashort pulse so that $t = t'$. We note at this point that, in textbook derivations of scattering in the minimal coupling picture, the incoming field is frequently treated quantum mechanically as a plane wave. The resulting mode-quantization prefactor, once accounting for the incoming photon flux, gives an additional factor of α/ω_p. The usual Thomson scattering cross section is then proportional to $\alpha^4\omega_s/\omega_p$. In this manuscript, we treat the incoming field in the semiclassical limit (i.e., as a large-amplitude coherent state) to allow a simple treatment of the x-ray temporal envelope. This method is more appropriate to consideration of ultrafast pump-probe diffraction rather than the more traditional static diffraction.

Though formally complete with the total sample electron density operator $\hat{\sigma}$, our final expression is more useful if recast in terms of single-molecule electron densities $\hat{\sigma}_\alpha$. Assuming a sample composed of identical molecules located at positions $\mathbf{r}_\alpha$, we have $\hat{\sigma}(\mathbf{r}) = \sum_\alpha \hat{\sigma}(\mathbf{r}-\mathbf{r}_\alpha)$. The charge density operators in Eq. (2.17) then generate a double sum, the diagonal (single-molecule) and off-diagonal (two-molecule) terms of which yield

$$S^{(2)}(\mathbf{q},T) = F(\mathbf{q}) \int dt |E_p(t-T)|^2 |\langle \hat{\sigma}(\mathbf{q},t) \rangle|^2, \tag{2.18}$$

$$S^{(1)}(\mathbf{q},T) = N \int dt |E_p(t-T)|^2 \langle |\hat{\sigma}(\mathbf{q},t)|^2 \rangle \tag{2.19}$$

where we have explicitly indicated the dependence on the central time T of the x-ray pulse temporal envelope $E_p(t-T)$ and defined the structure factor

$$F(\mathbf{q}) = \sum_{\alpha} \sum_{\beta \neq \alpha} e^{-i\mathbf{q}\cdot(\mathbf{r}_\alpha - \mathbf{r}_\beta)} \tag{2.20}$$

which encodes the long-range, intermolecular structure of the sample. Loop diagrams representing the single- and two-molecule contributions to scattering are shown in Fig. 2.2

2.0.3 Electric Field Intensity

In this section, the signal is defined as the intensity of the detected electric field

$$S = \int dt \int d\mathbf{r} \langle \mathbf{E}^\dagger(\mathbf{r},t) \mathbf{E}(\mathbf{r},t) \rangle \tag{2.21}$$

where the detected electric field is represented as

$$\hat{\mathbf{E}}(\mathbf{r},t) = \frac{1}{(2\pi)^4} \int d\omega \int d\mathbf{k} e^{-i\omega t + i\mathbf{k}\cdot\mathbf{r}} \hat{\mathbf{E}}(\mathbf{k},\omega) \tag{2.22}$$

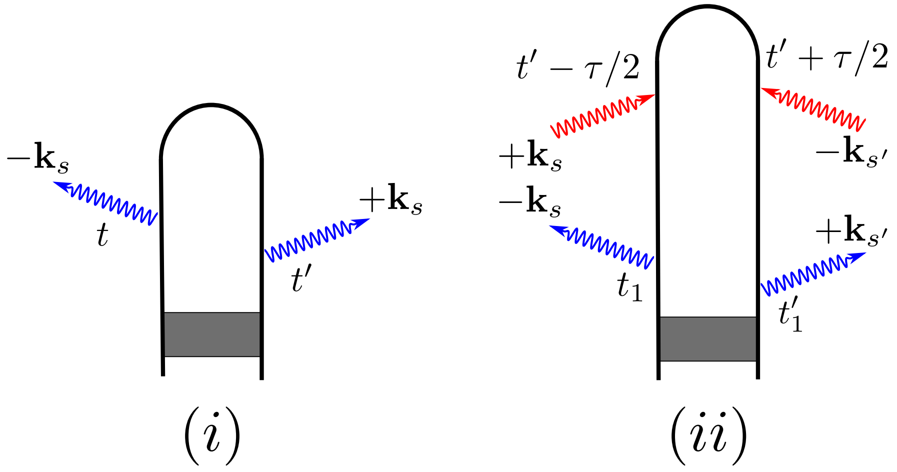

Figure 2.1: (i) Loop diagram representing light scattering and spontaneous emission as obtained from the photon-number-change approach. In the minimal coupling, this corresponds to Eq. (2.12) and the material operator that accompany the interaction arrows is the current $\hat{\mathbf{J}}$. If the field-matter interaction is dipolar, the same diagram pertains but with the material operator associated with interaction arrows then being the transition dipole operator. The shaded area represents an unspecified process that prepares the system in an arbitrary state. We denote the signal modes s, s'. (ii) Loop diagram representing bare spectrogram for light scattering and spontaneous emission calculated as the gated field intensity at a detector. Photon emission at the material sample is shown with blue arrows while photon absorption at the detector is shown with red arrows. For example, Eq. (2.33) is represented by this diagram when the field-matter interaction is treated in the minimal coupling and only the off-resonant scattering is considered. In this case, the material operator associated with the interaction arrows would be the charge density operator.

Following the procedure outlined in Ref. [64], we add a series of gating functions to the detected electric field:

$$\begin{aligned}
&\hat{\mathbf{E}}^{(t)}(\mathbf{r},t) = F_t(t,\bar{t})\hat{\mathbf{E}}(\mathbf{r},t) \\
&\hat{\mathbf{E}}^{(t\mathbf{r})}(\mathbf{r},t) = F_{\mathbf{r}}(\mathbf{r},\bar{\mathbf{r}})\hat{\mathbf{E}}^{(t)}(\mathbf{r},t) \\
&\hat{\mathbf{E}}^{(t\mathbf{r}f)}(\mathbf{r},t) = F_f(\omega,\bar{\omega})\hat{\mathbf{E}}^{(t\mathbf{r})}(\mathbf{r},\omega) \\
&\hat{\mathbf{E}}^{(t\mathbf{r}f\mathbf{k})}(\mathbf{r},t) = F_{\mathbf{k}}(\mathbf{k},\bar{\mathbf{k}})\hat{\mathbf{E}}^{(t\mathbf{r}f)}(\mathbf{k},\omega)
\end{aligned} \tag{2.23}$$

Each of these gating functions provides a selectivity and is used to model the ability of the detector to observe only particular frequencies, times, locations, and wavevectors. We will see that the spatial selectivity corresponds to pixel location in a detector array and describes the detector resolution in a diffraction experiment. The above definitions result in the total gated field

$$\hat{\mathbf{E}}^{(t\mathbf{r}f\mathbf{k})}(\mathbf{r},t;\bar{t},\bar{\omega},\bar{\mathbf{r}},\bar{\mathbf{k}}) = \int d\mathbf{r}' \int dt' \hat{\mathbf{E}}(\mathbf{r}',t')F_{\mathbf{k}}(\mathbf{r}-\mathbf{r}',\mathbf{k})F_f(t-t',\bar{\omega})F_{\mathbf{r}}(\mathbf{r}',\bar{\mathbf{r}})F_t(t',\bar{t}) \tag{2.24}$$

The observed signal is then given by

$$S(\bar{\omega},\bar{t},\bar{\mathbf{r}},\bar{\mathbf{k}}) = \int dt \int d\mathbf{r} \langle \mathbf{E}^{(t\mathbf{r}f\mathbf{k})\dagger}(\mathbf{r},t)\mathbf{E}^{(t\mathbf{r}f\mathbf{k})}(\mathbf{r},t)\rangle. \tag{2.25}$$

We define the bare and detector spectrograms via:

$$\begin{gathered}
W_B(t',\omega',\mathbf{r}',\mathbf{k}') = \\
\int_0^\infty d\tau e^{-i\omega'\tau} \int d\mathbf{R} e^{i\mathbf{k}'\cdot\mathbf{R}} \langle \mathcal{T}\hat{\mathbf{E}}_R^\dagger(\mathbf{r}'+\mathbf{R}/2,t'+\tau/2)\hat{\mathbf{E}}_L(\mathbf{r}'-\mathbf{R}/2,t'-\tau/2)\rangle
\end{gathered} \tag{2.26}$$

$$W_D(t',\omega',\mathbf{r}',\mathbf{k}';\bar{t},\bar{\omega},\bar{\mathbf{r}},\bar{\mathbf{k}}) = \tag{2.27}$$
$$\int\frac{d\omega}{2\pi}|F_f(\omega,\bar{\omega})|^2 W_t(t',\omega'-\omega,\bar{t})\int\frac{d\mathbf{k}}{(2\pi)^3}|F_{\mathbf{k}}(\mathbf{k},\bar{\mathbf{k}})|^2 W_{\mathbf{r}}(\mathbf{r}',\mathbf{k}'-\mathbf{k},\bar{\mathbf{r}})$$

Where we have defined the auxilliary functions

$$W_t(t',\omega,\bar{t}) \equiv \int d\tau F_t^*(t'+\tau/2,\bar{t})F_t(t'-\tau/2,\bar{t})e^{i\omega\tau} \tag{2.28}$$

and

$$W_{\mathbf{r}}(\mathbf{r}',\mathbf{k},\bar{\mathbf{r}}) \equiv \int d\mathbf{R} F_{\mathbf{r}}^*(\mathbf{r}'+\mathbf{R}/2,\bar{\mathbf{r}})F_{\mathbf{r}}(\mathbf{r}'-\mathbf{R}/2,\bar{\mathbf{r}})e^{-i\mathbf{k}\cdot\mathbf{R}}. \tag{2.29}$$

As is easily verified *via* substitution, the signal is then given by the overlap of the two spectrograms:

$$S(\bar{t},\bar{\omega},\bar{\mathbf{k}},\bar{\mathbf{r}}) = \int dt'\frac{d\omega'}{2\pi}\int d\mathbf{r}'\frac{d\mathbf{k}'}{(2\pi)^3}W_B(t',\omega',\mathbf{r}',\mathbf{k}')W_D(t',\omega',\mathbf{r}',\mathbf{k}';\bar{t},\bar{\omega},\bar{\mathbf{k}},\bar{\mathbf{r}}) \tag{2.30}$$

For brevity, the following definitions are used in the derivations:

$$W_D(t',\omega';\bar{t},\bar{\omega}) = \int\frac{d\omega}{2\pi}|F_f(\omega,\bar{\omega})|^2 W_t(t',\omega'-\omega,\bar{t}) \tag{2.31}$$

$$W_D(\mathbf{r}',\mathbf{k}';\bar{\mathbf{r}},\bar{\mathbf{k}}) = \int\frac{d\mathbf{k}}{(2\pi)^3}|F_{\mathbf{k}}(\mathbf{k},\bar{\mathbf{k}})|^2 W_{\mathbf{r}}(\mathbf{r}',\mathbf{k}'-\mathbf{k},\bar{\mathbf{r}}) \tag{2.32}$$

Having established the relationship between the bare material quantities, the detector gating functions, and the signal that is ultimately observed, we proceed to examine the bare material spectrogram. Beginning with equation (2.26), we expand to leading order in $\hat{H}_{\text{int}}$ (Eq. (1.7)). This requires two interactions (one each for the ket and bra) since the signal mode is initially in a vacuum state.

$$W_B(t',\omega',\mathbf{r}',\mathbf{k}') = \sum_{\mathbf{k}_s,\mathbf{k}_{s'}} \int d\tau e^{-i\omega'\tau} \int d\mathbf{R} e^{i\mathbf{k}'\cdot\mathbf{R}} \int_{-\infty}^{t'+\tau/2} dt_1' \int_{-\infty}^{t'-\tau/2} dt_1 \tag{2.33}$$

$$\int d\mathbf{r}_1 d\mathbf{r}_1' \langle \hat{\mathbf{E}}_R^{(s')\dagger}(\mathbf{r}'+\mathbf{R}/2, t'+\tau/2)\hat{\mathbf{E}}_L^{(s)}(\mathbf{r}'-\mathbf{R}/2, t'-\tau/2)$$

$$\times\, \hat{\mathbf{A}}_R^{(s')}(\mathbf{r}_1',t_1')\cdot\hat{\mathbf{A}}_R^{(p)\dagger}(\mathbf{r}_1',t_1')\hat{\sigma}_{T,R}(\mathbf{r}_1',t_1')\hat{\mathbf{A}}_L^{(s)\dagger}(\mathbf{r}_1,t_1)\cdot\hat{\mathbf{A}}_L^{(p)}(\mathbf{r}_1,t_1)\hat{\sigma}_{T,L}(\mathbf{r}_1,t_1)\rho_T(0)\rangle \tag{2.34}$$

Here, the total density matrix is the direct product of field and matter density matrices immediately following state preparation (i.e., $\rho_T(0) = \rho_F(0)\otimes\rho_M(0)$). This bare spectrogram can be represented as in the generic diagram shown in Fig. 2.1. The electric field and vector potential of the vacuum modes, $\hat{\mathbf{E}}^{(s)}(\mathbf{r},t)$ and $\hat{\mathbf{A}}^{(s)}(\mathbf{r},t)$, are given as mode expansions in Eqs. (A.2) and (A.3) while the vector potential for the classical probe beam $\hat{\mathbf{A}}^{(p)}(\mathbf{r},t)$ is represented as:

$$\hat{\mathbf{A}}^{(p)}(\mathbf{r},t) = \sum_{\nu} P_\nu \epsilon^{(\nu)}(\hat{\mathbf{k}}_p)\int \frac{d\omega_p}{2\pi} A_p(\omega_p) e^{-i\omega_p t + i\mathbf{k}_p\cdot\mathbf{r}} \tag{2.35}$$

where P_ν is the fraction of the probe pulse in polarization state ν and $\epsilon^{(\nu)}(\hat{\mathbf{k}}_p)$ is a unit vector in the direction of direction of polarization ν. Henceforth, we will use the shorthand $\sum_\nu P_\nu \epsilon^{(\nu)}(\hat{\mathbf{k}}_p) = \bar{\epsilon}(\hat{\mathbf{k}}_p)$ and assume a narrow beam so that $\hat{\mathbf{k}}_p = \hat{\mathbf{k}}_{p'}$. Note that, by starting the t_1' and t_1 integrations at $-\infty$, we assume that the scattered pulse is well-separated from the state preparation process. Inserting these definitions into Eq. (2.33) and separating matter and field correlation functions (and evaluating the latter with the conditions described above), we obtain

$$\begin{aligned}
W_B(t',\omega',\mathbf{r}',\mathbf{k}') &= \frac{1}{4V^2}\sum_{\mathbf{k}_s,\mathbf{k}_{s'}}\int d\tau e^{-i\omega'\tau}\int d\mathbf{R}e^{i\mathbf{k}'\cdot\mathbf{R}}\int_{-\infty}^{t'+\tau/2}dt_1'\int_{-\infty}^{t'-\tau/2}dt_1 \\
&\times e^{i\omega_{s'}(t'+\tau/2-t_1)-i\omega_s(t'-\tau/2-t_1')}\int d\omega_p d\omega_{p'}A_p(\omega_p)A_p^*(\omega_{p'})e^{-i\omega_p t_1}e^{i\omega_{p'}t_1'}\int d\mathbf{r}_1 d\mathbf{r}_1' \\
&\times\sum_{\alpha,\beta}^{N}\sum_{\lambda,\lambda'}\left(\epsilon^{(\lambda)}(\hat{\mathbf{k}}_s)\cdot\bar{\epsilon}(\hat{\mathbf{k}}_p)\right)\left(\epsilon^{(\lambda')}(\hat{\mathbf{k}}_{s'})\cdot\bar{\epsilon}(\hat{\mathbf{k}}_p)\right)\left(\epsilon^{(\lambda)}(\hat{\mathbf{k}}_s)\cdot\mu_D\right)\left(\epsilon^{(\lambda')}(\hat{\mathbf{k}}_{s'})\cdot\mu_D\right) \\
&\times e^{i\mathbf{k}_s\cdot(\mathbf{r}'-\mathbf{R}/2)}e^{-i\mathbf{k}_{s'}\cdot(\mathbf{r}'+\mathbf{R}/2)}e^{-i(\mathbf{k}_s-\mathbf{k}_p)\cdot\mathbf{r}_1}e^{i(\mathbf{k}_{s'}-\mathbf{k}_{p'})\cdot\mathbf{r}_1'}\langle\hat{\sigma}_R^{\beta\dagger}(\mathbf{r}_1',t_1')\hat{\sigma}_L^{\alpha}(\mathbf{r}_1,t_1)\rho_M(0)\rangle,
\end{aligned}\tag{2.36}$$

where we have taken a dipolar-interaction model for the detection event with μ_D the dipole moment of the detector. We have also defined $\hat{\sigma}^\alpha(\mathbf{r}) \equiv \hat{\sigma}(\mathbf{r}-\mathbf{r}_\alpha)$ so that $\hat{\sigma}_T(\mathbf{r}) = \sum_\alpha \hat{\sigma}^\alpha(\mathbf{r})$.

We first examine the $\alpha \neq \beta$ terms in the above, i.e., the two-molecule terms. Assuming that the molecules are un-entangled, we have $\rho_M(0) = \rho_\alpha(0)\otimes\rho_\beta(0)$. The correlation function therefore splits and we can separately collect factors associated with each molecule. That is, we define

$$\begin{aligned}
\Pi^{(\alpha)}(\mathbf{r},t) &= \frac{1}{2V}\sum_{\mathbf{k}_s,\lambda}\int_{-\infty}^{t}dt_1 e^{-i\omega_s(t-t_1)}\int\frac{d\omega_p}{2\pi}A_p(\omega_p)e^{-i\omega_p t_1}e^{i\mathbf{k}_s\cdot\mathbf{r}} \\
&\times\int d\mathbf{r}_1\left(\epsilon^{(\lambda)}(\hat{\mathbf{k}}_s)\cdot\bar{\epsilon}(\hat{\mathbf{k}}_p)\right)\left(\epsilon^{(\lambda)}(\hat{\mathbf{k}}_s)\cdot\mu_D\right)e^{-i(\mathbf{k}_s-\mathbf{k}_p)\cdot\mathbf{r}_1}\langle\hat{\sigma}^\alpha(\mathbf{r}_1,t_1)\rangle_\alpha,
\end{aligned}\tag{2.37}$$

where $\langle\ldots\rangle_\alpha = \mathrm{Tr}[\ldots\rho_\alpha(0)]$ is the trace over the product of the argument and the density matrix immediately after the state preparation process ($\rho_\alpha(0)$). The two-molecule bare spectrogram is then given by

$$\begin{aligned}
&W_B^{(2)}(t',\omega',\mathbf{r}',\mathbf{k}') = \\
&\sum_{\alpha,\beta}\int d\tau e^{-i\omega'\tau}\int d\mathbf{R}e^{i\mathbf{k}'\cdot\mathbf{R}}\Pi^{(\alpha)}(\mathbf{r}'-\mathbf{R}/2,t'-\tau/2)\Pi^{(\beta)\dagger}(\mathbf{r}'+\mathbf{R}/2,t'+\tau/2).
\end{aligned}\tag{2.38}$$

In order to carry out the integration over dt_1, we use the Fourier Transform

$$\langle \hat{\sigma}^{\alpha}(\mathbf{r}_1, t_1) \rangle_{\alpha} = \int \frac{d\tilde{\omega}}{2\pi} e^{i\tilde{\omega}t_1} \langle \hat{\sigma}^{\alpha}(\mathbf{r}_1, \tilde{\omega}) \rangle_{\alpha}. \tag{2.39}$$

We thus have

$$\begin{aligned}\Pi^{(\alpha)}(\mathbf{r},t) = \frac{1}{2V} \sum_{\mathbf{k}_s} \sum_{ij} \bar{\epsilon}_i(\hat{\mathbf{k}}_p) \mu_{Dj} \left(\delta_{ij} - \hat{k}_{si}\hat{k}_{sj} \right) \int d\mathbf{r}_1 \int \frac{d\omega_p}{2\pi} A_p(\omega_p) \\ \times \int \frac{d\tilde{\omega}}{2\pi} \langle \hat{\sigma}^{\alpha}(\mathbf{r}_1, \tilde{\omega}) \rangle_{\alpha} e^{i\mathbf{k}_s\cdot\mathbf{r}} e^{-i(\mathbf{k}_s - \mathbf{k}_p)\cdot\mathbf{r}_1} e^{-i\omega_s t} \int_{-\infty}^{t} dt_1 e^{i(\tilde{\omega}+\omega_s-\omega_p)t_1},\end{aligned} \tag{2.40}$$

where we have also expanded the dot products of the polarizations and used the identity

$$\sum_{\lambda} \epsilon_i^{(\lambda)}(\hat{\mathbf{k}}_s) \epsilon_j^{(\lambda)}(\hat{\mathbf{k}}_s) = \delta_{ij} - \hat{k}_{si}\hat{k}_{sj}. \tag{2.41}$$

We are now free to carry out the time integration

$$\int_{-\infty}^{t} e^{i(\tilde{\omega}+\omega_s-\omega_p)t_1} = \frac{(-i)e^{i(\tilde{\omega}+\omega_s-\omega_p)t}}{\omega + \omega_s - \omega_p - i\eta}, \tag{2.42}$$

where η is a positive infinitesimal. We change the summation over $\mathbf{k}_s$ to an integration via

$$\frac{1}{V} \sum_{\mathbf{k}_s} \rightarrow \frac{1}{(2\pi)^3} \int d\mathbf{k_s} = \int \frac{\omega_s^2 d\omega_s}{(2\pi c)^3} d\Omega_s \tag{2.43}$$

and make use of the relation [65]

$$\int d\Omega_s \left(\delta_{ij} - \hat{k}_{si}\hat{k}_{sj} \right) e^{\pm i\mathbf{k}_s\cdot\mathbf{r}} = \left(-\nabla^2 \delta_{ij} + \nabla_i \nabla_j \right) \frac{\sin k_s r}{k_s^3 r}. \tag{2.44}$$

This gives:

$$\Pi^{(\alpha)}(\mathbf{r},t) = \frac{-i}{2(2\pi)^3} \sum_{ij} \bar{\epsilon}_i(\hat{\mathbf{k}}_p)\mu_{Dj} \left(-\nabla^2\delta_{ij} + \nabla_i\nabla_j\right) \int d\mathbf{r}_1 \int \frac{d\omega_p}{2\pi} A_p(\omega_p) \tag{2.45}$$
$$\times \int \frac{d\tilde{\omega}}{2\pi} \langle\hat{\sigma}^\alpha(\mathbf{r}_1,\tilde{\omega})\rangle_\alpha e^{i\mathbf{k}_p\cdot\mathbf{r}_1} e^{i(\tilde{\omega}-\omega_p)t} \int d\omega_s \frac{\sin\omega_s\tilde{r}/c}{\omega_s(\omega_s-(\omega_p-\tilde{\omega}+i\eta))} \frac{1}{\tilde{r}}$$

Where we have defined $\tilde{\mathbf{r}} = \mathbf{r} - \mathbf{r}_1$. The $d\omega_s$ integral has poles at $\omega_s = 0$ and $\omega_s = \omega_p - \tilde{\omega}$. The term arising from the residue at the first pole will have a factor $\frac{1}{\omega_p-\tilde{\omega}}$. Because the interaction between the sample and the field is off-resonant, ω_p will not be close to any material frequency. The term arising from the residue of the pole at $\omega_s = 0$ is negligible in such a process. Thus, we may perform the $d\omega_s$ integration:

$$\int d\omega_s \frac{\sin\omega_s\tilde{r}/c}{\omega_s(\omega_s-(\omega_p-\tilde{\omega}+i\eta))} = \frac{\pi e^{i(\omega_p-\tilde{\omega})\tilde{r}/c}}{\omega_p-\tilde{\omega}} \tag{2.46}$$

Using the identity

$$\left(-\nabla^2\delta_{ij} + \nabla_i\nabla_j\right) e^{ikr} = \{(\delta_{ij} - 3\hat{r}_i\hat{r}_j)(ikr-1) + (\delta_{ij} - \hat{r}_i\hat{r}_j)k^2r^2\}\frac{e^{ikr}}{r^2} \tag{2.47}$$

and rotationally averaging so that $\hat{r}_i\hat{r}_j = \frac{1}{3}\delta_{ij}$ results in

$$\Pi^{(\alpha)}(\mathbf{r},t) = \tag{2.48}$$
$$\frac{-i(\bar{\epsilon}(\hat{\mathbf{k}}_p)\cdot\mu_D)}{6(2\pi c)^2\tilde{r}} \int \frac{d\omega_p}{2\pi} A_p(\omega_p) \int \frac{d\tilde{\omega}}{2\pi} \int d\mathbf{r}_1 e^{i\mathbf{k}_p\cdot\mathbf{r}_1} e^{-i(\omega_p-\tilde{\omega})(t-\tilde{r}/c)} (\omega_p-\tilde{\omega}) \langle\hat{\sigma}^\alpha(\mathbf{r}_1,\tilde{\omega})\rangle.$$

Placing the origin within the sample and taking the detector to be far away (in comparison to the size of the sample) allows the approximation $\tilde{r} = |\mathbf{r}' - \mathbf{R}/2 - \mathbf{r}_1| \simeq r' - \hat{\mathbf{r}}'\cdot(\mathbf{r}_1 + \mathbf{R}/2)$. We have substituted $\mathbf{r} = \mathbf{r}' - \mathbf{R}/2$ since that is the point at which we will eventually evaluate $\Pi^{(\alpha)}$. Although we will later formally integrate over all $\mathbf{R}$, this represents different detection locations and thus should only be carried out over the area of a detector pixel. The assumption that $\mathbf{R}$ is small compared to r' (the distance to the detector) is thus justified. Dropping the retardation due to r' (since this uniformly delays the signal by some constant due to travel time) and replacing the $\tilde{r}$ in the denominator by r' simplifies the expression yielding:

$$\begin{aligned}\Pi^{(\alpha)}(\mathbf{r}' - \mathbf{R}/2, t) = & \frac{-i(\bar{\epsilon}(\hat{\mathbf{k}}_p) \cdot \mu_D)}{6(2\pi c)^2 \tilde{r}} \int d\omega_p A_p(\omega_p) \int \frac{d\tilde{\omega}}{2\pi} e^{-i(\omega_p - \tilde{\omega})(t - \frac{1}{c}\hat{\mathbf{r}}' \cdot \mathbf{R}/2)} \\ & \times (\omega_p - \tilde{\omega}) \langle \hat{\sigma}(\mathbf{Q}(\tilde{\omega}), \tilde{\omega}) \rangle e^{-i\mathbf{Q}(\tilde{\omega}) \cdot \mathbf{r}_\alpha}\end{aligned} \tag{2.49}$$

Where we have also carried out the $d\mathbf{r}_1$ integration via

$$\int d\mathbf{r} e^{-i\mathbf{k}\cdot\mathbf{r}} \langle \hat{\sigma}^\alpha(\mathbf{r}, \tilde{\omega}) \rangle = \langle \hat{\sigma}(\mathbf{Q}(\tilde{\omega}), \tilde{\omega}) \rangle e^{-i\mathbf{Q}(\tilde{\omega}) \cdot \mathbf{r}_\alpha} \tag{2.50}$$

with $\mathbf{Q}^{(\prime)}(\tilde{\omega}) \equiv \frac{1}{c}(\omega_{p^{(\prime)}} - \tilde{\omega})\hat{\mathbf{r}}' - \mathbf{k}_{p^{(\prime)}}$. We are now in a position to perform the integrations over $d\tau$ and $d\mathbf{R}$ in equation (2.38):

$$\int d\tau e^{-i(\omega' - \frac{\Omega}{2})\tau} = 2\pi \delta(\omega' - \frac{\Omega}{2}) \tag{2.51}$$

$$\int d\mathbf{R} e^{-i(\mathbf{k}' - \frac{\Omega}{2c}\hat{\mathbf{r}}') \cdot \mathbf{R}} = (2\pi)^3 \delta(\mathbf{k}' - \frac{\Omega}{2c}\hat{\mathbf{r}}') \tag{2.52}$$

with $\Omega \equiv \omega_p + \omega_p' - \tilde{\omega} - \tilde{\omega}'$ defined for convenience. The bare two-molecule spectrogram is then:

$$\begin{aligned}W_B^{(2)}(t', \omega', \mathbf{r}', \mathbf{k}') = & \frac{|\bar{\epsilon}(\hat{\mathbf{k}}_p) \cdot \mu_D|^2}{36(2\pi)^2 c^4 r'^2} \sum_\alpha \sum_{\beta \neq \alpha} \int d\omega_p d\omega_{p'} d\tilde{\omega} d\tilde{\omega}' A_p(\omega_p) A_p^*(\omega_{p'}) \\ & \times (\omega_p - \tilde{\omega})(\omega_{p'} - \tilde{\omega}') \langle \hat{\sigma}(\mathbf{Q}(\tilde{\omega}), \tilde{\omega}) \rangle \langle \hat{\sigma}(-\mathbf{Q}'(-\tilde{\omega}'), -\tilde{\omega}') \rangle \\ & \times e^{-i\mathbf{Q}(\tilde{\omega}) \cdot \mathbf{r}_\alpha} e^{i\mathbf{Q}'(-\tilde{\omega}') \cdot \mathbf{r}_\beta} e^{-i(\omega_p - \omega_{p'} + \tilde{\omega}' - \tilde{\omega})t'} \delta(\omega' - \frac{\Omega}{2}) \delta(\mathbf{k}' - \frac{\Omega}{2c}\hat{\mathbf{r}}')\end{aligned} \tag{2.53}$$

The single-molecule ($\alpha = \beta$) terms differ, containing the correlation function:

$$\langle \mathcal{T} \hat{\sigma}_R^{\alpha\dagger}(\mathbf{r}_1', t_1') \hat{\sigma}_L^{\alpha}(\mathbf{r}_1, t_1) \rangle \tag{2.54}$$

Since there is only one operator on each side of the density matrix, there is no time ordering ambiguity and we may drop $\mathcal{T}$. The Hilbert space expression is then

$$\mathrm{Tr}[\hat{\sigma}^{\alpha\dagger}(\mathbf{r}_1', t_1') \hat{\sigma}^{\alpha}(\mathbf{r}_1, t_1) \rho_\alpha(0)] \tag{2.55}$$

Although we may not factor this into a product of correlation functions, we may still go through the same series of simplifications as in the two-molecule case resulting in:

$$\begin{aligned} W_{B,inc}(t', \omega', \mathbf{r}', \mathbf{k}') = 2\pi K \sum_\alpha \int d\omega_p d\omega_{p'} d\tilde{\omega} d\tilde{\omega}' A_p(\omega_p) A_p^*(\omega_{p'})(\omega_p - \tilde{\omega})(\omega_{p'} - \tilde{\omega}') \\ \langle \hat{\sigma}(-\mathbf{Q}'(-\tilde{\omega}'), -\tilde{\omega}') \hat{\sigma}(\mathbf{Q}(\tilde{\omega}), \tilde{\omega}) \rangle e^{-i(\mathbf{Q}(\tilde{\omega}) - \mathbf{Q}'(-\tilde{\omega}')) \cdot \mathbf{r}_\alpha} e^{-i(\omega_p - \omega_{p'} + \tilde{\omega}' - \tilde{\omega})t'} \delta(\omega' - \frac{\Omega}{2}) \delta(\mathbf{k}' - \frac{\Omega}{2c} \hat{\mathbf{r}}') \end{aligned} \tag{2.56}$$

where K is a prefactor related to the Thomson cross section and is discussed below (Eq. (2.61)). The total bare spectrogram may also be written in a form similar to this

$$\begin{aligned} W_{B,T}(t', \omega', \mathbf{r}', \mathbf{k}') = 2\pi K \int d\omega_p d\omega_{p'} d\tilde{\omega} d\tilde{\omega}' A_p(\omega_p) A_p^*(\omega_{p'})(\omega_p - \tilde{\omega})(\omega_{p'} - \tilde{\omega}') \\ \langle \hat{\sigma}_T(\mathbf{Q}(\tilde{\omega}), \tilde{\omega}) \hat{\sigma}_T(-\mathbf{Q}'(-\tilde{\omega}'), -\tilde{\omega}') \rangle e^{-i(\omega_p - \omega_{p'} + \tilde{\omega}' - \tilde{\omega})t'} \delta(\omega' - \frac{\Omega}{2}) \delta(\mathbf{k}' - \frac{\Omega}{2c} \hat{\mathbf{r}}') \end{aligned} \tag{2.57}$$

when given in terms of the total (many-particle) charge density. To proceed further, we must specify the detector gating functions that define the experiment. As shown above (Eqs. (2.27) and (2.31)-(2.32)) we have separate detector spectrograms for the time-frequency gating and the space-propagation gating. Both two- and single-molecule bare spectrograms (equations (2.53) and (2.56)) carry the delta function factor $\delta(\mathbf{k}' - \frac{\omega'}{c} \hat{\mathbf{r}}')$. This connects ω' to $\mathbf{k}'$ in the usual way (though this is not automatic since the two are not *a priori* related in this way but rather both begin as seperate gating variables) as well as fixing the direction of $\mathbf{k}'$. For this reason, the logical choice for the spatial detector spectrogram is

$$W_D(\mathbf{r}', \mathbf{k}'; \bar{\mathbf{r}}, \bar{\mathbf{k}}) = \delta(\mathbf{r}' - \bar{\mathbf{r}}) \tag{2.58}$$

This represents a spatially resolved signal; that is, the location of the detection event (the pixel location) is resolved.

Ordinarily, the time-resolution in ultrafast experiments is obtained by using ultrashort pulses for the pumping and probing. That is, there is no time-dependent shutter or special temporal sensitivity to the detector. If the detector spectrogram does not depend on t' (no time-gating is applied), we may separate the time-dependent phase factors from the auxilliary functions and carry out the time integration to give a factor of $\delta(\omega_p - \omega_{p'} + \tilde{\omega}' - \tilde{\omega})$. The two- and single-molecule signals are therefore given by

$$\begin{aligned} S^{(2)}(\bar{\omega}, \bar{\mathbf{r}}, \Lambda) =& K \int d\omega' |F_f(\omega', \bar{\omega})|^2 \omega'^2 \sum_{\alpha\beta} \int d\omega_p d\omega_{p'} A_p(\omega_p) A_p^*(\omega_{p'}) \\ & \times e^{-i(\mathbf{q}\cdot\mathbf{r}_\alpha - \mathbf{q}'\cdot\mathbf{r}_\beta)} \langle \hat{\sigma}(\mathbf{q}, \omega' - \omega_p) \rangle \langle \hat{\sigma}(-\mathbf{q}', \omega_{p'} - \omega') \rangle \end{aligned} \tag{2.59}$$

$$\begin{aligned} S^{(1)}(\bar{\omega}, \bar{\mathbf{r}}, \Lambda) =& K \int d\omega' |F_f(\omega', \bar{\omega})|^2 \omega'^2 \sum_{\alpha} \int d\omega_p d\omega_{p'} A_p(\omega_p) A_p^*(\omega_{p'}) e^{-i(\mathbf{q} - \mathbf{q}')\cdot\mathbf{r}_\alpha} \\ & \times \langle \hat{\sigma}(-\mathbf{q}', \omega_{p'} - \omega') \hat{\sigma}(\mathbf{q}, \omega' - \omega_p) \rangle \end{aligned} \tag{2.60}$$

where $\mathbf{q}^{(\prime)} \equiv \frac{\omega'}{c}\hat{\bar{\mathbf{r}}} - \mathbf{k}_{p^{(\prime)}}$ is the momentum transfer, $F_f(\omega, \bar{\omega})$ is the frequency gating function, and Λ stands for the set of parameters that define the external pulse envelopes (including $\mathbf{k}_{p^{(\prime)}}$). We approximate

$$K = \frac{|\bar{\epsilon}(\hat{\mathbf{k}}_p) \cdot \mu_D|^2}{72\pi c^4 r'^2} \tag{2.61}$$

as a constant on the assumption that all pixels are roughly equidistant from the sample.

In textbook approaches to static x-ray scattering, the incoming light is treated as a plane wave and the differential scattering cross section is found to be proportional to $r_0^2(\frac{\omega_s}{\omega_p})|\epsilon_p \cdot \epsilon_s|^2$ with r_0 the classical electron radius. Our incorporation of the detection event included a summation over polarizations of the signal field and an averaging over initial polarizations and emission directions. This was shown to lead to the replacement $\epsilon_p \cdot \epsilon_s \to \bar{\epsilon}(\hat{\mathbf{k}}_p) \cdot \mu_D$ while the use of atomic units equates $r_0^2 = \frac{1}{c^4}$. Finally, since we calculate the signal (defined as the expectation value of the gated electric field) by explicitly incorporating the detection event (which is linear in ω_s) our result is proportional to ω_s^2. Recalling that $\mathbf{A}(\omega) \propto \frac{1}{\omega}\mathbf{E}(\omega)$, we see that our result carries the appropriate proportionality factors compared to the usual differential scattering cross section ([66]). We henceforth neglect the constant K, focusing only on the $\mathbf{q}$-dependence that carries information on the spatial structure of the sample, the object of study in x-ray diffraction experiments.

That the arguments of Eqs. (2.59)-(2.60) are $\bar{\omega}$ and $\bar{\mathbf{r}}$ reflects the fact that they correspond to taking a spectrum at every pixel. Since the final observed signal frequency is $\bar{\omega}$, we may as well relabel it ω_s to make the interpretation more intuitive. Aside from the expected inverse-square dependence on $\bar{r}$, the signal only depends on $\bar{\mathbf{r}}$ through $\hat{\bar{\mathbf{r}}}$, i.e., the direction vector pointing from the sample to the pixel. Since $\hat{\bar{\mathbf{r}}}$ is the same as the direction of propagation of scattered light, this suggests representing the directional dependence by defining $\frac{\omega_s}{c}\hat{\bar{\mathbf{r}}} \equiv \mathbf{k}_s$. Finally, it is important to note that, althought these signals do not depend on time directly since we have assumed no time resolution (i.e., the pixels are simply left open to collect incoming light), the signal does depend parametrically on the central time of the incoming pulse through the field envelope $A_p(\omega)$ which carries a phase factor $e^{-i\omega T}$. Here, T is the central time of the pulse envelope and the zero of time is set at the end of the state preparation process (where the prepared state is presumed to be known). Since T therefore represents the time separation between state preparation and arrival of the center of the probe pulse and this is a key experimental control, we explicitly write this dependence in future expressions. In section 2.2, we consider this type of frequency-resolved pump-probe diffraction for cysteine and show that the signal exhibits ultrafast coherent oscillations indicative of the material frequencies.

We can of course simply compute the total electric field intensity at each pixel rather than taking a spectrogram. This corresponds to no frequency resolution and we have $\mathcal{F}_f(\omega, \bar{\omega}) = 1$ for the frequency gating function. The long-range (inter-molecular) structure of the sample is captured by the structure factors

$$\begin{aligned} F_1(\mathbf{q}) &= \sum_{\alpha} e^{-i\mathbf{q}\cdot\mathbf{r}_\alpha} && (2.62) \\ F_2(\mathbf{q}, \mathbf{q}') &= \sum_{\alpha} \sum_{\beta \neq \alpha} e^{-i(\mathbf{q}\cdot\mathbf{r}_\alpha - \mathbf{q}'\cdot\mathbf{r}_\beta)} \end{aligned}$$

in terms of which the diffraction signals can be written as

$$\begin{aligned} S^{(2)}(\mathbf{k}_s, \Lambda) &= \int d\omega \frac{\omega^2}{\omega_p \omega_p'} \int d\omega_p d\omega_{p'} E_p(\omega_p) E_p^*(\omega_{p'}) && (2.63) \\ &\quad \times F_1(\mathbf{q} - \mathbf{q}') \langle \hat{\sigma}(-\mathbf{q}', \omega_{p'} - \omega) \hat{\sigma}(\mathbf{q}, \omega - \omega_p) \rangle \\ S^{(2)}(\mathbf{k}_s, \Lambda) &= \int d\omega \frac{\omega^2}{\omega_p \omega_p'} \int d\omega_p d\omega_{p'} E_p(\omega_p) E_p^*(\omega_{p'}) && (2.64) \\ &\quad \times F_2(\mathbf{q}, \mathbf{q}') \langle \hat{\sigma}(-\mathbf{q}', \omega_{p'} - \omega) \rangle \langle \hat{\sigma}(\mathbf{q}, \omega - \omega_p) \rangle \end{aligned}$$

where we have substituted the electric field envelopes for the vector potential. For near-elastic scattering, we approximate $\frac{\omega}{\omega_p^{(\prime)}} \approx 1$, which is nearly valid even for inelasticities of several eV since the central frequency of the x-ray pulse is on the order of 10keV. Similarly, the momentum transfer is approximated as independent of frequency. For the purposes of time-resolved diffraction studies, a time-domain expression is more convenient to simulate due to the nuclear motion. We thus substitute the time-domain charge density operator

$$\hat{\sigma}(\mathbf{q}, \omega) = \int dt \hat{\sigma}(\mathbf{q}, t) e^{i\omega t}, \tag{2.65}$$

to obtain

$$S^{(2)}(\mathbf{q},\Lambda) = F_2(\mathbf{q},\mathbf{q}) \int d\omega \int dt dt' e^{i\omega(t-t')} E_p(t) E_p^*(t') \langle \hat{\sigma}(-\mathbf{q},t') \rangle \langle \hat{\sigma}(\mathbf{q},t) \rangle \tag{2.66}$$

$$S^{(1)}(\mathbf{q},\Lambda) = F_1(0) \int d\omega \int dt dt' e^{i\omega(t-t')} E_p(t) E_p^*(t') \langle \hat{\sigma}(-\mathbf{q},t') \hat{\sigma}(\mathbf{q},t) \rangle \tag{2.67}$$

where we have replaced $\mathbf{k}_s$ by $\mathbf{q}$ in the argument in accordance with the quasi-elastic approximation. Upon carrying out the $d\omega$ integration and using $\hat{\sigma}(-\mathbf{q}) = \hat{\sigma}^*(\mathbf{q})$, finally results in

$$S^{(2)}(\mathbf{q},\Lambda) = F(\mathbf{q}) \int dt |E_p(t)|^2 |\langle \hat{\sigma}(\mathbf{q},t) \rangle|^2 \tag{2.68}$$

$$S^{(1)}(\mathbf{q},\Lambda) = N \int dt |E_p(t)|^2 \langle |\hat{\sigma}(\mathbf{q},t)|^2 \rangle. \tag{2.69}$$

We have relabeled $F_2(\mathbf{q},\mathbf{q}) \to F(\mathbf{q})$ here to match Eq. (2.20) since, under the above approximations, F_2 is diagonal in $\mathbf{q}$ and F_1 only contributes at $F_1(0) = N$. Equations (2.68)-(2.69) are identical to (2.18) and (2.19) and we have completed the derivation from both perspectives.

2.1 Pump-Probe X-Ray Diffraction

Diffraction results from the interference of waves elastically scattered from different positions in space [67, 68]. Since the phase difference between waves originating from different spatial locations encodes the sample geometry, the diffraction of waves can be used to infer the spatial stucture of the arrangement of scatterers. This technique has long been used with off-resonant x-rays to reveal the atomic structure of crystalline solids, where the long-range order amplifies the diffraction signal for certain values of the momentum transfer scattering vector $\mathbf{q}$, known as the Bragg peaks. The location pattern of the Bragg peaks then reveals the long-range crystal structure while their intensity pattern reflects the unit-cell structure through the classical diffraction signal

$$S(\mathbf{q}) \propto |\sigma(\mathbf{q})|^2 \tag{2.70}$$

where $\sigma(\mathbf{q})$ is the charge density and $\mathbf{q}$ is the scattering momentum change. An important caveat to this technique is that the phase of the $\mathbf{q}$-space charge density is lost due to the squaring. This well-known "phase problem" complicates the retrieval of the real-space charge density by a Fourier transform of $\sigma(\mathbf{q})$. Several methods, such as oversampling, have been developed to overcome this difficulty [69, 70, 71]. Diffraction has also been employed in the absence of crystallinity, to reveal e.g., the interparticle distances in fluids. Moreover, increasingly bright x-ray light sources, such as x-ray free-electron lasers (FELs), hold the promise of producing detectible diffraction patterns even from single molecules, revealing the complete real-space structure of the molecular charge density without the need for often time-consuming crystallization [72, 73, 74, 75, 76, 77]. Recently demonstrated time-resolved spectroscopy on single molecular ions suggests the possibility for single ion time-resolved diffraction [77]

The development of synchrotron-based FELs [17, 16, 18] and tabletop high-harmonic generation (HHG) light sources [78, 79, 80] has permitted the generation of bright ultrashort x-ray pulses [21, 20, 81]. This has opened up the possibility to carry out time-dependent, pump-probe diffraction in which a system is first pumped to an excited state by a visible or UV pulse and is then probed *via* the diffraction of a second x-ray pulse at various time-delays, allowing the reconstruction of "molecular movies" to visualize the dynamics [22, 23, 24, 25, 26, 82, 27, 28, 29, 30, 31, 32, 36]. Intuitively, the time-dependent diffraction signal would then be given by simply replacing $\sigma(\mathbf{q})$ in Eq. 2.70 with a time-dependent charge density

$$S(\mathbf{q},t) \propto |\sigma(\mathbf{q},t)|^2. \tag{2.71}$$

However, a more thorough analysis reveals that Eq. (2.71) may apply in some parameter regimes but does not hold generally. It was, for example, demonstrated that the diffraction signal for a simple nonstationary system (an excited Hydrogen atom) does not possess the centrosymmetric property exhibited by Eq. (2.71) (i.e., $S(\mathbf{q},t) = S(-\mathbf{q},t)$) [35].

In sections 2.2-2.3, we discuss Eqs. (2.18)-(2.19) as the proper time-dependent generalization of Eq. (2.70) and explore the consequences of deviation from the form of Eq. (2.71). We show that the signal not only depends on the charge densities of the relevent electronic states but also on the transition charge densities, off-diagonal elements of the charge density operator. Section 2.2 calculates the x-ray scattering from an x-ray Raman pumped cysteine molecule to track the electronic evolution. Section 2.3 calculates the x-ray scattering from photo-excited NaF to track the resulting nuclear motion. Signals from gas-phase samples and single molecules are compared with those from systems which have structural order such as crystals and liquids. Formally, all results are equally applicable to the diffraction of femtosecond electron pulses as well. This is a new emerging field that can also probe the electronic charge density of material samples [23, 81, 83, 84, 85, 86, 87].

2.1.1 Ordered *vs.* Disordered Samples

In crystals, the structure factor $F(\mathbf{q})$ (Eq. (2.20)) is sharply peaked at the Bragg points $\mathbf{q}_{\text{Bragg}}$ directly related to reciprocal lattice vectors. At these Bragg peaks, the terms in the double summation coherently add up and the result scales as N^2, i.e., quadratically in the molecule number. Away from the Bragg peaks, the terms in the double sum have essentially random relative phase and the result is negligible. The positions of these Bragg peaks can

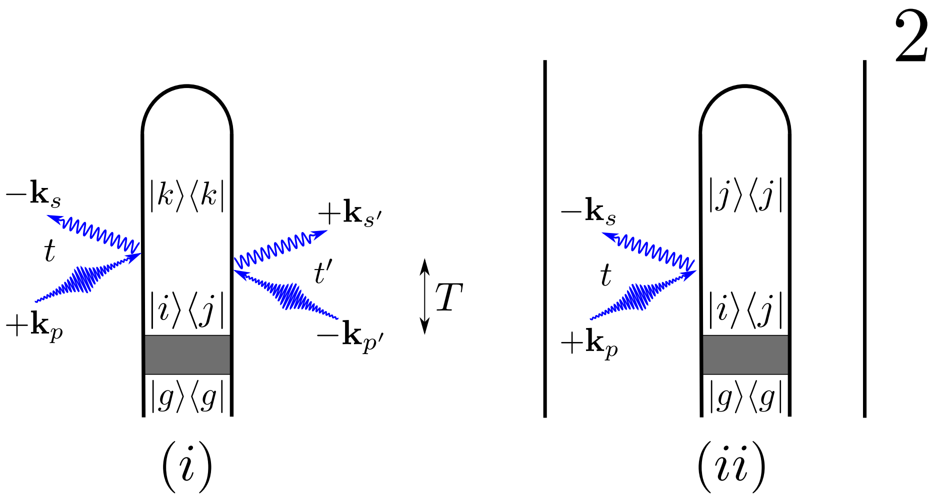

Figure 2.2: Loop diagrams for single- (i) and two-molecule (ii) x-ray scattering processes. The shaded area represents an unspecified process that prepares the system in an arbitrary state ($|g\rangle$ is the electronic ground state) and T is the pump-probe delay time. The amplitude-squared form of the two-molecule contribution is explicitly indicated. We denote modes of the pump with p and p' whereas s, s' represent relevant scattering modes ($\mathbf{k}_{p^{(\prime)}}$ has frequency $\omega_{p^{(\prime)}}$ and $\mathbf{k}_{s^{(\prime)}}$ has frequency $\omega_{s^{(\prime)}}$). Elastic scattering corresponds to $\omega_{ki} = \omega_{kj} = 0$ for the single-molecule and $\omega_{ij} = \omega_{kl} = 0$ for the two-molecule contributions. Elastic scattering therefore originates from scattering off populations. For diagram rules, see [64, 88]

then be used to obtain the crystal structure while the $\mathbf{q}$-space molecular charge density can then be sampled at the Bragg peaks or near the central maximum, the latter requiring that the molecules are sufficiently close compared to the probing wavelength.

The effect of structural disorder in a crystal is to blur the Bragg peaks. This is readily quantified with the Debye-Waller factor, which results from averaging the exponential in $F(\mathbf{q})$ over Gaussian spatial fluctuations and takes the form of

$$F_{\mathrm{DW}}(\mathbf{q}) = \langle e^{i\mathbf{q}\cdot\mathbf{u}_\alpha}\rangle_{\mathrm{T}}^2 = e^{-q^2\langle u_\alpha^2\rangle_{\mathrm{T}}/3} \tag{2.72}$$

where $\mathbf{u}_\alpha$ is the displacement from equilibrium of molecule α and $\langle\ldots\rangle_{\mathrm{T}}$ stands for a thermal average, though the same argument applies for any Gaussian disorder that can be treated exactly by the second order cumulant expansion. The Debye-Waller factor is commonly used to describe the degradation of the Bragg pattern due to unavoidable small-amplitude disorder from phonons in real samples. Here we use it for large fluctuations to interpolate between ordered and disordered samples. In the case of liquids, $F(\mathbf{q})$ reveals rings at the nearest- and next-nearest-neighbor distances etc., but decays to zero for larger values as there is no long-range structure in a liquid. In the most disordered case of a gas, the molecular distribution is flat in space and $F(\mathbf{q})$ vanishes except at the central maximum ($\mathbf{q} = 0$). This can be seen by taking the limit of large disorder in Eq. (2.72) or by taking the continuum limit of Eq. (2.20) and integrating over all space assuming a homogenous distribution of molecules to obtain a delta function $\delta(\mathbf{q})$.

When the terms in $F(\mathbf{q})$ add coherently, such as at the $\mathbf{q}_{\text{Bragg}}$, the resulting N^2-scaling overhwelms the N-scaling of the single-molecule signal S_1 and the diffraction pattern is well approximated by S_2 (Eq. (2.18)). In contrast, the signal between the Bragg peaks or from a sample lacking long-range order, such as a gas, will be dominated by the single-molecule signal (Eq. (2.19)) since $F(\mathbf{q})$) is negligible in these regimes. Similarly, diffraction of an intense FEL pulse by a single molecule is also given by Eq. (2.19) [22, 35, 89]

We note that, aside from the factor $F(\mathbf{q})$ and convolution with the x-ray temporal pulse envelope $\mathcal{E}(t - T)$ (shifted to be centered at zero argument), the two-molecule signal (Eq. (2.18)) matches the intuitive form of the time-resolved diffraction signal given in Eq. (2.71).

2.2 Frequency-Resolved Diffraction of a Single Cysteine Molecule

In this section, we discuss ultrafast pump-probe x-ray diffraction from a single oriented cysteine molecule. Cysteine is a sulfur-containing amino acid which affects the secondary structure of many proteins because of the disulfide bonds it forms. It has been implicated in biological charge transfer in respiratory complexes [90] and various resonant x-ray spectroscopic signals from this molecule, including stimulated x-ray Raman scattering (SXRS) and x-ray photon echo, have been studied [91, 92].

In this section, the pumping process will be an x-ray Raman excitation that prepares a wavepacket of electronic excitations. The nuclei will be assumed frozen throughout the experiment and the time-dependence will come only through the electronic evolution. As will be discussed further below, the elastic scattering is dominated by the core electrons, which closely track the position of the nuclei. In contrast, the inelastic scattering is dominated by electronic coherences, i.e., by scattering-induced transitions between excited states in the electronic wavepacket. The inelastic scattering therefore reveals information about the electronic excitation and we focus on the inelastic contributions in this section.

Two-particle scattering from populations is an elastic process and from coherences is inelastic. Single-molecule scattering, in contrast, generally produces both elastic and inelastic contributions regardless of the initial material state, as evident from Eqs. (2.59)-(2.60) and Fig. 2.2. Thus, the coherent terms can only induce transitions between states populated by the electronic wavepacket while the single-molecule terms can induce transitions to any electronic state (though transitions between states occupied by the wavepacket are strongest). Our QED approach generalizes previous treatments [66, 35] to properly account for arbitrary pulse bandshape, non-impulsive pulses, and detection details, and the role of electronic coherence.

In order to selectively observe the inelastic scattering, we consider a frequency-resolved signal. While this has not yet been demonstrated in the x-ray regime, it has been shown possible to discriminate a single wavelength component from multiwavelength scattering data in the EUV range [93]. From Eq. (2.60)) with $|F_f(\omega', \bar{\omega})|^2 = \delta(\omega' - \bar{\omega})$, this signal is given by

$$S(\mathbf{k}_s, \Lambda) = \sum_{ijk} \rho_{ij} \omega_s^2 e^{-i\omega_{ij}T} \mathcal{A}_p(\omega_s + \omega_{ki}) \mathcal{A}_p^*(\omega_s + \omega_{kj}) \sigma_{ki}(\mathbf{q}_{ki}) \sigma_{kj}^*(\mathbf{q}_{kj}), \tag{2.73}$$

where $\mathcal{A}_p(\omega)$ is the spectral envelope of the scattered pulse, $\sigma_{ij}(\mathbf{q})$ are Fourier transformed matrix elements of the charge-density operator and i, j, k index electronic states. We have also defined the momentum-transfer vector $\mathbf{q}_{ij} \equiv \mathbf{k}_s - \frac{\omega_s+\omega_{ij}}{c}\hat{\mathbf{k}}_p$.

The scattering signal from the ground state (the term in equation 2.73 with $i = j = g$, the ground state) is depicted in Figs. 2.3**a** and 2.3**b**. We also show the ground-state electron density, $\sigma_{gg}(\mathbf{r})$, the pulse power spectrum, and the pulse wave vector for reference. We take the scattering pulse to be a transform-limited Gaussian

$$\mathcal{A}_p(\omega) = \mathcal{A}_p\sqrt{2\pi}\tau_p e^{-\tau_p^2(\omega-\Omega_p)^2/2}. \tag{2.74}$$

The center frequency Ω_p is set to 10 keV, and we take the direction of propagation to be in the positive x direction (for molecule orientation, see Fig. 2.3.**c**). The pulse duration is $\tau_p = 300$ as which corresponds to a fwhm bandwidth of 3.65 eV. Future progress in pulse-generation may make such experiments realizable. For this frequency range, the difference between $\tilde{\mathbf{q}}$ and $\mathbf{q}_{ij}$ for any two states i and j is negligibly small, and is ignored in the calculations presented herein.

We take the signal detectors to be on square grid, 2 cm in length on each side, located 1 cm from the molecule in the positive x direction (i.e., we detect forward-scattered light). This corresponds to a maximum detected scattering angle of 54.7°. We consider two different values for the detection frequency ω_s, one inside and one outside the pulse bandwidth. When we set the detection frequency equal to the central pulse frequency, we get the signal shown in Fig. 2.3.**a**. This signal is dominated by the elastic scattering terms, where the scattering process does not change the state of the molecule. At this detection frequency, the elastic contribution is 4.4×10^6 larger than the inelastic.

The elastic scattering term can be eliminated by moving the detection frequency outside the pulse bandwidth. In Fig. 2.3.**b**, we show the scattering signal with a detection frequency

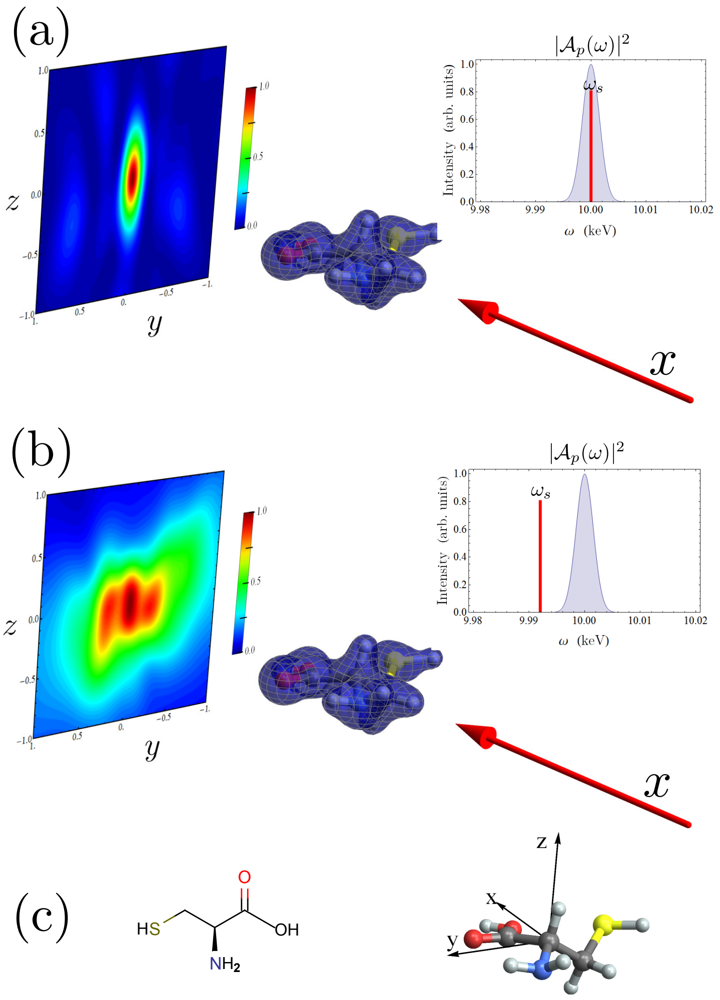

Figure 2.3: Off-resonant scattering of a Gaussian x-ray pulse from cysteine for different detection frequencies. On the right we show the pulse power spectrum in blue, with the detection frequency marked as a red line. The pulse propagation vector is shown as a red arrow, pointing at the molecule aligned in the lab frame, with the scattering pattern shown in the background. **a**: The detection frequency ω_s is set equal to the pulse center frequency Ω_p, and the scattering signal is dominated by the elastic term. **b**: The detection frequency is set to $\Omega_p - 9\,\mathrm{eV}$, and the inelastic terms are dominant. **c**: Chemical structure (left) and lab-frame orientation (right) of the cysteine molecule (O is red, S is green, N is blue, C is grey, H is white.

$\omega_s = \Omega_p - 9\,\mathrm{eV}$. With this detection frequency, we see inelastic terms from valence states e whose excitation energy satisfies the condition that $\omega_{eg} + \omega_s$ is within the pulse bandwidth. Therefore all states with an energy between 4 and 12 eV will contribute. The scattering pattern resulting from the elastic and inelastic process are vastly different. The former is more strongly centered around the origin, corresponding to $q = 0$, and elongated in the z direction. The inelastic term, in addition to the feature at the origin, has two equal-intensity peaks flanking the origin.

We next turn to time-resolved scattering, in which an x-ray Raman preparation pulse $E_R(\omega)$, resonant with the sulfur K edge, arrives at $t = 0$ followed by diffraction at time $t = T$. In this process, the Raman pulse acts twice on the same side of the loop, first promoting a sulfur 1s electron to the valence band before the transient core hole is filled by another valence electron. Raman excitation processes have been shown to dominate over photoionization for sufficiently short x-ray pulses (below $1fs$ in atomic sodium [94]) and can be used to target particular intermediate states (the Sulfur K edge excitations in this case). Because the Raman pulse is broadband, these two dipole interactions leave the molecule in a superposition of valence-excited states. This wavepacket is initially localized in the region surrounding the atom whose core is in resonance (sulfur in this case), but becomes delocalized across the molecule in a $< 5\,\mathrm{fs}$ time scale [95, 96].

The molecular density matrix immediately following the interaction with the first pulse is

$$\hat{\rho} = i\hat{\alpha}\hat{\rho}_0 - i\hat{\rho}_0\hat{\alpha}^\dagger \tag{2.75}$$

where

$$\hat{\alpha} = \sum_{c,e} \big|e\big\rangle \frac{(\boldsymbol{\epsilon}_R \cdot \boldsymbol{\mu}_{ec})(\boldsymbol{\epsilon}_R \cdot \boldsymbol{\mu}_{cg})}{2\pi} \int_{-\infty}^{\infty} d\omega \frac{E_R^*(\omega)\, E_R(\omega + \omega_{eg})}{\omega - \omega_{ce} + i\Gamma_c} \big\langle g\big| \tag{2.76}$$

is the effective polarizability operator (c is an intermediate core excitation in the x-ray

Raman process) and $\hat{\rho}_0$ is the initial (equilibrium) density matrix. In Eq. (2.76), $\boldsymbol{\epsilon}_R$ is the polarization vector for the Raman pulse and $\boldsymbol{\mu}_{ec}$ is the transition dipole between the valence-excited state e and the core-excited state c.

For a single-molecule system prepared in this manner (and with the simplification $\mathbf{q} \to \mathbf{q}_0$), equation (2.73) assumes the form

$$S(\boldsymbol{k}_s, T) = \sum_{e,e'} i\alpha_{e,g} e^{-i\omega_{eg}T} \mathcal{A}_p(\omega_s + \omega_{e'e}) \mathcal{A}_p^*(\omega_s + \omega_{e'g}) \sigma_{e'e}(\tilde{\mathbf{q}}) \sigma_{e'g}^*(\tilde{\mathbf{q}}) + \text{c.c} \tag{2.77}$$

Note that any amplitude in the ground state after the Raman pulse has passed (terms in equation (2.77) where $e = g$) will contribute to a background signal independent of the delay time, which can be filtered out. The remaining time-dependent scattering signal is a difference signal and will have positive and negative features, unlike the ground-state scattering signals from Fig. 2.3 which were only positive. The largest contributions will come from terms where e' in Eq. (2.77) is equal to either e or g.

We take the Raman pulse center frequency at the sulfur K-edge frequency $\Omega_R = 2.473\,\text{keV}$, and polarized along the x direction. The x-ray Raman signal is highly dependent upon the choice of polarization vector, and the nature of the underlying wavepacket is quite different for a y or z polarized pulses [97]. We take both the Raman and scattering pulses to be Gaussian with duration 100 as (fwhm of 10.96 eV). The broad bandwidth connects the ground state with the set of valence excited states with energies between 5.7 eV and 9.0 eV. Figure 2.4 shows the time-dependent x-ray scattering signal for interpulse delays ranging from 0 to 20 fs. For each signal, we also show the transition density for the Raman wavepacket prior to interaction with the scattering pulse. This is defined by

$$\text{Tr}\big[\hat{\sigma}(\boldsymbol{r})\hat{\rho}\big] = \sum_{e} i\alpha_{eg} e^{-i\omega_{eg}T} \sigma_{eg}(\boldsymbol{r}) + \text{c.c.} \tag{2.78}$$

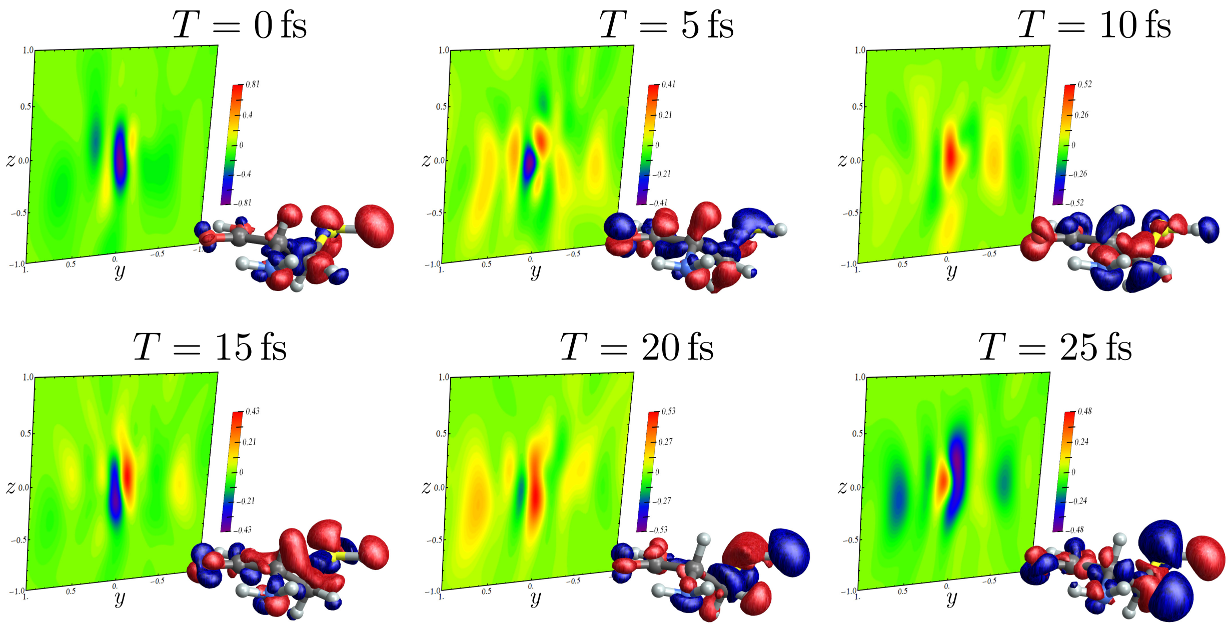

Figure 2.4: Background: time-dependent x-ray scattering (with $\omega_s = \Omega_p$) following x-ray Raman scattering (equation (2.77)) for various interpulse delay times. Foreground: real-space transition charge densities for the Raman wavepacket (equation (2.78)). Refer to Fig. 2.3c for the positions lab-frame orientation.

The left panel of Fig. 2.4 shows that the transition density is localized near the sulfur atom at $T = 0\,\mathrm{fs}$. From Fig. 2.4, we see that there is a good deal more structure in the scattering signal along the y direction than along the z direction. This is consistent with the fact that the electronic motion induced by the Raman pulse is mostly in the y direction. While the correspondence between electronic motion in real space and the resulting scattering pattern is highly suggestive, it is not immediately apparent whether the transition density can be recovered from the scattering pattern alone. This is because the scattering pattern (equation 2.77) is not simply the Fourier transform of the density (equation 2.78).

The scattering signal shows a complex dependence on time, reflecting interference between the many different electronic states which make up the superposition. The signal may not simply be thought of as a snapshot of the instantaneous time-dependent charge-density. The time variation strongly depends on the scattering direction, as can be seen in Fig. 2.5. Here we depict the time evolution of six points from the $T = 0\,\mathrm{fs}$ signal, corresponding to the

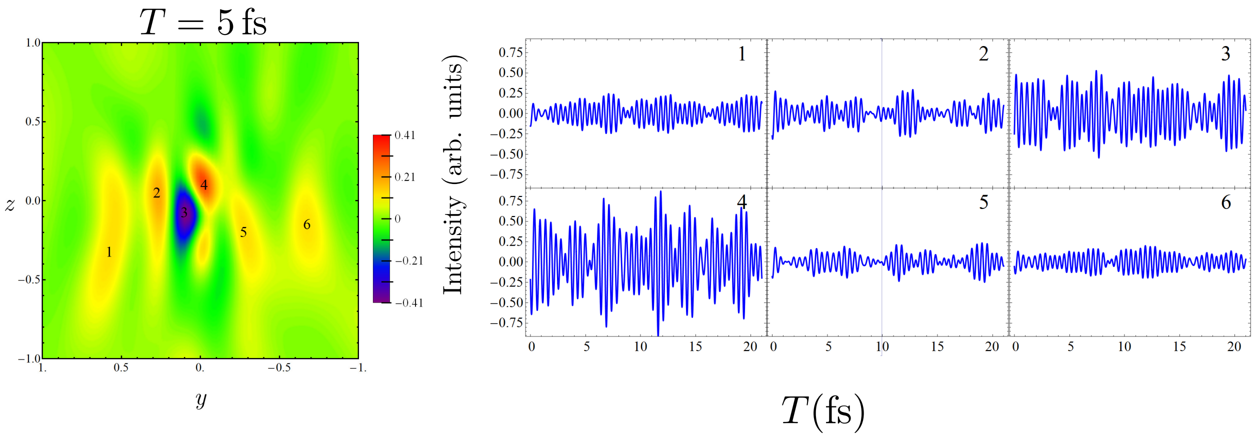

Figure 2.5: Time-dependence of the off-resonant x-ray scattering plot (with $\omega_s = \Omega_p$). Left: The scattering signal for $T = 5\,\mathrm{fs}$, with six different features labeled. Right: The evolution of these different features with increasing interpulse delay.

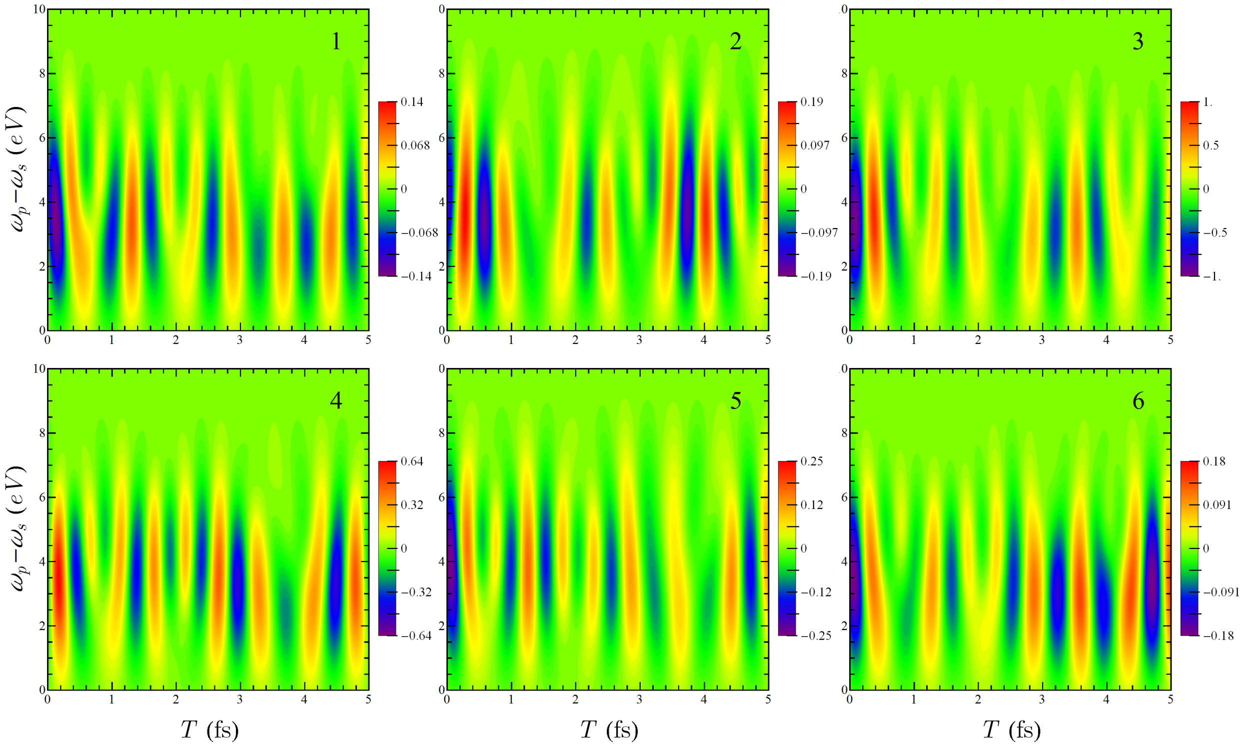

Figure 2.6: Variation of the six features in the $T = 0\,\mathrm{fs}$ scattering signal in Fig. (5) with detection frequency ω_s and delay time T.

highest and lowest peaks therein. Each trace has a beating pattern, representing a spatially resolved interferogram. Decay due to finite lifetime and dephasing is not included in the time-domain signals presented here. The contribution to the signal at a given detector due to a particular electronic coherence can be determined by Fourier transforming with respect to the delay time. This would give information on the transition density for the contributing excited states. However, we do not pursue this analysis here.

In Fig. 2.6 we show the variation of the time traces in Fig. 2.5 with the detection frequency ω_s. In the previous figures, ω_s was set equal to the scattering pulse center frequency, Ω_p. However, since purely elastic processes do not contribute to the time-dependent signal, the signal is larger for $\omega_s < \Omega_p$. The signal is maximized when, for a given e and e' from equation (2.77), both $\omega_s + \omega_{e'e}$ and $\omega_s + \omega_{e'g}$ lie within the pulse bandwidth.

2.3 Time-Resolved Diffraction of Nonadiabatic Molecular Dynamics

In the previous section, we analyzed the time- and frequency-resolved scattering from a nonstationary electronic state. While this is an exciting possible future class of experiments current interest and capabilities are toward tracking nuclear dynamics and structural changes in molecules. For illustration purposes, we take a model with two adiabatic electronic states, ground $|g\rangle$ and excited $|e\rangle$, and a nuclear degree of freedom $\mathbf{R}$ (the formal generalization to multiple excited states and nuclear coordinates is straightforward). The time-dependent wavefunction is then

$$|\Psi(t)\rangle = \sum_{i=e,g} c_i(t)|\chi_i(t)\rangle|i\rangle \qquad (2.79)$$

where $c_i(t)$ is the electronic state amplitude and $|\chi_i(t)\rangle$ is the time-dependent normalized nuclear wavepacket on the electronic state $|i\rangle$. Electronic operators, such as the charge density, generally depend on the nuclear configuration too, so that $\hat{\sigma}(\mathbf{q}) = \hat{\sigma}(\mathbf{q};\mathbf{R})$. The charge density will therefore remain an operator due to this dependence even after taking matrix elements in the electronic subspace (see appendix A.1). We thus denote

$$\langle i|\hat{\sigma}(\mathbf{q},\mathbf{R})|j\rangle = \hat{\sigma}_{ij}(\mathbf{q};\mathbf{R}) \tag{2.80}$$

with the circumflex notating the operator-valued nature of the charge density. Below, we will omit the explicit $\mathbf{R}$-dependence for conciseness.

In the case that the sample possesses long-range order, two-molecule scattering is dominant and the signal is given by Eq. (2.18) as described above. Expanding Eq. (2.18) using Eq. (2.79) gives the time-resolved scattering signal

$$\tilde{S}_2(\mathbf{q},t) = \tag{2.81}$$

$$\Bigg|\underbrace{\rho_{gg}(t)\langle\chi_g(t)|\hat{\sigma}_{gg}(\mathbf{q})|\chi_g(t)\rangle}_{\text{(i)}} + \underbrace{\rho_{ee}(t)\langle\chi_e(t)|\hat{\sigma}_{ee}(\mathbf{q})|\chi_e(t)\rangle}_{\text{(j)}} + \underbrace{2\Re\big[\rho_{eg}(t)\langle\chi_e(t)|\hat{\sigma}_{eg}(\mathbf{q})|\chi_g(t)\rangle\big]}_{\text{(k)+(l)}}\Bigg|^2,$$

$$S_2(\mathbf{q},T) = F(\mathbf{q})\int dt|E_p(t-T)|^2\tilde{S}_2(\mathbf{q},t), \tag{2.82}$$

where we have labeled the terms to allow for convenient discussion. While $F(\mathbf{q})$ is N^2 at bragg peaks and zero elsewhere (or broadened by the Debye-Waller factor for finite disorder), the structure of the molecular charge density is encoded in Eq. (2.81). The first and second of the three terms in the amplitude are, when squared, simply the elastic ground- and excited-state scattering respectively. Their coefficients are ρ_{ii}^2 $(i = e, g)$, the square of the electronic population which is the joint probability of finding two molecules in state $|i\rangle$.

Terms (i) and (j) of Eq. (2.81) generate cross terms when the amplitude is squared. These come as $\Re(\sigma_{gg}\sigma_{ee}^*)$ and constitute heterodyne interference between the ground- and excited-state diffraction. They are proportional to the product of ground- and excited-state populations $\rho_{gg}\rho_{ee}$, or the joint probability of finding one molecule each in the ground and excited states. Thus, they scale favorably compared to the direct excited-state diffraction for perturbatively prepared samples, a fact that has been utilized in crystalline and powder samples to record the excited-state charge density using the ground-state diffraction as a local oscillator to boost the excited-state signal [98, 99]. Moreover, these cross terms carry the relative phase information between ground and excited states. Thus, with knowledge of the ground state charge density, the phase problem can be solved and $\sigma_{ee}(\mathbf{q})$ can be inverted to obtain the excited state charge distribution.

Finally, terms (k) and (l) in Eq. (2.81) arise from the combination of inelastic scattering and electronic coherences. Depending on the dynamics, the electronic coherences may quickly decay, rendering this third term negligible so that the scattering is given only by the ground- and excited-state diffraction and their heterodyne interference. Moreover, the coherence $\rho_{eg}(t)$ oscillates at electronic frequencies and thus, the inelastic scattering is also negligible when the temporal envelope of the x-ray pulse is too long to capture this oscillation. More generally, the inelastic term as well as its cross-terms with the elastic scattering, can all contribute. The possibility of separating out these terms in the diffraction pattern and what could be learned by doing so is a largely unexplored area of inquiry that gradually becomes more relevant as ultrabright x-ray pulses on the timescale of electronic motion become available [100]. We also note that, even though our discussion has focused on electronic coherences, the same formalism applies to vibrational coherences. Indeed, vibrational wavepackets are unavoidably created in the ground state via Raman processes during the pumping.

In the absence of long-range, intermolecular order, the vanishing structure factor $F(\mathbf{q})$ renders the two-molecule scattering negligible and the signal is dominated by the single-molecule scattering. Expanding Eq. (2.19) using Eq. (2.79) gives the time-resolved gas-phase scattering signal

$$\begin{aligned}\tilde{S}_1(\mathbf{q},t) = \Big\{ & \underbrace{\rho_{gg}\langle\chi_g(t)|\hat{\sigma}^{\dagger}_{gg}\hat{\sigma}_{gg}|\chi_g(t)\rangle}_{\text{(a)}} + \underbrace{\rho_{gg}\langle\chi_g(t)|\hat{\sigma}^{\dagger}_{ge}\hat{\sigma}_{eg}|\chi_g(t)\rangle}_{\text{(b)}} \\ & + \underbrace{\rho_{ee}\langle\chi_e(t)|\hat{\sigma}^{\dagger}_{ee}\hat{\sigma}_{ee}|\chi_e(t)\rangle}_{\text{(c)}} + \underbrace{\rho_{ee}\langle\chi_e(t)|\hat{\sigma}^{\dagger}_{eg}\hat{\sigma}_{ge}|\chi_e(t)\rangle}_{\text{(d)}} \\ & + 2\Re\big[\underbrace{\rho_{eg}(t)\langle\chi_e(t)|\hat{\sigma}^{\dagger}_{ee}\hat{\sigma}_{eg}|\chi_g(t)\rangle}_{\text{(f)+(g)}} + \underbrace{\rho_{eg}(t)\langle\chi_e(t)|\hat{\sigma}^{\dagger}_{eg}\hat{\sigma}_{gg}|\chi_g(t)\rangle}_{\text{(e)+(h)}}\big]\Big\}\end{aligned} \tag{2.83}$$

$$S_1(\mathbf{q},T) = N\int dt|E_p(t-T)|^2\tilde{S}_1(\mathbf{q},T) \tag{2.84}$$

where $\hat{\sigma}_{ij} \equiv \hat{\sigma}_{ij}(\mathbf{q})$, i.e., the $\mathbf{q}$-dependence is suppressed for brevity. The first two terms ((a) and (b)) represent the elastic and inelastic scattering contributions from the ground state, while the following two terms ((c) and (d)) are the excited-state analogues. The last two terms correspond to mixed elastic-inelastic processes, which scatter off electronic coherences. Each off these terms originates from two processes, which are complex conjugates and are grouped by the final state (the excited state for (f) and (g) and the ground state for (e) and (h)).

X-ray diffraction is ordinarily taken to be purely elastic and the possibility of the inelastic and mixed terms in Eq. (2.83) is rarely considered [33, 22, 34, 89, 100]. In most experimental circumstances, the majority of the charge in a molecule can be definitively assigned to a particular atom. This inspires the independent atom approximation for the molecular charge density

$$\sigma(q) = \sum_{a} |f_a(\mathbf{q})| e^{i\mathbf{q}\cdot\mathbf{R}_a + i\phi_a(\mathbf{q})} \tag{2.85}$$

where $\phi_a(q)$ is the phase of f_a, the atomic form factor of the a-th atom, and R_a is the position of the ath atom. Evaluating, e.g., $\langle\chi_e(t)|\hat{\sigma}^\dagger_{ee}\hat{\sigma}_{ee}|\chi_e(t)\rangle$ with the density from Eq. (2.85) yields

$$I^{(e)}_{\text{mol}} + I^{(e)}_{\text{at}} = \sum_{a}\sum_{b} |f_a(\mathbf{q})||f_b(\mathbf{q})| e^{i(\phi_b(\mathbf{q})-\phi_a(\mathbf{q}))} \int \mathrm{d}\mathbf{R}\ \mathbf{e}^{i\mathbf{q}\cdot(\mathbf{R}_b-\mathbf{R}_a)} \chi^*_e(\mathbf{R})\chi_e(\mathbf{R}). \tag{2.86}$$

where we have identified the diagonal ($a = b$) and off-diagonal ($a \neq b$) terms in the double summation as the excited-state atomic ($I^{(e)}_{\text{at}}$) and molecular ($I^{(e)}_{\text{mol}}$) contributions to the scattering intensity. The former gives only q-dependence of the atomic form factors while the latter reveals the interatomic distances and thus the molecular structure. Discarding the atomic contributions and taking the rotational average then gives [101, 102, 87]

$$I^{(e)}_{\text{mol}}(q) = \sum_{a}\sum_{b\neq a} |f_a(q)||f_b(q)| \cos(\phi_a(q) - \phi_b(q)) \int \mathrm{d}R\ \frac{\sin(qR_{ab})}{qR_{ab}} P^{(e)}_{ab}(R_{ab}) \tag{2.87}$$

where $P^{(e)}_{ab}(R) = |\chi_e(R)|^2$ is the probability distribution of the nuclear separation $R_{ab} = |\mathbf{R}_a - \mathbf{R}_b|$ in the excited state. Compared to Eq. (2.83), this expression neglects the electronic coherences, since P only considers the nuclear wave packet in a single electronic state. However, the vibrational coherences are included in P_{ab} through the nuclear wave function. By using the atomic form factors f_a, contributions from valence electrons are generally neglected since there core electrons are dominant in the signal due to their much higher number.

2.3.1 Application to the Nonadiabatic Avoided-Crossing Dynamics in NaF

Virtually all photophysical and photochemical processes in polyatomic molecules with two or more vibrational coordinates take place via conical intersections (CoIns) [103], which raises the fundamental question if they may be observed in diffraction experiments. Once the molecule reaches a CoIn, a short-lived electronic coherence is created and can in principle be spectroscopically detected [104, 15] by soft x-Rays. One example for a photochemical prototype reaction, which is mediated by a CoIn and has been studied by x-Ray diffraction, is the ring opening reaction in cyclohexadiene [105, 106]. Potential signatures in time-resolved diffraction signals might also be useful to measure the Berry phase [107], which has so far eluded detection in molecules.

We illustrate the various possible contributions to the diffraction signal with sodium fluoride. Second and third row elements are of relevance for a broad variety of chemical reactions. Sodium fluoride posses a similar electronic structure to NaI which we studied recently [108]: an avoided crossing between the ionic and covalent state. Though well-known for faciliating populating transport between adiabatic electronic states, the passage of nuclear wavepackets through the region of a conical intersections also generates electronic coherences. The resulting coherent oscillations can be monitored with, e.g., photoelectron or Raman signals and reveal the time-evolving electronic energy gap as well as information on the differential topology of the electronic surfaces *via* the decoherence time [104, 12]. Here, we explore the consequences of these dynamics for ultrafast time-resolved x-ray diffraction in gas phase NaF. Iodine is an excellent x-ray scatterer and its large nuclear charge leads to a charge density distribution heavily dominated by its core electrons. While this is still the case for molecular form factors of lighter element compounds, they have a relatively more prominent contribution of valence electrons compared to the core electrons. For details on the electronic structure and calculation methods see appendix B.

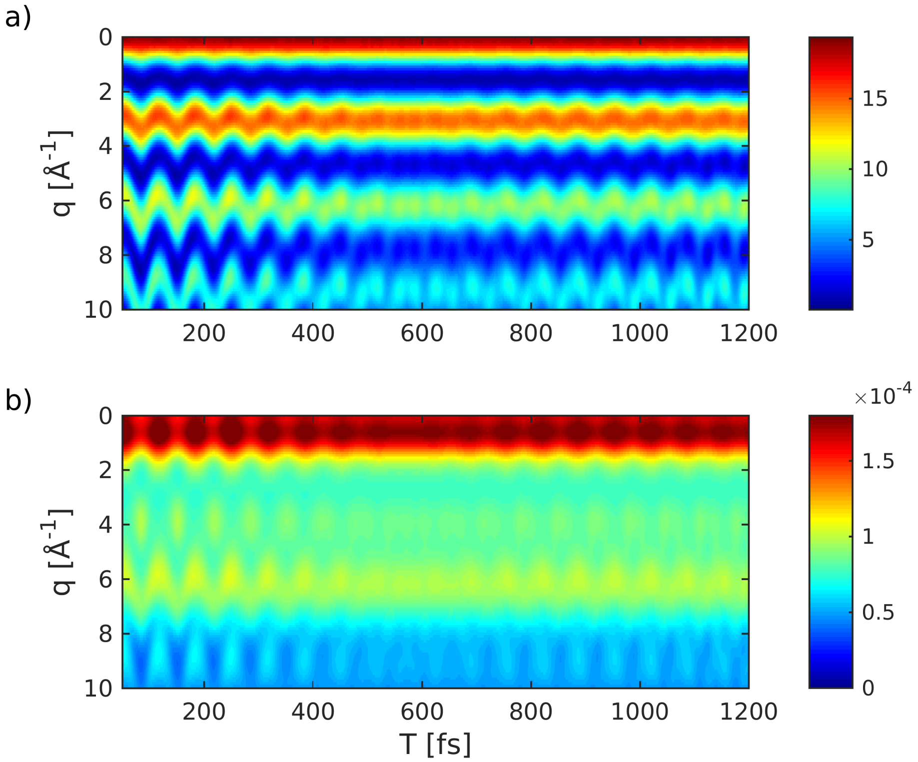

Figure 2.7: Ground state contributions to the gas phase diffraction signal of NaF $(S_1(q,T))$: (a) $\rho_{gg}\langle\chi_g(t)|\hat{\sigma}^{\dagger}_{gg}\hat{\sigma}_{gg}|\chi_g(t)\rangle$, (b) $\rho_{gg}\langle\chi_g(t)|\hat{\sigma}^{\dagger}_{eg}\hat{\sigma}_{ge}|\chi_g(t)\rangle$. Probe pulse length 2.5 fs (FWHM).

We first present the ground-state contributions to the time-dependent diffraction signal. Since an intense laser pulse has been used to create the non-stationary state, a superposition of vibrational states is also created in the bound electronic ground state. The result is an oscillatory pattern, which becomes clearly visible in the diffraction. Figure 2.7 shows the diffraction signal from the ground state density (Fig. 2.7(a)) and the transition density (Fig. 2.7(b)).

Figure 2.8(a) shows the inverse Fourier transform with respect to the momentum space. The oscillatory motion around the equilibrium position is revealed, while the respective part of the transition density does not add new information (Fig. 2.8(b)).

The various excited-state contributions to the diffraction signal are shown in Fig. 2.10. The contribution stemming from the excited-state density σ^2_{ee} (Eq. (2.83)(c)), is shown in Fig.

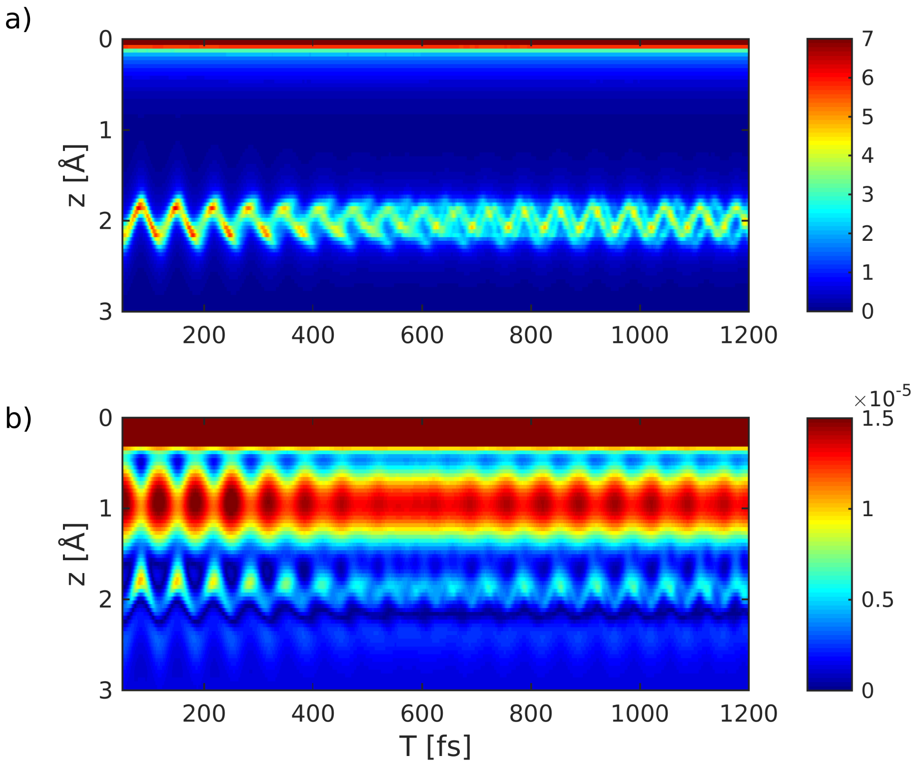

Figure 2.8: Contributions to the real space signal $S_1(q_z, T)$ (Fourier transform of $S_1(q_z, T)$) of the electronic ground state: The various panels are in the same order as in Fig. 2.10: (a) Contribution from $\hat{\sigma}_{gg}^2$, (b) $\hat{\sigma}_{gg}^\dagger \hat{\sigma}_{eg}$ and $\hat{\sigma}_{gg}^\dagger \hat{\sigma}_{eg}$. Signal intensities are relative to Fig. 2.10(a).

2.10(a). The forward time-evolution represents the wavepacket motion, i.e., the fringe spacing increases as the wave packet moves towards a longer bond length. Figure 2.10(b) depicts the contribution of the electronic coherences. At $\approx 220\,\mathrm{fs}$, when the wave packet hits the avoided-crossing regime, a coherence is created (see Fig. B.4), resulting in a slow temporal oscillation, which spreads over a wide range in q-space. The coherence contribution is ≈ 3 orders of magnitude weaker than the excited state density (Fig. 2.10(a)). The contribution which stems solely from the transition densities ($\hat{\sigma}_{eg}^2$ in Fig. 2.10(c)) is ≈ 4 orders of magnitude weaker. It carries no information about the electronic coherence but is dominated by the shape and magnitude of the transition density $\hat{\sigma}_{eg}^2$ and is closely related to the transition dipole moment (see Fig. B.1).

Figure 2.11 shows the inverse Fourier transforms of the excited state contribution of the

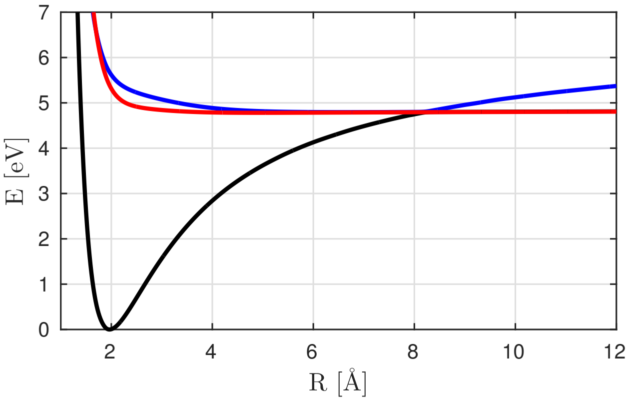

Figure 2.9: Relevant adiabatic potential energy surfaces of NaF (ionic $X^1\Sigma$ black, covalent $A^1\Sigma$, blue, $^1\Pi$, red).

diffraction signal components. A comparison of Fig. 2.11(a) (σ_{ee}^2) with the time evolution of the nuclear wavefunction (Fig. B.3) makes it clear that the features of the nuclear wavepacket motion can be retrieved directly from the excited-state contribution. The time-independent peak at $z = 0$ is derived from a magnitude squared signal and can thus be ignored. The inverse Fourier transform of the coherent contribution Fig. 2.11(b) shows a signature at 225 fs when the nuclear wave-packet passes through the avoided crossing for two distances: The pattern at 8 Å is at the position of the avoided crossing, while the signal at short distances (≈ 0.5 Å) is due to a p-orbital shaped feature in the transition density located at the fluorine. The contribution from the transition densities (Fig. 2.11(c)) vanishes for times where the wavepacket is located beyond 8 Å($|\sigma_{eg}|$ vanishes, see Fig. B.1). The internuclear distances and thus the shape of the nuclear wavepacket can be extracted directly from diffraction pattern.

2.4 Discussion

The formalisms laid out in sections 2.0.2-2.0.3 are very general and capable of handling a broad variety of scattering and spontaneous emission experiments. A treament of the dipolar interaction Hamiltonian (Eq. (1.8)) rather than the minimal coupling Hamiltonian (Eq.

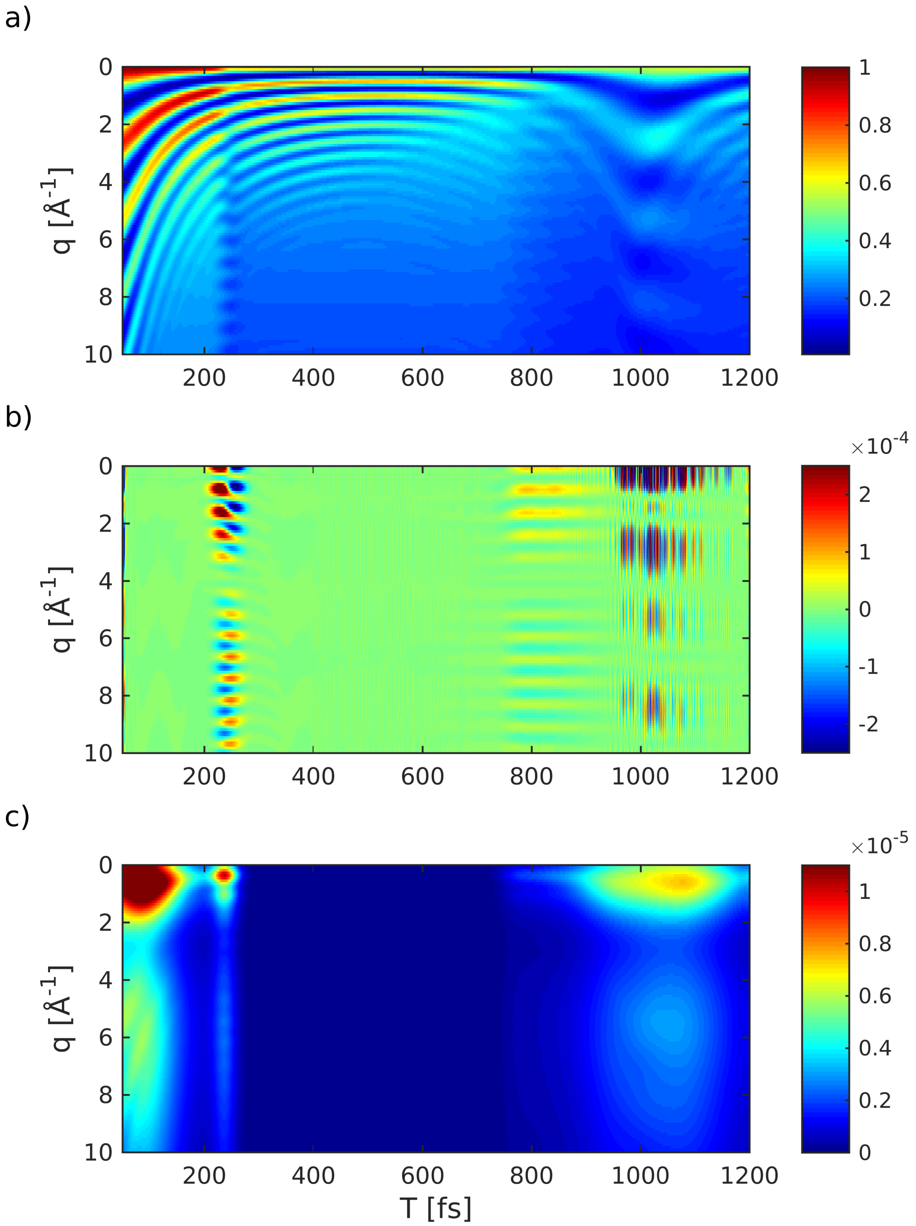

Figure 2.10: Excited state contributions to the gas-phase diffraction signal of NaF ($S_1(q,T)$) : (a) $\rho_{ee}\langle\chi_e(t)|\hat{\sigma}^\dagger_{ee}\hat{\sigma}_{ee}|\chi_e(t)\rangle$, (b) $2\Re\big[\rho_{eg}(t)\langle\chi_e(t)|\hat{\sigma}^\dagger_{ee}\hat{\sigma}_{eg} + \hat{\sigma}^\dagger_{eg}\hat{\sigma}_{gg}|\chi_g(t)\rangle\big]$, (c) $\rho_{ee}\langle\chi_e(t)|\hat{\sigma}^\dagger_{eg}\hat{\sigma}_{ge}|\chi_e(t)\rangle$. Signal intensities are relative to (a). Probe pulse length 2.5 fs (FWHM).

(1.7)) follows similarly and can be used to discuss Raman and fluorescence [109, 64]. Although the gated-field approach presented in section 2.0.3 is somewhat more cumbersome, it is intellectually quite satisfying and rigorously incorporates the finite sensitivity of de-

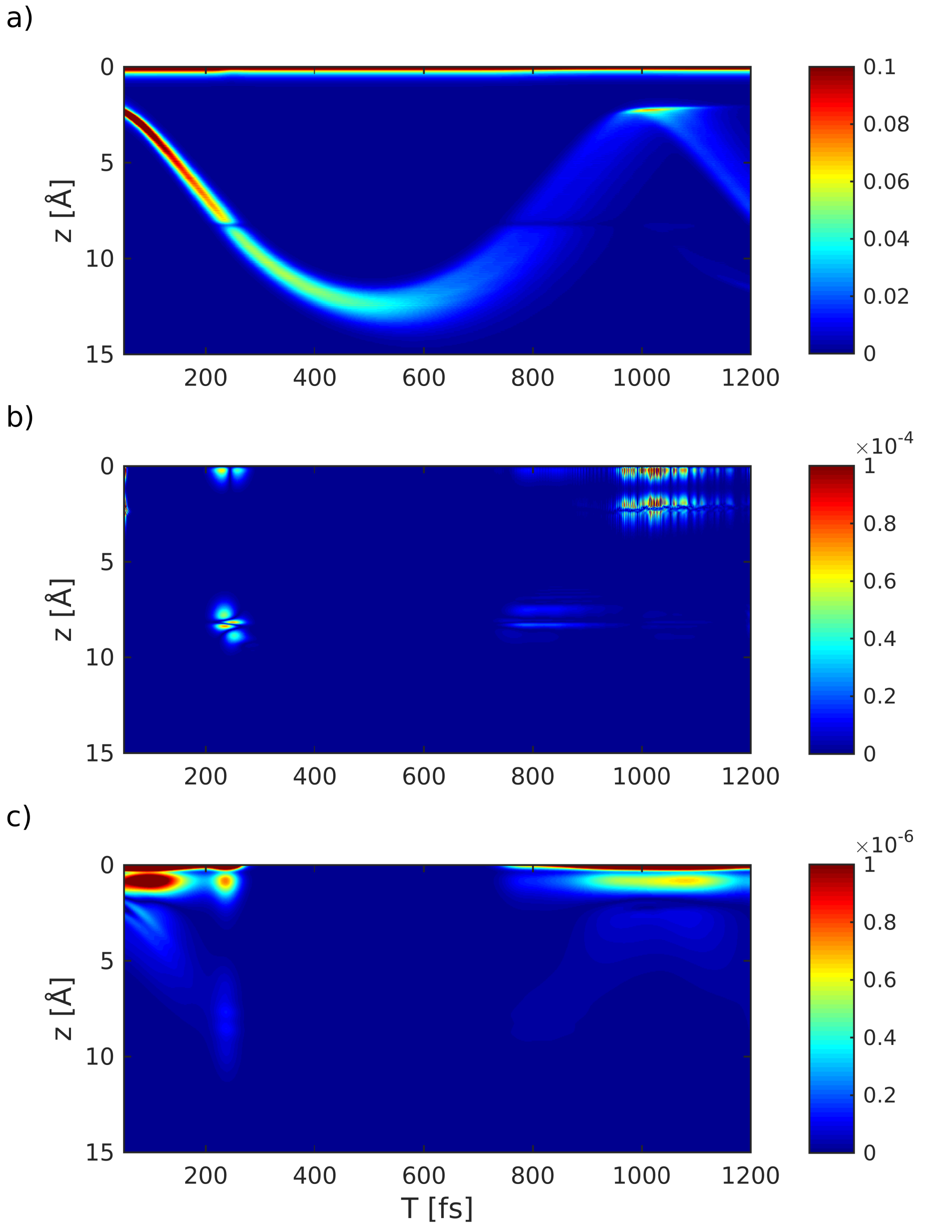

Figure 2.11: Contributions to the real space signal $S_1(q_z, T)$ (Fourier transform of $S_1(z, T)$). The various panels are in the same order as in Fig. 2.10: (a) Contribution from $\hat{\sigma}_{ee}^2$, (b) $\hat{\sigma}_{ee}^{\dagger}\hat{\sigma}_{eg}$ and $\hat{\sigma}_{gg}^{\dagger}\hat{\sigma}_{eg}$, (c) $\hat{\sigma}_{ge}^2$. Signal intensities are relative to (a).

tection processes. One important example of the difference between this and the photon number change definition for the signal (section 2.0.2) is that, since the detector can not distinguish between energies within its spectral resolution, states whose energies differ by less than this resolution should form a beating pattern in, e.g., a time-resolved spontaneous emission signal. Computing the photon change in a signal mode and then integrating over a sensitivity function after the fact simply blurs the signal but does not reproduce this beating phenomenon [64].

Light scattering and spontaneous emission were shown to have single- and two-molecule contributions. This separation holds for dipolar interactions as well, though we do not discuss these in detail. In that case, single-molecule terms result in incoherent signals such as (multi-photon induced) fluorescence and (hyper) Raman while the two-molecule terms generate coherent signals and the terms in the structure factor (Eq. (2.20)) add coherently due to phase-matching as in homodyne-detected sum/difference frequency generation and n-harmonic generation. Two-molecule terms can also contribute when short-range correlations, on the order of the scattered wavelength, induce (hyper) Rayleigh scattering signals, which scale as NN' where N' is the number of molecules within this correlation distance [110, 111].

In the case of x-ray diffraction, the two-molecule terms dominate when there is a long-range, intermolecular structure, such as in a crystal, while the single-molecule terms are all that remain in gas-phase diffraction. In principle, one can make the separation based on single- and two-*atom* or indeed -*electron* terms and this seems to be somewhat more common in the literature [67, 66, 112]. The problem with this is that the nature of the excitation is molecular and one usually treats the pumping process and subsequent evolution from the perspective of the quantum states of the molecule. One cannot then in general factor the density matrix of different atoms within the same molecule. The treatment in terms of molecules also makes clear how to handle electronic coherences and how to interpret inelastic contributions to diffraction through the transition charge densities.

The historical origins of diffraction as a ground-state technique for crystalline samples leads one to a simple generalization (Eq. (2.71)) that is nonetheless wrong. The intuitive notion that x-rays scatter from the instantaneous electronic charge-density (as an expectation value) turns out to be appropriate for two-molecule terms (Eq. (2.18)) but not for single-molecule terms (Eq. (2.19)), leading to several errors. As had been pointed out by others, the actual single-molecule signal from nonstationary systems does not possess inversion symmetry at all times [35]. Additionally, taking the expectation value before squaring (as opposed to taking the expectation value of the squared charge density as in Eq. (2.19)) yields terms that are quadratic in elements of the density matrix ρ, i.e., they are proportional to *joint* probability densities and cannot be single-molecule quantities. Considering an excited gas and neglecting coherences and inelasticities (transition charge densities), the diffraction signal (Eq. (2.83)) would then depend on

$$\tilde{S}_1(\mathbf{q}, t) = \rho_{gg}|\sigma_{gg}|^2 + \rho_{ee}|\sigma_{ee}|^2 \tag{2.88}$$

whereas the incorrect expression based on the intuitive Eq. (2.71) gives

$$\tilde{S}_1(\mathbf{q}, t) = |\rho_{gg}\sigma_{gg} + \rho_{ee}\sigma_{ee}|^2. \tag{2.89}$$

This has the aforementioned problem of being quadratic in the populations ρ_{ii} but also contains a cross-term upon squaring. This cross term allows a heterodyne-detection process in which a weakly-populated excited state (for which $\rho_{ee} \ll 1$) can be detected due to riding on the ground-state signal. However, this heterodyne term is linear in the excited state population, just as the actual single-molecule signal should be, clearly opening up the possibility of confusion. Finally, this heterodyne term carries information on the phase of the excited state relative to the ground state and could be used to solve the phase-problem and reconstruct the charge density. All of this works just fine in crystalline samples in which the signal is calculated along the lines of Eq. (2.89) (properly obtained from Eq. (2.81)). Unfortunately, the actual signal (Eq. (2.88)) contains no such phase information.

Section 2.2 presented time-dependent, frequency-resolved diffraction of electronic wavepackets in cysteine created by an x-ray Raman pumping process. It was shown that this corresponds to taking a spectrum at every pixel and one can thus selectively look at inelastic scattering (by out the elastic) or at specific electronic states in the wavepacket by selecting the appropriate narrow frequency range. A more thorough analysis, not pursued here, would be to carry out this filtering for each identifiable frequency in the wavepacket, obtaining a full diffraction pattern in each case. These diffraction patterns could then be transformed to give real-space information on the two states involved in the beating frequency

Section 2.3 discusses x-ray diffraction for the purposes of tracking nuclear dynamics. This can be used to monitor chemical reactions and molecular structure changes in real space. Using NaF as an example, we separately showed the various elastic and inelastic contributions from both ground and excited states. The Na and F atoms are sufficiently light so that their core electrons do not entirely overwhelm the contributions from transition charge densities, to which only electrons involved in the transition may contribute. The excited-state oscillation is clearly visible in the diffraction pattern (Figs. 2.10-2.11). The actinic pump-pulse creates a wave motion not only in the excited state potential but also in the ground state potential due to a Raman process. A small fraction of the population is moved from the ground to the excited state, creating a "particle" excited state wavepacket and a "hole" in the ground state. The respective signals in reciprocal momentum space and in real space given in Figs. 2.7-2.8 clearly show that the pump-pulse creates an oscillating wave packet in the ^{1}X state.

In conclusion, the simulated gas phase diffraction signal of NaF undergoing nonadiabatic avoided crossing dynamics in a non-stationary state is dominated by ground- and excited-state wavepacket motion and, to a lesser extent, shows signatures of the electronic coherence created at the avoided crossing. The interatomic distance can be extracted directly from the diffraction signal and thus one can qualitatively retrieve the shape of the nuclear wavepacket for a diatomic without further phase reconstruction.

Chapter 3

Many-Body Effects; Cascading

In chapter 2, the detected field was initially in the vacuum state $\rho_s(-\infty) = |0\rangle\langle 0|$ and the field-matter interaction created a photon population in the signal mode $\rho_s \to |1\rangle\langle 1|$, which was then detected. Ultrafast nonlinear optical signals in the condensed phase frequently use heterodyne detection, whereby the signal interferes with a reference local oscillator beam. The signal then scales linearly with the number of molecules N and is distinguished by its power dependence in the incoming fileds and its direction (phase matching) [1, 113]. Matter information is contained in multipoint correlation functions of the dipole operator. We will refer to such signals as direct.

Direct, heterodyne-detected nonlinear optical signals are ordinarily simulated semiclassically, i.e., the material is treated quantum mechanically and the fields enter as classical functions. Corrections to the semiclassical picture arise upon taking the infinite number of modes that are unoccupied. A fully quantum electrodynamical (QED) treatement results in a myriad of many-body effects caused by photon exchange, i.e., the emission of a photon by one molecule and its absorption by another. These effects include the scrambling of time-ordering of incoming short pulses where the free-induction decay produced by one molecule can be longlived and interacts with another molecule, a local-field $\chi^{(1)}$ effect [1, 114, 115, 116]. Additonal local-field effects include corrections to the transmission/reflection of a thin film [117] and the Rabi oscillations of a quantum dot [118]. Nonlinearities are also induced in ensembles of noninteracting harmonic oscillators which are otherwise linear [119]. Dipole-dipole coupling, responsible for, e.g., Forster resonant energy transfer (FRET) and spontaneous quantum synchronization, is also induced by the exchange of photons [120, 121]. Superradiance, a cooperative spontaneous emission process, is another well-studied effect that finds its origin in the quantum nature of the radiation field [122]. Quantum-field effects due to the quantum fluctuations of laser field rather than the unoccupied modes of the electromagnetic field have also been noted in stimulated signals [123]. This chapter analyzes a different effect, known as cascading, that makes an important contribution to heterodyne-detected nonlinear spectroscopic signals. This is shown to be part of the lowest-order many-body correction due to photon exchange.

Cascading occurs when some external fields interact with one molecule to generate a field that then acts on another molecule, together with the external fields, to finally produce a signal. Cascading signals scale quadratically in the molecule number N^2 and have the same power dependence in the incoming fields and the same phase matching as the direct signal [43, 44, 124, 124, 45, 46, 125, 116]. Cascading and direct signals are thus hard to distinguish from each other, with the former frequently dominating (e.g., in neat liquid CS_2 [43]) due to the quadratic *vs.* linear scaling in molecular density. It is then hard to separate the direct signal which carries a higher level of molecular information. An important example is the direct 5th-order Raman $\chi^{(5)}$ process which is accompanied by a product of two 3rd-order $\chi^{(3)}$ signals. In a pump-probe stimulated Raman experiment, a sample is excited by two interactions with an initial light pulse to a vibrational coherence which is then probed by a second pulse following a time delay T_1. This technique probes the vibrational structure of the molecule and is a 3rd order process in the electric field (and is therefore related to $\chi^{(3)}$, the 3rd order susceptibility). An extension of this technique is a 5th-order Raman process in which, following the initial delay T_1, a second pair of interactions transfers the sample from one vibrational coherence to another. The system then evovles freely during a second interpulse delay T_2 before being probed. This more general fifth-order ($\chi^{(5)}$) technique offers the possibility of probing the coupling between participating vibrational modes. Separating the direct $\chi^{(5)}$ signal from the cascading $\chi^{(3)}\chi^{(3)}$ signal had drawn considerable attention and took several years to fully understand [37, 38, 39, 40, 41, 42, 43, 44, 45, 46]. This has been the main obstacle for multidimensional Raman spectroscopy (5th-and-higher orders) [125].

A number of ideas have been pursued to separate the direct and cascading signals. The N *vs.* N^2 scaling is an obvious way but, in many cases, it is not possible to vary the molecular density over a sufficiently large range in order to seperate the N- and N^2-scaling contributions. Another idea comes from the fact that, in an infinite homogeneous sample, it follows from Maxwell's Equations that the electric field emitted by a polarization is $\pi/2$ phase-shifted relative to the polarization itself. From a macroscopic perspective, the electric field $\mathbf{E}$ created by a polarization $\boldsymbol{\mathcal{P}}$ is given by the Maxwell equation

$$\left(\frac{\partial^2}{\partial t^2} - c^2\nabla^2\right)\mathbf{E}(\boldsymbol{r}, t) = -\frac{\partial^2}{\partial t^2}\boldsymbol{\mathcal{P}}(\boldsymbol{r}, t) \tag{3.1}$$

which in the frequency domain reads

$$\mathbf{E}(\boldsymbol{k}, \omega) = \frac{\omega^2}{\omega^2 - k^2c^2 + i\eta}\boldsymbol{\mathcal{P}}(\boldsymbol{k}, \omega) \tag{3.2}$$

where η is a positive infinitessimal selecting the appropriate boundary conditions of an outgoing wave. In the limit of perfect phase matching $\omega^2 \to k^2c^2$, we have

$$\mathbf{E}(\boldsymbol{k}, \omega) = i\pi\delta(\omega^2 - k^2c^2)\omega^2\boldsymbol{\mathcal{P}}(\boldsymbol{k}, \omega). \tag{3.3}$$

This gives a $\pi/2$ phase shift between the polarization and the resulting field. The extra emission event (from the source molecule) in a cascading process thus renders the cascading signal out of phase relative to the direct nonlinear signal ($E \propto P - iPP$) [1, 46, 48]. This property has been parlayed into a number of successfully-implemented techniques to select for the direct 5th-order Raman signal and eliminate the cascading contributions [44, 43, 47, 48] (techniques based on polarization-sensitive measurements have also been pursued [126]).

In this chapter, we will derive a more general, geometry-dependent result and show under what conditions it reduces to this simple macroscopic relation. After tracing over quantum field degrees of freedom, general expressions for cascading signals are given that are valid in the non-perturbative regime with respect to arbitrary external fields. The result can then be expressed solely as a product of two single-molecule dipole correlation functions and a geometric factor describing the relative positions of the molecules in the sample. This presentation allows the calculation of cascading signals using only the single-molecule calculations familiar from standard treatments of nonlinear spectroscopy and a sum of c-numbers associated with the geometry.

Cascading shares a common origin with other collective effects observed in spectroscopic experiments. For example, superradiant emission a cooperative process between constituent molecules of the sample and scales quadratically in the number of molecules [127]. However, in superradiance the spontaneously emitted photons (or the associated excited-state population decay) are ordinarily the object of detection while in cascading the exchanged photons are virtual and the relevent experiment is a heterodyne detection with respect to the externally applied signal (laser) field. The Lamb shift and collective analogues are also due to virtual-photon exchange but these effects are observed as alterations of a material resonance rather than an entirely new signal as in cascading [128]. Forster transfer (discussed more thoroughly in the conclusion) can also be derived perturbatively as a vacuum-mediated interaction. When the field-matter interaction is treated in the dipole approximation, all of the above depend on the dipole-dipole coupling tensor, giving the derivations a similar flavor [120, 65].

Cascading therefore provides an interesting example of many-body, quantum-field effects both from the pedagogical and historical viewpoints. We hope that the detailed derivation and discussion of cascading in this chapter will thus provide the reader with a sound introduction to this ever-growing and exciting field. We first provide a generic microscopic derivation of cascading appropriate for arbitrary microscopic arrangements of molecules or macroscopic geometries 3.1. We then discuss several special cases, analyzing in particular the phase relationship between direct and cascading signals.

3.1 Direct *vs.* Cascading Signals

We consider a sample made of identical, noninteracting molecules with non-overlapping charge distributions for which the coupling to the radiation field can be treated in the dipole approximation. The total system dipole operator then takes the form of a sum over molecular dipoles $\hat{\boldsymbol{\mathcal{V}}}(\boldsymbol{r},t)=\sum_a \hat{\mathbf{V}}(t)\delta(\boldsymbol{r}-\boldsymbol{r}_a)$. The material is subjected to a set of classical laser modes $\mathbf{E}_j$ so that the total electric field is

$$\hat{\mathbf{E}}(\boldsymbol{r},t)\equiv\sum_j \mathbf{E}_j(\boldsymbol{r},t)+\hat{\mathbf{E}}_{\mathrm{v}}(\boldsymbol{r},t) \tag{3.4}$$

where $\hat{\mathbf{E}}_{\mathrm{v}}$ is an electric field operator representing the infinitely-many vacuum modes. The material system is coupled to this total electric field via the electric dipole interaction Hamiltonian (Eq. (1.8))

$$\begin{gathered}\hat{H}_{\mathrm{int}}=-\int d\boldsymbol{r}\hat{\mathbf{E}}(\boldsymbol{r},t)\cdot\hat{\boldsymbol{\mathcal{V}}}(\boldsymbol{r},t)= \\ -\int d\boldsymbol{r}\sum_j \mathbf{E}_j(\boldsymbol{r},t)\cdot\hat{\boldsymbol{\mathcal{V}}}(\boldsymbol{r},t)-\int d\boldsymbol{r}\hat{\mathbf{E}}_{\mathrm{v}}(\boldsymbol{r},t)\cdot\hat{\boldsymbol{\mathcal{V}}}(\boldsymbol{r},t)=\hat{H}_{\mathrm{LM}}+\hat{H}_{\mathrm{vM}}\end{gathered} \tag{3.5}$$

where the laser modes and the quantum vacuum interact with the material via Hamiltonians $\hat{H}_{\rm LM}$ and $\hat{H}_{\rm vM}$ respectively.

The heterodyne-detected nonlinear spectroscopic signals are given by the rate-of change of photon number in some signal mode s, taken to be in a coherent state. Identifying the total polarization as the expectation value of the total dipole operator $\langle \hat{\boldsymbol{\mathcal{V}}}(\boldsymbol{r},t)\rangle = \boldsymbol{\mathcal{P}}(\boldsymbol{r},t)$, the signal (Eq. (A.20)) may be written as

$$S(\boldsymbol{k}_s,\Lambda) = \Im\bigg[\int d\boldsymbol{r}dt\mathbf{E}^*_s(\boldsymbol{r},t)\cdot\langle\hat{\boldsymbol{\mathcal{V}}}(\boldsymbol{r},t)\rangle\bigg] = \Im\left[\mathbf{E}^*_s(\omega_s)\cdot\boldsymbol{\mathcal{P}}(\boldsymbol{k}_s,\omega_s)\right] \tag{3.6}$$

where $\mathbf{E}_s$ is the signal field, which we have assumed to have a precisely-defined direction $\hat{\boldsymbol{k}}_s$, and Λ stands for the set of parameters defining the classical fields which must be specified to simulate particular signals. The total polarization can be written in terms of time-ordered exponentials

$$\boldsymbol{\mathcal{P}}(\boldsymbol{r},t) = {\rm Tr}\left[\hat{\boldsymbol{\mathcal{V}}}(\boldsymbol{r},t)\mathcal{T}e^{-i\int_{-\infty}^{t}d\tau\hat{H}_{-,{\rm LM}}(\tau)}e^{-i\int_{-\infty}^{t}d\tau\hat{H}_{-,{\rm vM}}(\tau)}\rho(-\infty)\right] \tag{3.7}$$

where $\rho(-\infty)$ is the equilibrium field+matter density matrix. Expanding Eq. (3.7) order-by-order in $\hat{H}_{\rm LM}$ but to zeroth order in $\hat{H}_{\rm vM}$, i.e., neglecting the vacuum modes altogether, yields the standard semiclassical nonlinear optical signals, which we term the direct signal $S_{\rm d}$.

For a product of commuting operators (note that $\hat{\mathbf{E}}$ and $\hat{\mathbf{V}}$ act in separate spaces and therefore commute), we have $(\hat{A}\hat{B})_- = \hat{A}_-\hat{B}_+ + \hat{A}_+\hat{B}_-$. Since the $\mathbf{E}_i$ are c-numbers, $(\mathbf{E}_i)_- = 0$ and all interactions with classical fields are associated with a $\hat{\mathbf{V}}_-$. Since ${\rm Tr}[\hat{O}_-\rho] = 0$ for any ρ, the temporally latest interaction must be the interference with the signal field (associated with $\hat{\mathbf{V}}_L$) or a vacuum interaction ($\hat{\mathbf{E}}_{{\rm v},-}$ does not vanish). Moreover, the vacuum interaction on the emitting molecule must come prior to that on the absorbing molecule since otherwise the trace over the vacuum mode density matrix would vanish for this same reason. An important consequence of this reasoning is that the relevant correlation function for each molecule will be of the form $\langle V_+ V_- \dots V_- \rangle$ (i.e. one "+" and several "−" indices) as in standard response functions. In this sense, nothing unusual happens to second-order in the vacuum modes. This is in contrast to spectroscopy with externally generated quantum fields, which can access dipole correlation functions of the more general form $\langle \hat{V}_+ \hat{V}_\pm \dots \hat{V}_\pm \rangle$ [129]. It is worth noting however, that the classical correlation function of the vacuum mode $\langle \hat{E}_{\mathrm{v},+} \hat{E}_{\mathrm{v},+} \rangle$ turns out not to contribute while the cascading and local-field corrections are determined by $\langle \hat{E}_{\mathrm{v},+} \hat{E}_{\mathrm{v}-} \rangle$ which would vanish classically but is finite for the quantum vacuum. Thus, in the semiclassical approximation, all field-matter interactions in the perturbative expansion occur on a given molecule and the signal is obtained by summing over molecules. These signals thus scale linearly with N, the number of molecules in the sample, are proportional to the single-molecule signal suitably averaged, and contain no cooperative many-body contributions. In this sense, the quantum-vacuum field, being the mediator of intermolecular electromagnetic interactions, is the origin of many-body effects.

We can systematically generate corrections to the semiclassical approximation by expanding the second exponent in Eq. (3.7) (the vacuum-mode terms). Since $\mathrm{Tr}[\hat{a}^{(\dagger)}|0\rangle\langle 0|] = 0$, the 2nd-order expansion is the lowest nonvanishing correction which represents successive emission and re-absorption of a photon by the material. When the same molecule both emits and absorbs this photon, the result is the lowest-order radiative correction, or one-loop correction, to the energy (Lamb shift with radiative decay [130]). The terms in which the absorber and emitter are different molecules lead to a transfer of a coherent excitation between the two molecules which is the origin of cascading. This is depicted diagramatically in Fig. 3.1.

A derivation given in subsection 3.1.1 gives the total system polarization $\mathcal{P}$ in terms of the individual molecular polarizations P as

$$\begin{gathered}\mathcal{P}^{\nu}(\boldsymbol{k}_s,\omega) = \\ P^{\nu}(\boldsymbol{k}_a,\omega) f(\boldsymbol{k}_a - \boldsymbol{k}_s) + \int d\omega_b \tilde{P}^{\nu\nu_{\mathrm{v}}}(\boldsymbol{k}_a,\omega_s;-\omega_b) P^{\nu'_{\mathrm{v}}}(\boldsymbol{k}_b,\omega_b) G^{\nu_{\mathrm{v}}\nu'_{\mathrm{v}}}(\boldsymbol{k}_s - \boldsymbol{k}_a, -\boldsymbol{k}_b, \omega_b).\end{gathered} \tag{3.8}$$

where the ν's denote cartesian coordinates (with summation implicit), $P^{\nu}(\boldsymbol{k},\omega)$ is the polarization of a single molecule and $\tilde{P}^{\nu\nu'}(\boldsymbol{k},\omega;\omega')$ is the polarization of a molecule resulting from a single perturbative interaction with the polarization of another molecule in the sample and arbitrarily-many interactions with the classical fields (defined formally as a dipole correlation function in Eq. (3.16)). In Eq. (3.8), $\boldsymbol{k}_a$ and $\boldsymbol{k}_b$ stand for any linear combination of the set of incoming classical field modes and represent the set of laser modes that interact with molecules a and b respectively in a perturbative expansion. Since we work in the dipole approximation, the $\boldsymbol{k}$-dependence of the polarizations comes only as δ-functions, originating in the spatial phase factor, that enforce this. In practice, one must sum over the possible subsets that generate different choices of the $\boldsymbol{k}_a$, $\boldsymbol{k}_b$ (we have omitted integration over $d\boldsymbol{k}_a d\boldsymbol{k}_b$ for brevity). Finally, G is the photon Green's function defined in $(\boldsymbol{r},t)$-space in Eq. (3.34).

The first term in Eq. (3.8) is the direct nonlinear signal and comes proportional to the sample's form factor

$$f(\boldsymbol{k}) \equiv \sum_a e^{i\boldsymbol{k}\cdot\boldsymbol{r}_a}. \tag{3.9}$$

This factor carries information on the position of the molecules in the sample and, in the continuum limit, goes over to the delta function $f(\boldsymbol{k}) \to (2\pi)^3 n\delta(\boldsymbol{k})$, where $n = \frac{N}{V}$ is the molecular concentration. This corresponds to momentum conservation and yields the phase matching condition. The second term in Eq. (3.8) is the cascading signal in which the polarization of molecule b serves as a source, along with the external fields, for the polarization of molecule a. Note that, when this is expanded to, say, order m in the classical modes, we will have $\sum_{p+q=m-1} P^{(p)}P^{(q)}$. The traditional nomenclature is to refer to those terms with $p, q = 1$ as local field corrections and the remainder as cascading (the most familiar being $p = q = 3$ but 3,5 cascading has also been discussed [131]). Even though Eq. (3.8) thus represents a more general class of 2nd-order, vacuum-mediated interactions, we will refer to them collectively as cascading. The key quantity in Eq. (3.8) that connects the polarization emitted by molecule b with the effective field "felt" by molecule a is the $(\boldsymbol{k}, \omega)$-space photon Green's function

$$\begin{aligned} G(\boldsymbol{k}, \boldsymbol{k}', \omega) &= \sum_{ab} e^{-i(\boldsymbol{k}\cdot\boldsymbol{r}_a + \boldsymbol{k}'\cdot\boldsymbol{r}_b)} G(\boldsymbol{r}_a, \boldsymbol{r}_b, \omega) \\ &= \sum_{ab} e^{-i(\boldsymbol{k}\cdot\boldsymbol{r}_a + \boldsymbol{k}'\cdot\boldsymbol{r}_b)} \left(-\nabla^2 \delta_{\nu_{\mathrm{v}}\nu'_{\mathrm{v}}} + \nabla_{\nu_{\mathrm{v}}}\nabla_{\nu'_{\mathrm{v}}}\right) \frac{e^{i\frac{\omega_b}{c}r_{ab}}}{2\pi r_{ab}} \end{aligned} \tag{3.10}$$

which contains all information about the sample geometry and determines the relative phase of the cascading *vs.* direct contributions to the signal. Moreover, Eq. (3.8) reveals the important point that, in the off-resonant limit where $P(\omega)$ only has the phase imprinted by the external fields (as is relevant for Raman spectroscopy), the relative phase of cascading versus direct processes will be controlled entirely by $G(\boldsymbol{k}, \boldsymbol{k}', \omega)$. In the limit of a large, homogeneous sample, the spatial dependence of the photon Green's function is reduced to the single variable $\boldsymbol{r}_a - \boldsymbol{r}_b$, the difference vector, and we have

$$\begin{aligned} G^{\nu_{\mathrm{v}}\nu'_{\mathrm{v}}}(\boldsymbol{k}_s - \boldsymbol{k}_a, -\boldsymbol{k}_b, \omega_b) &\to f(\boldsymbol{k}_a + \boldsymbol{k}_b - \boldsymbol{k}_s) G^{\nu_{\mathrm{v}}\nu'_{\mathrm{v}}}(-\boldsymbol{k}_b, \omega_b) \\ &\to f(\boldsymbol{k}_a + \boldsymbol{k}_b - \boldsymbol{k}_s) \frac{\delta_{\nu_{\mathrm{v}},\nu'_{\mathrm{v}}}\omega_b^2}{\omega_b^2 - k_b^2c^2 + i\eta} \end{aligned} \tag{3.11}$$

where we have neglected proportionality constants and $G(\boldsymbol{k}, \omega)$ directly controls the phase (i.e., if this quantity is real then the cascading process is in phase with the direct process and if it is purely imaginary, the two processes are out of phase). The second relation follows on taking the integral in the continuum limit. In this regime, the total polarization is thus

$$\begin{gathered}\mathcal{P}^{\nu}(\boldsymbol{k}_s,\omega) = \\ P^{\nu}(\boldsymbol{k}_a,\omega_s)f(\boldsymbol{k}_a-\boldsymbol{k}_s) - ink_bc\tilde{P}^{\nu\nu_{\mathrm{v}}}(\boldsymbol{k}_a,\omega_s;\mp k_bc)P^{\nu_{\mathrm{v}}}(\boldsymbol{k}_b,\pm k_bc)f(\boldsymbol{k}_a+\boldsymbol{k}_b-\boldsymbol{k}_s).\end{gathered} \tag{3.12}$$

where we have assumed perfect phase-matching $k_bc = \omega_b$ and both choices of ± must be summed over.

Equation (3.12) is in the form of the simple macroscopic expression discussed in the introduction that is in common use to understand the cascading contribution to nonlinear signals. It reveals that the cascading contribution carries an additional factor of molecular density n compared to the direct signal. Recalling that the form factor also scales linearly with n in the continuum limit, the direct signal is linear while the cascading is quadratic. The crucial factor of i responsible for the phase shift that is used to filter out cascades is found to originate in the phase-matching condition. Finally, it is worthwhile to note the linear dependence on k_bc in the cascading contribution, indicating that it will be stronger at higher, such as x-ray, frequencies.

In making the assumption that $k_bc = \omega_b$, we have neglected the principal value of the denominator in Eq. (3.11) which generates a cascading contribution that is *in phase* with the direct signal. Additionally, the situation can be expected to be different in the case of few-molecule samples or oddly-shaped macroscopic systems. In the next section, we examine these effects in greater detail.

3.1.1 Microscopic Derivation of Cascading Signals

In this section, we will derive an expression for the cascading signal from a fully microscopic QED perspective while keeping the perturbative order in the external fields completely arbi-

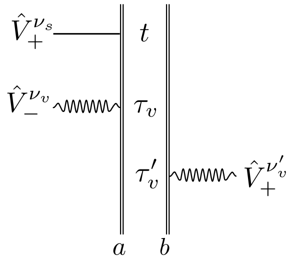

Figure 3.1: This diagram depicts the material quantities relevant for an arbitrary cascading (or, more generally, 2nd-order vacuum-mediated interaction) contribution. The vertical lines represent the density matrices of molecule a or b and associated propagators. We use doubled lines to clarify that the propagation is with respect to the full Hamiltonian, including interactions with externally applied fields, and not simply the free material propagation. The straight intersecting the density matrices of molecule a represents the heterodyne signal field while the wavy lines represent interactions with vacuum modes. In contrast to the more familiar double-sided Feynman diagrams, we make no distinction between action on the ket or bra. This is permissible since we work in Liouville space and convenient since it permits us to work in the $+/-$ representation in which the Liouvillian H_- is more compactly written. This therefore greatly reduces the number of diagrams. Since we work in the $+/-$ representation and without the rotating wave approximation, dressing the interactions with arrows (to indicate positive or negative Fourier components) is unneccesary. This diagram corresponds to the quantities relevant for equation (3.13).

trary. This will allow us to make very general conclusions without considering particulars of the laser fields. Expanding equation (3.6) to 2nd order in the vacuum modes of the electric field results in

$$
\begin{aligned}
S_{\mathrm{c}}(\Lambda) =& \Im\Bigg[(i)^2 \sum_{ab} \int dt \int_{-\infty}^{t} d\tau_{\mathrm{v}} \int_{-\infty}^{\tau_{\mathrm{v}}} d\tau'_{\mathrm{v}} E_s^{*\nu_s}(\boldsymbol{r}_a, t) \qquad (3.13)\\
& \times \langle \hat{V}_+^{\nu_s}(t)\hat{V}_-^{\nu_{\mathrm{v}}}(\tau_{\mathrm{v}})\rangle(\boldsymbol{r}_a)\langle \hat{V}_+^{\nu'_{\mathrm{v}}}(\tau'_{\mathrm{v}})\rangle(\boldsymbol{r}_b)\langle \hat{\mathbf{E}}_{\mathrm{v}+}(\boldsymbol{r}_a, \tau_{\mathrm{v}})\hat{\mathbf{E}}_{\mathrm{v}-}(\boldsymbol{r}_b, \tau'_{\mathrm{v}})\rangle_0\Bigg]
\end{aligned}
$$

where the factor of i^2 comes from the two orders of expansion in the interaction with the vacuum modes, the $\{\nu\}$ stand for cartesian coordinates coming from the dot products and are implicitly summed over, and $\langle \ldots \rangle_0 \equiv \mathrm{Tr}[\ldots |0\rangle\langle 0|]$ stands for an expectation value taken over the vacuum state. The $-(+)$ subscripts stand for the commutator (anti-commutator) as usual and we have selected the only appropriate contributing terms when performing the initial spatial integrations. In particular, 3-body terms (in which each of the three dipole operators occur at a different molecule) and that in which the action on molecule b preceedes that on a all vanish since $\mathrm{Tr}[\hat{O}_-\rho] = 0$ for all operators $\hat{O}$ and density matrices ρ. Note however, that 3-body cascading *does* occur when expanding to 4th order in the vacuum modes and cascading 3rd-order processes have been considered in 7th-order nonlinear techniques [131]. Equation (3.13) is represented diagramatically in Fig. 3.1.

It is important to note that the dipole expectation values in Eq. (3.13) includes propagation with respect to the full Hamiltonian (excepting only the vacuum modes). That is, the trace is taken over the exact $\rho(t)$ propagated with the externally applied semiclassical modes and the expression incorporates all orders of interaction between the matter and laser modes. Explicitly, we have

$$
\langle \hat{V}_+^{\nu_s}(t)\hat{V}_-^{\nu_{\mathrm{v}}}(\tau_{\mathrm{v}})\rangle = \mathrm{Tr}\left[\hat{V}_+^{\nu_s}(t)\mathcal{T}\hat{V}_-^{\nu_{\mathrm{v}}}(\tau_{\mathrm{v}})e^{-i\int_{-\infty}^{t} d\tau \hat{H}_{-,\mathrm{LM}}(\tau)}\rho(-\infty)\right], \qquad (3.14)
$$

where the time-dependence of the dipole operators is through $\hat{H}_0$, the free material Hamiltonian, and the new interaction Hamiltonian $\hat{H}_{\mathrm{LM}}$ only includes interactions with the laser fields. The dependence on molecule position is notated outside the expectation values since all interactions within each expectation value occur on a particular molecule. Within the dipole approximation, this spatial dependence comes as a simple exponential while the full multi-polar polarization operator has a more general dependence on position.

Equation (3.13) can be simplified by introducing the polarization of a molecule

$$P^{\nu}(\boldsymbol{r},t) = \langle \hat{V}^{\nu}(t) \rangle(\boldsymbol{r}) \tag{3.15}$$

as well as the quantity

$$\tilde{P}^{\nu\nu'}(\boldsymbol{r},t;t') = i\theta(t-t')\langle \hat{V}_{+}^{\nu_s}(t)\hat{V}_{-}^{\nu_{\mathrm{v}}}(\tau_{\mathrm{v}}) \rangle(\boldsymbol{r}) \tag{3.16}$$

which represents the polarization of a molecule in the laser fields due to a perturbative interaction with the polarization of another molecule. Finally, we identify the photon Green's function

$$G^{\nu\nu'}(\boldsymbol{r}_a,\boldsymbol{r}_b,\tau_{\mathrm{v}}-\tau_{\mathrm{v}}') = i\theta\left(\tau_{\mathrm{v}}-\tau_{\mathrm{v}}'\right)\langle \hat{E}_{\mathrm{v}+}^{\nu}(\boldsymbol{r}_a,\tau_{\mathrm{v}})\hat{E}_{\mathrm{v}-}^{\nu'}(\boldsymbol{r}_b,\tau_{\mathrm{v}}') \rangle_0 \tag{3.17}$$

which comes as a time-ordered, vacuum expectation value of electric field operators. In terms of these quantities, we may write the cascading signal as

$$S_{\mathrm{c}}(\Lambda) = \Im\Big[\sum_{ab}\int dt d\tau_{\mathrm{v}} d\tau_{\mathrm{v}}' E_s^{*\nu_s}(\boldsymbol{r}_a,t)\tilde{P}^{\nu_s\nu_{\mathrm{v}}}(\boldsymbol{r}_a,t;\tau_{\mathrm{v}})G^{\nu_{\mathrm{v}}\nu_{\mathrm{v}}'}(\boldsymbol{r}_a,\boldsymbol{r}_b,\tau_{\mathrm{v}}-\tau_{\mathrm{v}}')P^{\nu_{\mathrm{v}}'}(\boldsymbol{r}_b,\tau_{\mathrm{v}}')\Big] \tag{3.18}$$

In subsection 3.1.3, we simplify the photon Green's function. Remaining in the time domain for now, we substitute Eq. (3.42) to obtain

$$S_{\mathrm{c}}(\Lambda) = \tag{3.19}$$

$$\Im\Big[\sum_{ab}\int dt d\tau_v E_s^{*\nu_s}(\boldsymbol{r}_a,t)\tilde{P}^{\nu_s\nu_{\mathrm{v}}}(\boldsymbol{r}_a,t;\tau_{\mathrm{v}})\frac{\left(-\nabla^2\delta_{\nu_{\mathrm{v}}\nu'_{\mathrm{v}}}+\nabla_{\nu_{\mathrm{v}}}\nabla_{\nu'_{\mathrm{v}}}\right)}{2\pi r_{ab}}P^{\nu'_{\mathrm{v}}}(\boldsymbol{r}_b,\tau_{\mathrm{v}}-\frac{r_{ab}}{c})\Big]$$

where the spatial derivatives (the ∇'s) act on r_{ab}, the distance between molecules. This expression is very intuitive; the polarization of molecule b, evaluated at the retarded time and adjusted by the action of the dipole coupling tensor and factor of $\frac{1}{r}$, is in place of an external field interaction. We may make this identification explicit, writing the effective electric field that is felt by molecule a and caused by the polarization emitted from molecule b

$$E_{\mathrm{v}}^{\nu_{\mathrm{v}}}(\boldsymbol{r}_a,\tau_v) = \sum_b \frac{\left(-\nabla^2\delta_{\nu_{\mathrm{v}}\nu'_{\mathrm{v}}}+\nabla_{\nu_{\mathrm{v}}}\nabla_{\nu'_{\mathrm{v}}}\right)}{2\pi r_{ab}}P^{\nu'_{\mathrm{v}}}(\boldsymbol{r}_b,\tau_{\mathrm{v}}-\frac{r_{ab}}{c}), \tag{3.20}$$

in terms of which the cascading signal is

$$S_{\mathrm{c}}(\Lambda) = \Im\big[\sum_a\int dt d\tau_v E_s^{*\nu_s}(\boldsymbol{r}_a,t)E_{\mathrm{v}}^{\nu_v}(\boldsymbol{r}_a,\tau_v)\tilde{P}^{\nu_s\nu_{\mathrm{v}}}(\boldsymbol{r}_a,t;\tau_{\mathrm{v}})\big]. \tag{3.21}$$

Equations (3.18)-(3.21) have straightforward physical interpretations. In particular, it is clear that the phase of the cascading signal will depend on the phase of the effective electric field 3.20 which in turn depends on the geometry of the sample via the summation over positions of molecule b. In physical experiments, the material is subjected to a set of lasers with well-defined propagation vectors $\boldsymbol{k}_j$ and, within the dipole approximation, the real-space dependence of the polarizations will always come as a spatial phase factor $e^{i\sum_j^n \boldsymbol{k}_j\cdot\boldsymbol{r}}$ where n is the order to which the polarization is expanded with respect to the laser-matter interaction. Thus, the $\boldsymbol{k}$-space polarization will have a delta function setting $\boldsymbol{k}$ to some linear combination of the incoming wavevectors. In contrast, the spatial structure of the sample can be quite complicated. We thus transform to $\boldsymbol{k}$-space and, in the interests of brevity, we omit the integrations over $d\boldsymbol{k}_a\ d\boldsymbol{k}_b$ with the understanding that they will collapse to sums over different choices of $\boldsymbol{k}_a$, $\boldsymbol{k}_b$. To completely put all geometric dependence on a single term, all else that is required is to change to the frequency domain with respect to the retarded polarization. We obtain

$$\begin{gathered} S_{\mathrm{c}}(\boldsymbol{k}_s, \Lambda) = \\ \Im\left[E_s^{*\nu_s}(\omega_s) \int d\omega_b \tilde{P}^{\nu_s \nu_{\mathrm{v}}}(\boldsymbol{k}_a, \omega_s; -\omega_b) P^{\nu'_{\mathrm{v}}}(\boldsymbol{k}_b, \omega_b) \sum_{ab} e^{-i(\boldsymbol{k}_s - \boldsymbol{k}_a)\cdot \boldsymbol{r}_a} e^{i\boldsymbol{k}_b \cdot \boldsymbol{r}_b} G^{\nu_{\mathrm{v}}\nu'_{\mathrm{v}}}(\boldsymbol{r}_a, \boldsymbol{r}_b, \omega_b)\right] \end{gathered} \tag{3.22}$$

where we have used the fact that the detected signal field is $E_s^{*\nu_s}(\boldsymbol{r}_a, t) \to E_s^{*\nu_s}(\omega_s) e^{-i(\boldsymbol{k}_s \cdot \boldsymbol{r}_a - \omega_s t)}$ representing ideal frequency resolution. We explicitly highlight the signal's dependence on this detected mode rather than continuing to include it implicitly in the set of field parameters Λ. Additionally, we have substituted the spatiotemporal Fourier transforms of Eqs. (3.15)-(3.16). In terms of the discrete Fourier transform of the photon Green's function

$$G^{\nu_{\mathrm{v}}\nu'_{\mathrm{v}}}(\boldsymbol{k}_a, \boldsymbol{k}_b, \omega_b) = \sum_{ab} e^{-i\boldsymbol{k}_a \cdot \boldsymbol{r}_a} e^{-i\boldsymbol{k}_b \cdot \boldsymbol{r}_b} G^{\nu_{\mathrm{v}}\nu'_{\mathrm{v}}}(\boldsymbol{r}_a, \boldsymbol{r}_b, \omega_b) \tag{3.23}$$

we have

$$S_{\mathrm{c}}(\boldsymbol{k}_s, \Lambda) = \Im\left[E_s^{*\nu_s}(\omega_s) \int d\omega_b \tilde{P}^{\nu_s \nu_{\mathrm{v}}}(\boldsymbol{k}_a, \omega_s; -\omega_b) P^{\nu'_{\mathrm{v}}}(\boldsymbol{k}_b, \omega_b) G^{\nu_{\mathrm{v}}\nu'_{\mathrm{v}}}(\boldsymbol{k}_s - \boldsymbol{k}_a, -\boldsymbol{k}_b, \omega_b)\right] \tag{3.24}$$

or

$$\begin{gathered} S_{\mathrm{c}}(\boldsymbol{k}_s, \Lambda) = \\ \Im\left[E_s^{*\nu_s}(\omega_s) \int d\omega_b \tilde{P}^{\nu_s \nu_{\mathrm{v}}}(\boldsymbol{k}_a, \omega_s; -\omega_b) P^{\nu'_{\mathrm{v}}}(\boldsymbol{k}_b, \omega_b) \sum_{a} e^{i(\boldsymbol{k}_a + \boldsymbol{k}_b - \boldsymbol{k}_s)\cdot \boldsymbol{r}_a} I^{\nu_{\mathrm{v}}\nu'_{\mathrm{v}}}(\boldsymbol{r}_a, \boldsymbol{k}_b, \omega_b)\right], \end{gathered} \tag{3.25}$$

where we have substituted the quantity

$$\begin{aligned} I^{\nu_{\mathrm{v}}\nu'_{\mathrm{v}}}(\boldsymbol{r}_a, \boldsymbol{k}_b, \omega_b) &\equiv \sum_{\boldsymbol{r}_b} e^{-i\boldsymbol{k}_b\cdot\boldsymbol{r}_{ab}} G^{\nu_{\mathrm{v}}\nu'_{\mathrm{v}}}(\boldsymbol{r}_a, \boldsymbol{r}_b, \omega_b) \\ &= \sum_{\boldsymbol{r}_b} e^{-i\boldsymbol{k}_b\cdot\boldsymbol{r}_{ab}} \left(-\nabla^2\delta_{\nu_{\mathrm{v}}\nu'_{\mathrm{v}}} + \nabla_{\nu_{\mathrm{v}}}\nabla_{\nu'_{\mathrm{v}}}\right) \frac{e^{i\frac{\omega_b}{c}r_{ab}}}{r_{ab}} \end{aligned} \tag{3.26}$$

that forms the basis of our discussion of the geometric differences between cascading and direct signals in section 3.2. Formally, Eq. (3.19) in the time domain and Eqs. (3.24) or (3.25) in the frequency domain are our general results. They give the cascading contribution to a heterodyne-detected signal in terms of the molecular polarization and the photon Green's function, which encodes all geometric information that shapes the cascading signal.

As an aside, we note that one may wish to remain in the time-domain with respect to molecule a, while still handling the geometry more completely than in Eq. (3.19). This can be accomplished by writing

$$E_{\mathrm{v}}^{\nu_{\mathrm{v}}}(\boldsymbol{r}_a, \boldsymbol{k}_b, \tau_{\mathrm{v}}) = \int d\omega_b e^{-i\omega_b\tau_{\mathrm{v}}} \langle \hat{V}_{+}^{\nu'_{\mathrm{v}}}(\omega_b)\rangle I^{\nu_{\mathrm{v}}\nu'_{\mathrm{v}}}(\boldsymbol{r}_a, \boldsymbol{k}_b, \omega_b), \tag{3.27}$$

$$S_{\mathrm{c}}(\boldsymbol{k}_s, \Lambda) = \Im\big[\sum_a \int dtd\tau_v E_s^{*\nu_s}(\omega_s) e^{i\omega_s t} E_{\mathrm{v}}^{\nu_v}(\boldsymbol{r}_a, \boldsymbol{k}_b, \tau_{\mathrm{v}}) \tilde{P}^{\nu_s\nu_{\mathrm{v}}}(t, \tau_{\mathrm{v}}) e^{i(\boldsymbol{k}_a+\boldsymbol{k}_b-\boldsymbol{k}_s)\cdot\boldsymbol{r}_a}\big]. \tag{3.28}$$

where the $\boldsymbol{r}_a$-dependence of E_{v} goes away in the homogeneous limit.

In summary, we first derived an intuitive formula (Eq. (3.19)) for the cascading signal based on the polarization of molecule b at the retarded time acting as a source to interact with molecule a. We then obtained a convenient, compact expression (Eq. (3.25)) for the cascading terms in the heterodyne signal based on the photon Green's function. It can be readily expanded to any order to obtain cascading corrections to particular nonlinear signals and can also be recast as interaction between an effective electric field and the molecule (Eqs. (3.20)-

(3.21) and (3.27)-(3.28)). The effect of the sample geometry is contained in the exponential phase factor, which approaches the molecule number under good phase matching, and the integral over the photon Green's function $I(\boldsymbol{r}_a, \boldsymbol{k}_b, \omega_b)$. Under off-resonant excitation, the phase of the cascading signal is determined solely by this Green's function. Finally, we note that everything is currently written in terms of discrete summations over molecular positions but we may take the continuum limit by replacing summation by integration $\sum_{\boldsymbol{r}} \to \int d\boldsymbol{r} n(\boldsymbol{r})$ where n denotes molecular concentration.

3.1.2 Alternative Derivation of the Macroscopic Homogeneous Limit

In section 3.1.1, we performed all possible simplifications, such as vacuum mode summations, bundling all geometric dependence into the photon Green's function and a phase-matching exponential factor. Such an approach allows full generality in treating different geometries and provides the necessary ingredients for a simulation of cascading processes in few-molecule samples. The resulting expressions can then be applied directly to microscopic geometries or, after converting summations over molecular locations to spatial integrations, various marcroscopic geometries and smoothly taken to the infinite limit by integrating over all space. Some additional insight into this may be obtained by pursuing an alternative derivation in which this spatial integration is performed first, generating δ-functions that determine the participating vacuum mode and collapse the mode sum.

We begin with

$$\begin{aligned} S_{\mathrm{c}}(\Lambda) =& 2\Im\Bigg[(i)^2 \sum_{ab}\sum_{\{\nu\}} \int dt \int_{-\infty}^{t} d\tau_{\mathrm{v}} \int_{-\infty}^{\tau_{\mathrm{v}}} d\tau'_{\mathrm{v}} E_s^{*\nu_s}(\boldsymbol{r}_a, t)\langle \hat{V}_+^{\nu_s}(t)\hat{V}_-^{\nu_{\mathrm{v}}}(\tau_{\mathrm{v}})\rangle(\boldsymbol{r}_a) \\ & \times \langle \hat{V}_+^{\nu'_{\mathrm{v}}}(\tau'_{\mathrm{v}})\rangle(\boldsymbol{r}_b) \sum_{\boldsymbol{k}_{\mathrm{v}}\lambda} \frac{2\pi\omega_{\mathrm{v}}}{\mathcal{V}} \{\epsilon_{\nu_{\mathrm{v}}}^{(\lambda)*}(\hat{\boldsymbol{k}}_{\mathrm{v}})\epsilon_{\nu'_{\mathrm{v}}}^{(\lambda)}(\hat{\boldsymbol{k}}_{\mathrm{v}}) e^{i(\boldsymbol{k}_{\mathrm{v}}\cdot(\boldsymbol{r}_a - \boldsymbol{r}_b) - \omega_{\mathrm{v}}(\tau_{\mathrm{v}} - \tau'_{\mathrm{v}})} - \mathrm{c.c}\}\Bigg], \end{aligned} \tag{3.29}$$

obtained from inserting Eq. (3.37) into (3.13) which we then use Eqs. (3.38) and (3.9) to rewrite as

$$\begin{aligned}S_{\mathrm{c}}(\boldsymbol{k}_s,\Lambda) =&2\Im\Big[(i)^2\sum_{\{\nu\}}\int dt\int_{-\infty}^{t}d\tau_{\mathrm{v}}\int_{-\infty}^{\tau_{\mathrm{v}}}d\tau_{\mathrm{v}}'E_s^{*\nu_s}(\omega_s)e^{i\omega_s t}\\ &\times\langle\hat{V}_{+}^{\nu_s}(t)\hat{V}_{-}^{\nu_{\mathrm{v}}}(\tau_{\mathrm{v}})\rangle\langle\hat{V}_{+}^{\nu_{\mathrm{v}}'}(\tau_{\mathrm{v}}')\rangle\sum_{\boldsymbol{k}_{\mathrm{v}}}\frac{2\pi\omega_{\mathrm{v}}}{\mathcal{V}}\left(\delta_{\nu_{\mathrm{v}}\nu_{\mathrm{v}}'}-\hat{\boldsymbol{k}}_{\mathrm{v}}^{\nu_{\mathrm{v}}}\hat{\boldsymbol{k}}_{\mathrm{v}}^{\nu_{\mathrm{v}}'}\right)\\ &\times\{f(\boldsymbol{k}_a+\boldsymbol{k}_{\mathrm{v}}-\boldsymbol{k}_s)f(\boldsymbol{k}_b-\boldsymbol{k}_{\mathrm{v}})e^{-i\omega_{\mathrm{v}}(\tau_{\mathrm{v}}-\tau_{\mathrm{v}}')}-f(\boldsymbol{k}_a-\boldsymbol{k}_{\mathrm{v}}-\boldsymbol{k}_s)f(\boldsymbol{k}_b+\boldsymbol{k}_{\mathrm{v}})e^{i\omega_{\mathrm{v}}(\tau_{\mathrm{v}}-\tau_{\mathrm{v}}')}\}\Big]\end{aligned}\tag{3.30}$$

where we have substituted the spatial dependence of the dipole expectation values and the signal field E_s as before. Switching to frequency domain, this can be written as

$$\begin{aligned}S_{\mathrm{c}}(\boldsymbol{k}_s,\Lambda) =&-2\Im[\sum_{\{\nu\}}\int d\omega_b P^{\nu_s\nu_{\mathrm{v}}}(\omega_s;\omega_b)P^{\nu_{\mathrm{v}}'}(\omega_b)\sum_{\boldsymbol{k}_v}\frac{2\pi\omega_{\mathrm{v}}}{\mathcal{V}}\left(\delta_{\nu_{\mathrm{v}}\nu_{\mathrm{v}}'}-\hat{\boldsymbol{k}}_{\mathrm{v}}^{\nu_{\mathrm{v}}}\hat{\boldsymbol{k}}_{\mathrm{v}}^{\nu_{\mathrm{v}}'}\right)\\ &\times\{\frac{f(\boldsymbol{k}_a+\boldsymbol{k}_{\mathrm{v}}-\boldsymbol{k}_s)f(\boldsymbol{k}_b-\boldsymbol{k}_{\mathrm{v}})}{\omega_b-\omega_{\mathrm{v}}+i\eta}-\frac{f(\boldsymbol{k}_a-\boldsymbol{k}_{\mathrm{v}}-\boldsymbol{k}_s)f(\boldsymbol{k}_b+\boldsymbol{k}_{\mathrm{v}})}{\omega_b+\omega_{\mathrm{v}}+i\eta}\}\end{aligned}\tag{3.31}$$

where we have used the definitions of the frequency-domain polarizations of the previous section to simplify the expression. In the infinite homogeneous limit, we have $f(\boldsymbol{k})\rightarrow(2\pi)^3 n\delta(\boldsymbol{k})$

$$\begin{aligned}S_{\mathrm{c}}(\boldsymbol{k}_s,\Lambda) =&-2(2\pi)^4 n^2\Im[E_s^{*\nu_s}(\omega_s)\int d\omega_b P^{\nu_s\nu_v}(\omega_s;\omega_b)\\ &\times P^{\perp\nu_v}(\boldsymbol{k}_b,\omega_b)\delta(\boldsymbol{k}_a+\boldsymbol{k}_b-\boldsymbol{k}_s)\{\frac{k_b c}{\omega_b-k_b c+i\eta}-\frac{k_b c}{\omega_b+k_b c+i\eta}\}],\end{aligned}\tag{3.32}$$

where we have identified the transverse part of the polarization

$$P^{\perp\nu_{\mathrm{v}}}(\boldsymbol{k}_b,\omega_b)=\sum_{\nu_{\mathrm{v}}'}\left(\delta_{\nu_{\mathrm{v}}\nu_{\mathrm{v}}'}-\hat{\boldsymbol{k}}_b^{\nu_{\mathrm{v}}}\hat{\boldsymbol{k}}_b^{\nu_{\mathrm{v}}'}\right)P^{\nu_{\mathrm{v}}'}(\omega_b).\tag{3.33}$$

Finally, we can combine the two terms above to obtain Eq. (3.59)

3.1.3 Field Vacuum Expectation Value

In this section, we evaluate the relevant photon Green's function for this problem defined as a time-ordered, vacuum expectation value of electric field operators

$$G^{\nu\nu'}(\boldsymbol{r}_a, \boldsymbol{r}_b, \tau_{\mathrm{v}} - \tau'_{\mathrm{v}}) = i\theta\left(\tau_{\mathrm{v}} - \tau'_{\mathrm{v}}\right) \langle \hat{E}^{\nu}_{\mathrm{v}+}(\boldsymbol{r}_a, \tau_{\mathrm{v}}) \hat{E}^{\nu'}_{\mathrm{v}-}(\boldsymbol{r}_b, \tau'_{\mathrm{v}}) \rangle_0 \tag{3.34}$$

Ignoring the prefactors for the moment and expanding first the $\hat{\mathcal{E}}_-$ operator gives

$$-i \sum_{\mathbf{k}_v \lambda} \sqrt{\frac{2\pi\omega_{\mathrm{v}}}{\mathcal{V}}} \mathrm{Tr}[\hat{\mathbf{E}}_{v+}(\mathbf{r}_a, \tau_{\mathrm{v}}) \{\epsilon^{*(\lambda)}(\hat{\mathbf{k}}_{\mathrm{v}}) e^{-i(\mathbf{k}_{\mathrm{v}}\cdot\mathbf{r}_b - \omega_{\mathrm{v}}\tau'_{\mathrm{v}})} \hat{a}^{\dagger}_{\mathbf{k}_{\mathrm{v}},\lambda} \rho_{\mathrm{v}} + \epsilon^{(\lambda)}(\hat{\mathbf{k}}_{\mathrm{v}}) e^{i(\mathbf{k}_{\mathrm{v}}\cdot\mathbf{r}_b - \omega_{\mathrm{v}}\tau'_{\mathrm{v}})} \rho_{\mathrm{v}} \hat{a}_{\mathbf{k}_{\mathrm{v}},\lambda}\} \tag{3.35}$$

where $\rho_{\mathrm{v}} \equiv |0\rangle\langle 0|$ is the vacuum density matrix and we have kept only non-vanishing terms. Due to the cyclic invariance of the trace, we may consider only action from the left with respect to the $\hat{\mathbf{E}}_+$ operator that remains. This results in

$$\begin{aligned} 2 \sum_{\mathbf{k}_{\mathrm{v}} \lambda} \sum_{\mathbf{k}'_{\mathrm{v}} \lambda'} \sqrt{\frac{2\pi\omega_{\mathrm{v}}}{\mathcal{V}}} \sqrt{\frac{2\pi\omega'_{\mathrm{v}}}{\mathcal{V}}} \Big[& \epsilon^{*(\lambda)}(\hat{\mathbf{k}}_{\mathrm{v}}) \epsilon^{(\lambda')}(\hat{\mathbf{k}}'_{\mathrm{v}}) e^{i(\mathbf{k}'_{\mathrm{v}}\cdot\mathbf{r}_a - \omega'_{\mathrm{v}}\tau_{\mathrm{v}})} e^{-i(\mathbf{k}_{\mathrm{v}}\cdot\mathbf{r}_b - \omega_{\mathrm{v}}\tau'_{\mathrm{v}})} \mathrm{Tr}[\hat{a}_{\mathbf{k}'_{\mathrm{v}},\lambda'} \hat{a}^{\dagger}_{\mathbf{k}_v,\lambda} \rho_{\mathrm{v}}] \\ & - \epsilon^{(\lambda)}(\hat{\mathbf{k}}_v) \epsilon^{*(\lambda')}(\hat{\mathbf{k}}'_{\mathrm{v}}) e^{i(\mathbf{k}_{\mathrm{v}}\cdot\mathbf{r}_b - \omega_{\mathrm{v}}\tau'_{\mathrm{v}})} e^{i(\mathbf{k}'_{\mathrm{v}}\cdot\mathbf{r}_a - \omega'_v\tau_v)} \mathrm{Tr}[\hat{a}^{\dagger}_{\mathbf{k}'_{\mathrm{v}},\lambda'} \rho_{\mathrm{v}} \hat{a}_{\mathbf{k}_{\mathrm{v}},\lambda}] \Big]. \end{aligned} \tag{3.36}$$

The basic commutation relation then gives $\mathrm{Tr}[\hat{a}_{\mathbf{k}'_v,\lambda'} \hat{a}^{\dagger}_{\mathbf{k}_v,\lambda} \rho_v] = \mathrm{Tr}[\hat{a}^{\dagger}_{\mathbf{k}'_v,\lambda'} \rho_v \hat{a}_{\mathbf{k}_v,\lambda}] = \delta_{\mathbf{k}'_v \mathbf{k}_v} \delta_{\lambda'\lambda}$ and we obtain the expression

$$\begin{aligned} & \langle \hat{\mathbf{E}}_{v+}(\mathbf{r}_a, \tau_v) \hat{\mathbf{E}}_{v-}(\mathbf{r}_b, \tau'_v) \rangle_0 \\ = 2 \sum_{\mathbf{k}_v \lambda} \frac{2\pi\omega_v}{\mathcal{V}} & \epsilon^{*(\lambda)}(\hat{\mathbf{k}}_v) \epsilon^{(\lambda)}(\hat{\mathbf{k}}_v) \{ e^{i(\mathbf{k}_v\cdot(\mathbf{r}_a - \mathbf{r}_b) - \omega_v(\tau_v - \tau'_v))} - e^{-i(\mathbf{k}_v\cdot(\mathbf{r}_a - \mathbf{r}_b) - \omega_v(\tau_v - \tau'_v))} \} \end{aligned} \tag{3.37}$$

To simplify, we perform the polarization sum and change the vacuum mode summation to an integration (see [132, 133])

$$\sum_{\lambda} \epsilon^{(\lambda)*}_{\nu_v}(\hat{\boldsymbol{k}}_v)\epsilon^{(\lambda)}_{\nu'_v}(\hat{\boldsymbol{k}}_v) = \delta_{\nu_v\nu'_v} - \hat{\boldsymbol{k}}_v^{\nu_v}\hat{\boldsymbol{k}}_v^{\nu'_v} \tag{3.38}$$

$$\frac{1}{\mathcal{V}}\sum_{\boldsymbol{k}_v} \to \int \frac{d\omega_v d\Omega_v \omega_v^2}{(2\pi c)^3} \tag{3.39}$$

after which the integration over solid angle can be carried out

$$\int d\Omega_v \left(\delta_{\nu_v\nu'_v} - \hat{\boldsymbol{k}}_v^{\nu_v}\hat{\boldsymbol{k}}_v^{\nu'_v}\right) e^{\pm i\boldsymbol{k}_v\cdot\boldsymbol{r}} = \left(-\nabla^2\delta_{\nu_v\nu'_v} + \nabla_{\nu_v}\nabla_{\nu'_v}\right)\frac{\sin k_v r}{k_v^3 r} \tag{3.40}$$

which then allows us to easily perform the ω_v integration

$$\int d\omega_v \sin\left(\omega_v\frac{r_{ab}}{c}\right)\left[e^{-i\omega_v(\tau_v-\tau'_v)} - e^{i\omega_v(\tau_v-\tau'_v)}\right] = i\pi\left[\delta(\tau'_v - \tau_v - \frac{r_{ab}}{c}) - \delta(\tau'_v - \tau_v + \frac{r_{ab}}{c})\right]. \tag{3.41}$$

Combining this with Eq. (3.34) yields

$$G^{\nu\nu'}(\boldsymbol{r}_a, \boldsymbol{r}_b, \tau_v - \tau'_v) = \left(-\nabla^2\delta_{\nu\nu'} + \nabla_\nu\nabla_{\nu'}\right)\frac{\delta(\tau'_v - \tau_v + \frac{r_{ab}}{c})}{2\pi r_{ab}}. \tag{3.42}$$

with temporal Fourier transform

$$G^{\nu\nu'}(\boldsymbol{r}_a, \boldsymbol{r}_b, \omega) = \int d(\tau_v - \tau'_v) e^{i\omega(\tau_v-\tau'_v)} G^{\nu\nu'}(\boldsymbol{r}_a, \boldsymbol{r}_b, \tau_v - \tau'_v) = \left(-\nabla^2\delta_{\nu\nu'} + \nabla_\nu\nabla_{\nu'}\right)\frac{e^{i\omega\frac{r_{ab}}{c}}}{2\pi r_{ab}} \tag{3.43}$$

where acting the differential operators results in Eq. (3.57) below.

3.2 Sample Geometry Determines the Phase of the Cascading Signal

From the previous section, it is clear that, for the off-resonant response, the $\boldsymbol{k}$-space photon Green's function (Eq. (3.11) determines the phase of the cascading signal. In the semiclassical description, the effective electric field emitted by molecule b is given by a phase-shift of the polarization $E \propto iP$. The extra factor of i, which in this semiclassical picture comes from the additional emision event inherent in cascading processes, renders the cascading terms out of phase with the direct nonlinear terms. This effect has been used to discriminate between the two [44, 43, 47, 48]. In this section, we evaluate the photon Green's function for different geometries and show under what conditions the cascaded signal acquires this well-defined phase shift.

To simplify the analysis, we will seperate the summations (integrations) over the positions over the two molecules. We thus re-write

$$G^{\nu_{\mathrm{v}}\nu'_{\mathrm{v}}}(\boldsymbol{k}_s - \boldsymbol{k}_a, -\boldsymbol{k}_b, \omega_b) = \sum_a e^{i(\boldsymbol{k}_a + \boldsymbol{k}_b - \boldsymbol{k}_s)\cdot \boldsymbol{r}_a} I^{\nu_{\mathrm{v}}\nu'_{\mathrm{v}}}(\boldsymbol{r}_a, \boldsymbol{k}_b, \omega_b) \tag{3.44}$$

$$I^{\nu_{\mathrm{v}}\nu'_{\mathrm{v}}}(\boldsymbol{r}_a, \boldsymbol{k}_b, \omega_b) = \sum_b e^{i\boldsymbol{k}_b\cdot(\boldsymbol{r}_a - \boldsymbol{r}_b)} G^{\nu_{\mathrm{v}}\nu'_{\mathrm{v}}}(\boldsymbol{r}_a, \boldsymbol{r}_b, \omega_b) \tag{3.45}$$

where the second summation differs from the discrete Fourier transform of G with respect to $\boldsymbol{r}_b$ only by the spatial phase factor $e^{i\boldsymbol{k}_b\cdot \boldsymbol{r}_a}$. In the macroscopic homogenous limit, I does not depend on the choice of $\boldsymbol{r}_a$ and we have

$$I^{\nu_{\mathrm{v}}\nu'_{\mathrm{v}}}(\boldsymbol{r}_a, \boldsymbol{k}_b, \omega_b) \to I^{\nu_{\mathrm{v}}\nu'_{\mathrm{v}}}(\boldsymbol{k}_b, \omega_b) = G^{\nu_{\mathrm{v}}\nu'_{\mathrm{v}}}(\boldsymbol{k}_b, \omega_b) \tag{3.46}$$

in line with Eq. (3.11). Thus, we will primarily be concerned with the evaluation of Eq. (3.45).

3.2.1 A Simplified Treatment for a Scalar Field

The presence of the dipole coupling tensor $(-\nabla^2\delta_{\nu\nu'} + \nabla_\nu\nabla_{\nu'})$ in Eq. (3.10) complicates matters somewhat. For clarity, in this section, we first treat the problem by replacing the electromagnetic field, which is a vector gauge field, with a scalar field. This simplified model still maintains all qualitative features of the original model. The effects will be extended for the original electromagnetic field setting later, and we will show that the scalar model describes the relation between the cascaded and direct signals absolutely adequately.

We assume the following interaction Hamiltonian

$$H_{\text{int}} = -\int d\boldsymbol{r}\varphi(\boldsymbol{r})\rho(\boldsymbol{r}), \tag{3.47}$$

where $\rho(\boldsymbol{r})$ is the scalar polarization, and $\varphi(\boldsymbol{r})$ is the scalar field that replaces the full electromagnetic counterpart, so that the Maxwell equations are replaced with the Helmholtz equation $((\nabla^2 + k^2)\phi(\boldsymbol{r}) = 0)$, whose Green's function (that replaces the Green's function of the Maxwell equations, also known as the Green's function of the electromagnetic field) has the form

$$G(\boldsymbol{r}, \boldsymbol{r}'; \omega) = \frac{e^{i\frac{\omega}{c}|\boldsymbol{r}-\boldsymbol{r}'|}}{|\boldsymbol{r} - \boldsymbol{r}'|}. \tag{3.48}$$

We will further switch to the uniform continuum limit wherein all properties of the cascaded signal, compared to its direct counterpart are fully contained in the integral

$$I(\boldsymbol{r}_a, \boldsymbol{k}_b, \omega_b) = \int_V d\boldsymbol{r}_b e^{i\boldsymbol{k}_b\cdot(\boldsymbol{r}_b-\boldsymbol{r}_a)} G(\boldsymbol{r}_a, \boldsymbol{r}_b; \omega_b), \tag{3.49}$$

where V denotes the integration region, occupied by the sample. We will focus on three special cases. In cases (i) and (ii) there is a poor phase matching, whereas in case (iii) phase matching is good.

Case (i): the region V is a convex $3D$ region with the size large, compared to the wavelength. Introducing an inhomogeneous spherical coordinate system, associated with the convex region V, centered at r_0, with the z-axis oriented in the direction of $\boldsymbol{k}_0$ (see appendix C.2.2) we recast the integral I in a form

$$I = \int_0^R r_b^2 dr_b \int_0^\pi \sin\theta d\theta \int_0^{2\pi} d\varphi \xi^3(\theta,\varphi)(\xi(\theta,\varphi)r_b)^{-1} e^{i\xi(\theta,\varphi)(\frac{\omega_b}{c}+k_b\cos\theta)r_b}, \tag{3.50}$$

where R and $\xi(\theta,\varphi)$, are determined by the shape and size of the region V, as well as the position $\boldsymbol{r}_a$. Assuming a natural condition $k_b < \omega_b$, integration over r_a can be performed for any values of θ and φ, resulting in

$$\begin{aligned} I = & -\int_0^{2\pi} d\varphi \int_0^\pi \sin\theta d\theta \frac{1}{(\frac{\omega_b}{c}+k_b\cos\theta)^2} + \\ & \int_{S^2} d\boldsymbol{n} \left(\frac{1}{(\frac{\omega_b}{c}+\boldsymbol{k}_b\cdot\boldsymbol{n})^2} - \frac{iR\xi(\boldsymbol{n})}{\frac{\omega_b}{c}+\boldsymbol{k}_b\cdot\boldsymbol{n}} \right) e^{iR\xi(\boldsymbol{n})(\frac{\omega_b}{c}+\boldsymbol{k}_b\cdot\boldsymbol{n})} \end{aligned} \tag{3.51}$$

The second integral over the unit sphere represents the integral over the boundary of the sample. If the point $\boldsymbol{r}_a$ is not within the wavelength region from the boundary (which is the typical case), the integrand is a fast oscillating function and the integration can be performed using the saddle point method. In subsection C.2.3, we briefly estimate this contribution and demonstrate that the second integral can safely be neglected. Performing the integration in the first term in the r.h.s. of Eq. (3.51) explicitly we arrive at

$$I = -\frac{4\pi}{\left(\frac{\omega_b}{c}\right)^2 - k_b^2}. \tag{3.52}$$

This result is natural, it just means that, when $\boldsymbol{r}_a$ is not within a wavelength distance from the boundary the result is the same as in the infinite medium. Since the contribution of the thin layer in the vicinity of the boundary provides minor contribution, the cascaded signal can be computed using the simple expression for I, given by Eq. (3.52). Note that we have implicitly assumed poor phase matching, i.e. Eq. (3.52) only applies in a principal value sense and neglects the perfect phase matching point $\omega_b = k_b c$. In the absense of such phase matching, I is clearly real and the cascading signal is in phase with the direct signal. We will see later that the singular point gives an imaginary, out-of-phase contribution which is dominant under good phase matching.

Case (ii): V is a convex $2D$ region with the size large, compared to the wavelength, such as a molecular monolayer or thin film with thickness smaller than the wavelength. We can use an inhomogeneous polar coordinate system, resulting in the following expression for the integral I

$$I = \int_0^R r_b dr_b \int_0^{2\pi} d\varphi \xi^2(\varphi)(\xi(\varphi) r_b)^{-1} e^{i\xi(\varphi)(\frac{\omega_b}{c} + k_b \cos\varphi) r_b}, \tag{3.53}$$

where in this $2D$ case $\boldsymbol{k}_b$ naturally denotes the projection of the cascading field wave vector onto to the monolayer/film plane. Performing integration over r_b we obtain

$$I = -i \int_0^{2\pi} d\varphi \frac{1}{\frac{\omega_b}{c} + k_b \cos\varphi} + i \int_0^{2\pi} d\varphi \frac{1}{\frac{\omega_b}{c} + k_b \cos\varphi} e^{i(\frac{\omega_b}{c} + k_b \cos\varphi) a \xi(\varphi)} = I_0 + I_1 \tag{3.54}$$

Neglecting, similar to the $3D$ case the second contribution occurring from a fast-oscillating integral we obtain

$$
\begin{aligned}
I = I_0 &= -i \int_C \frac{dz}{2\pi i z} \frac{1}{\frac{\omega_b}{c} + k_b(z + z^{-1})/2} \\
&= -i \int_C \frac{dz}{2\pi i} \frac{1}{k_b z^2 + \frac{\omega_b}{c} z + k_b} = \frac{-i}{\sqrt{\left(\frac{\omega_b}{c}\right)^2 - k_b^2}}
\end{aligned}
\tag{3.55}
$$

This means that in the off-resonance case, when the susceptibilities are real, the direct and cascaded signals are in phase for $3D$, whereas in the $2D$ case there is a $\pi/2$ phase shift between the two signals.

Case (iii): the region V is a cylinder of generically irregular shape, located on a reflecting plane. Let $\boldsymbol{r} = (x, y, z)$, which describes Cartesian coordinates. We assume the region V to be a cylinder of thickness l, so that $0 \le z \le l$, where $z = 0$ identifies a reflecting plane. The shape of the cross section of V at $0 \le z \le l$ is generically irregular, but convex, and may depend on z. We also assume $\boldsymbol{k}_b = (0, 0, k_b)$ to be directed along the z-axis, i.e., the cascading wavevector is normal to the plane. The derivation of this signal follows a similar form to case (ii) but is followed by an integration over z. It is given in detail in appendix C.1 and results in

$$
I(\boldsymbol{r}_a, \boldsymbol{k}_b, \omega_b) = 2\pi i \frac{c}{\omega_b} z_a e^{i k_b z_a}. \tag{3.56}
$$

where we have taken the limit of good phase matching so that $|\omega_b - k_b| l \ll 1$ and z_a is not within the wavelength scale from the borders.

To summarize, we note that the i factor in the r.h.s. of Eq. (C.10) appeared due to the $2D$-integration over a cross section (Eq. (C.3)), exactly along the lines of the Feynman's argument [134]. The third contribution in Eq. (C.8), which is due to the reflecting surface, vanishes in the good phase matching limit. This tells us that in this limit the effect of the reflecting boundary is negligible, even if it is not perfectly reflecting. Finally, we note that, for a co-linear beam geometry, we have $\boldsymbol{k}_b c = \omega_b$ and this phase-matching condition is automatically satisfied. In this case, as long as a sufficient number of molecules are involved so as to permit the continuous $2D$-integration over a cross-section of the interaction region, we will obtain a cascading signal exactly out-of-phase with respect to the direct signal.

3.2.2 The Vector Guage Field

The previous section demonstrated how to perform the sorts of integrals needed to evaluate $G(\boldsymbol{r}_a, \boldsymbol{k}_b, \omega_b)$ for different geometries utilizing a simplifiedscalar field. Restoring the vector nature of the coupling gives, for the real space Green's function

$$
\begin{aligned}
G^{\nu\nu'}(\boldsymbol{r}_a, \boldsymbol{r}_b, \omega_b) &= \left(-\nabla^2 \delta_{\nu\nu'} + \nabla_\nu \nabla_{\nu'}\right) \frac{e^{i\frac{\omega_b}{c} r}}{2\pi r} \qquad (3.57)\\
&= \frac{-e^{i\frac{\omega_b}{c} r}}{2\pi r^3} \left[(\delta_{\nu\nu'} - 3\hat{r}_\nu \hat{r}_{\nu'})(1 - i\frac{\omega_b}{c} r) - (\delta_{\nu\nu'} - \hat{r}_\nu \hat{r}_{\nu'}) \left(\frac{\omega_b}{c}\right)^2 r^2 \right]
\end{aligned}
$$

where we have used $r = |\boldsymbol{r}_a - \boldsymbol{r}_b|$ for brevity. Equation (3.57) has terms proportional to r^{-3}, r^{-2}, and r^{-1}. The last of these terms is purely transverse and, aside from the ω_b^2 factor, matches the Helmholtz Green's function used as an example in the previous section. In the limit of an isotropic sample, we have $\hat{r}_{\nu_v} \hat{r}_{\nu'_v} \to \frac{1}{3} \delta_{\nu_v \nu'_v}$ and this r^{-1} term is the only to survive yielding

$$
G(\boldsymbol{k}_b, \omega_b) = \frac{-4}{3} \frac{\omega_b^2}{\omega_b^2 - k_b^2 c^2 + i\eta} \qquad (3.58)
$$

where we have omitted the cartesian components since the result is proportional to $\delta_{\nu_v \nu'_v}$. This is the equivalent to Eq. (3.52) for the vector coupling field and holds under the same geometric assumptions as that equation. In fact, in the isotropic limit, we may directly obtain the result for the full vector Green's function by simply multiplying the corresponding result obtained above for a scalar field by the factor $\frac{\omega_b^2}{3\pi c^2}$. More generally, the far-field term is dominant when $\frac{\omega_b r}{c} \gg 1$, corresponding to seperations of greater than $2\pi\lambda$ or roughly 6 times the wavelength of the cascading light. Thus, for intermolecular seperations much less than this, the static dipole-dipole coupling is dominant while for much larger distances, the long-range $\frac{1}{r}$ term is dominant. As demonstrated above, it is this far-field term that leads to a factor of i in the case of a thin sample under good phase matching $|k_b - \frac{\omega_b}{c}|l \ll 1$. Note that the r^{-2} term comes with an i factor and hence, when the sample is anisotropic, we may expect that the cascading signal has both in-phase and out-of-phase contributions relative to the direct nonlinear signal.

The limit of an infinite, homogeneous sample can be obtained in a somewhat simpler fashion by integrating over space before handling any vacuum mode summations. The result is a δ-function selecting the participating vacuum mode and we obtain (see section 3.1.2)

$$S_{\rm c}(\boldsymbol{k}_s, \Lambda) = -n^2 \Im \left[E_s^{*\nu_s}(\omega_s) \int d\omega_b P^{\nu_s \nu_v}(\omega_s; \omega_b) P^{\perp \nu_v}(\boldsymbol{k}_b, \omega_b) \delta(\boldsymbol{k}_a + \boldsymbol{k}_b - \boldsymbol{k}_s) \frac{k_b^2 c^2}{\omega_b^2 - k_b^2 c^2 + i\eta} \right], \tag{3.59}$$

where we omit factors of 2π for brevity. It is thus apparent that the cascading signal consists of a real, principal value part and an imaginary part with a δ-function selecting $\omega_b^2 c^2 = k_b^2$. Note that $\boldsymbol{k}_b$ is a linear combination of classical modes interacting with molecule b and ω_b is the corresponding linear combination of frequencies. Both parameters are therefore externally controlled (up to permutation since which particular classical modes interact with molecule b versus a must clearly be summed over) and we obtain a $\pi/2$ phase shift (factor of i) only under perfect phase matching $\omega_b^2 = k_b^2 c^2$. As demonstrated in the previous section, this phase-shifted component is dominant for finite samples when the phase-matching is such that $|\omega_b - k_b c|l \ll 1$ where l is the optical path length.

Equation (3.59) strongly resembles the commonly-invoked marcroscopic relation that the cascading field comes as a product of two polarizations $E_\mathrm{c} \propto PP$. Our microscopic derivation reveals the precise sense in which they are related, i.e., through integration over the $(\boldsymbol{k}, \omega)$-space photon Green's function.

The case of two-molecules is also easily treated and instructive. Arranging our coordinate system such that the two molecules both lie on the z-axis, we obtain the simplified form of the integrated Green's function

$$I^{\nu\nu'}(\boldsymbol{r}_a, \boldsymbol{k}_b, \omega_b) = \frac{-\delta_{\nu\nu'} e^{i(\frac{\omega_b}{c} r - \boldsymbol{k}_b \cdot \boldsymbol{r})}}{2\pi r^3} \left[(1 - 3\delta_{\nu\nu' z})(1 - i\frac{\omega_b}{c} r) - (1 - \delta_{\nu\nu' z}) \left(\frac{\omega_b}{c}\right)^2 r^2 \right]. \tag{3.60}$$

We immediately notice that the Green's function is now a diagonal tensor. In this two-molecule case, the phase of the cascading signal is sensitively dependent on the distance between molecules and the angle between the cascading beam and the intermolecular axis and comes via the factor $e^{i(\frac{\omega_b}{c} r - \boldsymbol{k}_b \cdot \boldsymbol{r})}$. Considering, for example, a co-linear beam geometry perpendicular to the intermolecular axis, we have $\boldsymbol{k}_b \cdot \boldsymbol{r} = 0$ and the phase $e^{i\frac{\omega_b}{c} r}$ is a sensitive probe of the intermolecular distance. Similarly, with a co-linear beam geometry parallel to the intermolecular axis, we obtain a phase of $e^{i(\frac{\omega_b}{c} r - k_b r)} = 0$ and the long-range cascading signal is *in phase* with the direct signal. Finally, we note that the long-range term which usually generates cascading does not contribute to the G^{zz} component. This means that, if the dipoles are aligned along the axis connecting the two molecules, no long-range cascading takes place.

3.3 Conclusions

Cascading is a vacuum-mediated exchange of coherent polarization between two molecules in a sample. Being a coherent process, it generates terms with the same phase-matching and scaling with external field amplitudes as direct signals that are ordinarily of more interest since they reveal higher nonlinearities. In this chapter, we have provided a microscopic QED derivation of cascading processes to arbitrary order in the classical modes and connected this to the common macroscopic result obtained via Maxwell's equations. In particular, we have demonstrated that the i factor used to discriminate cascading from direct signals originates in phase-matching and geometric concerns. In few-molecule samples for example, the cascading signal will generally produce both in phase and out of phase terms of varying dependence on the intermolecualr seperation vector $\boldsymbol{r}$ and cascading wavevector $\boldsymbol{k}_b$. The uniform integration over the interaction volume cross-section was found to be responsible for this phase-shift, along the same lines as explicated by Feynman for a sheet of dipoles [134]. A phase-matching condition $|\frac{\omega_b}{c} - k_b| l \ll 1$, where l is the thickness of the sample, was identified as necessary for the in-phase component of the cascaded signal to vanish. This condition can be achieved in thin films or guaranteed by a co-linear beam geometry. Because they scale quadratically in molecular concentration, the cascading terms often dominate direct nonlinear signals. Additionally, the cascading signal scales linearly with the frequency ω_b of the emitting polarization. This implies that cascading processes will become even more dominant at higher frequencies, such as in x-ray Raman experiments, necessitating a thorough understanding of cascading processes for data analysis purposes [135].

We are now in a position to appreciate the difference between cascading and fluorescence resonant energy transfer (FRET). FRET processes are evaluated by taking the square of the Hilbert space amplitude for molecule b to emit a photon then aborbed by molecule a [132, 133]. But this square transition amplitude involves 4 orders in the vacuum mode, and is thus 2 orders higher than cascading. In fact, in a FRET process, the emitting molecule *populates* a photon mode while in cascading the only intermediate photon state is a coherence between the 0- and 1-photon states. Despite these differences, the derivations given above have much the same flavor as QED derivations of FRET [132, 136, 133, 137] with the principal difference being that cascading depends directly on the dipole coupling tensor rather than its square. The derivation of section 3.1.1 can thus be extended to account for FRET and other higher-order processes. At fourth-order, the same as FRET, we also encounter a 3-body cascading contribution that comes as

$$\begin{aligned}\mathcal{P}^{\nu}_{3-\text{body}}(\boldsymbol{k}_s,\omega_s) = \int d\omega_b d\omega_c \tilde{P}^{\nu\nu_{\text{v}}\mu_{\text{v}}}(\boldsymbol{k}_a,\omega_s;-\omega_b,\omega_c) P^{\nu'_{\text{v}}}(\boldsymbol{k}_b,\omega_b) P^{\mu'_{\text{v}}}(\boldsymbol{k}_c,\omega_c) \\ \times \sum_{abc} e^{i(\boldsymbol{k}_a+\boldsymbol{k}_b+\boldsymbol{k}_c-\boldsymbol{k}_s)\cdot\boldsymbol{r}_a} I^{\nu_{\text{v}}\nu'_{\text{v}}}(\boldsymbol{r}_a,\boldsymbol{k}_b,\omega_b) I^{\mu_{\text{v}}\mu'_{\text{v}}}(\boldsymbol{r}_a,\boldsymbol{k}_c,\omega_c)\end{aligned} \tag{3.61}$$

and will, under phase matching, provide terms that scale cubically in the molecular concentration n. Higher-order corrections generate n-body cascading terms that follow similarly. From the perspective of Feynman diagrams, cascading is like a vertex insertion (with four free branches corresponding to the two in-states and two out-states of the participating molecules) while the Lamb shift is the corresponding self-energy insertion. Both come from vacuum interactions but only the former can be incorporated into a Dyson equation. The n-body cascading terms similarly behave like vertex insertions with $2n$ free branches.

An interesting future extension of this work would be to consider manipulating the cascading signal from a system of molecules embedded in an optical cavity, systems which have drawn recent interest [56, 57, 138, 139, 140, 141]. Optical cavities alter the density of electromagnetic field modes from its free-space value, suppressing cascading in all but the cavity mode. In particular, we note that the field mode participating in a cascading process is determined only for infinite samples (when the mode summation collapses to a δ-function as in section 3.1.2) while, for few-molecule samples, all vacuum modes participate. By strongly coupling a few-molecule sample to an optical cavity, we can effectively force the cascading to occur with a particular field mode (the cavity mode). On the other hand, by suppressing the density of field-modes at the cascading wave-vector for a macroscopic system, the cascading signal can be suppressed for arbitrary sample-sizes and beam geometries. Moreover, molecular coupling to the cavity mode can be tuned by the cavity volume and made much larger than the coupling to the vacuum field. This would allow for enhancement and control of the cavity-mode cascading.

Chapter 4

Molecules in Optical Cavities

The fate of a molecule after excitation with light is determined by the shape of its excited-state potential energy surface (PES). While most molecules make their way back to the ground state by spontaneous emission or non-radiative relaxation, some dissociate, isomerize, or are funneled through conical intersections (CoIn) [103]. It is well-known that molecular photochemistry can be meaningfully altered *via* specialized fields [142, 60, 61, 143, 144, 145, 146]. The modified photonic vacuum in nano-scale fabricated cavities allows for influencing molecular potential energy surfaces in a nondestructive manner and without the use of an external laser field that would allow multi-photon pathways that could interfere with the intended control scheme. The radiation matter coupling is enhanced in small cavity modes [52] (the coupling increases with $1/\sqrt{V}$, where we use V for the mode volume in the chapter, reserving the symbol Ω for the Rabi frequency), and substantial couplings can be induced between electronic states with just a single photon [56] or even in the vacuum state [147, 148]. The strongly coupled molecule-field states are known as dressed states [54] or polaritons [58] and are well-studied in atomic samples [52, 53, 54] and the treatment has been applied to atomic trapping and cooling [149]. Potential application to molecular cooling [150, 151], as a tool to probe larger molecules [152, 153], to enhance vibrational spectra

[154, 57, 155, 138], for use with electromagnetically induced transparency [156], and to allow cavity-modified photochemistry [157, 139] have been objects of intensive studies. Recent experimental developments show promising results, paving the way for strong coupling in the single molecule regime [59].

While optical cavities can couple to vibrational transitons [57, 158], we discuss only the cavity coupling to the electrons in this chapter as this is most directly relevant for manipulating excited-state potential surfaces. For simplicity, we assume only two active electronic levels, a ground state $|g\rangle$ and excited state $|e\rangle$. To set the stage, we first neglect the nuclear degrees of freedom and only introduce them at a later point. This will allow us to introduce the basic structure of the Hamiltonian and the cavity coupling. The Hamiltonian describing the light-matter interaction of a two-level system linearly coupled to a quantized radiation field is given by the quantum Rabi model [159]

$$\hat{H}_{\text{el-c}} = H_{\text{el}} + H_{\text{c}} + H_{\text{I}} = \frac{\omega_0}{2}(2\hat{\sigma}^\dagger\hat{\sigma} - 1) + \omega_c\hat{a}^\dagger\hat{a} + g(\hat{a}^\dagger + \hat{a})(\hat{\sigma}^\dagger + \hat{\sigma}) \tag{4.1}$$

where $H_{\text{el(c)}}$ is the electronic (cavity) Hamiltonian, $\omega_0 = \omega_e - \omega_g$ is the energy difference between the exited state $|e\rangle$ and the ground state $|g\rangle$, $\hat{\sigma} = |g\rangle\langle e|$ is the annihilation operator for the bare electronic excitation, and $\hat{a}^{(\dagger)}$ annihilates (creates) a cavity photon of mode frequency ω_c. The vacuum Rabi-frequency $g = \sqrt{n}\mu_{eg}\varepsilon_c$, the coupling between the photon mode and the electronic degrees of freedom, depends on the electronic transition dipole moment μ_{eg} and the vacuum field amplitude

$$\varepsilon_c = \sqrt{\frac{2\pi\omega_c}{V}}\,. \tag{4.2}$$

This amplitude is determined by the active volume V of the cavity mode. Nano-scale cavities can thus induce very strong coupling. The cavity coupling is further enhanced by a factor of $\sqrt{n}$ if an ensemble of n molecules contributes in a coherent fashion in a cavity smaller than

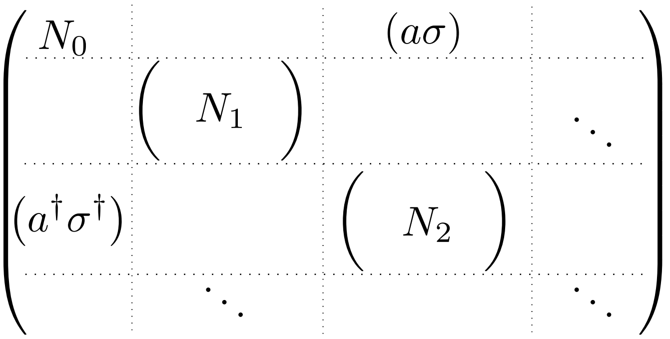

$$\pi = +1 : \; |g,0\rangle \to |e,1\rangle, |g,2\rangle \to |e,3\rangle, |g,4\rangle \to \dots$$

$$\pi = -1 : \; |e,0\rangle, |g,1\rangle \to |e,2\rangle, |g,3\rangle \to \dots$$

Figure 4.1: (Upper) Schematic depiction of the Hamiltonian. Under the RWA, $\hat{H}$ has a block-diagonal structure. Each block with nonzero total excitation number is 2-by-2 and composed, in this basis, of $|e, n_c\rangle, |g, n_c + 1\rangle$. Adding back in the counter-rotating terms couples states that differ by 2 in total excitation number $\hat{N}$. (Lower) The simultaneous eigenstates of parity and excitation number. States with even (odd) excitation number have even (odd) parity.

the optical wavelength $2\pi c/\omega_c$.

Different approximations can be used to find the eigenvalues of Eq. 4.1 depending on the magnitude of g. Perturbative solutions are possible when g is much smaller than all other system frequencies. If the time scale g^{-1} is faster than possible decay processes, we enter the strong coupling regime though the counter rotating terms ($a\sigma$ and $a^\dagger\sigma^\dagger$) in the Hamiltonian can still be neglected. This is known as the Jaynes-Cummings (JC) model [53] and approximate solutions to the Hamiltonian are in the form of dressed states, which are then expressed in the basis of the photon number states:

$$\Psi_c = \sum_{n=0}^{M} c_{g,n_c}|g, n_c\rangle + c_{e,n_c}|e, n_c\rangle. \tag{4.3}$$

Here n_c is the number of photons in the cavity mode and M is the highest photon number in the expansion. Because the JC model keeps only the $a\sigma^\dagger$ and $a^\dagger\sigma$ terms in the cavity-molecule coupling, the total matter+field excitation number, $\hat{N} \equiv \hat{n}_c + \hat{\sigma}^\dagger\hat{\sigma}$, is a conserved quantity ($[\hat{N}, \hat{H}] = 0$), reducing the Hamiltonian to a 2-by-2 block-diagonal form (see Fig. 4.1). Assuming that the cavity is initially in the vacuum state (no photons), the wavefunction in the JC model can thus be expressed by the two bare states $|g, 0\rangle$, $|e, 0\rangle$ and the 1-photon dressed ground state $|g, 1\rangle$, which is dynamically accessible through the excitation $|e, 0\rangle$ initialized by the pump. An extension of the JC model to include the nuclear degrees of freedom is presented in section 4.1. There, we present examples illustrating how the cavity coupling can be tailored to suppress or enhance reaction rates relative to the bare system.

The RWA is justified in the regime of a weakly-driven system ($\tilde{g} \ll \omega_c$) and a reasonably-large transition frequency ($\omega_0/\omega_c > 0$). Both conditions are violated if we consider ultrastrong coupling to a molecule with a bare avoided crossing or CoIn. In this parameter regime, the Hamiltonian acquires a band-diagonal structure as compared to a block diagonal structure (Fig. 4.1 upper panel) and the expansion for the eigenstates (Eq. 4.3) requires a large number of Fock states to converge, becoming intractable for quantum dynamics time propagation (scaling with $\mathcal{O}(M^2)$).

The full Quantum Rabi Hamiltonian has been well-studied. Analytic expressions in terms of continued fractions were found by Judd for an isolated set of eigenstates and the approach was further explicated in terms of the Bargmann representation and extended [160, 161, 162]. While a purely analytic, complete solution without the RWA is not possible, the problem has been treated in the Fock space to allow for a numerically exact solution [163, 164]. Operator methods have been discussed as well [165, 166]. Section 4.2 presents a method for obtaining the potential energy surfaces of the coupled cavity-matter system, as well as the non-adiabatic couplings between them, in the ultrastrong coupling regime in which the RWA fails.

In principle, these can be used to simulate wavepacket dynamics and spectroscopic signals. In practice, this requires great care as the system can move between the weak, strong, and ultrastrong regimes as the nuclear parameters change. Different techniques should really be used in these different regimes (this is not so great a problem for the potentials but the non-adiabatic couplings are more demanding), with final curves patched together appropriately, but this more detailed analysis is not pursued here. Instead, in section 4.2.2, we present a method for directly simulating spectroscopic observables by real-time wavepacket propagation in the joint cavity-matter space. This allows direct quantitative access to signals of interest, skipping the dressed potential surfaces and couplings. The two techniques are thus complementary, one providing the signals (section 4.2.2) and the other providing the underlying quantities that determine it (section 4.2). We demonstrate these points with photoexcitation of NaI as an example.

4.1 Molecule-Cavity Coupling in the Rotating Wave Approximation

Within the RWA, the eigenstates of $H_{\text{el-c}}$ are the dressed (polariton) states $|\pm, n_c\rangle$:

$$|+, n_c\rangle = \cos\theta|e, n_c\rangle + \sin\theta|g, n_c+1\rangle \tag{4.4}$$

$$|-, n_c\rangle = -\sin\theta|e, n_c\rangle + \cos\theta|g, n_c+1\rangle\,, \tag{4.5}$$

where the mixing angle θ is given by

$$\cos\theta = \sqrt{\frac{\Omega_n - \delta_c}{2\Omega_n}}, \quad \sin\theta = \sqrt{\frac{\Omega_n + \delta_c}{2\Omega_n}}, \tag{4.6}$$

and the Rabi-frequency Ω_n and molecule-cavity detuning δ_c are

$$\Omega_n = \sqrt{4g^2(n_c+1) + \delta_c^2}\,, \quad \delta_c = \omega_0 - \omega_c = V_e - V_g - \omega_c. \tag{4.7}$$

The corresponding eigenvalues are then

$$E_{\pm,n} = \frac{1}{2}\omega_0 + \omega_c\left(n_c + \frac{1}{2}\right) \pm \frac{1}{2}\Omega_n\,. \tag{4.8}$$

We assume that the cavity is initially in the vacuum state (i.e., $n_c = 0$) and omit the photon number n_c (and the zero-point energy) in the remainder of the section.

The JC model was developed for atomic transitions and does not include nuclear degrees of freedom. To generalize to molecules, we include the dependence of the nuclear coordinates $\mathbf{q} = (q_1, \ldots, q_N)$ into the JC model and the quantities δ_c, Ω_n, g, and the mixing angle θ (Eq. 4.6) then depend parametrically on $\mathbf{q}$. The new dressed potential energy surfaces are then

$$V_{\pm,0} = \frac{1}{2}(V_e - V_g) \pm \frac{1}{2}\Omega_0 \tag{4.9}$$

$$V_{g,0} = V_g \tag{4.10}$$

where $V_g \equiv V_g(\mathbf{q})$ and $V_e \equiv V_e(\mathbf{q})$ are the bare state potential energy surfaces of the free molecule.

We follow the standard procedure to derive the non-adiabatic coupling terms in the adiabatic basis [103, 167, 168]. Instead of the bare adiabatic electronic states, we use the dressed states from Eqs. 4.4 denoted $|\phi_k\rangle \equiv |\phi_k(\mathbf{r}, \mathbf{q})\rangle$, where $\mathbf{r} = (r_1, \ldots, r_M)$ are the electronic coordinates. The total wave function is expanded in the adiabatic basis:

$$\Psi = \sum_k \psi_k(\mathbf{q})\phi_k(\mathbf{r}, \mathbf{q}) \tag{4.11}$$

where k runs over the set of dressed states $(|g, 0\rangle, |\pm, 0\rangle)$. The full molecular Hamiltonian consists of the electronic part and the nuclear kinetic energy term $\hat{T} = -\sum_i \frac{1}{2m_i}\nabla_i$ where $\nabla_i \equiv \frac{\partial^2}{\partial q_i^2}$ is the nuclear spatial derivative operator and m_i is the mass of the i-th nuclear coordinate (see appendix B.2). Taking the matrix elements $\langle\Psi|\hat{H}|\Psi\rangle$ and integrating over r

yields:

$$\hat{H}_{kl} = \delta_{kl}\left(\hat{T} + \hat{V}_{kl}\right) + \sum_i \frac{1}{m_i}\left(f_{kl}^{(i)}\frac{\partial}{\partial q_i} + \frac{1}{2}h_{kl}^{(i)}\right) \tag{4.12}$$

where f and h recover the derivative coupling term and the scalar coupling as they appear in the theory of CoIns:

$$f_{kl}^{(i)}(\mathbf{q}) = \langle \phi_k(\mathbf{q})|\nabla_i|\phi_l(\mathbf{q})\rangle_{\mathbf{r}} \tag{4.13}$$

$$h_{kl}^{(i)}(\mathbf{q}) = \langle \phi_k(\mathbf{q})|\nabla_i^2|\phi_l(\mathbf{q})\rangle_{\mathbf{r}} \tag{4.14}$$

where $\langle \dots \rangle_{\mathbf{r}}$ indicates integration over electronic coordinates $\mathbf{r}$. No assumptions have been made on the bare electronic states. This result holds even if V_g and V_e undergo a crossing. In the following we discuss the relevant matrix elements of f and h in the dressed states basis and show how the cavity affects the non-adiabatic couplings. Inserting the definitions of the dressed states (Eqs. 4.4) into Eq. 4.13 yields the derivative coupling term between $|-, 0\rangle$ and $|+, 0\rangle$:

$$f_{-,+}^{(i)} = \frac{\Delta G_i}{4g}\left(1 - \frac{\delta_c^2}{4g^2 + \delta_c^2}\right) - \frac{\delta_c}{4g^2 + \delta_c^2}\nabla_i g \tag{4.15}$$

where $\Delta G_i = \nabla_i(V_e - V_g)$ is the gradient difference. The dressed state coupling has two contributions: The first term is governed by the gradient difference of the two bare state PESs whereas the second term depends on the gradient of the transition dipole moment through $\nabla_i g$. The latter vanishes in the Condon approximation but may be substantial in regions where the transition dipole varies rapidly with the q_i. Note that Eq. (4.15) does not contain any coupling terms involving the bare state crossings ($f_{g,e}^{(i)}$) since terms containing these couplings vanish due to the orthogonality of the photon states. This is in contrast to the couplings between the ground and the dressed states which solely contain the bare state derivative couplings but no contribution from the cavity:

$$f_{g,+}^{(i)} = f_{g,e}^{(i)} \cos\theta \tag{4.16}$$

$$f_{g,-}^{(i)} = -f_{g,e}^{(i)} \sin\theta \tag{4.17}$$

These terms may be safely neglected when the bare state energies are well separated. Note that all diagonal matrix elements of f vanish ($f_{kk} = 0$).

To evaluate the scalar coupling terms h of the second derivatives we introduce the following decomposition, which breaks down the equations and simplifies the results.

$$h_{kl}^{(i)} = \nabla_i f_{kl}^{(i)} - F_{k,l}^{(i)} \tag{4.18}$$

The second term $F_{k,l}^{(i)} = \langle \partial_{q_i}\phi_k | \partial_{q_i}\phi_l \rangle$ now also contains diagonal contributions:

$$F_{+,+}^{(i)} = F_{g,g}^{(i)} \sin^2\theta + F_{e,e}^{(i)} \cos^2\theta + \frac{\Lambda_i^2}{4} + \frac{\delta_c^2 \Lambda_i^2}{16 g^2} \tag{4.19}$$

$$F_{-,-}^{(i)} = F_{g,g}^{(i)} \cos^2\theta + F_{e,e}^{(i)} \sin^2\theta + \frac{\Lambda_i^2}{4} + \frac{\delta_c^2 \Lambda_i^2}{16 g^2} \tag{4.20}$$

$$F_{-,+}^{(i)} = \sin\theta\cos\theta \left(F_{g,g}^{(i)} - F_{e,e}^{(i)}\right) \tag{4.21}$$

$$F_{g,+}^{(i)} = F_{g,e}^{(i)} \cos\theta + \frac{\Lambda_i f_{ge}^{(i)}}{4\cos\theta} \tag{4.22}$$

$$F_{g,-}^{(i)} = -F_{g,e}^{(i)} \sin\theta + \frac{\Lambda_i f_{ge}^{(i)}}{4\sin\theta} \tag{4.23}$$

with

$$\Lambda_i = \frac{\delta_c}{\Omega^3}\left(4g\nabla_i g + \delta_c \Delta G_i\right) - \frac{\Delta G_i}{\Omega}. \tag{4.24}$$

Together, $f_{kl}^{(i)}$ and $F_{kl}^{(i)}$ contain all possible couplings: intrinsic non-adiabatic couplings of the bare states and cavity induced non-adiabatic couplings. The Hamiltonian (Eq. (4.38)) thus describes the dynamics in the most general case. The only approximation made is the

RWA and the condition that the system can not access higher photon states during the time evolution (this is consistent with the RWA and a linear pumping process initially exciting the system).

The non-adiabatic couplings may be further simplified in specific parameter regimes. Assuming that the bare states are well separated in energy and do not undergo any curve crossings, all terms $f^{(i)}_{g,e}$, $F^{(i)}_{g,g}$, $F^{(i)}_{e,e}$, and $F^{(i)}_{g,e}$ may be neglected. The $F^{(i)}_{g,e}$ terms are usually neglected in molecular dynamics simulations and quantum dynamics of the bare states. Note that $F_{-,+}$ does not contain any contribution from the cavity. $F^{(i)}_{\pm,\pm}$ vanishes for small gradient differences and in the Condon approximation and may also be neglected in most cases, since they only make a minor contribution to the shape of the PESs. Dropping all F terms leads to the approximate Hamiltonian:

$$\hat{H}_{kl} = \delta_{kl}\left(\hat{T} + \hat{V}_l\right) + \sum_i \frac{1}{2m_i}\left(2f^{(i)}_{kl}\nabla_i + \nabla_i f^{(i)}_{kl}\right) \tag{4.25}$$

The hermitian Hamilton (Eq. (4.25)) will be used in the following to calculate the wave packet dynamics. Hamiltonians with this structure are commonly used to simulate the dynamics in the vicinity of CoIns [167] by numerical propagation of the wavefunction. This is done by using a grid in the nuclear coordinates, rather than expanding in nuclear eigenstates which scales unfavorably with the number of nuclear modes.

Operators which represent molecular properties can be expressed in the bare state basis by transforming them into the dressed state basis using Eqs. 4.4 to 4.6. The transition dipole moments then read:

$$\langle +,0|\hat{\mu}|g,0\rangle = \cos\theta\mu_{eg} \tag{4.26}$$

$$\langle -,0|\hat{\mu}|g,0\rangle = -\sin\theta\mu_{eg} \tag{4.27}$$

$$\langle +,0|\hat{\mu}|-,0\rangle = \cos\theta\sin\theta\left(\mu_{ee} - \mu_{gg}\right)\ , \tag{4.28}$$

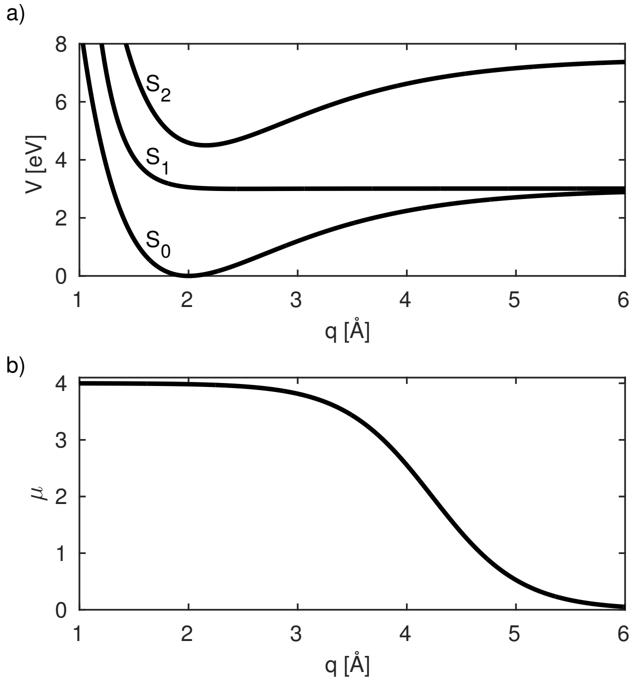

Figure 4.2: (a) Bare state PESs used for the photonic catalyst model as well as the photonic bound state model. The minimum of the S_2 state is displaced by 0.3 Å with respect to the ground state. (b) Transition dipole curve used in the different models. The parameters for the model are given in Appendix B.3.

where μ_{eg} is the bare state electronic transition dipole moment and μ_{gg} and μ_{ee} are dipole moments of the ground and excited state respectively.

4.1.1 Photochemistry in the Strong-Coupling Regime

In this section, we present calculations on two simple model systems with a single active nuclear coordinate q to illustrate the basic possibilities opened up by cavity coupling and the corresponding effects on the non-adiabatic couplings. The level structure of the dressed states creates new pathways for the nuclear dynamics and new transitions for spectroscopic measurements. Our goal is to use the influence of the cavity to modify the reactivity of a molecule. Photodissociation in the dressed state basis can then be enhanced or suppressed.

In the first model (Fig. 4.2(a)), we assume that a bound state S_2 is accessible by a dipole

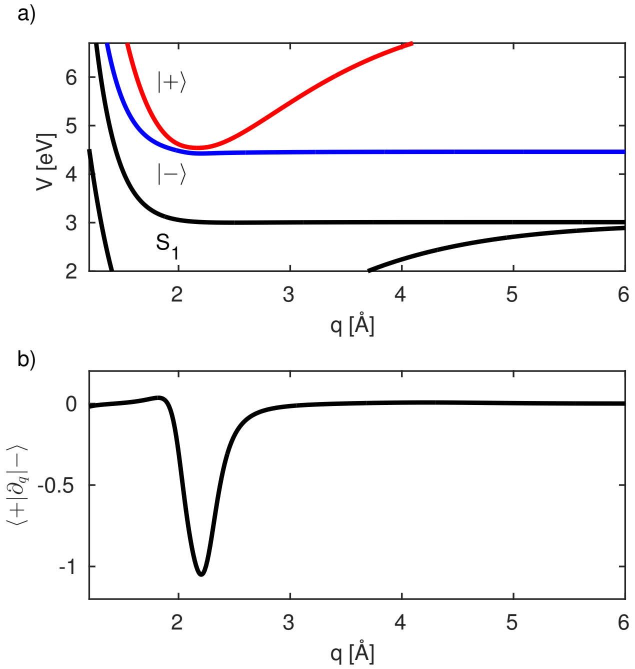

Figure 4.3: (a) Dressed state PESs for the photonic-catalyst model. The S_2 state is now coupled to the dissociative state. (b) Non-adiabatic coupling matrix element for the polariton states. Dominated by the gradient difference term of Eq. 4.15. Parameters: $g = 54\,\text{meV}$

transition from the ground state S_0. The dissociative state S_1 does not have a transition dipole moment with the ground state, but is accessible from S_2. The cavity couples the states S_2 and S_1 through the transition dipole moment shown in Fig. 4.2(b). The cavity mode frequency ω_c is set be in resonance at the minimum of S_2 (1.45 eV) and with a maximum cavity coupling of $g = 54\,\text{meV}$. The states $|g\rangle \equiv \text{S}_1$ and $|e\rangle \equiv \text{S}_2$ are used along with Eq. 4.10 to form the dressed states, shown in Fig. 4.3(a). The resulting dressed states $|\text{S}_1\rangle$, $|-\rangle$, and $|+\rangle$ undergo an avoided crossing close to resonance, while their shape remains similar to the bare states. The corresponding non-adiabatic coupling matrix element $f_{+,-}$ (Eq. 4.13), which is responsible for the transition between the dressed states, is shown in Fig. 4.3(b). The initially dark state S_1 now becomes radiatively accessible from S_0 through the non-adiabatic couplings via the S_2 state. It is evident that the dressed states are coupled to each other in the region where the bare states are close to resonance with the cavity mode. The upper dressed state, whose shape still resembles the shape of the S_2 state, is thus not

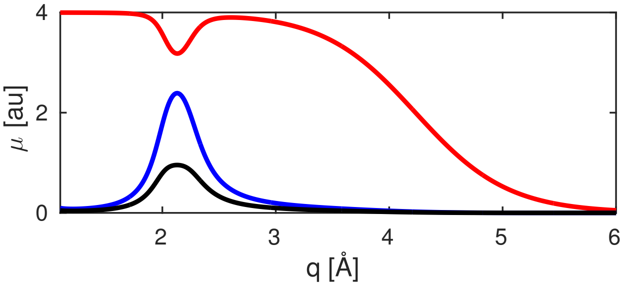

Figure 4.4: Transition dipole moments in the dressed state basis for the photonic-catalyst model: μ_{g+} (red), μ_{g-} (blue),μ_{-+} (black).

stable anymore and the molecule can dissociate through the non-adiabatic coupling to the unbound lower dressed state.

Figure 4.4 displays the relevant transformed transition dipole moments calculated from Eqs. (4.26)-(4.28). All curves show a dip around 2.2 Å where the non-adiabatic coupling, and thus the mixing between the molecular states and the photon states, is strongest. The transition dipole between the dressed states vanishes if the cavity coupling vanishes. The coupling to the cavity creates a new transition and modified dynamics, which can be probed with various time-resolved spectroscopies.

The excited state evolution was simulated by wave packet dynamics on a spatial grid (for details see appendix B.3). Figure 4.5(a) depicts the dynamics after impulsive excitation from the ground state (S_0) to the dressed excited states $|\pm\rangle$. The initial population pattern is caused by the mixing of the transition dipole moments, followed by a rapid decay of the upper dressed state facilitated by the dissociative/unbound character of the lower dressed state. The oscillation pattern is caused by the wavepacket oscillation in the $|+\rangle$ state passing through the coupling region. Figure 4.5(b) shows the transient absorption signal (see Appendix A.2) probing the system via the $|g\rangle$ state. The signal shows a clear decay of stimulated emission modulated by the wave packet motion in the $|+\rangle$ state.

In the second model, we reverse the roles of bound and unbound states to create a situation where a purely dissociative state can be stabilized *via* cavity-induced coupling to a bound

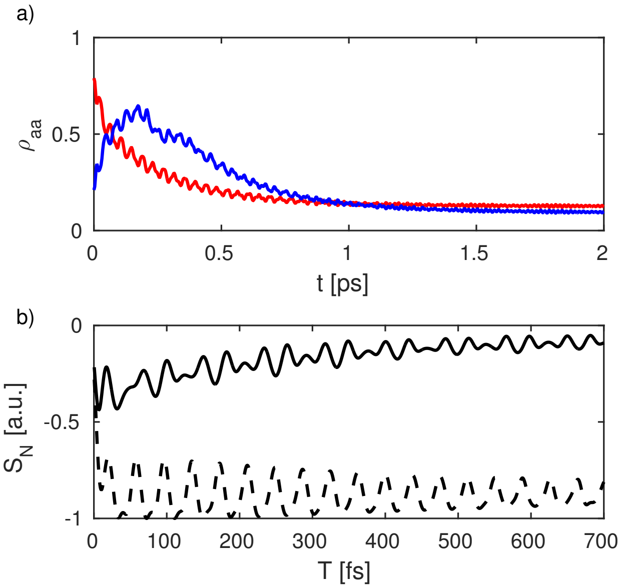

Figure 4.5: (a) Populations of the dressed states $|+\rangle$ (red) and $|-\rangle$ (blue) in the photonic catalyst model *vs.* time. The decay of the $|+\rangle$ state can be fitted to a bi-exponential model yielding the time constants 228 fs and 42 ps. (b) Transient absorption signal in depenence of the probe delay T and. The laser is set to be resonant between S_1 and the $|\pm\rangle$ state (1.5 eV) and has a pulse length of 10 fs (FWHM). The dashed line is the signal for a wave packet in the S_2 bare state potential.

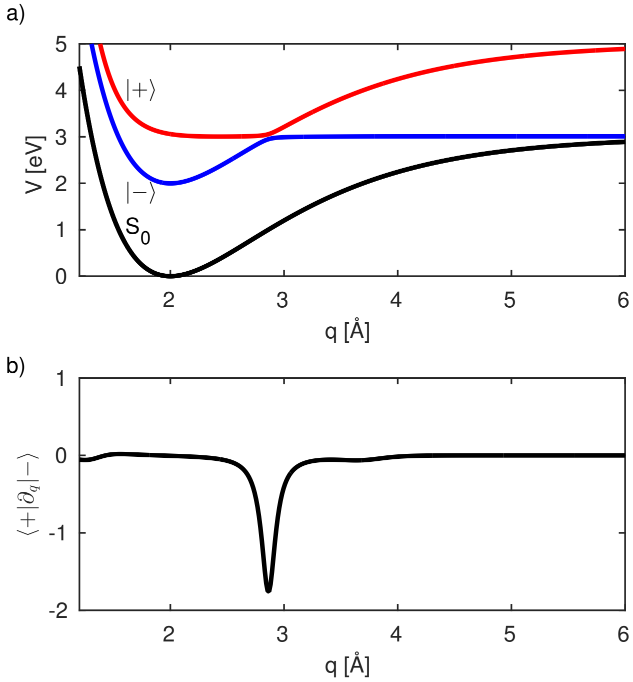

Figure 4.6: (a) Dressed state PESs for the photonic-bound-state model. (b) Non-adiabatic coupling matrix element causing transition between the dressed states.

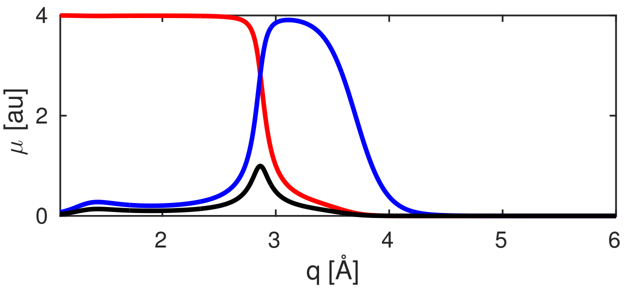

Figure 4.7: Tranistion dipole moments for the photonic-bound-state model in the dressed state basis: μ_{g+} (red), μ_{g-} (blue), μ_{-+} (black).

state. We use the model from Fig. 4.2(a) but consider only states S_0 and S_1. An excitation from S_0 to S_1 causes immediate dissociation of the molecule in the bare state model. Setting the cavity mode on resonance with S_0 and S_1 at $\approx 2\,\mathrm{eV}$ creates a set of dressed states, which experience an avoided crossing at 2.9 Å (Fig. 4.6(a)) with a non-adiabatic coupling matrix element (Fig. 4.6(b)) peaking at the crossing. The lower dressed state resembles the ground state around the Franck-Condon point and forms a bound state potential. The upper dressed state now also appears as a partially-bound potential, which is coupled to the dissociative curve by the avoided crossing.

The transition dipole moments are shown in Fig. 4.7. Due to the large detuning δ_c in the Franck-Condon region, the lower dressed state has a weak transition dipole moment with respect to the S_0 state. The state character change at the crossing at 2.9 Å manifests itself in the rapid change of the transition dipole moments (the crossing of the red and blue curve in Fig. 4.7.).

The population dynamics after excitation is shown in Fig. 4.8(a)). The clear distribution of the dipole moments between ground state and the dressed states (Fig. 4.7) leads to a population in the upper dressed state upon impulsive excitation. The quasi-bound character of the upper dressed state becomes clear from Fig. 4.8(a)): Instead of immediately dissociating, the wavepacket in the upper dressed state acquires a significant lifetime. The population of $|+\rangle$ leaks into $|-\rangle$ on a picosecond time scale. The corresponding transient absorption signal

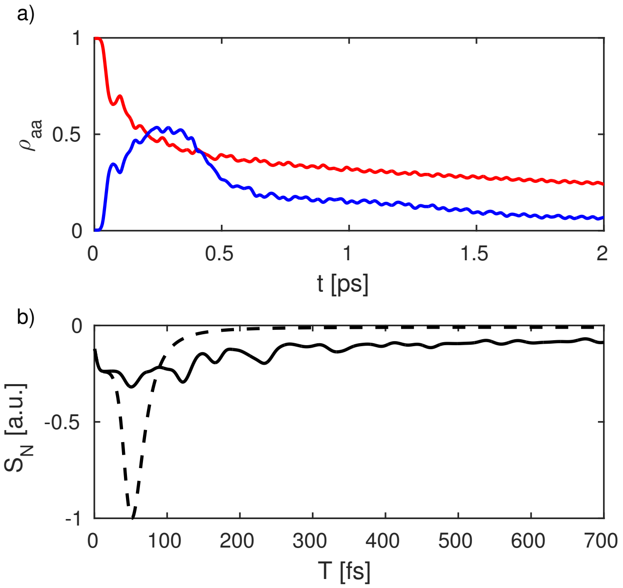

Figure 4.8: (a) Population of the dressed states $|+\rangle$ (red) and $|-\rangle$ (blue) in the photonic-bound-state model *vs.* time. The decay of the $|+\rangle$ state can be fitted to a bi-exponential model yielding the time constants 234 fs and 5.2 ps. (b) Transient absorption signal. Laser is set to be resonant between S_1 and the $|\pm\rangle$ state (1.5 eV) and has a pulse length of 10 fs (FWHM). The dashed line is the signal for a wave packet in the S_1 bare state potential

is shown in Fig. 4.8(b)) along with the signal for the bare state system (dashed curve).

In the two models described above, we have demonstrated the non-adiabatic couplings induced by the cavity in terms avoided curve crossings, which stem from the fact that a non-vanishing dipole in the coupling region creates a splitting between the dressed states (see Eq. (4.8)). By choosing a point of vanishing transition dipole moments, one can in principle also create a crossing, which exhibits a degeneracy between the dressed states. This is the basic requirement to obtain a CoIn, i.e., the coupling between the adiabatic electronic states has to vanish at the intersection point [103]. Setting the cavity on resonance at a nuclear configuration where the transition dipole moments vanishes yields a degenerate point in the dressed state basis. This can be achieved by choosing an electronic transition which is dipole forbidden at a certain configuration of high symmetry and becomes allowed as the symmetry is lowered. This has recently been demonstrated for formaldehyde, for which the lowest-energy transition is dipole-forbidden in the planar equilibrium structure [139].

4.2 Molecule-Cavity Coupling Beyond the Rotating Wave Approximation

In this section, we present a solution to the quantum Rabi Hamiltonian (Eq. (4.1)) without invoking the RWA. Our approach is based on an adaptation of [169]. Taking matrix elements in the basis $\{|+\rangle \equiv \frac{1}{\sqrt{2}}(|g\rangle + |e\rangle), |-\rangle \equiv \frac{1}{\sqrt{2}}(|g\rangle - |e\rangle)\}$ and dividing through by the cavity frequency (re-defining the unit of energy to be ω_c) gives

$$H = \begin{pmatrix} \hat{a}^\dagger \hat{a} + \frac{\tilde{g}}{\omega_c}(\hat{a}^\dagger + \hat{a}) & \frac{-\omega_0}{2\omega_c} \\ \frac{-\omega_0}{2\omega_c} & \hat{a}^\dagger \hat{a} - \frac{\tilde{g}}{\omega_c}(\hat{a}^\dagger + \hat{a}) \end{pmatrix} \tag{4.29}$$

which is a special (zero-bias) case of the model studied by [169] with parameters $g = \frac{\tilde{g}}{\omega_c}$, $\Delta = \frac{\omega_0}{\omega_c}$ (in this section, we reserve the symbol g for this scaled coupling). This eigenvalue problem can be solved in a variety of ways. Numerical diagonalization using cavity-field Fock states is possible but, for high values of g, requires that many states be taken into account (up to 10^5 when $g \sim 1$ depending on convergence criteria [169]). Since our goal is to do non-BOA dynamics simulations, it is beneficial to use as few states as possible (this is particularly true for the calculation of the non-adiabatic couplings (NACs)). Using a Bargmann transformation and analyticity, Braak obtained a transcendental equation the roots of which yield the energies and this solution was later re-derived using extended coherent states [170, 166]. The eigenstates and energies had also been derived earlier using tunable coherent states [169]. Both of these representations have an advantage over the Fock-space representation in that they automatically include many-body correlations amongst infinitely-many photons in the cavity mode. This is particularly useful in the ultrastrong-coupling regime $g \sim 1$. Both of these representations have numerical difficulties when $g \ll 1$ but this regime is solvable within the RWA and can be smoothly connected provided we choose an appropriate separation point. More importantly, the former representation (extended coherent states) involves expressions that have periodic divergences, complicating numerical evaluation. For this reason, we choose to work in the basis of tunable, photon-added coherent states (i.e., the basis of photon-added coherent states with a tunable coherence parameter) and make the eigenstate ansatz

$$\begin{aligned} |\epsilon_l\rangle =& |+\rangle \otimes \sum_{n=0}^{M} c_{nl} (\hat{a}^\dagger)^n e^{\alpha_l \hat{a}^\dagger} |0\rangle + \pi_l |-\rangle \otimes \sum_{n=0}^{M} c_{nl} (-\hat{a}^\dagger)^n e^{-\alpha_l \hat{a}^\dagger} |0\rangle \\ =& \begin{pmatrix} \sum_{n=0}^{M} c_{nl} (\hat{a}^\dagger)^n e^{\alpha_l \hat{a}^\dagger} |0\rangle \\ \pi_l \sum_{n=0}^{M} c_{nl} (-\hat{a}^\dagger)^n e^{-\alpha_l \hat{a}^\dagger} |0\rangle \end{pmatrix} \end{aligned} \tag{4.30}$$

where the c_{nl} coefficients represent the l-th eigenstate in the basis of n-photon-added tunable coherent states, α_l is the tunable coherent state parameter corresponding to the l-th eigenvalue, and $\pi_l = \pm 1$ is the parity of the l-th eigenstate. Since the Hamiltonian conserves the parity, we can consider separately the even and odd parity manifolds and we write π_l explicitly rather than simply $\pm$ because we will later need to keep track of the two parities in matrix elements $\langle \epsilon_k | \hat{\mathcal{O}} | \epsilon_l \rangle$ succinctly. In order that the π_l not be functions of the nuclear coordinates, we do not simply order the eigenstates by energy but rather list first the even then the odd in ascending order of energy. In this ansatz, M is the truncation number. In practice, we must take M large enough to ensure convergence. This will be addressed in more detail later. Following the analysis of [169] and inserting this wavefunction into the Schrödinger equation yields a connection between the energy and α_l

$$\epsilon_l = \alpha_l g - \pi_l \frac{\Delta}{2} \tag{4.31}$$

and a recurrence relation for the coefficients

$$c_{n+1} = \frac{-c_0}{(n+1)g} \Big[(n + \pi_l \frac{\Delta}{2}) c_n + (\alpha_l + g) c_{n-1} - \pi_l (-1)^n \frac{\Delta}{2} \sum_{j=0}^{n} \frac{(2\alpha_l)^j}{j!} c_{n-j} \Big]. \tag{4.32}$$

Note that we have used $c_1 = 0$ (permitted since α_l can completely determine the 1-photon contribution to $|\epsilon_l\rangle$) and that c_0 remains an arbitrary constant that can be used to normalize the states. This normalization and its consequences are discussed in detail in Appendix D.3 but we will otherwise formally work with the normalized coefficients c_{nl}. Setting $c_{M+1} = 0$ (required for convergence) gives a degree M polynomial equation for α_l

$$\big(M + \pi_l \frac{\Delta}{2}\big)c_M + (\alpha_l + g)c_{M-1} - \pi_l(-1)^M \frac{\Delta}{2} \sum_{j=0}^{M} \frac{(2\alpha_l)^j}{j!} c_{M-j} = 0. \tag{4.33}$$

Chen et al. had examined this recurrence relation for various regimes of the parameters Δ and g and we now briefly summarize their findings. For $0.1 < g < 0.5$ and $0.5 < \Delta < 1.5$, $M = 60$ is sufficient to ensure convergence (in the sense of a relative difference of 10^{-8} or less on increasing M further) for the first 20 or more eigenstates and energies match those obtained via Fock-state diagonalization (at a much higher truncation order). Moreover, the coefficients are found to die down by around $n = 40$ for $\Delta = 1, g = .1$ and this improves to $n = 10$ for $\Delta = 1, g = 1$. This shows the strength of this representation for handling the ultrastrong-coupling regime. We discuss the parameters used and the truncation below. Given a pair g, Δ, we can solve Eq. (4.33) for the first N roots such that ϵ_N is sufficiently large to account for the system energetics. The details of this truncation will depend on the way in which the system is probed and the signal being examined.

It is worth repeating the findings of Braak regarding the distribution of the zeroes of his G-function (not shown here for brevity) and thus, the energies. The zeroes of $G^{\pm}(x)$ are distributed relatively regularly, with the property that the number of eigenenergies in the range $[n\omega_c, (n + 1)\omega_c]$ is restricted to be 0, 1, or 2. Additionally, two intervals each containing two eigenenergies will never be adjacent to each other (nor will two intervals each containing no eigenenergies). Since the G-function gives the exact energies as well, we are guaranteed that, for reasonably large ω_c, we will not have to include too many states $|\epsilon_l\rangle$ to obtain converged calculations. This is trivially true for weak coupling at resonance ($g \ll 1$, $\Delta = 1$)

but is good to confirm for all parameter regimes.

Besides the energies, we also need the non-adiabatic couplings $f_{kli}(\mathbf{q})$, and $h_{kli}(\mathbf{q})$. Computing these quantities is tedious but it is fairly straightforward. We outline the, rather lengthy, derivation in Appendix D.2 and make frequent use of auxilliary quantities defined in Appendix D.1 to arrive at

$$f_{kli} = f_{egi}(\pi_l - \pi_k)B^{(1)}_{kl} + (1 + \pi_k\pi_l)\big[A^{(2)}_{kl} + A^{(3)}_{kl}\nabla_i\alpha_l\big] \tag{4.34}$$

for the first-derivative couplings and

$$\begin{aligned} h_{kli} =& \nabla_i f_{kli} - F_{kli} \\ F_{kli} =& \frac{F_{gg} + F_{ee}}{2}\delta_{kl} + \frac{F_{gg} - F_{ee}}{2}(\pi_l + \pi_k)B^{(1)}_{kl} + F'_{eg}(1 - \pi_k\pi_l)A^{(1)}_{kl} \\ &+ \Big[\big\{f_{egi}(\pi_k - \pi_l)\big[B^{(2)}_{kl} - B^{(3)}_{kl}\nabla_i\alpha_l\big]\big\} + k \leftrightarrow l\Big] \\ &+ (1 + \pi_k\pi_l)\Big(A^{(4)}_{kl}\nabla_i\alpha_k + A^{(4)}_{lk}\nabla_i\alpha_l + A^{(5)}_{kl}\nabla_i\alpha_k\nabla_i\alpha_l + A^{(6)}_{kl}\Big) \end{aligned} \tag{4.35}$$

for the second (we have suppressed the explicit $\mathbf{q}$-dependence for brevity).

4.2.1 Application to Avoided Crossing in Sodium Iodide

The influence of ultrastrong cavity coupling is demonstrated on the nonadiabatic dynamics of photoexcited sodium iodide, a well known example for femtochemistry [171]. The adiabatic electronic states of the bare sodium iodide experience an avoided crossing near $q \sim 8\,\text{Å}$(Fig. 4.9 (a)), leading to dissociation into the neutral products through the ^{1}X state upon photoexcitation. The bare nonadiabatic coupling matrix element f_{eg} is shown in Fig. 4.9 (b). The branching ratio, i.e., the amount of population transferred to the ^{1}X state, is determined by the acquired momentum of the wavepacket, which depends on the excitation

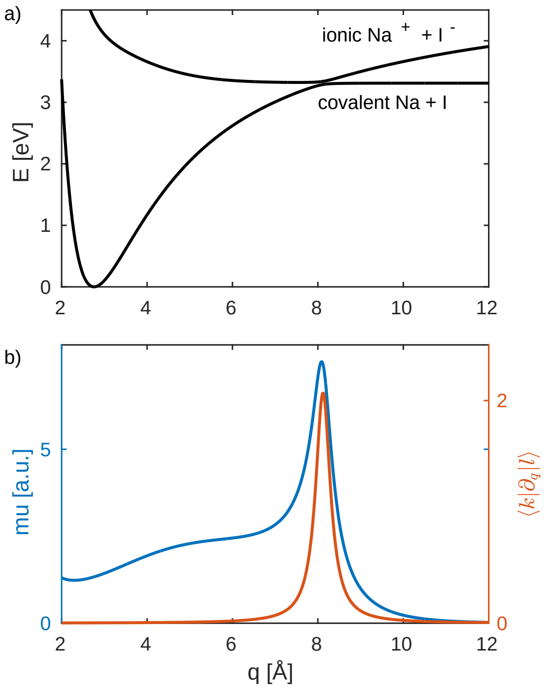

Figure 4.9: (a) Bare ground (^{1}X) and excited (^{1}A) electronic potential energy surfaces of NaI. Dissociation on the ^{1}X potential leads to the neutral reaction products. (b) Transition dipole moment μ_{eg} (blue) and the derivative coupling matrix element f_{eg} (red).

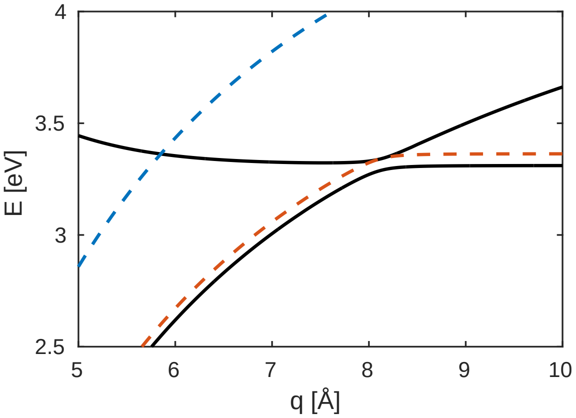

Figure 4.10: Potential curve crossings for two different cavity detunings: ground state potential wave function shifted by the cavity frequency ($V_g + \omega_c$), for $\omega_c = 815\,\text{meV}$ (blue, dashed) and $\omega_c = 52.6\,\text{meV}$ (red, dashed).

laser frequency. We will investigate two scenarios: the cavity is set in resonance at ≈ 6 Å(case 1), i.e., before the wave packet in the A state reaches the bare avoided crossing, ($\omega_c = 815$ meV) and a low frequency cavity ($\omega_c = 52.6$ meV) resonant directly at the crossing (case 2). Both cases are illustrated in Fig. 4.10 by plotting the ^{1}X-state curve shifted by the photon energy of the cavity.

For case 1, Eq. (4.30) is used to calculate the resulting potential energy curves in the basis of the photon-added, tunable coherent states. Figure 4.11 shows the lowest ten potential energy curves for four values of the couping strength g. For small g, the result converges to curves which coincide with a molecular Jaynes-Cummings model as described in section 4.1 (Fig. 4.11(a)) [139]. New avoided crossings are created in the region at 6 Å, where the cavity mode is in resonance with the bare electronic states ($\Delta = 1$). New crossings are also created at higher-order resonances $\Delta = n$ between states of the same- (n odd) and opposite-parity (n even) states. As the coupling strength increases, the splitting between dressed states at the resonances points increases but much faster for lower-photon resonances. The splitting thus seems to depend inversly on n and directly on the absolute energy of the two states in question (with larger gaps for higher-energy pairs). Another notable feature is a ground-state modification [172, 59] which becomes clearly visible with increasing coupling

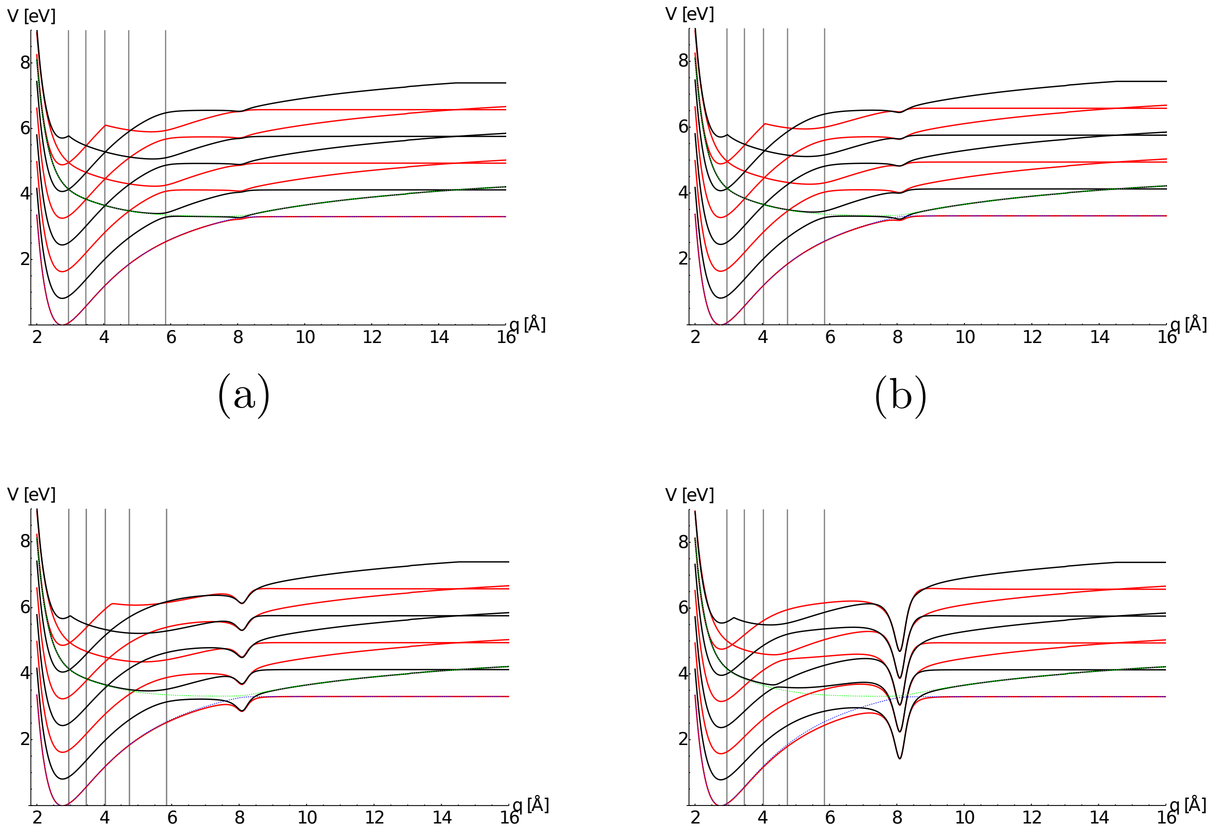

(a) (b)

(c) (d)

Figure 4.11: Positive (red solid) and negative (black solid) parity electronic potential energy surfaces of NaI dressed with a ω_c = 815 meV cavity mode obtained from Eq. (4.31) and the first five solutions to Eq. (4.33) with $\pi_l = +1$ and $\pi_l = -1$ respectively. Vertical gray lines indicate points where the bare states are resonant with integer multiples of the cavity frequency ($\omega_0 = n\omega_c$ for n an integer, $n = 1$ for the rightmost line and counts up going to the left). (a) Peak coupling of 200 meV. (b) Peak coupling of 300 meV. (c) Peak coupling of 600 meV. (d) Peak coupling of 1240 meV.

(Fig. 4.11). This dip is a clear signature of the ultrastrong-coupling regime.

Figure 4.12(a) shows the NACs (evaluated from Eq. (4.34)) between the lowest positive-parity state (black) and the first 4 negative-parity states (energy surfaces in the upper panel and NACs in the lower panel). Figure 4.12(b) shows the same but with the second-lowest positive-parity state). From this figure, it is clear that the NACs in the region of the original avoided crossing are strengthened relative to their bare values (Fig. 4.9 lower panel). Moreover, the coupling strength remains of the same order even for states separated by a large distance in energy. Figure 4.13(a) shows the NACs between 3 pairs of opposite-parity states. Note that no NAC is induced in the region of crossing between such pairs (only the coupling in the region of the original avoided crossing remains). We can see that crossings between states of opposite parity do not generate any NACs. In contrast, the avoided crossings between states of the same parity correspond to peaks in the NAC curves. For a given resonance point (e.g., $\omega_0 = 3\omega_c$), these peaks become smaller as one considers dressed states of higher energy (corresponding to larger separations at the avoided crossings). Finally, we note that these NAC curves do not cover the entire range of q due to convergence problems. This makes the NAC curves useful for a qualitative understanding of dynamics but more effort would be needed to make them quantitatively useful. We next discuss a simulation protocol that solves this problem by avoiding the explicit calculation of electronic eigenvalues or NACs.

4.2.2 Wavepacket Simulations and the Field Quadrature

In the previous section, we outlined a method for obtaining the dressed-state eigenvalues and NACs and the difficulty of obtaining converged results for the latter was discussed. To overcome this difficulty, we employ an efficient computational scheme obtained by the direct treatment of the cavity mode as a quantum harmonic oscillator in quadrature space. We first express the annihilation and creation operators of the cavity mode in terms of their

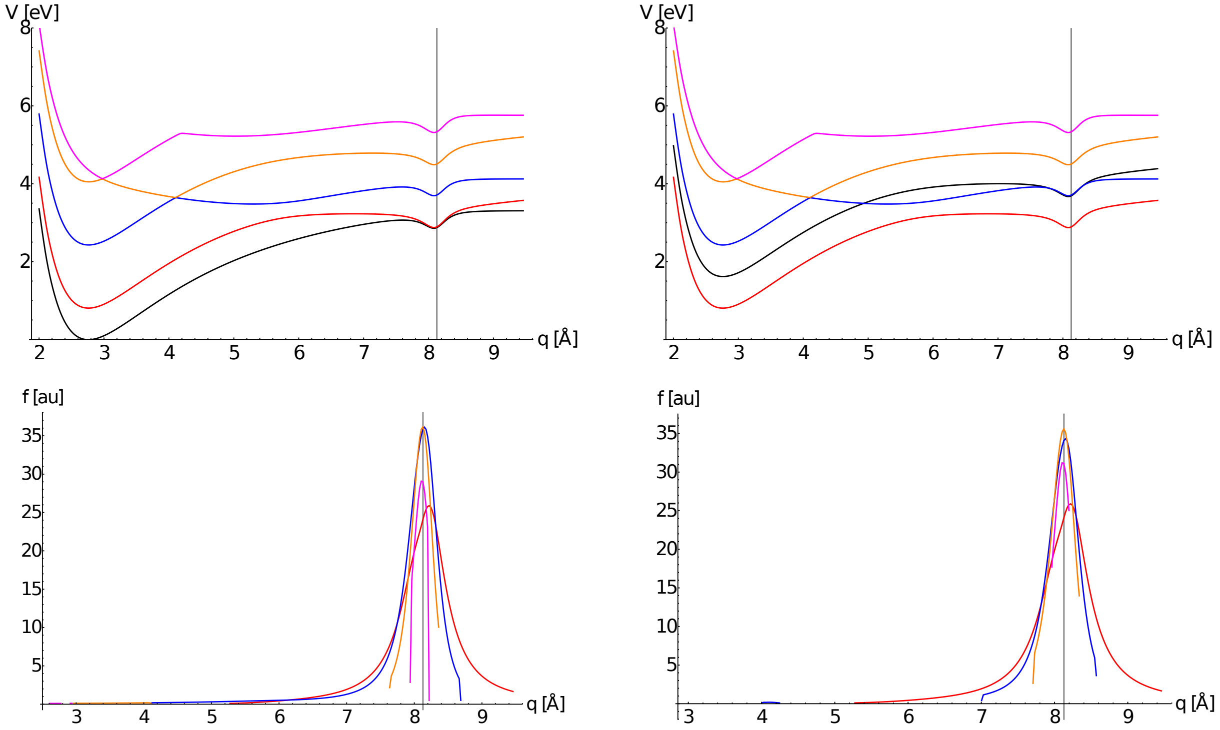

(a) (b)

Figure 4.12: (a): Potential curves for the lowest energy positive-parity eigenstate (black) and the 4 lowest energy negative-parity eigenstates (upper) and their corresponding NACs (all couplings are betwen the "black" state and one of the others and therefore labeled by the color of the latter state). (b): Potential curves for the second-lowest positive-parity state (black) and the 4 lowest energy negative-parity eigenstates (upper) and their corresponding NACs.

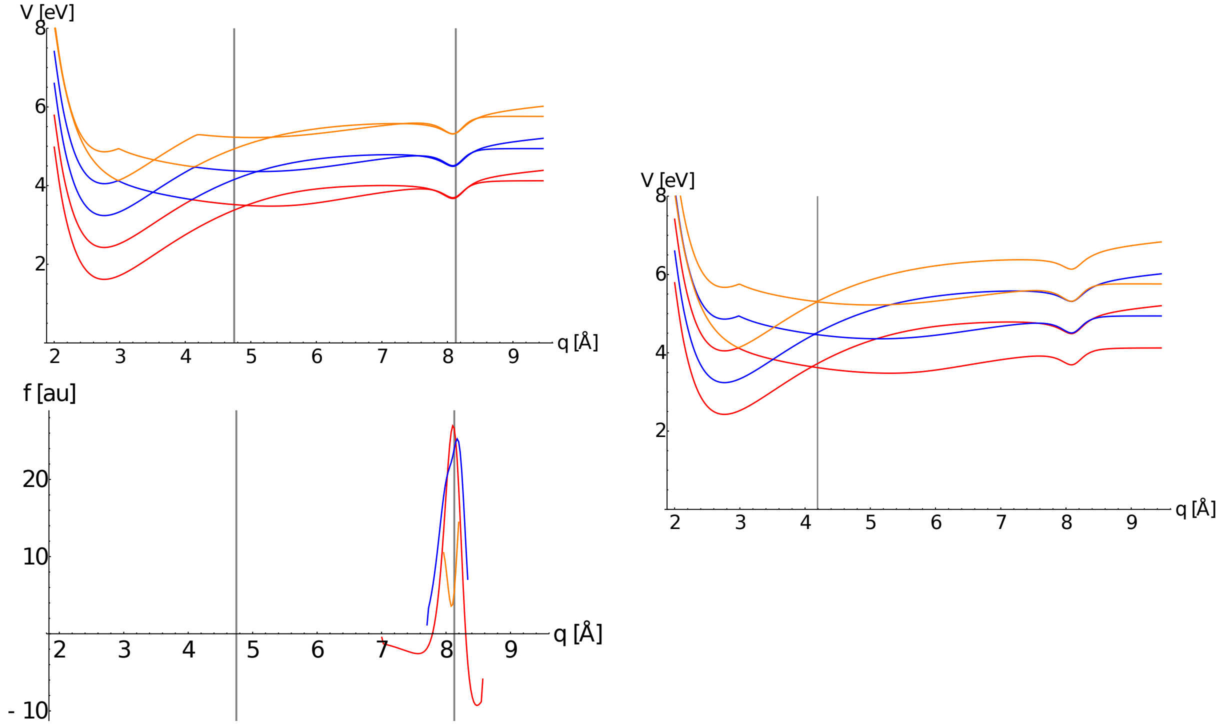

(a)

(b)

Figure 4.13: (a): Potential curves (upper) and corresponding NACs (lower) for 3 different pairs of opposite-parity eigenstates. (b): Potential curves for 3 different pairs of same-parity eigenstates. Corresponding NACs are sharply peaked at the avoided crossings near the gray line and are otherwise negligible.

quadrature coordinates x and p [159]:

$$a = \sqrt{\frac{\omega_c}{2}} \left(\hat{x} + \frac{i}{\omega_c} \hat{p} \right) , \tag{4.36}$$

with $\hat{p} = i\frac{\partial}{\partial x}$. The extension of the Hamiltonian to the molecular case is now straightforward: The nuclear degrees of freedom $\mathbf{q}$ are accounted for by treating ω_0 and g as functions of $\mathbf{q}$ The coupled light-molecule Hamiltonian Eq. (4.1) then reads:

$$H_{ec} = \frac{\omega_0(q)}{2} \left(2\hat{\sigma}^\dagger \hat{\sigma} - 1\right) - \frac{1}{2}\frac{\partial^2}{\partial x^2} + \frac{1}{2}\omega_c^2 \hat{x}^2 + g(q)\sqrt{2\omega_c}\hat{x} \left(\hat{\sigma}^\dagger + \hat{\sigma}\right) \tag{4.37}$$

and the matrix elements of the cavity-molecule Hamiltonian in the basis of the bare adiabatic states are then

$$H_{kl} = \delta_{kl} \left(\hat{T} + \hat{V}_k - \frac{1}{2}\frac{\partial^2}{\partial x^2} + \frac{1}{2}\omega_c^2 \hat{x}^2 \right) + (1 - \delta_{kl})\, g\sqrt{2\omega_c}\hat{x} \tag{4.38}$$

Here, the indices k and l run over the bare electronic states g and e since we avoid calculation of the joint cavity-electronic Hamiltonian (Eq. (4.1). The coordinate x is expanded in a numerical grid, putting the nuclear coordinates and the cavity mode on an equal footing in a numerical simulation. The time stepping was done with a Chebychev propagation scheme [173]. The potential energy curves NaI, as well as the non-adiabatic coupling matrix element and the transition dipole moment has been calculated with the program package MOLPRO [174] at the MRCI/CAS(6/7)/aug-cc-VQZ level of theory with an effective core potential for Iodine (ECP46MWB). The second derivative with respect to x can be conveniently calculated by a discrete Fourier transform [175], just as with the nuclear kinetic energy. For a diatomic molecule, this results in 2-dimensional potential energy surfaces for the electronic ground and excited state, each depending on q and x.

The effect of ultra strong cavity coupling on nonadiabatic dynamics is demonstrated on the excited state dynamics of sodium iodide, which has been an important landmark in femtochemistry [171]. The adiabatic electronic states of the bare sodium iodide experience an avoided crossing near $q \sim 8\,\text{Å}$(Fig. 4.9 (a)), which leads to dissociation into the neutral products through the ^{1}X state. Upon photo-excitation, a nuclear wave packet is launched in the ^{1}A state and then oscillates back and forth [108]. Part of the wave packet couples to the ^{1}X state via the avoided crossing into the covalent dissociation channel.

The amount of population in the dissociative part of the ^{1}X state after the wavepacket has reached the crossing point for the first time ($\approx 480\,\text{fs}$) serves as an indicator of the effect on the dynamics. Figure 4.14(a) depicts the population in the covalent channel for varying coupling strengths. While an intermediate coupling strength ($g < 0.3$) can increase the dissociation probability, the transfer to the ^{1}X state is suppressed for larger values of g. This behavior can be explained by the increased splitting between the dressed states: for larger splittings, the state which corresponds to the ^{1}A state is well-separated from the lower-lying state, effectively suppressing the population transfer [139, 59]. The dynamics is mainly influenced by two modifications of the potential energy surfaces: the new avoided crossings created by the cavity and the modified avoided crossing already present in the bare molecule. With increasing cavity coupling, the cavity-created crossing at the 1-photon resonance point generates well-separated states such that a nuclear wavepacket is trapped and a much smaller fraction even reaches the original crossing. This partially coincides with the effect described by Galego *et al.* [59] that for higher coupling strengths the states become well-separated and the Born-Oppenheimer approximation is valid again.

An alternative view is provided by the time evolution of the population of the ^{1}X state (Fig. 4.15). Zewail had measured a stepwise increase in the covalent state population of $\approx 11\%$ at each passage through the avoided crossing [108]. for moderate coupling strength, The time traces are still similar to the uncoupled case but already show the influence of the cavity coupling (Fig. 4.15(b)). With increasing coupling strength, the dissociation is suppressed and the oscillation period increases with the wavepacket becoming trapped in a

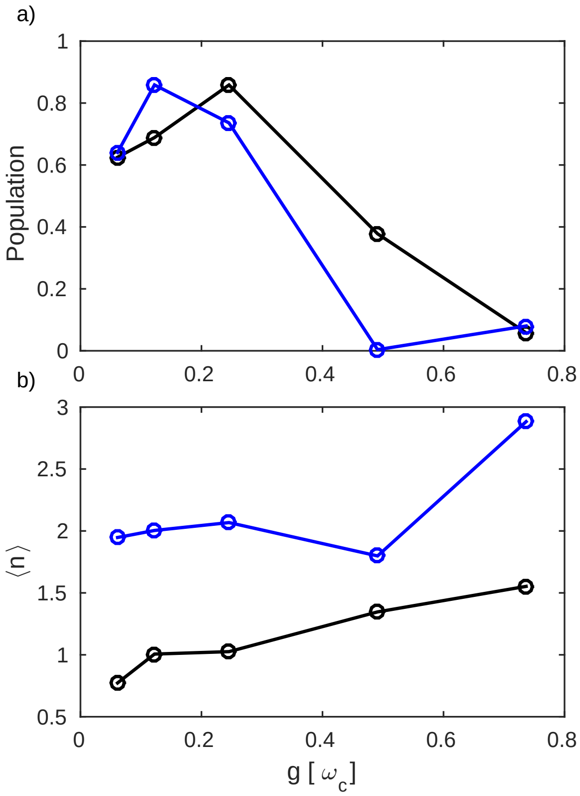

Figure 4.14: Cavity coupling with $\omega_c = 815\,\text{meV}$. (a) Population of the covalent states after 480 fs for a cavity with initially zero photons (black) and one photons (blue) *vs.* the coupling strength. (b) Average photon number 480 fs.

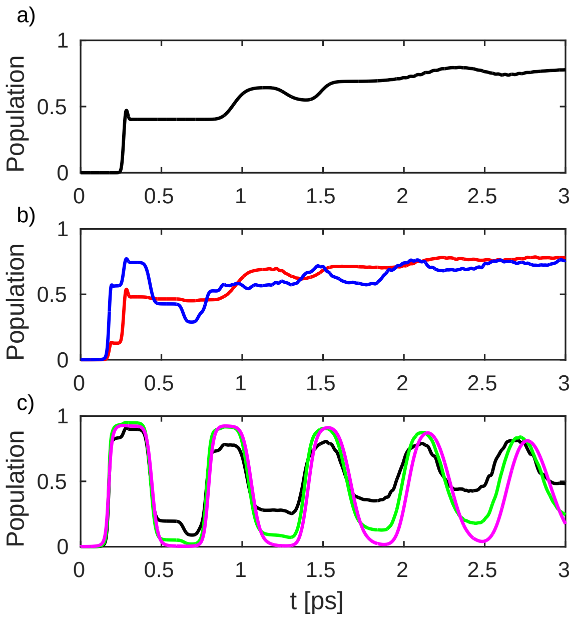

Figure 4.15: Selected time traces of the ^{1}X state population ($\omega_c = 815\,\mathrm{meV}$). No cavity (black line), $g = (0.0502, 0.1256, 0.1884, 0.2512, 0.3793)$ red, blue, black, green, magenta respectively.

tighter effective potential and its recurrence time becoming shorter. Additionally, both the NAC and the shape of the potential surface at the bare state avoided crossing is affected by the counter-rotating terms, creating a barrier for the nuclear wavepacket from which it reflects and allowing for further suppression of population transfer into the ^{1}X dissociation channel. The dissociation is strongly suppressed for large coupling strengths. The average photon number shown in Fig. 4.14 is a clear indicator that the system can not be represented by only two Fock states, but requires the present approach.

4.3 Discussion

Molecular cavity QED offers many exciting possibilities from enhanced probing techniques [152, 153, 154, 57, 155, 138] to molecular cooling [150] and cavity-modified photochemistry [157, 139]. The underlying quantum Rabi model Hamiltonian, is well-studied in the atomic context and has been solved in a number of ways [53, 163, 160, 161, 162, 165, 176, 169, 170, 166]. In this chapter, we extended these treatments to the case of a molecular Hamiltonian with electronic parameters dependent on the nuclear configuration. We considered both the strong-coupling regime (section 4.1), in which a perturbative treatment is insufficient but the RWA applies, and the ultrastrong-coupling regime (4.2), in which the RWA is violated. Besides requiring small coupling strength relative to the cavity frequency $g/\omega_c \ll 1$, the validity of the RWA depends on the negligibility of the counter-rotating terms relative to the rotating $(\omega_0 + \omega_c)^{-1} \ll (\omega_0 - \omega_c)^{-1}$. This latter condition is clearly violated when the bare states possess an avoided crossing or a CoIn. In this way, the ultrastrong regime is achievable despite difficulties due to technical limitations of the nano-structures, such as the achievable size of the mode volume, and the applicable field strength, which is limited by the ionization potential of the molecule.

In both the strong- and ultrastrong-coupling regimes, we derive transformation formulas for electronic operators as well as expressions for the non-adiabatic coupling due to the nuclear kinetic-energy operator. Combined with the eigenstates, this is all information necessary to carry-out and interpret dynamical simulations. The formalism is expressed in terms of well-known derivative couplings and is thus suitable for various simulations protocols such as full quantum propagation and semi-classical methods, e.g., surface hopping [177] or *ab initio* multiple spawning [178]. The quantities required to express the molecular system in terms of dressed states, i.e., the potential energy surfaces and transition dipole moments can be directly obtained from state of the art quantum chemistry methods. By reducing the problem to familiar adiabatic energy surfaces and corresponding NACs, the dynamics can be understood even in non-intuitive parameter regimes. In particular, in the ultrastrong regime, such as when a molecule possesing a CoIn or avoided crossing is dressed with an ultrastrong cavity field, the potential surfaces and NACs can be strongly modified (the Bloch-Siegert shift) from their bare or Jaynes-Cummings (RWA) shape.

The effective mode volume used for the sodium iodide simulations range from $0.002\lambda_c^3$ to for $0.04\lambda_c^3$ for couplings presented in Fig. 4.14 under the assumption that $\approx 10^5$ particles contribute collectively [179]. Nano-cavities [49, 180], nano-plasmon antennas [50], or nano-guides [51] may provide a solution for the realization of such small effective mode volumes. Additionally, the collective enhancement effects can be leveraged to reach the ultrastrong coupling regime. In molecular systems however, these effects are subject to vibrational dephasing. The collective chemistry in a cavity is a many body effect, which needs further investigation. Its theoretical treatment is more challenging since all particles are coupled and the dimensionality increase with the number of particles. Finally the superradiant regime [181] might be used to engineer the reactivity of molecules in a novel way, though we do not discuss this here.

In section 4.1.1, we demonstrated some basic possibilities for the manipulation of the excited state photochemistry. For photo-dissociation model systems, the lifetime can potentially be significantly influenced by the cavity coupling. Cavity-induced NACs between the dressed states can be used to funnel the nuclear wavepacket into a bound potential to increase the lifetime or to a dissociative potential to decrease the lifetime. These examples were explored with a model system and the altered population dynamics was shown to be clearly visible in the linear absorption signal.

In section 4.2, we explore a pair of complementary solutions to handle the difficulties inherent in the ultrastrong-coupling regime. Since the counter-rotating terms do not conserve the excitation number, the Hamiltonian is no longer seperable into 2x2 blocks. Expansion in Fock states can then become impractical. In the first approach, we apply the solution to the quantum Rabi model in terms of tunable-coherent states provided by Chen *et al.* and calculate the dressed potential surfaces and NACs. Examining the potential energy surfaces for increasing g (Fig. 4.11) reveals the opening of a gap at the 1-photon resonance ($\Delta \sim 1$) and the creation of a dip in the potential surface at the original avoided crossing while the NACs (Fig. 4.12) connect all pairs of opposite-parity states, providing decay paths to lower-energy pairs. For a nuclear wavepacket prepared in the ^{1}A state, these effects combine to create oscillations in the electronic populations, suppressing the final dissosciation of the molecule. In the second approach (section 4.2.2), we treat the cavity mode on the same footing as the nuclear coordinates rather than bundling into the electronic eigenvalue problem. This is done by switching to a real-space picture (the field quadrature) and propagating a joint nuclear-cavity wavepacket on a multidimensional grid. This approach bypasses calculation of the potential surfaces or NACs.

The first approach therefore provides access to the familiar picture of nuclear wavepackets evolving on electronic potentials while the second approach avoids difficulties in obtaining precise quantitative results for the associated NACs. We demonstrate both methods on NaI. The avoided crossing of the bare states is the site of the strongest coupling and the large modifications to the potentials indicative of RWA violations are clearly shown (section 4.2). The consequences of these modifications for population transfer between bound and dissociative states are then shown (section 4.2.2, Fig. 4.15), with higher coupling causing population oscillations rather than dissociation. These oscillations eventually die-down to a nearly-even population.

Chapter 5

Conclusion

Spectroscopic signals are commonly simulated under the semiclassic approximation, with the matter treated quantum mechanically and the field treated classically. In this manuscript, we have presented an introduction to the many effects that are missed by this approximation and owe their origin to the quantum nature of the radiation field. We have limited our consideration to such effects as they manifest from vacuum or single-photon states and all laser fields were treated classically.

Chapter 2 discussed spontaneous emission and scattering as processes that populate a vacuum mode of the electromagnetic field, with the created photon being subsequently detected. Two fundamental signal definitions, the photon number change and the gated electric field intensity, were given. Derivations are simpler using the former definition but the latter is more realistic and provides a consistent account of the various detector resolutions (temporal, spectral, spatial, and directional). Within specified approximations, the two approaches were shown to lead to the same formula for off-resonant scattering under the minimal coupling interaction Hamiltonian, which describes, e.g., x-ray diffraction. Frequency-resolved, ultrafast x-ray scattering of excited-state electron dynamics in cysteine was discussed in section 2.2 and different electronic oscillations were scene to correlate with different spatial positions on the detector. This exciting technique could allow a complete diffraction pattern for every state in the electronic wavepacket, providing spatial information on the associated transition charge density.

Time-resolved x-ray scattering was then discussed in the context of tracking nuclear dynamics and the example of NaF was treated. This diatomic possesses an avoided crossing and electronic coherences are generated when a nuclear wavepacket traverses this region. Inelastic scattering events connecting states involved in these coherences then become possible. These types of inelastic scattering events are orders of magnitude stronger than direct absorptive inelasticities and, though still weak, are in principle detectible as oscilliatory features in the diffraction pattern. Single- and two-molecule terms in the scattering signal were identified and the differences in their calculation were explicated. The topic of excited-state elastic diffraction *via* heterodyne interference with the ground-state elastic signal was discussed and shown to be possible in systems with long-range, intermolecular order but not in the gas phase or for single-molecule samples.

Chapter 3 discussed heterodyne-detected stimulated emission. Vacuum fields of the electromagnetic field were shown to mediate a long-range interaction called cascading that permits the exchange of an induced polarization between two molecules. That is, the laser-induced polarization of one molecule serves as a source that interacts with another molecule, the final polarization of which produces the cascading contribution to the heterodyne-detected signal. Since this process involves only the creation of a photonic coherence and not a population (i.e., coherences $|1\rangle\langle 0|$ and $|0\rangle\langle 1|$ are created but not the population $|1\rangle\langle 1|$), it is directly proportional to the dipole-dipole coupling tensor rather than its square, as is the case for resonant energy transfer processes.

Cascading processes come with the same phase-matching and external field dependence as single-molecule nonlinear signals but their many-body nature makes them dominant in condensed samples. Historically, experimental observation of multidimensional Raman signals has been complicated by cascading contributions and early efforts at detecting $\chi^{(5)}$ Raman signals observed $\chi^{(3)}\chi^{(3)}$ cascades, mistakingly attributing the signals to direct single-molecule nonlinearities. Several techniques have since been developed to select against the cascading terms, most prominently based on a $\pi/2$ phase shift present in cascading signal from macroscopic samples. We explicated the geometric origin of this phase shift and connected the microscopic picture of cascading as photon exchange to the usual macroscopic understanding based on Maxwell's equations.

Chapter 4 discussed coupling of molecules to optical cavity modes. This chapter departs from the perturbative treatments of chapters 2-3 to account for the strong couplings that can be induced in high-finesse cavities and nano-structures as well as with plasmonics and many-body effects. Formulas for electronic potential surfaces and non-adiabatic couplings were given in terms of the equivalent bare-state quantities. The rotating wave approximation was discussed and shown to immediately yield a conserved excitation number that allows diagonalization of the Hamiltonian. A simple model system was used to illustrate how coupling to the cavity can be used to catalyze the dissociation of a bound system or increase the lifetime of a dissociative system. In both cases, the effect is achieved by coupling states of opposite character through the cavity mode. We presented a pair of methods to go beyond the rotating wave, the first of which yields the joint electron-cavity potentials and non-adiabatic couplings, the latter of which is particularly demanding numerically, and the second of which overcomes this numerical difficulty by treating the cavity mode through its quadrature coordinates and propagating a joint nuclear-photon wavefunction in real space, providing direct access to expectation values and signals. We gave the example of NaI and showed how ultrastrong cavity coupling can create a pronounced dip in the potentials at the location of the bare-state avoided crossing. The consequences for this were explored by tracking the population dynamics between dissociative and bound states, with more and more pronounced oscillations taking over as the coupling is increased.

The above are but a small subset of possible quantum field effects as quantum fluctuations of the laser fields, multi-photon processes, and interactions with specialized states of light, such as entangled photons and higher-photon Fock states, are all neglected in this thesis. We have endeavored to help arm the reader with the tools to understand these and other effects of quantum light in spectroscopy. We hope to have had some small success in this and, along the way, conveyed some measure of this author's abiding passion for the subject.

Bibliography

[1] Shaul Mukamel. *Principles of Nonlinear Optical Spectroscopy.* Oxford University Press, USA, 1st edition, January 1995.

[2] Henning Meyer. The molecular hamiltonian. *Annu. Rev. Phys. Chem.*, 53(1):141–172, 2002.

[3] Graham A Worth and Lorenz S Cederbaum. Beyond born-oppenheimer: molecular dynamics through a conical intersection. *Annu. Rev. Phys. Chem.*, 55:127–158, 2004.

[4] Dario Polli, Piero Altoe, Oliver Weingart, Katelyn M. Spillane, Cristian Manzoni, Daniele Brida, Gaia Tomasello, Giorgio Orlandi, Philipp Kukura, Richard A. Mathies, Marco Garavelli, and Giulio Cerullo. Conical intersection dynamics of the primary photoisomerization event in vision. *Nature*, 467(7314):440–443, September 2010.

[5] Silvia Rinaldi, Federico Melaccio, Samer Gozem, Francesca Fanelli, and Massimo Olivucci. Comparison of the isomerization mechanisms of human melanopsin and invertebrate and vertebrate rhodopsins. *P. Natl. Acad. Sci. USA*, 111(5):1714–1719, February 2014.

[6] Mario Barbatti, Giovanni Granucci, Maurizio Persico, Matthias Ruckenbauer, Mario Vazdar, Mirjana Eckert-Maksić, and Hans Lischka. The on-the-fly surface-hopping program system Newton-X: Application to ab initio simulation of the nonadiabatic photodynamics of benchmark systems. *J. Photochem. Photobiol. A*, 190(2-3):228–240, 2007.

[7] Mario Barbatti, Adélia J. A. Aquino, Jaroslaw J. Szymczak, Dana Nachtigallová, Pavel Hobza, and Hans Lischka. Relaxation mechanisms of UV-photoexcited DNA and RNA nucleobases. *Proc. Natl. Acad. Sci. USA*, 107(50):21453–21458, December 2010.

[8] A. L. Sobolewski, W. Domcke, C. Dedonder-Lardeux, and C. Jouvet. Excited-state hydrogen detachment and hydrogen transfer driven by repulsive $1\pi\sigma^*$ states: A new paradigm for nonradiative decay in aromatic biomolecules. *Phys. Chem. Chem. Phys.*, 4(7):1093–1100, 2002.

[9] Spiridoula Matsika. Radiationless decay of excited states of uracil through conical intersections. *The Journal of Physical Chemistry A*, 108(37):7584–7590, 2004.

[10] Serhiy Perun, Andrzej L Sobolewski, and Wolfgang Domcke. Conical intersections in thymine. *The Journal of Physical Chemistry A*, 110(49):13238–13244, 2006.

[11] Benjamin P Fingerhut, Konstantin E Dorfman, and Shaul Mukamel. Probing the conical intersection dynamics of the rna base uracil by uv-pump stimulated-raman-probe signals; ab initio simulations. *Journal of chemical theory and computation*, 10(3):1172–1188, 2014.

[12] Kochise Bennett, Markus Kowalewski, and Shaul Mukamel. Nonadiabatic dynamics may be probed through electronic coherence in time-resolved photoelectron spectroscopy. *Journal of chemical theory and computation*, 12(2):740–752, 2016.

[13] Donald H Kobe. Gauge transformations and the electric dipole approximation. *American Journal of Physics*, 50(2):128–133, 1982.

[14] Konstantin E Dorfman and Shaul Mukamel. Nonlinear spectroscopy with time-and frequency-gated photon counting: A superoperator diagrammatic approach. *Physical Review A*, 86(1):013810, 2012.

[15] Markus Kowalewski, Kochise Bennett, Jérémy R Rouxel, and Shaul Mukamel. Monitoring nonadiabatic electron-nuclear dynamics in molecules by attosecond streaking of photoelectrons. *Physical Review Letters*, 117(4):043201, 2016.

[16] Massimo Altarelli et al. The european X-ray free-electron laser. *Technical Design Report, DESY*, 97, 2006.

[17] J. Feldhaus, J. Arthur, and J. B. Hastings. X-ray free-electron lasers. *J. Phys. B-At. Mol. Opt.*, 38(9):S799, May 2005.

[18] Brian W. J. McNeil and Neil R. Thompson. X-ray free-electron lasers. *Nat. Photon.*, 4(12):814–821, December 2010.

[19] Henry N Chapman, Petra Fromme, Anton Barty, Thomas A White, Richard A Kirian, Andrew Aquila, Mark S Hunter, Joachim Schulz, Daniel P DePonte, and Uwe Weierstall. Femtosecond X-ray protein nanocrystallography. *Nature*, 470(7332):73–77, February 2011.

[20] Ch Bostedt, JD Bozek, PH Bucksbaum, RN Coffee, JB Hastings, Z Huang, RW Lee, S Schorb, JN Corlett, P Denes, et al. Ultra-fast and ultra-intense x-ray sciences: first results from the linac coherent light source free-electron laser. *Journal of Physics B: Atomic, Molecular and Optical Physics*, 46(16):164003, 2013.

[21] Anton Barty, Jochen Küpper, and Henry N Chapman. Molecular imaging using x-ray free-electron lasers. *Annual review of physical chemistry*, 64:415–435, 2013.

[22] S Bratos, F Mirloup, R Vuilleumier, and M Wulff. Time-resolved x-ray diffraction: statistical theory and its application to the photo-physics of molecular iodine. *J. Chem. Phys.*, 116(24):10615–10625, 2002.

[23] Bradley J Siwick, Jason R Dwyer, Robert E Jordan, and RJ Dwayne Miller. An atomic-level view of melting using femtosecond electron diffraction. *Science*, 302(5649):1382–1385, 2003.

[24] Philip Coppens, Ivan I Vorontsov, Tim Graber, Milan Gembicky, and Andrey Yu Kovalevsky. The structure of short-lived excited states of molecular complexes by time-resolved x-ray diffraction. *Acta Crystallographica Section A: Foundations of Crystallography*, 61(2):162–172, 2005.

[25] Hyotcherl Ihee, Maciej Lorenc, Tae Kyu Kim, Qin Y Kong, Marco Cammarata, Jae Hyuk Lee, Savo Bratos, and Michael Wulff. Ultrafast x-ray diffraction of transient molecular structures in solution. *Science*, 309(5738):1223–1227, 2005.

[26] M Wulff, S Bratos, A Plech, R Vuilleumier, F Mirloup, M Lorenc, Q Kong, and H Ihee. Recombination of photodissociated iodine: A time-resolved x-ray-diffraction study. *J. Chem. Phys.*, 124(3):034501, 2006.

[27] Marco Cammarata, Matteo Levantino, Friedrich Schotte, Philip A Anfinrud, Friederike Ewald, Jungkweon Choi, Antonio Cupane, Michael Wulff, and Hyotcherl Ihee. Tracking the structural dynamics of proteins in solution using time-resolved wide-angle x-ray scattering. *Nature methods*, 5(10):881–886, 2008.

[28] C. W. Siders, A. Cavalleri, K. Sokolowski-Tinten, Cs Tth, T. Guo, M. Kammler, M. Horn von Hoegen, K. R. Wilson, D. von der Linde, and C. P. J. Barty. Detection of nonthermal melting by ultrafast X-ray diffraction. *Science*, 286(5443):1340–1342, November 1999.

[29] Michael Woerner, Flavio Zamponi, Zunaira Ansari, Jens Dreyer, Benjamin Freyer, Mirabelle Prémont-Schwarz, and Thomas Elsaesser. Concerted electron and proton transfer in ionic crystals mapped by femtosecond x-ray powder diffraction. *J. Chem. Phys.*, 133(6):064509, 2010.

[30] Philip Coppens. Molecular excited-state structure by time-resolved pump- probe x-ray diffraction. what is new and what are the prospects for further progress? *J. Phys. Chem. Lett.*, 2(6):616–621, 2011.

[31] Richard Neutze and Keith Moffat. Time-resolved structural studies at synchrotrons and x-ray free electron lasers: opportunities and challenges. *Current opinion in structural biology*, 22(5):651–659, 2012.

[32] J. Larsson, R. W. Falcone, et al. Ultrafast structural changes measured by time-resolved X-ray diffraction. *Appl. Phys. A Mater. Sci. Process.*, 66(6):587–591, June 1998.

[33] Jianshu Cao and Kent R. Wilson. Ultrafast x-ray diffraction theory. *J. Phys. Chem. A*, 102(47):9523–9530, November 1998.

[34] Niels E. Henriksen and Klaus B. Møller. On the theory of Time-Resolved x-ray diffraction. *J. Phys. Chem. B*, 112(2):558–567, January 2008.

[35] Gopal Dixit, Oriol Vendrell, and Robin Santra. Imaging electronic quantum motion with light. *Proc. Natl. Acad. Sci.*, 109(29):11636–11640, 2012.

[36] JM Glownia, A Natan, JP Cryan, R Hartsock, M Kozina, MP Minitti, S Nelson, J Robinson, T Sato, T van Driel, et al. Self-referenced coherent diffraction x-ray movie of ångstrom-and femtosecond-scale atomic motion. *Phys. Rev. Lett.*, 117(15):153003, 2016.

[37] Yoshitaka Tanimura and Shaul Mukamel. Two-dimensional femtosecond vibrational spectroscopy of liquids. *The Journal of chemical physics*, 99(12):9496–9511, 1993.

[38] Keisuke Tominaga and Keitaro Yoshihara. Fifth-order nonlinear spectroscopy on the low-frequency modes of liquid cs2. *The Journal of chemical physics*, 104(12):4419–4426, 1996.

[39] Keisuke Tominaga and Keitaro Yoshihara. Temporally two-dimensional femtosecond spectroscopy of binary mixture of cs2. *The Journal of chemical physics*, 104(3):1159–1162, 1996.

[40] Thomas Steffen and Koos Duppen. Time resolved four-and six-wave mixing in liquids. ii. experiments. *The Journal of chemical physics*, 106(10):3854–3864, 1997.

[41] Thomas Steffen and Koos Duppen. Analysis of nonlinear optical contributions to temporally two-dimensional raman scattering. *Chemical physics letters*, 273(1-2):47–54, 1997.

[42] A Tokmakoff and GR Fleming. Two-dimensional raman spectroscopy of the intermolecular modes of liquid cs. *The Journal of chemical physics*, 106:2569, 1997.

[43] David A Blank, Laura J Kaufman, and Graham R Fleming. Fifth-order two-dimensional raman spectra of CS2 are dominated by third-order cascades. *The Journal of Chemical Physics*, 111(7):3105–3114, August 1999.

[44] O. Golonzka, N. Demirdven, M. Khalil, and A. Tokmakoff. Separation of cascaded and direct fifth-order raman signals using phase-sensitive intrinsic heterodyne detection. *The Journal of Chemical Physics*, 113(22):9893–9896, December 2000.

[45] Kevin J Kubarych, Chris J Milne, and RJ Dwayne Miller. Fifth-order two-dimensional raman spectroscopy: a new direct probe of the liquid state. *International Reviews in Physical Chemistry*, 22(3):497–532, 2003.

[46] YL Li, L Huang, RJ Dwayne Miller, Taisuke Hasegawa, and Yoshitaka Tanimura. Two-dimensional fifth-order raman spectroscopy of liquid formamide: Experiment and theory. *The Journal of chemical physics*, 128(23):234507, 2008.

[47] Bin Zhao, Zhigang Sun, and Soo-Y Lee. Quantum theory of time-resolved femtosecond stimulated raman spectroscopy: Direct versus cascade processes and application to CDCl3. *The Journal of Chemical Physics*, 134(2):024307–024307–12, January 2011.

[48] Hadas Frostig, Tim Bayer, Nirit Dudovich, Yonina C Eldar, and Yaron Silberberg. Single-beam spectrally controlled two-dimensional raman spectroscopy. *Nature Photonics*, 9(5):339–343, 2015.

[49] S. Tomljenovic-Hanic, M. J. Steel, C. Martijn de Sterke, and J. Salzman. Diamond based photonic crystal microcavities. *Opt. Express*, 14(8):3556+, 2006.

[50] Myung-Ki Kim, Hongchul Sim, Seung J. Yoon, Su-Hyun Gong, Chi W. Ahn, Yong-Hoon Cho, and Yong-Hee Lee. Squeezing photons into a Point-Like space. *Nano Lett.*, 15(6):4102–4107, June 2015.

[51] Sanli Faez, Pierre Türschmann, Harald R. Haakh, Stephan Götzinger, and Vahid Sandoghdar. Coherent interaction of light and single molecules in a dielectric nanoguide. *Phys. Rev. Lett.*, 113(21), November 2014.

[52] E. M. Purcell. Spontaneous emission propabilities at radio frequencies. *Physical Review*, 69:681+, 1946.

[53] E. T. Jaynes and F. W. Cummings. Comparison of quantum and semiclassical radiation theories with application to the beam maser. *Proc. IEEE*, 51(1):89–109, January 1963.

[54] Serge Haroche and Jean-Michel Raimond. *Exploring the Quantum: Atoms, Cavities, and Photons (Oxford Graduate Texts).* Oxford University Press, 1 edition, October 2006.

[55] C. J. Hood, M. S. Chapman, T. W. Lynn, and H. J. Kimble. Real-Time cavity QED with single atoms. *Phys. Rev. Lett.*, 80(19):4157–4160, May 1998.

[56] James A. Hutchison, Tal Schwartz, Cyriaque Genet, Eloïse Devaux, and Thomas W. Ebbesen. Modifying chemical landscapes by coupling to vacuum fields. *Angew. Chem. Int. Ed.*, 51(7):1592–1596, February 2012.

[57] Atef Shalabney, Jino George, Hidefumi Hiura, James A. Hutchison, Cyriaque Genet, Petra Hellwig, and Thomas W. Ebbesen. Enhanced raman scattering from Vibro-Polariton hybrid states. *Angew. Chem. Int. Ed.*, 54(27):7971–7975, June 2015.

[58] J. J. Hopfield. Theory of the contribution of excitons to the complex dielectric constant of crystals. *Phys. Rev.*, 112(5):1555–1567, December 1958.

[59] Javier Galego, Francisco J. Garcia-Vidal, and Johannes Feist. Cavity-Induced modifications of molecular structure in the Strong-Coupling regime. *Phys. Rev. X*, 5(4):041022+, November 2015.

[60] Jaehee Kim, Hongli Tao, James L. White, Vladimir S. Petrović, Todd J. Martinez, and Philip H. Bucksbaum. Control of 1,3-Cyclohexadiene photoisomerization using Light-Induced conical intersections. *J. Phys. Chem. A*, 116(11):2758–2763, March 2012.

[61] Philipp von den Hoff, Markus Kowalewski, and Regina de Vivie-Riedle. Searching for pathways involving dressed states in optimal control theory. *Faraday Discuss.*, 153(0):159–171, 2011.

[62] Jaehee Kim, Hongli Tao, Todd J. Martinez, and Phil Bucksbaum. Ab initio multiple spawning on laser-dressed states: a study of 1,3-cyclohexadiene photoisomerization via light-induced conical intersections. *J. Phys. B: At. Mol. Opt. Phys.*, 48(16):164003+, August 2015.

[63] Jonathan D. Pritchard, Kevin J. Weatherill, and Charles S. Adams. Nonlinear optics using cold rydberg atoms. Volume 1:301–350, October 2013.

[64] Konstantin E. Dorfman, Kochise Bennett, Yu Zhang, and Shaul Mukamel. Nonlinear light scattering in molecules triggered by an impulsive X-ray Raman process. *Phys. Rev. A*, 87:053826, 2013.

[65] Akbar Salam. *Molecular Quantum Electrodynamics: Long-Range Intermolecular Interactions*. Wiley, 2010.

[66] Winfried Schulke. *Electron dynamics by inelastic X-ray scattering*. Oxford University Press, Oxford; New York, 2007.

[67] André Guinier. *X-ray diffraction: in crystals, imperfect crystals, and amorphous bodies*. Courier Dover Publications, 1994.

[68] J Als-Nielsen and Des McMorrow. *Elements of modern X-ray physics*. Wiley, Hoboken, 2011.

[69] Jianwei Miao, Tetsuya Ishikawa, Erik H Anderson, and Keith O Hodgson. Phase retrieval of diffraction patterns from noncrystalline samples using the oversampling method. *Phys. Rev. B*, 67(17):174104, 2003.

[70] Ian K Robinson, Ivan A Vartanyants, GJ Williams, MA Pfeifer, and JA Pitney. Reconstruction of the shapes of gold nanocrystals using coherent x-ray diffraction. *Phys. Rev. Lett.*, 87(19):195505, 2001.

[71] Jianwei Miao, Pambos Charalambous, Janos Kirz, and David Sayre. Extending the methodology of x-ray crystallography to allow imaging of micrometre-sized non-crystalline specimens. *Nature*, 400(6742):342–344, 1999.

[72] Raymond C Stevens. High-throughput protein crystallization. *Curr. Opin. Struct. Biol.*, 10(5):558–563, October 2000.

[73] Alexander McPherson. *Crystallization of biological macromolecules*. Cold Spring Harbor Laboratory Press, 1999.

[74] Janos Hajdu. Single-molecule X-ray diffraction. *Curr. Opin. Struct. Biol.*, 10(5):569–573, 2000.

[75] Henry N. Chapman. X-ray imaging beyond the limits. *Nat. Mater.*, 8(4):299–301, April 2009.

[76] D Starodub, A Aquila, S Bajt, M Barthelmess, A Barty, C Bostedt, JD Bozek, N Coppola, RB Doak, SW Epp, et al. Single-particle structure determination by correlations of snapshot X-ray diffraction patterns. *Nat. Commun.*, 3:1276, December 2012.

[77] Steffen Kahra, Günther Leschhorn, Markus Kowalewski, Agustin Schiffrin, Elisabeth Bothschafter, Werner Fuß, Regina de Vivie-Riedle, Ralph Ernstorfer, Ferenc Krausz, Reinhard Kienberger, et al. A molecular conveyor belt by controlled delivery of single molecules into ultrashort laser pulses. *Nature Physics*, 8(3):238–242, 2012.

[78] PB Corkum and Ferenc Krausz. Attosecond science. *Nature Physics*, 3(6):381–387, 2007.

[79] Ferenc Krausz and Misha Ivanov. Attosecond physics. *Rev. Mod. Phys.*, 81(1):163, 2009.

[80] Tenio Popmintchev, Ming-Chang Chen, Paul Arpin, Margaret M Murnane, and Henry C Kapteyn. The attosecond nonlinear optics of bright coherent x-ray generation. *Nat. Photon.*, 4(12):822–832, 2010.

[81] Peter Baum and Ahmed H. Zewail. 4D attosecond imaging with free electrons: Diffraction methods and potential applications. *Chemical Physics*, 366(1-3):2–8, December 2009.

[82] Henry N Chapman, Anton Barty, Michael J Bogan, Sébastien Boutet, Matthias Frank, Stefan P Hau-Riege, Stefano Marchesini, Bruce W Woods, Saša Bajt, and W Henry Benner. Femtosecond diffractive imaging with a soft-X-ray free-electron laser. *Nat. Phys.*, 2(12), 2006.

[83] Ahmed H Zewail. Four-dimensional electron microscopy. *Science*, 328(5975):187–193, 2010.

[84] Sascha Schäfer, Wenxi Liang, and Ahmed H Zewail. Structural dynamics and transient electric-field effects in ultrafast electron diffraction from surfaces. *Chemical Physics Letters*, 493(1):11–18, 2010.

[85] RJ Dwayne Miller. Femtosecond crystallography with ultrabright electrons and x-rays: capturing chemistry in action. *Science*, 343(6175):1108–1116, 2014.

[86] Renske M van der Veen, Thomas J Penfold, and Ahmed H Zewail. Ultrafast core-loss spectroscopy in four-dimensional electron microscopy. *Structural dynamics*, 2(2):024302, 2015.

[87] Jie Yang, Markus Guehr, Xiaozhe Shen, Renkai Li, Theodore Vecchione, Ryan Coffee, Jeff Corbett, Alan Fry, Nick Hartmann, Carsten Hast, et al. Diffractive imaging of coherent nuclear motion in isolated molecules. *Phys. Rev. Lett.*, 117(15):153002, 2016.

[88] Jason D. Biggs, Judith A. Voll, and Shaul Mukamel. Coherent nonlinear optical studies of elementary processes in biological complexes; diagrammatic techniques based on the wavefunction vs. the density matrix. *Phil. Trans. R. Soc. A*, 370:3709–3727, 2012.

[89] Kochise Bennett, Jason D Biggs, Yu Zhang, Konstantin E Dorfman, and Shaul Mukamel. Time-, frequency-, and wavevector-resolved x-ray diffraction from single molecules. *J. Chem. Phys.*, 140(20):204311, 2014.

[90] Tomoyuki Hayashi and Alexei A. Stuchebrukhov. Electron tunneling in respiratory complex I. *Proc. Natl. Acad. Sci.*, 107:19157, 2010.

[91] Yu Zhang, Jason D. Biggs, Daniel Healion, Niranjan Govind, and Shaul Mukamel. Core and valence excitations in resonant X-ray spectroscopy using restricted excitation window time-dependent density functional theory. *J. Chem. Phys.*, 137:194306, 2012.

[92] Jason D. Biggs, Yu Zhang, Daniel Healion, and Shaul Mukamel. Multidimensional X-ray spectroscopy of valence and core excitations in cysteine. *J. Chem. Phys.*, 138:144303, 2013.

[93] Ruben A. Dilanian, Bo Chen, Garth J. Williams, Harry M. Quiney, Keith A. Nugent, Sven Teichmann, Peter Hannaford, Lap V. Dao, and Andrew G. Peele. Diffractive imaging using a polychromatic high-harmonic generation soft-X-ray source. *J. Appl. Phys.*, 106(2):023110, 2009.

[94] S Miyabe and P Bucksbaum. Transient impulsive electronic raman redistribution. *Physical review letters*, 114(14):143005, 2015.

[95] Daniel Healion, Yu Zhang, Jason D. Biggs, Niranjan Govind, and Shaul Mukamel. Entangled valence electronhole dynamics revealed by stimulated attosecond X-ray Raman scattering. *J. Phys. Chem. Lett.*, 3(17):2326–2331, 2012.

[96] Jason D. Biggs, Yu Zhang, Daniel Healion, and Shaul Mukamel. Watching energy transfer in metalloporphyrin heterodimers using stimulated X-ray Raman spectroscopy. *Proc. Natl. Acad. Sci.*, 110(39):15597–15601, 2013.

[97] Daniel Healion, Jason D. Biggs, and Shaul Mukamel. Manipulating one- and two-dimensional stimulated-X-ray resonant-Raman signals in molecules by pulse polarizations. *Phys. Rev. A*, 86:033429, 2012.

[98] Marc JJ Vrakking and Thomas Elsaesser. X-ray photonics: X-rays inspire electron movies. *Nature Photonics*, 6(10):645–647, 2012.

[99] Michael Woerner, Flavio Zamponi, Zunaira Ansari, Jens Dreyer, Benjamin Freyer, Mirabelle Prmont-Schwarz, and Thomas Elsaesser. Concerted electron and proton transfer in ionic crystals mapped by femtosecond x-ray powder diffraction. *The Journal of Chemical Physics*, 133(6), 2010.

[100] Kochise Bennett, Markus Kowalewski, and Shaul Mukamel. Heterodyne-detected ultrafast x-ray diffraction and scattering from nonstationary states. *arXiv preprint arXiv:1611.07085*, 2016.

[101] L. S. Bartell and R. M. Gavin. Effects of electron correlation in X-Ray and electron diffraction. *J. Am. Chem. Soc.*, 86(17):3493–3498, September 1964.

[102] I. Waller and D. R. Hartree. On the intensity of total scattering of X-Rays. *P. Roy. Soc. A-Math. Phys.*, 124(793):119–142, May 1929.

[103] Wolfgang Domcke, David R. Yarkony, and Horst Köppel. *Conical Intersections*, volume 17. WORLD SCIENTIFIC, November 2011.

[104] Markus Kowalewski, Kochise Bennett, Konstantin E Dorfman, and Shaul Mukamel. Catching conical intersections in the act: monitoring transient electronic coherences by attosecond stimulated x-ray raman signals. *Physical review letters*, 115(19):193003, 2015.

[105] M. . P. Minitti, J. . M. Budarz, A. Kirrander, J. . S. Robinson, D. Ratner, T. . J. Lane, D. Zhu, J. . M. Glownia, M. Kozina, H. . T. Lemke, M. Sikorski, Y. Feng, S. Nelson, K. Saita, B. Stankus, T. Northey, J. . B. Hastings, and P. . M. Weber. Imaging molecular motion: Femtosecond X-Ray scattering of an electrocyclic chemical reaction. *Phys. Rev. Lett.*, 114(25), June 2015.

[106] Angelika Hofmann and Regina de Vivie-Riedle. Adiabatic approach for ultrafast quantum dynamics mediated by simultaneously active conical intersections. *Chem. Phys. Lett.*, 346(3-4):299–304, October 2001.

[107] Di Xiao, Ming-Che Chang, and Qian Niu. Berry phase effects on electronic properties. *Rev. Mod. Phys.*, 82(3):1959–2007, July 2010.

[108] Todd S. Rose, Mark J. Rosker, and Ahmed H. Zewail. Femtosecond realtime probing of reactions. IV. the reactions of alkali halides. *J. Chem. Phys.*, 91(12):7415–7436, December 1989.

[109] Konstantin E. Dorfman and Shaul Mukamel. Nonlinear spectroscopy with time- and frequency-gated photon counting: A superoperator diagrammatic approach. *Phys. Rev. A*, 86(1):013810, July 2012.

[110] Oleksiy Roslyak and Shaul Mukamel. A unified description of sum frequency generation, parametric down conversion and two-photon fluorescence. *Molecular physics*, 107(3):265–280, 2009.

[111] Oleksiy Roslyak and Shaul Mukamel. A unified quantum field description of spontaneous and stimulated nonlinear wave mixing and hyper-rayleigh scattering. *EVU Lecture Notes, Lectures of Virtual University, Max-Born Institute*, 2010.

[112] J Als-Nielsen and Des McMorrow. *Elements of modern X-ray physics*. Wiley, Hoboken, 2011.

[113] Robert W Boyd. *Nonlinear optics*. San Diego, CA (United States); Academic Press Inc., 1992.

[114] Vadim V Lozovoy, Igor Pastirk, Matthew G Comstock, and Marcos Dantus. Cascaded free-induction decay four-wave mixing. *Chemical Physics*, 266(2):205–212, 2001.

[115] ST Cundiff. Time domain observation of the lorentz-local field. *Laser Physics*, 12(8):1073–1078, 2002.

[116] Kochise Bennett and Shaul Mukamel. Cascading and local-field effects in non-linear optics revisited: A quantum-field picture based on exchange of photons. *The Journal of chemical physics*, 140(4):044313, 2014.

[117] MG Benedict, VA Malyshev, ED Trifonov, and AI Zaitsev. Reflection and transmission of ultrashort light pulses through a thin resonant medium: Local-field effects. *Physical Review A*, 43(7):3845, 1991.

[118] Emmanuel Paspalakis, Anastasia Kalini, and Andreas F Terzis. Local field effects in excitonic population transfer in a driven quantum dot system. *Physical Review B*, 73(7):073305, 2006.

[119] Rachel Glenn, Kochise Bennett, Konstantin E Dorfman, and Shaul Mukamel. Photon-exchange induces optical nonlinearities in harmonic systems. *Journal of Physics B: Atomic, Molecular and Optical Physics*, 48(6):065401, 2015.

[120] T Thirunamachandran. Intermolecular interactions in the presence of an intense radiation field. *Molecular Physics*, 40(2):393–399, 1980.

[121] Bihui Zhu, Johannes Schachenmayer, Minghui Xu, F Herrera, Juan G Restrepo, Murray J Holland, and Ana Maria Rey. Synchronization of interacting quantum dipoles. *New Journal of Physics*, 17(8):083063, 2015.

[122] Robert H Dicke. Coherence in spontaneous radiation processes. *Physical Review*, 93(1):99, 1954.

[123] R de J León-Montiel, Zixuan Hu, and Joel Yuen-Zhou. Genuinely quantum effects in nonlinear spectroscopy: vacuum fluctuations and their induced superradiance. *arXiv preprint arXiv:1606.05717*, 2016.

[124] V Astinov, KJ Kubarych, CJ Milne, and RJ Dwayne Miller. Diffractive optics implementation of six-wave mixing. *Optics letters*, 25(11):853–855, 2000.

[125] Randy D Mehlenbacher, Brendon Lyons, Kristina C Wilson, Yong Du, and David W McCamant. Theoretical analysis of anharmonic coupling and cascading raman signals observed with femtosecond stimulated raman spectroscopy. *The Journal of Chemical Physics*, 131(24):244512–244512–20, December 2009.

[126] Maxim F Gelin and Wolfgang Domcke. Simple recipes for separating excited-state absorption and cascading signals by polarization-sensitive measurements. *The Journal of Physical Chemistry A*, 2013.

[127] Michel Gross and Serge Haroche. Superradiance: an essay on the theory of collective spontaneous emission. *Physics reports*, 93(5):301–396, 1982.

[128] Marlan O Scully. Collective lamb shift in single photon dicke superradiance. *Physical review letters*, 102(14):143601, 2009.

[129] Konstantin E Dorfman, Frank Schlawin, and Shaul Mukamel. Nonlinear optical signals and spectroscopy with quantum light. *Reviews of Modern Physics*, 88(4):045008, 2016.

[130] Claude Cohen-Tannoudji, Jacques Dupont-Roc, Gilbert Grynberg, and Patricia Thickstun. *Atom-photon interactions: basic processes and applications*. Wiley Online Library, 1992.

[131] Minhaeng Cho, David A Blank, Jaeyoung Sung, Kisam Park, Sangjoon Hahn, and Graham R Fleming. Intrinsic cascading contributions to the fifth-and seventh-order electronically off-resonant raman spectroscopies. *The Journal of Chemical Physics*, 112(5):2082–2094, 2000.

[132] David Parker Craig and Thiru Thirunamachandran. *Molecular quantum electrodynamics: an introduction to radiation-molecule interactions*. Courier Corporation, 1984.

[133] Akbar Salam. *Molecular quantum electrodynamics: long-range intermolecular interactions*. John Wiley & Sons, 2010.

[134] Richard P Feynman, Robert B Leighton, and Matthew Sands. *The Feynman Lectures on Physics, Desktop Edition Volume I*, volume 1. Basic books, 2013.

[135] Shaul Mukamel, Daniel Healion, Yu Zhang, and Jason D Biggs. Multidimensional attosecond resonant x-ray spectroscopy of molecules: Lessons from the optical regime. *Annual review of physical chemistry*, 64:101–127, 2013.

[136] David L Andrews. A unified theory of radiative and radiationless molecular energy transfer. *Chemical Physics*, 135(2):195–201, 1989.

[137] Gregory D Scholes and David L Andrews. Resonance energy transfer and quantum dots. *Physical Review B*, 72(12):125331, 2005.

[138] B. S. Simpkins, Kenan P. Fears, Walter J. Dressick, Bryan T. Spann, Adam D. Dunkelberger, and Jeffrey C. Owrutsky. Spanning strong to weak normal mode coupling between vibrational and Fabry-Pérot cavity modes through tuning of vibrational absorption strength. *ACS Photon.*, 2(10):1460–1467, October 2015.

[139] Markus Kowalewski, Kochise Bennett, and Shaul Mukamel. Non-adiabatic dynamics of molecules in optical cavities. *J. Chem. Phys.*, 144:054309, January 2016.

[140] Markus Kowalewski, Kochise Bennett, and Shaul Mukamel. Cavity femtochemistry; manipulating nonadiabatic dynamics at avoided crossings. *The journal of physical chemistry letters*, 2016.

[141] Felipe Herrera and Frank C Spano. Cavity-controlled chemistry in molecular ensembles. *Physical Review Letters*, 116(23):238301, 2016.

[142] Philipp V. Demekhin and Lorenz S. Cederbaum. Light-induced conical intersections in polyatomic molecules: General theory, strategies of exploitation, and application. *J. Chem. Phys.*, 139(15):154314, October 2013.

[143] Philipp von den Hoff, Sebastian Thallmair, Markus Kowalewski, Robert Siemering, and Regina de Vivie-Riedle. Optimal control theory - closing the gap between theory and experiment. *Phys. Chem. Chem. Phys.*, 14:14460, 2012.

[144] Peter Gross, Daniel Neuhauser, and Herschel Rabitz. Optimal control of curve-crossing systems. *J. Chem. Phys.*, 96(4):2834–2845, 1992.

[145] Paul Brumer and Moshe Shapiro. Control of unimolecular reactions using coherent light. *Chem. Phys. Lett.*, 126(6):541–546, May 1986.

[146] David J. Tannor, Ronnie Kosloff, and Stuart A. Rice. Coherent pulse sequence induced control of selectivity of reactions: Exact quantum mechanical calculations. *J. Chem. Phys.*, 85(10):5805–5820, November 1986.

[147] Giovanna Morigi, Pepijn W. H. Pinkse, Markus Kowalewski, and Regina de Vivie-Riedle. Cavity cooling of internal molecular motion. *Phys. Rev. Lett.*, 99(7):073001, August 2007.

[148] Markus Kowalewski, Giovanna Morigi, Pepijn W. H. Pinkse, and Regina de Vivie Riedle. Cavity sideband cooling of trapped molecules. *Phys. Rev. A*, 84:033408, September 2011.

[149] Stefan Nuszmann, Karim Murr, Markus Hijlkema, Bernhard Weber, Axel Kuhn, and Gerhard Rempe. Vacuum-stimulated cooling of single atoms in three dimensions. *Nature Phys.*, 1(2):122–125, November 2005.

[150] Markus Kowalewski, Giovanna Morigi, Pepijn W. H. Pinkse, and Regina de Vivie Riedle. Cavity sideband cooling of trapped molecules. *Physical Review A*, 84:033408+, September 2011.

[151] Benjamin L. Lev, András Vukics, Eric R. Hudson, Brian C. Sawyer, Peter Domokos, Helmut Ritsch, and Jun Ye. Prospects for the cavity-assisted laser cooling of molecules. *Physical Review A (Atomic, Molecular, and Optical Physics)*, 77(2):023402+, 2008.

[152] F. C. Spano. Optical microcavities enhance the exciton coherence length and eliminate vibronic coupling in j-aggregates. *J. Chem. Phys.*, 142(18):184707, May 2015.

[153] Filippo Caruso, Semion K. Saikin, Enrique Solano, Susana F. Huelga, Alán A. Guzik, and Martin B. Plenio. Probing biological light-harvesting phenomena by optical cavities. *Phys. Rev. B*, 85:125424+, March 2012.

[154] Prasoon Saurabh and Shaul Mukamel. Two-dimensional infrared spectroscopy of vibrational polaritons of molecules in an optical cavity. *J. Chem. Phys.*, 144(12):124115, March 2016.

[155] Javier del Pino, Johannes Feist, and F. J. Garcia-Vidal. Signatures of vibrational strong coupling in raman scattering. *J. Phys. Chem. C*, 119(52):29132–29137, December 2015.

[156] Felipe Herrera, Borja Peropadre, Leonardo A. Pachon, Semion K. Saikin, and Alán Aspuru-Guzik. Quantum nonlinear optics with polar J-Aggregates in microcavities. *J. Phys. Chem. Lett.*, 5(21):3708–3715, November 2014.

[157] Felipe Herrera and Frank C. Spano. Cavity-controlled chemistry in molecular ensembles, December 2015. (accessed May 12, 2016).

[158] Merav Muallem, Alexander Palatnik, Gilbert D. Nessim, and Yaakov R. Tischler. Strong Light-Matter coupling and hybridization of molecular vibrations in a Low-Loss infrared microcavity. *J. Phys. Chem. Lett.*, page doi:10.1021/acs.jpclett.6b00617 (just accepeted manuscript), May 2016.

[159] Wolfgang P. Schleich. *Quantum Optics in Phase Space*. Wiley-VCH, 1 edition, February 2001.

[160] BR Judd. Exact solutions to a class of jahn-teller systems. *Journal of Physics C: Solid State Physics*, 12(9):1685, 1979.

[161] HG Reik, H Nusser, and LA Amarante Ribeiro. Exact solution of non-adiabatic model hamiltonians in solid state physics and optics. *Journal of Physics A: Mathematical and General*, 15(11):3491, 1982.

[162] M. Kus and M. Lewenstein. Exact isolated solutions for the class of quantum optical systems. *J. Phys. A: Math. Gen.*, 19(2):305–318, February 1986.

[163] S. Swain. Continued fraction expressions for the eigensolutions of the hamiltonian describing the interaction between a single atom and a single field mode: comparisons with the rotating wave solutions. *J. Phys. A: Math. Gen.*, 6(12):1919–1934, December 1973.

[164] Shu He, Chen Wang, Qing-Hu Chen, Xue-Zao Ren, Tao Liu, and Ke-Lin Wang. First-order corrections to the rotating-wave approximation in the jaynes-cummings model. *Physical Review A*, 86(3):033837, 2012.

[165] I. D. Feranchuk, L. I. Komarov, and A. P. Ulyanenkov. Two-level system in a one-mode quantum field: numerical solution on the basis of the operator method. *J. Phys. A: Math. Gen.*, 29(14):4035–4047, July 1996.

[166] Qing-Hu Chen, Chen Wang, Shu He, Tao Liu, and Ke-Lin Wang. Exact solvability of the quantum rabi model using bogoliubov operators. *Phys. Rev. A*, 86(2):023822, 2012.

[167] Angelika Hofmann and Regina de Vivie-Riedle. Adiabatic approach for ultrafast quantum dynamics mediated by simultaneously active conical intersections. *Chem. Phys. Lett.*, 346(3-4):299–304, October 2001.

[168] T. J. Martínez, M. Ben-Nun, and R. D. Levine. Molecular collision dynamics on several electronic states. *J. Phys. Chem. A*, 101(36):6389–6402, September 1997.

[169] Qing-Hu Chen, Tao Liu, Yu-Yu Zhang, and Ke-Lin Wang. Exact solutions to the jaynes-cummings model without the rotating-wave approximation. *Europhys. Lett.*, 96(1):14003, 2011.

[170] Daniel Braak. Integrability of the rabi model. *Physical Review Letters*, 107(10):100401, 2011.

[171] A. Mokhtari, P. Cong, J. L. Herek, and A. H. Zewail. Direct femtosecond mapping of trajectories in a chemical reaction. *Nature*, 348(6298):225–227, November 1990.

[172] Tao Liu, Ke-Lin Wang, and Mang Feng. Lower ground state due to counter-rotating wave interaction in a trapped ion system. *Journal of Physics B: Atomic, Molecular and Optical Physics*, 40(11):1967, 2007.

[173] H. Tal Ezer and R. Kosloff. An accurate and efficient scheme for propagating the time dependent schrödinger equation. *J. Chem. Phys.*, 81(9):3967–3971, 1984.

[174] H.-J. Werner, P. J. Knowles, G. Knizia, F. R. Manby, M. Schütz, et al. Molpro, version 2010.1, a package of ab initio programs, 2010. see http://www.molpro.net (visited on 11/01/2015).

[175] David J. Tannor. *Introduction to Quantum Mechanics: A Time-Dependent Perspective.* University Science Books, October 2006.

[176] Jorge Casanova, Guillermo Romero, Ion Lizuain, Juan José García-Ripoll, and Enrique Solano. Deep strong coupling regime of the jaynes-cummings model. *Physical review letters*, 105(26):263603, 2010.

[177] Sharon HammesSchiffer and John C. Tully. Proton transfer in solution: Molecular dynamics with quantum transitions. *J. Chem. Phys.*, 101(6):4657, September 1994.

[178] M. Ben-Nun, Jason Quenneville, and Todd J. Martínez. Ab initio multiple spawning: photochemistry from first principles quantum molecular dynamics. *J. Phys. Chem. A*, 104(22):5161–5175, May 2000.

[179] Tal Schwartz, James A. Hutchison, Jérémie Léonard, Cyriaque Genet, Stefan Haacke, and Thomas W. Ebbesen. Polariton dynamics under strong LightMolecule coupling. *ChemPhysChem*, 14(1):125–131, January 2013.

[180] Andrew D. Greentree, Charles Tahan, Jared H. Cole, and Lloyd C. L. Hollenberg. Quantum phase transitions of light. *Nature Phys.*, 2(12):856–861, November 2006.

[181] R. H. Dicke. Coherence in spontaneous radiation processes. *Phys. Rev.*, 93(1):99–110, January 1954.

[182] Attila Szabo and Neil S. Ostlund. *Modern Quantum Chemistry.* Dover Publications, New York, 1996.

[183] Alexander L Fetter and John Dirk Walecka. *Quantum theory of many-particle systems.* Courier Corporation, 2012.

[184] Alexander I. Kuleff and Lorenz S. Cederbaum. Radiation generated by the ultrafast migration of a positive charge following the ionization of a molecular system. *Phys. Rev. Lett.*, 106(5):053001, January 2011.

[185] M. J. Frisch, G. W. Trucks, H. B. Schlegel, G. E. Scuseria, M. A. Robb, J. R. Cheeseman, G. Scalmani, V. Barone, B. Mennucci, G. A. Petersson, H. Nakatsuji, M. Caricato, X. Li, H. P. Hratchian, A. F. Izmaylov, J. Bloino, G. Zheng, J. L. Sonnenberg, M. Hada, M. Ehara, K. Toyota, R. Fukuda, J. Hasegawa, M. Ishida, T. Nakajima, Y. Honda, O. Kitao, H. Nakai, T. Vreven, J. A. Montgomery, Jr., J. E. Peralta, F. Ogliaro, M. Bearpark, J. J. Heyd, E. Brothers, K. N. Kudin, V. N. Staroverov, R. Kobayashi, J. Normand, K. Raghavachari, A. Rendell, J. C. Burant, S. S. Iyengar, J. Tomasi, M. Cossi, N. Rega, J. M. Millam, M. Klene, J. E. Knox, J. B. Cross, V. Bakken, C. Adamo, J. Jaramillo, R. Gomperts, R. E. Stratmann, O. Yazyev, A. J. Austin, R. Cammi, C. Pomelli, J. W. Ochterski, R. L. Martin, K. Morokuma, V. G. Zakrzewski, G. A. Voth, P. Salvador, J. J. Dannenberg, S. Dapprich, A. D. Daniels, ?. Farkas, J. B. Foresman, J. V. Ortiz, J. Cioslowski, and D. J. Fox. Gaussian 09. Gaussian Inc. Wallingford CT 2009.

[186] Axel D. Becke. Density-functional thermochemistry. III. the role of exact exchange. *J. Chem. Phys.*, 98:5648, 1993.

[187] P. J. Stephens, F. J. Devlin, C. F. Chabalowski, and M. J. Frisch. Ab initio calculation of vibrational absorption and circular dichroism spectra using density functional force fields. *J. Phys. Chem.*, 98:11623–11627, 1994.

[188] T. Yanai, D. Tew, and N. Handy. A new hybrid exchangecorrelation functional using the coulomb-attenuating method (CAM-B3LYP). *Chem. Phys. Lett.*, 393:51, 2004.

[189] S. Hirata and M. Head-Gordon. Time-dependent density functional theory within the tammdancoff approximation. *Chem. Phys. Lett.*, 314:291, 1999.

[190] Yoshihiro Tawada, Takao Tsuneda, Susumu Yanagisawa, Takeshi Yanai, and Kimihiko Hirao. A long-range-corrected time-dependent density functional theory. *The Journal of chemical physics*, 120:8425, 2004.

[191] Ilaria Ciofini and Carlo Adamo. Accurate evaluation of valence and low-lying rydberg states with standard time-dependent density functional theory. *J. Phys. Chem. A*, 111(25):5549–5556, 2007.

[192] M. Valiev, E.J. Bylaska, N. Govind, K. Kowalski, T.P. Straatsma, H.J.J. van Dam, D. Wang, J. Nieplocha, E. Apra, T.L. Windus, and W.A. de Jong. NWChem: A comprehensive and scalable open-source solution for large scale molecular simulations. *Comput. Phys. Commun.*, 181:1477–1489, 2010.

[193] K. Lopata, B. E. Van Kuiken, M. Khalil, and N. Govind. Linear-response and real-time time-dependent density functional theory studies of core-level near-edge x-ray absorption. *J. Chem. Theory Comput.*, 8:3284–3292, 2012.

[194] Nicholas C. Handy and Henry F. Schaefer. On the evaluation of analytic energy derivatives for correlated wave functions. *J. Chem. Phys.*, 81(11):5031–5033, 1984.

[195] Y. Yamaguchi, Y. Osamura, J. D. Goddard, and H. F. Schaefer. *A new dimension to quantum chemistry: Analytic derivative methods in* ab initio *molecular electronic structure theory.* Oxford University Press, New York, 1994.

[196] Marvin Douglas and Norman M. Kroll. Quantum electrodynamical corrections to the fine structure of helium. *Ann. Phys.-New York*, 82(1):155, January 1974.

[197] Bernd A. Hess. Relativistic electronic-structure calculations employing a two-component no-pair formalism with external-field projection operators. *Phys. Rev. A*, 33(6):3742, June 1986.

[198] X. Y. Chang, R. Ehlich, A. J. Hudson, P. Piecuch, and J. C. Polanyi. Dynamics of harpooning studied by transition state spectroscopy NaFH. *Faraday Discuss.*, 108(0):411–425, 1997.

[199] M. Polanyi. *Atomic Reactions.* Williams and Norgate, 1932.

[200] Anna Nissen, Hans O. Karlsson, and Gunilla Kreiss. A perfectly matched layer applied to a reactive scattering problem. *J. Chem. Phys.*, 133(5):054306, 2010.

[201] Edward S. Smyth, Jonathan S. Parker, and K. T. Taylor. Numerical integration of the time-dependent schrödinger equation for laser-driven helium. *Comput. Phys. Commun.*, 114(1-3):1–14, November 1998.

Appendix A

Definitions and Useful Formulas

We collect here various important formulas used in calculating the signals discussed in the main text. Due to it's intimate connection with the material time-propagator, the Fourier transform of the Heaviside theta function

$$\int dt\theta(t)e^{it(\omega-\omega_0+i\Gamma)} = \frac{i}{\omega-\omega_0+i\Gamma} \tag{A.1}$$

plays an important role. The mode expansions of the magnetic vector potential and the electric field respectively are given by

$$\hat{\mathbf{E}}(t) = i\sum_{\mathbf{k}\lambda}\sqrt{\frac{2\pi\omega_{\mathbf{k}}}{\mathcal{V}}}\epsilon^{(\lambda)}(\hat{\mathbf{k}})e^{-i\omega t}\hat{a}_{\mathbf{k},\lambda} + \text{H.c.} \equiv \hat{\mathbf{E}}^{(+)}(t) + \hat{\mathbf{E}}^{(-)}(t) \tag{A.2}$$

$$\hat{\mathbf{A}}(t) = \sum_{\mathbf{k}\lambda}\sqrt{\frac{2\pi}{\omega_{\mathbf{k}}\mathcal{V}}}\epsilon^{(\lambda)}(\hat{\mathbf{k}})e^{-i\omega t}\hat{a}_{\mathbf{k},\lambda} + \text{H.c.} \equiv \hat{\mathbf{A}}^{(+)}(t) + \hat{\mathbf{A}}^{(-)}(t) \tag{A.3}$$

where "H.c." stands for the Hermitian conjugate, λ is the photon polarization, $\mathcal{V}$ is the quantization volume, and we have separated the positive and negative frequency components of the field. In a quantum field representation, electronic operators are written in terms of $\hat{\psi}^\dagger(\mathbf{r})$ and $\hat{\psi}(\mathbf{r})$, the electron field creation and annihilation operators, which satisfy the Fermi anti-commutation relation $\{\hat{\psi}(\mathbf{r}), \hat{\psi}^\dagger(\mathbf{r}')\} = \delta(\mathbf{r} - \mathbf{r}')$. The electronic momentum, current, and charge density operators are then given by

$$\hat{\mathbf{p}}(\mathbf{r}) = \hat{\psi}^\dagger(\mathbf{r}) \left(-\frac{1}{2}\nabla^2\right) \hat{\psi}(\mathbf{r}), \tag{A.4}$$

$$\hat{\mathbf{j}}(\mathbf{r}) = \frac{1}{2i} \left(\hat{\psi}^\dagger(\mathbf{r})\nabla\hat{\psi}(\mathbf{r}) - (\nabla\hat{\psi}^\dagger(\mathbf{r}))\hat{\psi}(\mathbf{r})\right), \tag{A.5}$$

$$\hat{\sigma}(\mathbf{r}) = \hat{\psi}^\dagger(\mathbf{r})\hat{\psi}(\mathbf{r}). \tag{A.6}$$

A.1 The Electronic Charge Density Operator

In this section, we discuss the operator nature of the charge density and its consequences. In this section, we will ignore nuclear dependence and will begin by considering a one-electron system. The content of this section is well-known from many sources [182, 183, 184] but we broach the subject here because of the common picture of diffraction as simply the square the momentum-space charge density as a c-number (see discussion at the beginning of section 2.1).

We seek an operator $\hat{\sigma}(\mathbf{r})$ such that the expectation value in a given state is the charge density

$$\begin{aligned} |\psi(\mathbf{r})|^2 \equiv \langle\psi|\hat{\sigma}(\mathbf{r})|\psi\rangle &= \int d\mathbf{r}' d\mathbf{r}'' \langle\psi|\mathbf{r}''\rangle\langle\mathbf{r}''|\hat{\sigma}(\mathbf{r})|\mathbf{r}'\rangle\langle\mathbf{r}'|\psi\rangle \\ &= \int d\mathbf{r}' d\mathbf{r}'' \psi^*(\mathbf{r}'')\psi(\mathbf{r}')\langle\mathbf{r}''|\hat{\sigma}(\mathbf{r})|\mathbf{r}'\rangle \end{aligned} \tag{A.7}$$

This identifies the real-space matrix elements of the electronic charge density field operator

$$\sigma_{\mathbf{r}''\mathbf{r}'}(\mathbf{r}) \equiv \langle\mathbf{r}''|\hat{\sigma}(\mathbf{r})|\mathbf{r}'\rangle = \delta(\mathbf{r} - \mathbf{r}')\delta(\mathbf{r} - \mathbf{r}''). \tag{A.8}$$

For a state decomposed into eigenmodes $|\psi\rangle = \sum_k c_i|i\rangle$, we have

$$\langle\psi|\hat{\sigma}(\mathbf{r})|\psi\rangle = \sum_{ij} \rho_{ij}\psi_i^*(\mathbf{r})\psi_j(\mathbf{r}) \tag{A.9}$$

where $\rho_{ij} = c_i^* c_j$ are the electronic populations and coherences. Note that this matches the usual field-theoretic definition of the charge density $\hat{\sigma}(\mathbf{r}) = \hat{\psi}^\dagger(\mathbf{r})\hat{\psi}(\mathbf{r})$

A.1.1 The One-Electron Charge Density Operator of a Many-Electron System

In this section, we extend the reasoning of the previous section to an n-electron state $|\Psi\rangle$. The real-space identity operator in the space spanned by such states is

$$\int d\mathbf{r}_1 \ldots d\mathbf{r}_n |\mathbf{r}_1, \ldots, \mathbf{r}_n\rangle\langle\mathbf{r}_1, \ldots, \mathbf{r}_n| \equiv \int \{d\mathbf{r}\}\big|\{\mathbf{r}\}\rangle\langle\{\mathbf{r}\}\big| \tag{A.10}$$

and the one-electron charge density is [182]

$$\begin{aligned}\int d\mathbf{r}_2 \ldots d\mathbf{r}_n \big|\Psi\left(\{\mathbf{r}\}\right)\big|^2 &= \langle\Psi|\hat{\sigma}(\mathbf{r})|\Psi\rangle \\ = \int \{d\mathbf{r}'\}\{d\mathbf{r}''\}\Psi^*(\{\mathbf{r}''\})\Psi(\{\mathbf{r}'\})\langle\{\mathbf{r}''|\hat{\sigma}(\mathbf{r})|\{\mathbf{r}'\}\rangle\end{aligned} \tag{A.11}$$

Since the charge-density operator is a one-electron operator, we have the straightforward n-electron generalization of Eq. (A.8)

$$\langle\{\mathbf{r}''|\hat{\sigma}(\mathbf{r})|\{\mathbf{r}'\}\rangle = \sum_m \delta(\mathbf{r} - \mathbf{r}'_l)\delta(\mathbf{r} - \mathbf{r}''_l) \prod_{m\neq l} \delta(\mathbf{r}'_m - \mathbf{r}''_m) \tag{A.12}$$

which is directly confirmed by substitution into Eq. (A.11) and gives

$$\langle\Psi|\hat{\sigma}(\mathbf{r})|\Psi\rangle = \sum_{ij} \rho_{ij}\sigma_{ij}(\mathbf{r}) \tag{A.13}$$

where we have identified

$$\sigma_{ij}(\mathbf{r}) = \int d\mathbf{r}_2 \dots d\mathbf{r}_n \Psi_i^*(\mathbf{r}_1, \dots \mathbf{r}_n)\Psi_j(\mathbf{r}_1, \dots \mathbf{r}_n) \tag{A.14}$$

We note that this result can equally well be obtained by use of real-space field operators for many-electron systems as explicated by Cederbaum [184]. Moreover, Eq. (A.14) is readily generalized to account for nuclear degrees of freedom $\mathbf{R}$ as

$$\hat{\sigma}_{ij}(\mathbf{r}) = \int d\mathbf{r}_2 \dots d\mathbf{r}_n \Psi_i^*(\mathbf{R}, \mathbf{r}_1, \dots \mathbf{r}_n)\Psi_j(\mathbf{R}, \mathbf{r}_1, \dots \mathbf{r}_n) \tag{A.15}$$

where the circumflex indicates that the left hand side remains an operator in the nuclear subspace due to dependence on $\mathbf{R}$

A.2 Frequency-Dispersed Photon Number Change

In this section, we present a derivation of the general frequency-dispersed signal defined in Eq. (1.9) using the dipolar (Eq. (1.8)) forms of the interaction Hamiltonian.

From Eqs. (1.8), (1.9), and (A.2), we have

$$S(\mathbf{k}_s, \Lambda) = i \int d\mathbf{r} dt \langle [\hat{N}_s, (\hat{\mathbf{E}}^{(+)} + \hat{\mathbf{E}}^{(-)}) \cdot \hat{\boldsymbol{\mathcal{V}}}] \rangle \tag{A.16}$$

where we suppress the interaction-picture time-dependence and $\mathbf{r}$-dependence for brevity.

Basic commutation relations of a harmonic oscillator give

$$[\hat{N}_s, \hat{\mathbf{E}}^{(-)}] = \hat{\mathbf{E}}^{(-)}_{\mathbf{k}_s} \tag{A.17}$$

$$[\hat{N}_s, \hat{\mathbf{E}}^{(+)}] = -\hat{\mathbf{E}}^{(+)}_{\mathbf{k}_s}, \tag{A.18}$$

which immediately yields

$$S(\mathbf{k}_s, \Lambda) = -\Im[\int d\mathbf{r}dt\langle\hat{\mathbf{E}}^{(-)}_{\mathbf{k}_\mathrm{s}}(\mathbf{r}, t) \cdot \hat{\boldsymbol{\mathcal{V}}}(\mathbf{r}, t)\rangle] \tag{A.19}$$

Equation (A.19) is sufficiently general to accomodate both spontaneous and stimulated signals. When considering the photon gain/loss of externally applied laser beams or pulses, it is permissible to take the field to be in a coherent state (i.e., an eigenstate of $\hat{a}$). Upon neglecting quantum fluctuations of the laser beams, this then reduces the signal to

$$S(\mathbf{k}_s, \Lambda) = -\Im[\int d\mathbf{r}dt\mathbf{E}^{(-)}_{\mathbf{k}_\mathrm{s}}(\mathbf{r}, t) \cdot \langle\hat{\boldsymbol{\mathcal{V}}}(\mathbf{r}, t)\rangle] = -\Im[\int dt\mathbf{E}^{*}(\mathbf{k}_\mathrm{s})e^{-i(\mathbf{k}_\mathrm{s}\cdot\mathbf{r}-\omega_\mathrm{s}t)} \cdot \langle\hat{\boldsymbol{\mathcal{V}}}(\mathbf{r}, t)\rangle] \tag{A.20}$$

$$= -\Im[\mathbf{E}^{*}(\mathbf{k}_\mathrm{s}) \cdot \langle\hat{\boldsymbol{\mathcal{V}}}(\mathbf{k}_s, \omega_s)\rangle] = -\Im[\sum_{\alpha} e^{-i\mathbf{k}_\mathrm{s}\cdot\mathbf{r}_\alpha}\mathbf{E}^{*}(\mathbf{k}_\mathrm{s}) \cdot \langle\hat{\mathbf{V}}(\mathbf{r}_\alpha, \omega_s)\rangle],$$

in which the electric field is now merely a spectral envelope function. Either of the time- or frequency-domain expressions may be preferred for simulation purposes depending on how the dipole expectation-value is more readily calculable. For example, in atomic or static molecular spectra, the frequency domain is most easily computed. In the more complex molecular calculations wherein the nuclear-dependencies and non-adiabatic couplings play a significant role, the dynamics may be sufficiently complicated that it is difficult to propogate for the long times necessary for a numeric evaluation of the Fourier Transform. In this manuscript, we only simulate heterodyne-detected signals (chapter 3) or off-resonant x-ray scattering (section 2.1). In both of these cases, the timing of the emission event is limited by the temporal field envelope (of the heterodyne or scattering pulse respectively).

Spontaneous emission can be accounted for by considering the case of a signal mode initially in the vacuum state $|0\rangle$. With this initial field state, the expectation value of $\hat{\mathbf{E}}_s^{(-)}$ vanishes to 0-th order. To obtain a leading-order expression for spontaneous emission, we thus expand to first order in the interaction with the signal mode. We can then trace over the signal mode while taking the remaining field modes to be in coherent states and replacing them by their classical field-envelopes. This is discussed under the minimal coupling interaction Hamiltonian in chapter 2.

The transient absorption signal is linear in the probe intensity and can be obtained from the time-dependent signal given in Eq. (A.20)

$$S(T) = -\Im \int dt \int_{-\infty}^{t} \mathcal{E}^*(t-T)\mathcal{E}(t-T)\langle \hat{V}_L(t)\hat{V}_-(t')\rangle_0 \tag{A.21}$$

where $\mathcal{E}(t-T)$ is the temporal field envelope shifted to be centered at zero argument and $\langle \dots \rangle_0$ indicates expectation value over the initial state. This expression can also be recast in Hilbert space as

$$\begin{aligned} S(T) = &-\Im \int_{-\infty}^{\infty} dt \int_{-\infty}^{t} d\tau \mathcal{E}^*(t-T)\mathcal{E}(\tau-T) \\ &\times \langle \Psi_0|U^\dagger(t,0)\hat{\mu}U(t,\tau)\hat{\mu}^\dagger U(\tau,0)|\Psi_0\rangle \end{aligned} \tag{A.22}$$

where we have seperated the molecular dipole operator into excitation/de-excitation parts $\mu^\dagger/\mu$ and assumed the rotating wave approximation. We have also explicitly written the time-dependence through the propagators $U(t,t') = \exp\left(-i\hat{H}(t-t')\right)$, which propagates the system from t' to t. The probe field is given by a gaussian

$$\mathcal{E}(t) = e^{-i\omega_L t - t^2/2\sigma^2}\,, \tag{A.23}$$

where ω_L is the center frequency and σ the temporal width of the laser pulse and T is the delay with respect to the initial state preparation.

Appendix B

Simulation Methods

In this appendix, we collect information on the methods used to simulate the various signals.

B.1 X-Ray Scattering and Raman Excitation of Cysteine

This section describes the calculations used chapter 2, section 2.2 The details of the electronic structure calculations can be found in Ref. [91], and are recounted briefly here. The optimized geometry of cysteine was obtained with the Gaussian09 package [185] at the B3LYP [186, 187]/6-311G** level of theory. All TDDFT calculations were done at the CAM-B3LYP [188]/6-311++G(2d,2p) level of theory, and with the Tamm-Dancoff approximation (TDA) [189]. It was found that TDDFT with this type of long-range-corrected density functionals and diffused basis functions can describe Rydberg states well [190, 191]. In these calculations, we include 50 valence excited states, with energies ranging from 5.4 eV to 9.0 eV. Core-excited states, in which a sulfur 1s electron is excited to the valence band, were calculated using restricted excitation windown (REW) TDDFT with a locally modified version of NWChem code [192, 193]. We also include 50 core-excited states for core excitations, with energies ranging from 2473.5 eV to 2495.9 eV (shifted to match experimental XANES results).

Transition density matrices between different valence excited states are calculated using the CI coefficients from the TDDFT/TDA results, and are therefore in an unrelaxed sense. More accurate relaxed state-to-state transition density matrices could be calculated using the Z-vector method [194, 195], and this research is ongoing.

B.2 Electronic Structure Calculations and Nonadiabatic Wavepacket Dynamics of NaF

The electronic structure of NaF used in section 2.3 was calculated with the program package Molpro [174] at the CAS(8/9)/MRCI/aug-cc-pVTZ level of theory. A Douglas-Kroll-Hess 10th order correction has been used [196, 197] to account for relativistic effects caused by the core electrons. All densities were evaluated from the state specific density matrices (and transition density matrices) $P^{(ij)}$, expanded in the atomic orbital basis functions $\phi(\mathbf{r})$:

$$\hat{\sigma}_{ij}(\mathbf{q};R) = \int \mathrm{d}\mathbf{r} \mathrm{e}^{-i\mathbf{q}\cdot\mathbf{r}} \sum_{rs} P_{rs}^{(ij)}(R)\phi_r^*(\mathbf{r};R)\phi_s(\mathbf{r};R). \tag{B.1}$$

The lowest potential energy surfaces are shown in Fig. 2.9 with the two states relevant for the dynamics being the ionic $X^1\Sigma$ state ($|g\rangle$) and the covalent $A^1\Sigma$ state ($|e\rangle$). The potential energy curves are similar to the ones from NaI [108]. The $X^1\Sigma$ and the $A^1\Sigma$ state are coupled via a nonadiabatic coupling matrix element which induces an avoided crossing at 8 Å . The electron jump between the ionic and covalent states at this long distance is sometimes known as harpooning [198, 199]. Both the transition dipole and the integrated transition density $\int dr|\sigma_{ge}|$ shown in Fig. B.1 peak at the avoided crossing point. The electronic density operators matrix elements $\sigma_{ik}^*(\mathbf{q};R)\sigma_{kj}(\mathbf{q};R)$ are displayed in Fig. B.2.

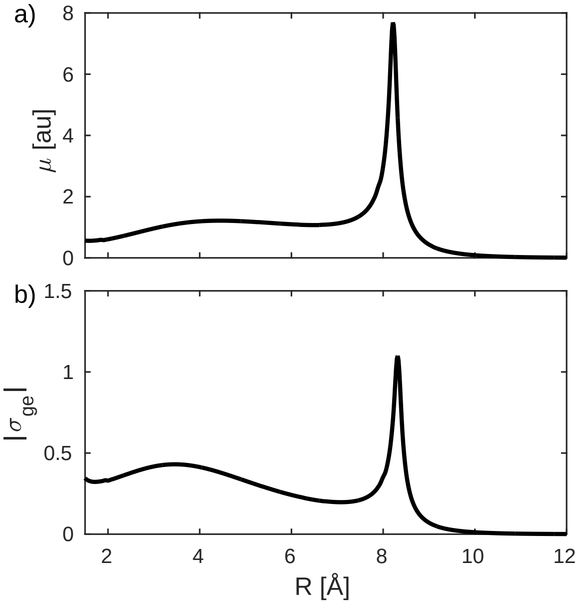

Figure B.1: Transition dipole moment μ_{ge} between the X and A states of NaF (a) and magnitude of the transition density σ_{ge} (b).

For clarity, only the projection along the direction of molecular axis obtained by integrating over the perpendicular directions is shown. The diagonal density σ_{ee}^2 (Fig. B.2 (a)) is clearly dominated by contributions from the core electrons and the stripe pattern reflects the bond length in reciprocal space (see Eq. 2.87). The transition density σ_{ge}^2 (Fig. B.2 (b)) mainly contains contributions from the valence orbitals that are involved in the $|e\rangle \leftrightarrow |g\rangle$ transition. Its magnitude is about 4 orders weaker than the diagonal matrix element (Fig. B.2 (a)). However, it peaks at the avoided crossing, making it most suitable for the detection of inelastic contributions. The mixed matrix element $\sigma_{ee}^{\dagger}\sigma_{eg}$ (Fig. B.2 (c)) is a product of the nuclear densities and the transition densities and its magnitude is about 2 orders weaker than the diagonal matrix element. The transition charge density may thus be measurable through this term in which it is amplified by the diagonal charge density.

Nuclear wavepacket dynamics simulations were carried out on a numerical grid in the nuclear coordinate R. This is a fully quantum mechanical non-perturbative calculation of the joint nuclear-electronic dynamics. The Hamiltonian, which describes the coupled electronic and

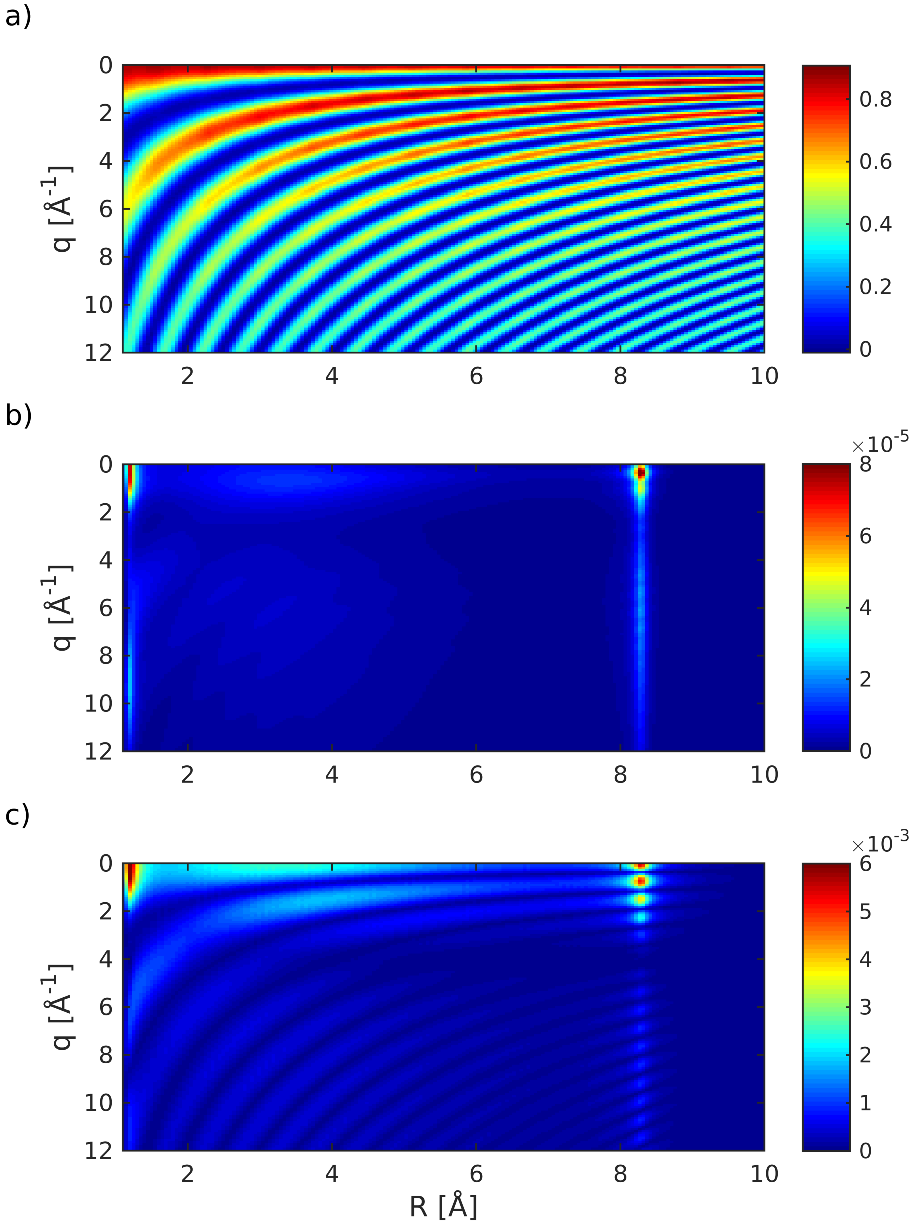

Figure B.2: Relevant density operator matrix elements in the nuclear subspace of NaF (obtained using Eq. (B.1)): (a) $\hat{\sigma}_{ee}^2(\mathbf{q}, R)$, (b) $\hat{\sigma}_{ge}^2(\mathbf{q}, R)$, (c) $|\hat{\sigma}_{ee}^\dagger(\mathbf{q}, R)\hat{\sigma}_{ge}(\mathbf{q}, R)|$.

vibrational degrees of freedom, is given by

$$\hat{H} = \begin{pmatrix} \hat{T} + V_g(R) & -E_{pu}(t)\mu_{eg}(R) + \hat{K}_{ge} \\ -E_{pu}(t)\mu_{ge}(R) - \hat{K}_{eg} & \hat{T} + V_e(R), \end{pmatrix} \tag{B.2}$$

where

$$\hat{T} = -\frac{1}{2m}\frac{\partial^2}{\partial R^2} \tag{B.3}$$

is the kinetic operator of the nuclei, m the reduced mass of the nuclei, and

$$\hat{K}_{ge} = \frac{1}{2m}\left(2f_{ge}\frac{\partial}{\partial R} + \frac{\partial}{\partial R}f_{ge}\right) \tag{B.4}$$

approximates the non-adiabatic couplings [103, 106]. We assume a Gaussian pump-pulse envelope

$$E_{pu}(t) = E_0 \cos(\omega t)\exp(-2\ln(2)t^2/w^2) \tag{B.5}$$

where w is the full width at half maximum of the intensity profile E_{pu}^2. The probe pulse is not included in the propagation but is treated pertubatively and included in the final signal calculation (Eq. (2.18)). The wave function $\chi(R,t)$ is obtained by propagating the vibrational ground state of the $X^1\Sigma$ state with a Chebychev scheme [173] using the Hamiltonian Eq. (B.2). The signal is then obtained by evaluating Eq. (2.84) and inserting the time-dependent wavefunctions and density operators $(\hat{\sigma}_{ik}^{\dagger}\hat{\sigma}_{kj})$, as shown in Fig. (B.2). The electronic coherence is obtained from the combined electronic-nuclear wave function as the overlap of the nuclear wave packets

$$\rho_{eg} = \langle \chi_e | \chi_g \rangle, \tag{B.6}$$

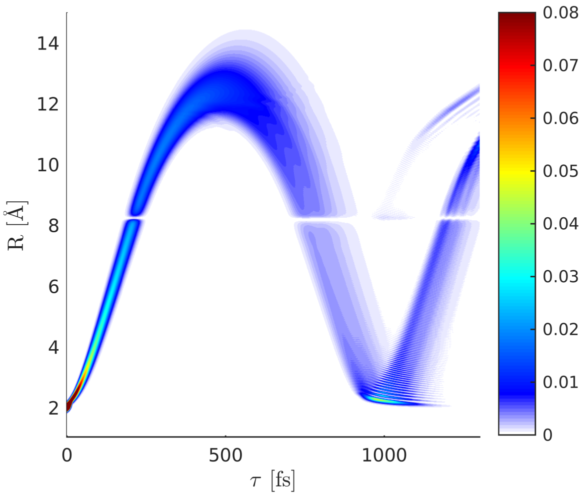

Figure B.3: Nuclear wavepacket dynamics in the covalent $A^1\Sigma$ state following excitation with a 10 fs pump-pulse (FWHM).

resulting in the decay and revival of the electronic coherence. The wavepacket dynamics in the excited state potential ($\chi_e(R,t)$) is depicted in Fig. B.3. The nuclear wavepacket passes through the avoided crossing between 200 and 240 fs and reaches its outer turning point around 500 fs.

Figure B.4 shows the time-dependent excited-state population alongside with the magnitude of the electronic coherence. When the wavepacket passes through the avoided crossing for the first time, $\approx 10\,\%$ of the population is transferred to the ground state and a coherence ρ_{eg} is created.

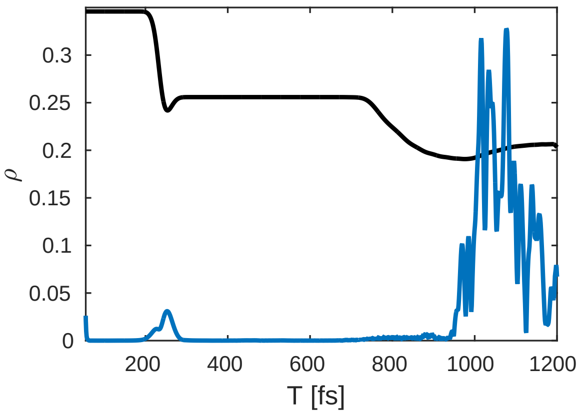

Figure B.4: Time evolution of the excited state population ($A^1\Sigma$, black) and the magnitude of the coherence $|\rho_{eg}|$ (blue). The inital coherence created by the pump-pulse ($T < 50\,\mathrm{fs}$) is not shown.

Table B.1: Parameters for the potentials shown in Fig. 4.2.

i	D_i [eV]	a_i [Å^{-1}]	$q_{0,i}$ [Å]	V_0 [eV]
S_0	3.0	1	2.0	0
S_1	0.01	2.43	2.5	3
S_2	3.0	1	2.3	4.5

B.3 Model Parameters for Cavity-Modified Photochemistry

The model potentials used in chapter 4, section 4.1.1 for the photonic-catalyst and photonic-bound-state models (shown in Fig. 4.2(a)) are obtained from Morse potentials:

$$V_i(q) = D_i\left[1 - \exp\left(-a_i(q - q_{0,i})\right)\right]^2 + V_0 \tag{B.7}$$

The respective parameters are given in table B.1. The transition dipole shown in Fig. 4.2(b) is defined by the sigmoid function:

$$\mu(q) = \frac{4}{1 + \exp[2.4575(q - 4.232)]} \tag{B.8}$$

Wavepacket propagations are carried out on a numerical grid using the Hamiltonian from Eq. (4.25) where the nuclear kinetic energy was calculated using a reduced mass of $m = 3650$au. For all dissociative potentials, the kinetic energy term $\hat{T}$ is replaced by a perfectly matched layer [200] to avoid spurious reflections at the edge of the grid. The time evolution is calculated with an Arnoldi propagation scheme [175, 201].

Appendix C

Geometric Derivations for Cascading

In this appendix, we collect several derivations used in chapter 3.

C.1 Cylindrical Geometry

In this section, we describe the derivation of I for the case of a cylindrical geometry as discussed in Section 3.2, case (iii). The field Green function in this case has a form

$$\begin{aligned} G(\boldsymbol{r}_a, \boldsymbol{r}_b; \omega_b) &= \frac{1}{\sqrt{(x_a - x_b)^2 + (y_a - y_b)^2 + (z_a - z_b)^2}} e^{i \frac{\omega_b}{c} \sqrt{(x_a - x_b)^2 + (y_a - y_b)^2 + (z_a - z_b)^2}} \\ &- \frac{1}{\sqrt{(x_a - x_b)^2 + (y_a - y_b)^2 + (z_a + z_b)^2}} e^{i \frac{\omega_b}{c} \sqrt{(x_a - x_b)^2 + (y_a - y_b)^2 + (z_a + z_b)^2}} \\ &= G_M(\boldsymbol{r}_a, \boldsymbol{r}_b; \omega_b) + G_S(\boldsymbol{r}_a, \boldsymbol{r}_b; \omega_b), \end{aligned} \tag{C.1}$$

where G_M is the field Green function in the complete space $\mathbb{R}^3$, and G_S is the correction associated with the surface S, determined by the condition $z = 0$, so that G is the complete Green function in the half-space $z \geq 0$, with the reflecting boundary conditions. The representation of Eq. (C.1) represents the integral I of Eq. (3.49)

$$I(\boldsymbol{r}_a, \boldsymbol{k}_b, \omega_b) = I_M(\boldsymbol{r}_a, \boldsymbol{k}_b, \omega_b) + I_S(\boldsymbol{r}_a, \boldsymbol{k}_b, \omega_b) \tag{C.2}$$

We start with computing I_M; the second integral I_S is computed in a similar fashion. Fixing z we compute the integral over the corresponding cross section

$$I(z_b; \boldsymbol{r}_a, \boldsymbol{k}_b, \omega_b) = e^{ik_b(z_b - z_a)} \int_{S_z} dxdy G_M(\boldsymbol{r}_a, x_b, y_b, z_b; \omega_b), \quad S_z = \{(x, y) \mid (x, y, z) \in V\} \tag{C.3}$$

by using inhomogeneous polar coordinates with the center in (x_a, y_a) followed by integration over the inhomogeneous radius, resulting in

$$I_M(z_b; \boldsymbol{r}_a, \boldsymbol{k}_b, \omega_b) = 2\pi i \frac{c}{\omega_b} e^{ik_b(z_b - z_a) + i\frac{\omega_b}{c}|z_b - z_a|} - i\frac{c}{\omega_b} e^{ik_b(z_b - z_a)} \int_0^{2\pi} d\varphi e^{i\frac{\omega_b}{c}\sqrt{(R\xi(\varphi))^2 + (z_0 - z)^2}}. \tag{C.4}$$

The integration is performed in a similar way to how it has been carried out for the $2D$ case, using the identity

$$\frac{\xi^2 r_b dr_b}{\sqrt{(\xi r_b)^2 + (z_a - z_b)^2}} = d\sqrt{(\xi r_b)^2 + (z_a - z_b)^2}, \tag{C.5}$$

and the fact that the projection of $\boldsymbol{k}_b$ onto the plane is 0. For the surface contribution we obtain in a similar way

$$I_S(z_b;\boldsymbol{r}_a,\boldsymbol{k}_b,\omega_b) = 2\pi i\frac{c}{\omega_b}e^{ik_b(z_b+z_a)+i\frac{\omega_b}{c}|z_a+z_b|} - i\frac{c}{\omega_b}e^{ik_b(z_b+z_a)}\int_0^{2\pi} d\varphi e^{i\frac{\omega_b}{c}\sqrt{(R\xi(\varphi))^2+(z_a+z_b)^2}} \tag{C.6}$$

By a similar to case (ii) argument, which involves saddle-point approximation for computing a fast oscillating integral, the second contribution in the r.h.s. of Eq. (C.4) and (C.6) can be neglected resulting in

$$\begin{aligned} I_M(z_b;\boldsymbol{r}_a,\boldsymbol{k}_b,\omega_b) &= 2\pi i\frac{c}{\omega_b}e^{ik_b(z_b-z_a)+i\frac{\omega_b}{c}|z_b-z_a|} \\ I_S(z_b;\boldsymbol{r}_a;\omega_b,V) &= 2\pi i\frac{c}{\omega_b}e^{ik_b(z_b+z_a)+i\frac{\omega_b}{c}|z_b+z_a|}. \end{aligned} \tag{C.7}$$

Finally performing integration over z we obtain

$$\begin{aligned} I(\boldsymbol{r}_a,\boldsymbol{k}_b,\omega_b) &= 2\pi i\frac{c}{\omega_b}\Bigg[e^{i\frac{\omega_b}{c}z_a}e^{\frac{i(k_b-\frac{\omega_b}{c})z_a}{2}}z_a\mathrm{sinc}\left(\frac{(\frac{\omega_b}{c}-k_b)z_a}{2}\right) \\ &+ e^{-i\frac{\omega_b}{c}z_a}e^{\frac{i(k_b+\frac{\omega_b}{c})(l+z_a)}{2}}(l-z_a)\mathrm{sinc}\left(\frac{(\frac{\omega_b}{c}+k_0)(l-z_0)}{2}\right) \\ &+ e^{i\frac{\omega_b}{c}z_a}e^{\frac{i(k_b-\frac{\omega_b}{c})z_a}{2}}z_a\mathrm{sinc}\left(\frac{(\frac{\omega_b}{c}-k_b)z_a}{2}\right)\Bigg], \end{aligned} \tag{C.8}$$

where we have expressed the answer in terms of the sinc function

$$\mathrm{sinc}(x) = \frac{\sin x}{x}, \tag{C.9}$$

with the properties $\mathrm{sinc}(x) \approx 1$, for $|x| \ll 1$, and $|\mathrm{sinc}(x)| \leq |x|^{-1}$. In the case $|\omega_b - k_b|l \ll 1$

of a good phase matching and if z_a is not within the wavelength scale from the borders, the first contribution is dominating, so that we reproduce a well-known result

$$I(\boldsymbol{r}_a, \boldsymbol{k}_b, \omega_b) = 2\pi i \frac{c}{\omega_b} z_a e^{ik_b z_a}. \tag{C.10}$$

C.2 Integration Measure for Inhomogeneous Coordinates

C.2.1 Polar Coordinates

In this section we compute the integration measure for inhomogeneous polar coordinates. Inhomogeneous in this context mans that the radius depends on the angle. Formally, let $\xi(\varphi)$ be a positively-defined function of angle that has a property that the region $\{\boldsymbol{r} \in \mathbb{R}^2 \mid r(\boldsymbol{r}) \leq \xi(\varphi \boldsymbol{r})\}$ is convex, where $r(\boldsymbol{r})$ and $\varphi(\boldsymbol{r})$ are the standard polar coordinates of $\boldsymbol{r}$. The inhomogeneous polar coordinates are defined by

$$r_x = r\xi(\varphi)\cos\varphi, \quad r_y = r\xi(\varphi)\sin\varphi. \tag{C.11}$$

It is easy to demonstrate that the inhomogeneous polar coordinates is a well-defined coordinate system for the region defined by the condition $r < r_0$ for any r_0, provided the convexity condition is satisfied. A reverse statement is also true, i.e., for any connected convex region and any reference point in it one can (and very easily) identify r_0 and $\xi(\varphi)$ so that the region is defined by the condition $r < r_0$ in the inhomogeneous polar coordinate system, centered in the reference point.

To compute the integration measure we first differentiate

$$
\begin{aligned}
dr_x &= \xi \cos\varphi dr + r\left(\frac{\partial\xi}{\partial\varphi}\cos\varphi - \xi\sin\varphi\right)d\varphi \\
dr_y &= \xi \sin\varphi dr + r\left(\frac{\partial\xi}{\partial\varphi}\sin\varphi + \xi\cos\varphi\right)d\varphi
\end{aligned} \tag{C.12}
$$

and then apply the concept of the wedge (i.e., antisymmetric) product to obtain

$$
\begin{aligned}
dr_x \wedge dr_y &= r\xi\cos\varphi dr \wedge r\left(\frac{\partial\xi}{\partial\varphi}\sin\varphi + \xi\cos\varphi\right)d\varphi \\
&+ r\left(\frac{\partial\xi}{\partial\varphi}\cos\varphi - \xi\sin\varphi\right)d\varphi \wedge \xi\sin\varphi dr = r\xi^2(\varphi)dr\wedge d\varphi
\end{aligned} \tag{C.13}
$$

where in the derivation we have used the antisymmetric properties of the wedge product, namely $dr \wedge dr = d\varphi \wedge d\varphi = 0$ and $d\varphi \wedge dr = -dr \wedge d\varphi$. This provides a very simple result for the integration measure

$$dr_x dr_y = \xi^2(\varphi) r dr d\varphi, \tag{C.14}$$

in particular the integration measure does not contain derivative of the function $\xi(\varphi)$ that describes the inhomogeneity of the coordinate system. We will refer to the above property as the homogeneous property of the inhomogeneous coordinate system.

C.2.2 Spherical Coordinates

An inhomogeneous spherical coordinate system is introduced in a similar way:

$$r_x = r\xi(\theta,\varphi)\sin\theta\cos\varphi, \quad r_y = r\xi(\theta,\varphi)\sin\theta sin\varphi, \quad r_z = r\xi(\theta,\varphi)\cos\theta. \tag{C.15}$$

Obviously, the inhomogeneous spherical system satisfies the same convexity properties as the inhomogeneous polar system. A much more tedious computation, similar to the one for the polar system, presented in Eq. (C.13), provides a very simple result

$$dr_x dr_y r_z = \xi^3(\theta,\varphi) r^2 \sin\theta dr d\theta d\varphi = \xi^3(\boldsymbol{n}) r^2 dr d\boldsymbol{n}, \tag{C.16}$$

which shows that the measure is also homogeneous. This means that the homogeneity of an inhomogeneous measure takes place in all dimensions, and there is a general geometrical argument that derives Eq. (C.16) for all dimensions that bypasses tedious computations.

C.2.3 Estimates for the Boundary Contributions Using the Saddle-Point Approximation

We start with the $2D$ case Denoting in Eq. (3.54)

$$S(\varphi) = (\omega_0 + k_0\cos\varphi) a\xi(\varphi) \tag{C.17}$$

we obtain in the saddle-point approximation

$$I_1 = \frac{1}{\sqrt{2\pi\lambda_0}} \frac{1}{\omega_0 + k_0 \cos\varphi_0} e^{i(\omega_0 + k_0 \cos\varphi_0) a \xi(\varphi_0)}, \quad \left(\frac{dS(\varphi)}{d\varphi} \right)_{\varphi=\varphi_0} = 0, \quad \lambda_0 = \left(\frac{d^2 S(\varphi)}{d\varphi^2} \right)_{\varphi=\varphi_0} \tag{C.18}$$

Estimating $\lambda_0 \sim a\omega_0 \gg 1$ we see that I_1 is small compared to I_0 by a factor $\sim (\sqrt{a\omega_0})^{-1}$.

Appendix D

Cavity-Molecule Coupling Beyond the Rotating Wave Approximation

D.1 Working Formulas for the Tunable-Coherent-State Basis

It is a known fact that eigenvectors corresponding to distinct eigenvalues are orthogonal. Thus, working with the normalized coefficients c_{nl}

$$\langle\epsilon_k|\epsilon_l\rangle = \delta_{kl}\langle\epsilon_l|\epsilon_l\rangle = \sum_{mn=0}^{M} c_{mk}c_{nl}\left(\langle\alpha_k, m|\alpha_l, n\rangle + (-1)^{n+m}\pi_k\pi_l\langle-\alpha_k, m| - \alpha_l, n\rangle\right) \quad \text{(D.1)}$$

where

$$|\alpha_l, n\rangle \equiv (\hat{a}^\dagger)^n e^{\alpha_l \hat{a}^\dagger}|0\rangle \quad \text{(D.2)}$$

is the (un-normalized) n-photon-added coherent state with parameter α_l. For this orthogonality relation and for other purposes, we will need the quantity

$$\langle\alpha_k, m|\alpha_l, n\rangle = \sum_{pq=0}^{\infty} \langle q+m| \frac{\alpha_k^q \alpha_l^p \sqrt{q+m}\sqrt{p+n}}{q!p!} |p+n\rangle = \sum_{p=0}^{\infty} \frac{\alpha_l^p \alpha_k^{p+n-m}(p+n)!}{p!(p+n-m)!} \tag{D.3}$$

This last formula is only valid for $n > m$ but, since all quantities in this overlap are real, it is symmetric with respect to the simultaneous exchange $k \leftrightarrow l$, $n \leftrightarrow m$ so that this presents no difficulty. This form is convenient for seeing symmetries such as

$$\begin{aligned} \langle -\alpha_k, m| -\alpha_l, n\rangle &= (-1)^{n+m}\langle\alpha_k, m|\alpha_l, n\rangle \qquad \text{(D.4)} \\ \langle\alpha_k, m| -\alpha_l, n\rangle &= (-1)^{n+m}\langle -\alpha_k, m|\alpha_l, n\rangle \end{aligned}$$

and others that arise later in calculating the non-BOA couplings. For now, we use these relations to reduce the orthonormality condition to

$$\delta_{kl} = (1+\pi_k\pi_l) \sum_{mn=0}^{M} c_{mk}c_{nl}\langle\alpha_k, m|\alpha_l, n\rangle = (1+\pi_k\pi_l)\, A_{kl}^{(1)}(\mathbf{q}) \tag{D.5}$$

where the last equality defines $A_{kl}^{(1)}$ which depends on $\mathbf{q}$ indirectly via the g and Δ. It is clear from the pre-factor that this condition is automatically satisfied for $\pi_k\pi_l = -1$, corresponding to states of opposite parity, while considering states of the same parity restricts $A_{kl}^{(1)}$ to vanish for $k \neq l$. The orthonormality condition also directly determines the initial coefficients c_{0l}. From Eqs. (4.32)-(4.33) and (D.3), (D.5), it is clear that it is not practical to solve directly for the normalized coefficients c_{nl}. In practice, one must first solve for a set of un-normalized coefficients using some other initial coefficient $\tilde{c}_{0l}$ (which we take to be 1 for all states) and then normalize after the fact. This will be discussed further in section D.3

In calculating signals, we will be interested in evaluating expectation values or correlation functions of electronic operators such as the dipole or polarizability. The propagators in such an expression are easily evaluated via diagonalizing the truncated non-BOA Hamiltonian or a real-time propagation scheme. However, we will also need the operator matrix elements in the eigenbasis

$$\begin{gathered}\hat{\mathcal{O}}_{kl}(\mathbf{q}) = \langle \epsilon_k | \hat{\mathcal{O}}(\mathbf{q}) | \epsilon_l \rangle = \\ \hat{\mathcal{O}}_{++}(\mathbf{q}) \sum_{mn=0}^{M} c_{mk} c_{nl} \langle \alpha_k, m | \alpha_l, n \rangle + \hat{\mathcal{O}}_{--}(\mathbf{q}) \pi_k \pi_l \sum_{mn=0}^{M} c_{mk} c_{nl} \langle \alpha_k, m | \alpha_l, n \rangle \\ + \hat{\mathcal{O}}_{+-}(\mathbf{q}) \pi_l \sum_{mn=0}^{M} (-1)^n c_{mk} c_{nl} \langle \alpha_k, m | -\alpha_l, n \rangle + \hat{\mathcal{O}}_{-+}(\mathbf{q}) \pi_k \sum_{mn=0}^{M} (-1)^m c_{mk} c_{nl} \langle -\alpha_k, m | \alpha_l, n \rangle\end{gathered} \tag{D.6}$$

Where we have written the $\mathbf{q}$-dependence for $\hat{\mathcal{O}}$ explicitly while omitting this dependence from the other variables (g and Δ and through them, the coefficients c_n as well as the α) for brevity. Defining the following summation

$$B_{kl}^{(1)}(\mathbf{q}) \equiv \sum_{mn=0}^{M} (-1)^n c_{mk} c_{nl} \langle \alpha_k, m | -\alpha_l, n \rangle, \tag{D.7}$$

we obtain

$$\begin{aligned}\hat{\mathcal{O}}_{kl} = & \frac{\hat{\mathcal{O}}_{gg} + \hat{\mathcal{O}}_{ee}}{2} (1 + \pi_k \pi_l) A_{kl}^{(1)} + \frac{\hat{\mathcal{O}}_{gg} - \hat{\mathcal{O}}_{ee}}{2} (\pi_k + \pi_l) B_{kl}^{(1)} \\ & + \Re\{\hat{\mathcal{O}}\}_{eg} (1 - \pi_k \pi_l) A_{kl}^{(1)} + i \Im\{\hat{\mathcal{O}}_{eg}\} (\pi_l - \pi_k) B_{kl}^{(1)}\end{aligned} \tag{D.8}$$

where we have suppressed the $\mathbf{q}$-dependence for brevity. The $B_{kl}^{(1)}$ are complementary to the $A_{kl}^{(1)}$, differing only by the placement of the minus signs, and arise from cross terms between $|+\rangle$ and $|-\rangle$. Two particular operators are relevant for our purposes. The ionic state projection operator $|e\rangle\langle e| \equiv \hat{P}_e$ is given by

$$(\hat{P}_e)_{kl} = \frac{\delta_{kl} - (\pi_k + \pi_l) B_{kl}^{(1)}(\mathbf{q})}{2} \tag{D.9}$$

and the transition dipole operator (or any operator with vanishing diagonal elements in the bare space) is given by

$$\hat{\mu}_{kl}(\mathbf{q}) = \Re\{\hat{\mu}\}_{eg}(\mathbf{q})(1-\pi_k\pi_l)A^{(1)}_{kl}(\mathbf{q}) + i\Im\{\hat{\mu}\}_{eg}(\mathbf{q})(\pi_l-\pi_k)B^{(1)}_{kl}(\mathbf{q}) \to \hat{\mu}_{eg}(\mathbf{q})(1-\pi_k\pi_l)A^{(1)}_{kl} \tag{D.10}$$

where the last relation is on the assumption of real transition dipole moments. We notice that this expression, whether real or complex, clearly vanishes for states of the same parity (as would be expected by the symmetry of the dipole operator). These two special cases correspond to the observables considered in the main text.

D.2 Derivation of the Non-BOA Couplings

To propagate nuclear wavepackets along the energy surfaces will require the non-BOA couplings f_{kli}, h_{kli}, which we obtain in this section. Since we will have frequent occasion to consider the derivative by the i-th nuclear coordinate, we notate such derivatives by a prime for brevity (i.e., $\nabla_i[...] \equiv [...]'$ and there is no ambiguity since no terms mix nuclear derivatives) in the appendix. Using the expansion for the eigenstates (Eq. (4.30)) and the product rules, we have

$$\begin{aligned} f_{kli} = \langle\epsilon_k|\nabla_i|\epsilon_l\rangle &= \langle+|\nabla_i|+\rangle A^{(1)}_{kl} + \langle-|\nabla_i|-\rangle \pi_k\pi_l A^{(1)}_{kl} \\ &+ \langle+|\nabla_i|-\rangle \pi_l B^{(1)}_{kl} + \langle-|\nabla_i|+\rangle \pi_k B^{(1)}_{kl} \\ &+ (1+\pi_k\pi_l)\sum_{mn=0}^{M} c_{mk}c'_{nl}\langle\alpha_k, m|\alpha_l, n\rangle \\ &+ \alpha'_l(1+\pi_k\pi_l)\sum_{mn=0}^{M} c_{mk}c_{nl}\langle\alpha_k, m|\alpha_l, n+1\rangle \end{aligned} \tag{D.11}$$

where we have used $\nabla_i|\pm\alpha, n\rangle = \pm\alpha'|\pm\alpha, n+1\rangle$ and $\langle-\alpha_k, m|-\alpha_l, n+1\rangle = (-1)^{n+m+1}\langle\alpha_k, m|\alpha_l, n+1\rangle$, easily obtained from equations (D.2)-(D.3). From basic considerations, $\langle e|\nabla_i|g\rangle =$

$-\langle g|\nabla_i|e\rangle$ so that $\langle +|\partial_q|+\rangle = 0 = \langle -|\partial_q|-\rangle$ and the first two terms in the above vanish. The derivative coupling can then be easily written as

$$f_{kli} = \langle e|\nabla_i|g\rangle(\pi_l - \pi_k)B_{kl}^{(1)} + (1 + \pi_k\pi_l)\left[A_{kl}^{(2)} + \alpha_l' A_{kl}^{(3)}\right] \tag{D.12}$$

where, for brevity, we have defined shorthand for two additional summations

$$\begin{aligned} A_{kl}^{(2)}(\mathbf{q}) &\equiv \sum_{mn=0}^{M} c_{mk}c_{nl}'\langle \alpha_k, m|\alpha_l, n\rangle \\ A_{kl}^{(3)}(\mathbf{q}) &\equiv \sum_{mn=0}^{M} c_{mk}c_{nl}\langle \alpha_k, m|\alpha_l, n+1\rangle. \end{aligned} \tag{D.13}$$

The first term in Eqn. (D.12) is simply the result of transforming a purely molecular-electronic operator with the appropriate symmetries and is thus proportional to the derivative coupling in the bare basis. The second term contains the two summations $A^{(2)}$ and $A^{(3)}$ which originate from the $\mathbf{q}$-derivative acting on the coefficients c_{nl} and the photonic state $|\alpha_l, n\rangle$ respectively.

To calculate the second-derivative coupling is somewhat more difficult but we can use the separation

$$h_{kli} = \langle \epsilon_k|\nabla_i^2|\epsilon_l\rangle = \nabla_i\langle \epsilon_k|\nabla_i|\epsilon_l\rangle - \langle \nabla_i\epsilon_k|\nabla_i|\epsilon_l\rangle = \nabla_i f_{kli} - F_{kli} \tag{D.14}$$

where the last equality defines F_{kli} and the first term can be calculated numerically from the

f_{kli} already obtained above. From

$$\nabla_i|\epsilon_l\rangle = \sum_{n=0}^{M}\Big[\nabla_i|+\rangle\otimes c_{nl}|\alpha_l,n\rangle + \pi_l\nabla_i|-\rangle\otimes(-1)^n c_{nl}|-\alpha_l,n\rangle + |+\rangle\otimes c'_{nl}|\alpha_l,n\rangle \tag{D.15}$$

$$+\,\alpha'_l|+\rangle\otimes c_{nl}|\alpha_l,n+1\rangle + \pi_l|-\rangle\otimes(-1)^n c'_{nl}|-\alpha_l,n\rangle$$

$$-\,\alpha'_l\pi_l|-\rangle\otimes(-1)^n c_{nl}|-\alpha_l,n+1\rangle\Big]$$

it is straightforward, if somewhat tedious, to calculate the F_{kli}. It is convenient to separate the result into three terms

$$F_{kli} = \sum_{j=1}^{3} F_{kli}^{(j)} \tag{D.16}$$

based on where the $\mathbf{q}$-derivatives (the ∇_i) act. The first term arises from transforming F from the $|e\rangle, |g\rangle$ basis as though it were an ordinary electronic operator

$$\begin{aligned}F_{kli}^{(1)} &= \frac{F_{gg}+F_{ee}}{2}(1+\pi_k\pi_l)A_{kl}^{(1)} + \frac{F_{gg}-F_{ee}}{2}(\pi_l+\pi_k)B_{kl}^{(1)} \\ &\quad + \Re\{F_{eg}\}(1-\pi_k\pi_l)A_{kl}^{(1)} + i\Im\{F_{eg}\}(\pi_l-\pi_k)B_{kl}^{(1)}.\end{aligned} \tag{D.17}$$

This is an unsurprising result and easily calculated from the bare F and the already-obtained $A^{(1)}, B^{(1)}$. The $F^{(1)}$ contribution can be thought of as collecting the terms in which both (of the two available) $\mathbf{q}$-derivatives act on the bare molecule states $|+\rangle$, $|-\rangle$ (due exclusively to the first two terms in Eq. (D.15)). The second term contributing to F_{kl} arises when only one $\mathbf{q}$-derivative acts on the bare molecular states, while the other acts on the coefficients c_{nl} or the photonic state $|\alpha_l, n\rangle$ (i.e., cross terms between the first two and latter four elements of Eq. (D.15)). These contributions come as

$$F_{kli}^{(2)} = \Big\{f_{egi}(\pi_k-\pi_l)\big[B_{kl}^{(2)} - \alpha'_l B_{kl}^{(3)}\big]\Big\} + k\leftrightarrow l, \tag{D.18}$$

where we have defined two more associated summations

$$
\begin{aligned}
B^{(2)}_{kl}(\mathbf{q}) &\equiv \sum_{mn=0}^{M} (-1)^n c_{mk} c'_{nl} \langle \alpha_k, m| - \alpha_l, n\rangle \\
B^{(3)}_{kl}(\mathbf{q}) &\equiv \sum_{mn=0}^{M} (-1)^n c_{mk} c_{nl} \langle \alpha_k, m| - \alpha_l, n+1\rangle
\end{aligned}
\tag{D.19}
$$

that again differ from their respective A summations only by the minus signs. These again arise as cross terms between $|+\rangle$ and $|-\rangle$ states with derivative operators intervening (directly leading to the matrix element f_{egi}). The final contribution to F_{kli} arises when both **q**-derivatives act on coefficients or photonic states. There are several ways to distribute the derivative operations leading to

$$
F^{(3)}_{kli} = (1-\delta_{kl})(1+\pi_k\pi_l)(\alpha'_l A^{(4)}_{kl} + \alpha'_k A^{(4)}_{lk} + \alpha'_k \alpha'_l A^{(5)}_{kl} + A^{(6)}_{kl})
\tag{D.20}
$$

where

$$
\begin{aligned}
A^{(4)}_{kl}(\mathbf{q}) &\equiv \sum_{mn=0}^{M} c'_{mk} c_{nl} \langle \alpha_k, m|\alpha_l, n+1\rangle \\
A^{(5)}_{kl}(\mathbf{q}) &\equiv \sum_{mn=0}^{M} c_{mk} c_{nl} \langle \alpha_k, m+1|\alpha_l, n+1\rangle \\
A^{(6)}_{kl}(\mathbf{q}) &\equiv \sum_{mn=0}^{M} c'_{mk} c'_{nl} \langle \alpha_k, m|\alpha_l, n\rangle
\end{aligned}
\tag{D.21}
$$

are the three relevent ways to distribute the two **q**-derivatives betwen the coefficients and photon modes (the remaning conceivable combination doesn't contribute due to orthogonality) and the factor $(1-\delta_{kl})$ is introduced to make clear that $F^{(3)}$ vanishes for diagonal elements (this can be shown analytically using the results of the following section).

D.3 Normalization

As mentioned briefly in appendix D.1 above, it is not convenient to solve directly for the normalized coefficients c_{nl}. Instead, we recursively determine un-normalized coefficients $\tilde{c}_{nl}$ using the initial condition $\tilde{c}_{0l} = 1$ and then normalize afterwards. Thus, the normalization constant is

$$c_{0l} = \frac{1}{\sqrt{2\tilde{A}^{(1)}_{ll}(\mathbf{q})}} \tag{D.22}$$

where the "tilde" indicates that the un-normalized coefficients $\tilde{c}_{nl}$ were used rather than the normalized c_{nl} as implied by Eq. (D.5) and we can clearly obtain

$$A^{(1)}_{kl} = \frac{\tilde{A}^{(1)}_{kl}}{2\sqrt{\tilde{A}^{(1)}_{kk}\tilde{A}^{(1)}_{ll}}} \equiv \bar{A}^{(1)}_{kl}. \tag{D.23}$$

This last definition is superfluous for the $A^{(1)}$ summation but the consequences of a **q**-dependent normalization will not always be quite so straightforward and defining the quantities

$$\bar{A}^{(j)}_{kl} = \frac{\tilde{A}^{(j)}_{kl}}{2\sqrt{\tilde{A}^{(1)}_{kk}\tilde{A}^{(1)}_{ll}}} \qquad \bar{B}^{(j)}_{kl} = \frac{\tilde{B}^{(j)}_{kl}}{2\sqrt{\tilde{A}^{(1)}_{kk}\tilde{A}^{(1)}_{ll}}} \tag{D.24}$$

facilitates compact expression of the correction terms. This straigthforward normalization procedure only runs into difficulties when the **q**-derivative of the coefficients c_{nl} are called for. As will becomes apparent from numerical implementation, the relative size of these coefficients spans many orders of magnitude, complicating numerical differentiation of the normalized coefficients. However, as we will show below, they can be obtained via a recurrence relation. We thus summarize the connections between normalized and un-normalized quantities

$$\begin{aligned}
A_{kl}^{(j)} &= \bar{A}_{kl}^{(j)}, \quad j = 1,3,5 \\
B_{kl}^{(j)} &= \bar{B}_{kl}^{(j)}, \quad j = 1,3 \\
A_{kl}^{(2)} &= \bar{A}_{kl}^{(2)} - (\bar{A}_{ll}^{(2)} + \alpha'_l \bar{A}_{ll}^{(3)})\bar{A}_{kl}^{(1)} \\
B_{kl}^{(2)} &= \bar{B}_{kl}^{(2)} - (\bar{A}_{ll}^{(2)} + \alpha'_l \bar{A}_{ll}^{(3)})\bar{B}_{kl}^{(1)} \\
A_{kl}^{(4)} &= \bar{A}_{kl}^{(4)} - (\bar{A}_{kk}^{(2)} + \alpha'_k \bar{A}_{kk}^{(3)})\bar{A}_{kl}^{(3)} \\
A_{kl}^{(6)} &= \bar{A}_{kl}^{(6)} - \left[(\bar{A}_{ll}^{(2)} + \alpha'_l \bar{A}_{ll}^{(3)})\bar{A}_{lk}^{(2)} + k \leftrightarrow l\right] + (\bar{A}_{kk}^{(2)} + \alpha'_k \bar{A}_{kk}^{(3)})(\bar{A}_{ll}^{(2)} + \alpha'_l \bar{A}_{ll}^{(3)})\bar{A}_{kl}^{(1)}
\end{aligned} \tag{D.25}$$

where we have used the readily-confirmed identity

$$\nabla_i \tilde{A}_{ll}^{(1)} = 2(\tilde{A}_{ll}^{(2)} + \alpha'_l \tilde{A}_{ll}^{(3)}) \tag{D.26}$$

One can thus begin with the un-normalized coefficients $\tilde{c}_{nl}$ obtained from the initial condition $\tilde{c}_{0l} = 1$ and Eqs. (4.32)-(4.33). One can then normalize the coefficients c_{nl} via Eq. (D.22) and the amplitudes $\tilde{A}_{ll}^{(1)}$ before calculating all auxilliary summations directly from the c_{nl}. Alternatively, one can work with the un-normalized coefficients $\tilde{c}_{nl}$ and the un-normalized summations $\tilde{A}$ and $\tilde{B}$ can then be easily calculated and normalized afterwards via Eq. (D.25). However, to do this requires the nuclear derivative of the un-normalized coefficients, $\tilde{c}'_{nl}$. These can of course be obtained numerically but the better way is to take the derivative of the original recurrance relation to obtain

$$\begin{aligned}
-g(n+1)\tilde{c}'_{n+1} = &- \left[(n+\pi_l)\frac{\Delta}{2}\tilde{c}'_n + (\alpha_l + g)\tilde{c}'_{n-1} - \pi_l(-1)^n \frac{\Delta}{2}\sum_{j=0}^{n} \frac{(2\alpha_l)^j}{j!}\tilde{c}'_{n-j}\right] \\
&+ (n+1)\tilde{c}_{n+1}(g' - g\frac{\Delta'}{\Delta}) + n\tilde{c}_n(2g\alpha'_l - \frac{\Delta}{\Delta}) \\
&+ \tilde{c}_{n-1}(g' + \alpha'_l(2n - 1 + \Delta\pi_l) - \frac{\Delta'}{\Delta}(\alpha_l + g)) + 2\alpha_l \tilde{c}_{n-2}(\alpha_l + g)
\end{aligned} \tag{D.27}$$

where we have used the original recursion relation to simplify the result. The derivatives of coefficients then depend only on the g, Δ, α, which are already available, and their derivatives g', Δ', α', the former two of which can be obtained numerically while the latter can be obtained self-consistently from the truncation relation (i.e., setting $\tilde{c}'_M = 0$). In this paper, we take this latter approach to avoid numerically differentiating the coefficients.

D.4 Summary of Formulas

In this section, we summarize the final formulas obtained for all key quantities. Namely, the The following table summarizes the various summations necessary for the transformation of electronic operators and the calculation of the derivative couplings. For brevity, we have ommitted the summation symbol $\sum_{mn}^{M}$ from the entries of columns two and three. The

i	$A_{kl}^{(i)}$	$B_{kl}^{(i)}$	Type of terms
1	$c_{mk}c_{nl}\langle\alpha_k, m\vert\alpha_l, n\rangle$	$(-1)^n c_{mk}c_{nl}\langle\alpha_k, m\vert-\alpha_l, n\rangle$	0th-order direct/cross
2	$c_{mk}c'_{nl}\langle\alpha_k, m\vert\alpha_l, n\rangle$	$(-1)^n c_{mk}c'_{nl}\langle\alpha_k, m\vert-\alpha_l, n\rangle$	1st order direct/cross
3	$c_{mk}c_{nl}\langle\alpha_k, m\vert\alpha_l, n+1\rangle$	$(-1)^n c_{mk}c_{nl}\langle\alpha_k, m\vert-\alpha_l, n+1\rangle$	
4	$c'_{mk}c_{nl}\langle\alpha_k, m\vert\alpha_l, n+1\rangle$		2nd order direct
5	$c_{mk}c_{nl}\langle\alpha_k, m+1\vert\alpha_l, n+1\rangle$		
6	$c'_{mk}c'_{nl}\langle\alpha_k, m\vert\alpha_l, n\rangle$		

Table D.1: Summary of direct ($A_{kl}^{(j)}$) and complementary cross term ($B_{kl}^{(j)}$) summations used as auxilliary quantities to obtain operator matrix elements $\mathcal{O}_{kl}$ and non-BOA coupling f_{kli} and F_{kli} coming from first- and second-order derivative couplings respectively.

photon-added coherent state overlaps are given by Eq. (D.3) which may be recast as

$$\langle\alpha_k, m|\alpha_l, n\rangle = {}_1F_1(1+n, 1+n-m, \alpha_k\alpha_l)\alpha_l^{n-m}(n)_m \tag{D.28}$$

where $(n)_m = n(n-1)(n-(m-1))$ is the falling factorial and ${}_1F_1(a, b, c)$ is the Kummer confluent hypergeometric function. This form is particularly useful for numeric implementation. The un-normalized coefficients $\tilde{c}_{nl}$ are given as polynomials in α by the recurrence relation Eq. (4.32) with $\tilde{c}_{ol} = 1$. After solving Eq. (4.33), we obtain the α_l, and thus the $\tilde{c}_{nl}$, numerically. The sums given in Table D.1 can then be calculated and used to evaluate the three key quantities necessary for evaluation of signals (transformed electronic operators, and first and second derivative couplings), which we write here in terms of the easily calculated "tilde" and "bar" quantities for completion

$$\begin{aligned}
\hat{\mathcal{O}}_{kl} =& \frac{\hat{\mathcal{O}}_{gg} + \hat{\mathcal{O}}_{ee}}{2}(1 + \pi_k\pi_l)\bar{A}^{(1)}_{kl} + \frac{\hat{\mathcal{O}}_{gg} - \hat{\mathcal{O}}_{ee}}{2}(\pi_k + \pi_l)\bar{B}^{(1)}_{kl} \\
&+ \Re\{\hat{\mathcal{O}}_{eg}\}(1 - \pi_k\pi_l)\bar{A}^{(1)}_{kl} + i\Im\{\hat{\mathcal{O}}_{eg}\}(\pi_l - \pi_k)\bar{B}^{(1)}_{kl} \\
f_{kli} =& f_{egi}(\pi_l - \pi_k)\bar{B}^{(1)}_{kl} + (1 + \pi_k\pi_l)\big[\bar{A}^{(2)}_{kl} - \bar{A}^{(2)}_{ll}\bar{A}^{(1)}_{kl} + \alpha'_l\left(\bar{A}^{(3)}_{kl} - \bar{A}^{(3)}_{ll}\bar{A}^{(1)}_{kl}\right)\big] \\
F_{kli} =& \frac{F_{gg} + F_{ee}}{2}\delta_{kl} + \frac{F_{gg} - F_{ee}}{2}(\pi_l + \pi_k)\bar{B}^{(1)}_{kl} + F'_{eg}(1 - \pi_k\pi_l)\bar{A}^{(1)}_{kl} \\
&+ f_{egi}(\pi_k - \pi_l)\left[\big\{\big[\bar{B}^{(2)}_{kl} - \alpha'_l\bar{B}^{(3)}_{kl}\big] - (\bar{A}^{(2)}_{ll} + \alpha'_l\bar{A}^{(3)}_{ll})\bar{B}^{(1)}_{kl}\big\} + k \leftrightarrow l\right] \\
&+ (1 - \delta_{kl})(1 + \pi_k\pi_l)\left[\left(\alpha'_l\bar{A}^{(4)}_{kl} + \alpha'_k\bar{A}^{(4)}_{lk}) + \alpha'_k\alpha'_l\bar{A}^{(5)}_{kl} + \bar{A}^{(6)}_{kl}\right)\right. \\
&\left. + \left((\bar{A}^{(2)}_{kk} + \alpha'_k\bar{A}^{(3)}_{kk})(\bar{A}^{(2)}_{kl} + \bar{A}^{(3)}_{kl}) + k \leftrightarrow l\right) + A^{(1)}_{kl}(\bar{A}^{(2)}_{ll} + \alpha'_{)}\bar{A}^{(3)}_{ll})^2\right]
\end{aligned} \tag{D.29}$$